

What can we learn about light-meson interactions at electron–positron colliders?

Shuang-shi Fang^{1,2}, Bastian Kubis³, Andrzej Kupść^{4,5}

¹Institute of High Energy Physics, Chinese Academy of Sciences,
100049 Beijing, People’s Republic of China

²University of Chinese Academy of Sciences, 100049 Beijing, People’s Republic of China

³Helmholtz-Institut für Strahlen- und Kernphysik (Theorie) and Bethe Center for Theoretical Physics,
Universität Bonn, 53115 Bonn, Germany

⁴Uppsala University, Box 516, 75120 Uppsala, Sweden

⁵National Centre for Nuclear Research, 02-093 Warsaw, Poland

July 16, 2021

Abstract

Precision studies at electron–positron colliders with center-of-mass energies in the charm–tau region and below have strongly contributed to our understanding of light-meson interactions at low energies. We focus on the processes involving two or three light mesons with invariant masses below nucleon–antinucleon threshold. A prominent role is given to the interactions of the nine lightest pseudoscalar mesons (pions, kaons, η , and η') and the two narrow neutral isoscalar vector mesons ω and ϕ . Experimental methods used to produce the mesons are reviewed as well as theory tools to extract properties of the meson–meson interactions. Examples of recent results from the DAΦNE, BEPCII, and VEPP-2000 colliders are presented. In the outlook we briefly discuss prospects for further studies at future super-charm–tau factories.

Contents

1	Introduction	3
1.1	Light mesons and their interactions	3
1.2	Historical note	8
1.3	Meson resonances	10
1.4	Meson–meson scattering	12
1.5	Theory of low-energy strong interactions	17
1.5.1	Chiral perturbation theory	17
1.5.2	Dispersion relations; Omnès formalism	22
1.5.3	Inverse-amplitude method	23
1.5.4	Roy equations	24
1.6	Amplitude analyses for three-body decays	24

2	Experiments at symmetric electron–positron colliders	27
2.1	Experimental facilities	27
2.1.1	Frascati: DAΦNE and KLOE	27
2.1.2	Beijing: BEPC and BES	28
2.1.3	Novosibirsk: VEPP and SND, CMD	29
2.2	Production of hadronic systems	30
2.2.1	Single-photon annihilation	30
2.2.2	Strong and radiative decays of vector mesons	32
2.2.3	Higher-order electromagnetic processes	33
2.2.4	Tau lepton decays	36
2.2.5	Weak decays of K and D mesons	38
2.3	Radiative corrections	39
2.3.1	Initial-state-radiation corrections	39
2.3.2	Hadronic vacuum polarization	41
3	Example analyses	44
3.1	$e^+e^- \rightarrow P\bar{P}$	44
3.1.1	$e^+e^- \rightarrow \pi^+\pi^-$	44
3.1.2	$e^+e^- \rightarrow K^+K^-$ and $e^+e^- \rightarrow K_L K_S$	48
3.2	$e^+e^- \rightarrow PV$	50
3.3	$V \rightarrow P_1 P_2 \gamma$	56
3.3.1	Radiative ϕ decays	58
3.3.2	Radiative J/ψ decays	59
3.4	$P \rightarrow \pi^+\pi^-\gamma$	62
3.5	$D \rightarrow P_1 P_2 \ell^+ \nu_\ell$	65
3.6	$V \rightarrow V' P_1 P_2$	70
3.6.1	$\psi' \rightarrow J/\psi \pi \pi$	71
3.6.2	$J/\psi \rightarrow \omega(\pi^+\pi^-, K^+K^-)$ and $J/\psi \rightarrow \phi(\pi^+\pi^-, K^+K^-)$	72
3.6.3	Observation of $a_0^0(980) - f_0(980)$ mixing in $J/\psi \rightarrow \phi \eta \pi^0$	76
3.6.4	Search for isovector strangeonium-like states Z_s	77
3.7	$e^+e^- \rightarrow P_1 P_2 P_3$	78
3.7.1	Continuum cross sections	78
3.7.2	Dynamics of three-pion final states	81
3.8	Other $J/\psi \rightarrow \gamma X$ and $J/\psi \rightarrow VX$ reactions	86
3.8.1	Observation and properties of the $X(1835)$ state	86
3.8.2	$J/\psi \rightarrow \gamma \pi^+ \pi^- \pi^0 (3\pi^0)$	88
3.9	Strong three-body decays of nonvector states	88
3.10	Weak decays $D \rightarrow P_1 P_2 P_3$ and $\tau \rightarrow P_1 P_2 P_3 \nu_\tau$	94
4	Summary and perspectives	96

1 Introduction

1.1 Light mesons and their interactions

In principle, the spectrum and interactions of all hadrons can be deduced from Quantum Chromodynamics (QCD), the fundamental theory of the strong interactions. In general, up to this date this is an impossible task, we are often surprised by the discoveries of unexpected hadronic states [1–8] and do not understand their interactions. In the long term, the most promising approach to connect experimental data and the fundamental short-distance processes is lattice QCD. The vast majority of lattice QCD calculations to date have focused on the properties of states that are stable with respect to the strong forces, and these calculations have matured to the level where they can be considered realistic: they reproduce the masses of known hadronic states or calculate form factors and pseudoscalar meson decay constants [9]. A much more difficult task for lattice QCD is the determination of meson–meson scattering and three-body decays of resonances [10, 11].

Many present applications require a more precise description of the low-energy strong interactions than currently achievable from lattice QCD. One example is the unprecedented high-statistics data on hadronic systems from the presently running or planned facilities like LHCb [12], Belle-II [13], JLab [14], and PANDA [15]. Precision information on the interactions of the lightest mesons is crucial input for searches of physics beyond the Standard Model. There are two prominent examples of such applications: the interpretation of the muon $g - 2$ measurement [16], where the calculation of hadronic contributions within the Standard Model dominates the uncertainty [17, 18]; and studies of CP symmetry violations in s - and c -quark hadrons. Pion–pion final-state interactions have a large impact on the determination of ϵ'/ϵ from kaon decays [19–22], and final-state interactions predominantly between pions and/or kaons similarly affect D - and B -meson multihadronic decays [23–25]. Detailed knowledge of interactions of the known mesons is also necessary for the interpretation of the recently discovered exotic hadronic states. In particular, the most important question is if the states can be explained in terms of the long-range physics, such as final-state interaction of the known hadrons, molecular states, or threshold effects, or are the unambiguous signature of multiquark states or glueballs.

The required precision for the above applications can instead be reached by approaches based on effective field theories (EFT) using approximate low-energy symmetries of QCD, and general properties of field theories such as analyticity and unitarity (the mathematical consequences of causality and probability conservation) allow us to describe and interrelate results from various precision experiments. The main objects of the present review are the lowest-mass mesons, see Fig. 1, and their interaction amplitudes, see Fig. 2, the basic building blocks needed to study interactions in hadronic systems. One question is how to extract these amplitudes from data, and the other how to apply the extracted amplitudes to study multibody hadronic systems.

We start with the first question. QCD at very low energies can be expressed in terms of the pseudoscalar meson octet fields, see Fig. 1(a): the effective degrees of freedom connected to approximate, spontaneously broken chiral symmetry. Therefore the goal is to determine interactions of the pseudoscalar meson octet like $\pi\pi$, $K\pi$, and $K\bar{K}$. The two-body meson–meson scattering $1 + 2 \rightarrow 3 + 4$ shown schematically in Fig. 2(a) cannot be studied directly in experiments, since it is not possible to have mesonic targets and the availability of mesonic beams is limited to kaons and charged pions. Therefore the interaction will in general be a sub-process that should be extracted from more complicated reactions. Ideally it will be well isolated or embedded in a well-understood process (in particular, electromagnetic or weak). In addition it should have a cross section large enough to provide a sufficient number of events for precision studies. Finally, it should provide access to a reasonable range of kinematic variables in the meson–meson scattering sub-process. These variables can be expressed in terms

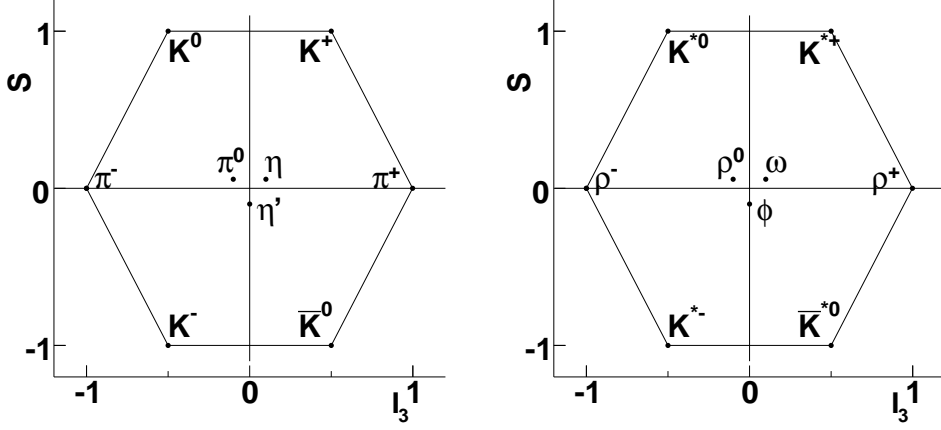


Figure 1: Lowest-mass meson nonets in the quark model: (a) pseudoscalar mesons; (b) vector mesons.

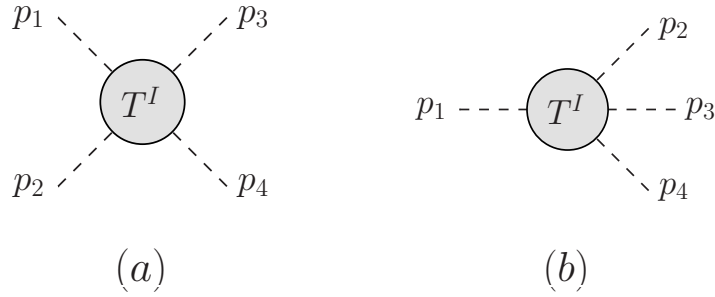


Figure 2: (a) A generic meson–meson scattering amplitude (of isospin I); (b) a three-body meson decay, linked to (a) by crossing symmetry.

of the following Mandelstam invariants defined as

$$s = (p_1 + p_2)^2, \quad t = (p_1 - p_3)^2, \quad u = (p_1 - p_4)^2, \quad (1)$$

where p_i are the four-momenta as indicated in Fig. 2(a). The sum of the three variables is equal to the sum of squares of the masses of the initial and final particles:

$$s + t + u = m_1^2 + m_2^2 + m_3^2 + m_4^2 \equiv 3s_0. \quad (2)$$

The kinematic regions are illustrated in Fig. 3. The colored regions represent experimentally accessible processes related by crossing symmetry: $1 + 2 \rightarrow 3 + 4$ (s -channel), $1 + \bar{3} \rightarrow \bar{2} + 4$ (t -channel), and $1 + \bar{4} \rightarrow \bar{2} + 3$ (u -channel). In addition, if $m_1 > m_2 + m_3 + m_4$ the decay process $1 \rightarrow \bar{2} + 3 + 4$ shown in Fig. 3(b) is also possible. The partial-wave decomposition of the amplitude for spinless particles in $1 + 2 \rightarrow 3 + 4$ scattering of total isospin I reads

$$T^I(s, \cos \theta) = 16\pi S \sum_{\ell=0}^{\infty} (2\ell + 1) t_{\ell}^I(s) P_{\ell}(\cos \theta), \quad (3)$$

where θ is the scattering angle between particles 3 and 1 in the $1 + 2$ center-of-mass (c.m.) system directly related to the variable t , P_{ℓ} are the Legendre polynomials, and the symmetry factor is given by $S = 2$ for identical particles and $S = 1$ otherwise. The partial-wave amplitude t_{ℓ}^I corresponding to angular momentum ℓ can be expressed in terms of phase δ_{ℓ}^I and inelasticity η_{ℓ}^I according to

$$t_{\ell}^I = \frac{\eta_{\ell}^I \exp(2i\delta_{\ell}^I) - 1}{2i}. \quad (4)$$

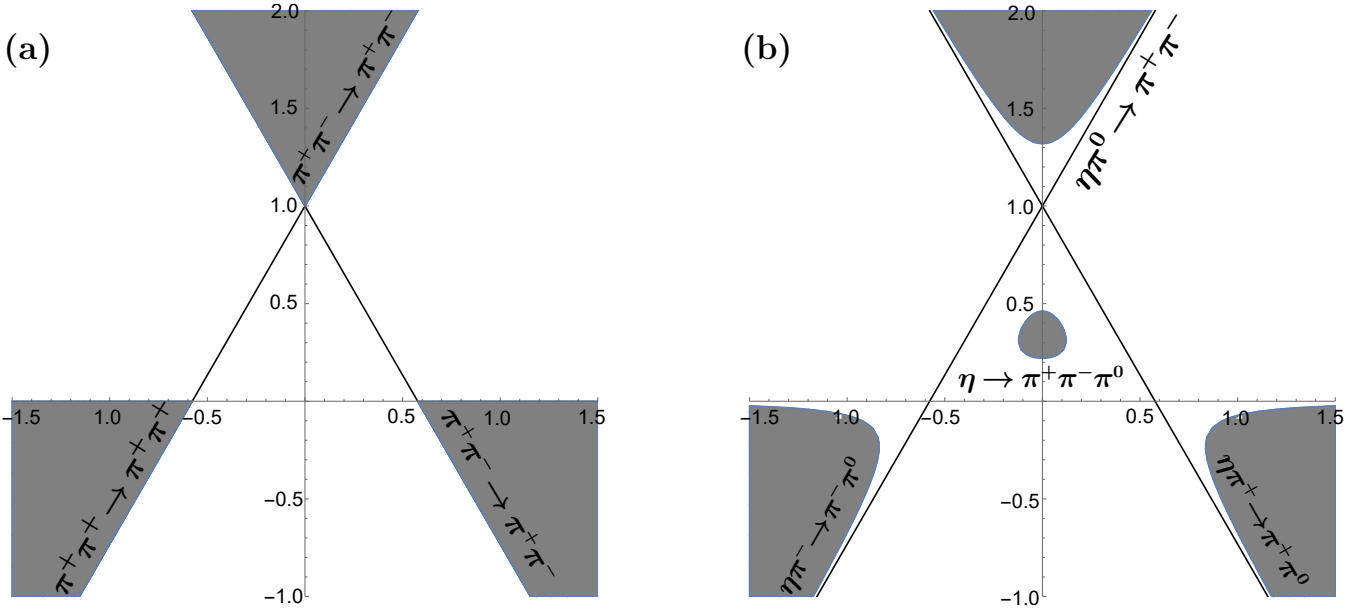


Figure 3: Mandelstam planes indicating physical regions as shaded areas for (a) $\pi^+\pi^- \rightarrow \pi^+\pi^-$ and (b) $\eta\pi^0 \rightarrow \pi^+\pi^-$ and the corresponding crossed channels. The units are chosen such that the vertical axes correspond to $s/(3s_0)$ and the horizontal ones to $(t-u)/(6s_0)$; see Eq. (2). The borders of the regular triangle denote the lines $s=0$, $t=0$, and $u=0$. The physical regions for the s -, t -, and u -channels are located at the top, right, and left, respectively, with the decay region for $\eta \rightarrow \pi^+\pi^-\pi^0$ at the center of the Mandelstam plane.

Traditional experimental approaches to study meson scattering with pions use reactions like $\pi^\pm N \rightarrow \pi\pi N$, $\pi^\pm N \rightarrow K\bar{K}N$, or $KN \rightarrow K\pi N$. For low four-momentum transfer squared t , one-pion-exchange is assumed to be the main contribution as shown in Fig. 4(a), and meson-meson scattering is supposed to be kinematically well separated. Many such experiments were performed in the past, see Refs. [26–29], but they only allow to study $\pi\pi$ and $K\pi$ scattering and are often plagued by ambiguities or large systematic effects. Another example of kinematic separation at high-energy hadron accelerators is central production; e.g., the reaction $pp \rightarrow p(MM)p$ at large c.m. energies where the regions with low four-momentum transfer to the final protons are selected [30–33]. The two mesons produced are well separated from the protons in rapidity, and their production is well described within the Regge model [34]. The reaction can be regarded as $(p\bar{p})(p\bar{p}) \rightarrow \pi\pi$, where the $(p\bar{p})$ exchanges have vacuum quantum numbers carried by the “pomeron”, see Fig. 4(b). Such a reaction is in many ways similar to the $\gamma\gamma \rightarrow \pi\pi$ process. Another well-known process is the semileptonic kaon decay $K^\pm \rightarrow \pi^+\pi^- e^\pm\nu$, the so-called K_{e4} decay mode, where a recent example comes from the NA48/2 experiment [35]. The processes involve only two hadrons in the final state. The formalism for studies of such reactions was given by Cabibbo and Maksymowicz in 1965 [36].

The aim of this review is to show a broad spectrum of precision light-hadron experiments carried out at the modern high-intensity electron-positron colliders. Here, the elementary electroweak production mechanisms shown in Fig. 4(c) can provide very clean conditions to study the strong interactions in few-meson systems. The initial approach was to study the energy dependences of the single-photon annihilation processes into $\pi^+\pi^-$, K^+K^- , and $K_S K_L$ pairs, which is closely related to P -wave two-meson scattering amplitudes. However, a variety of options are available to determine two-meson scattering amplitudes in a direct and clean way, using reactions where only two hadrons are involved. These reactions are in the first place higher-order electromagnetic processes involving initial- or final-

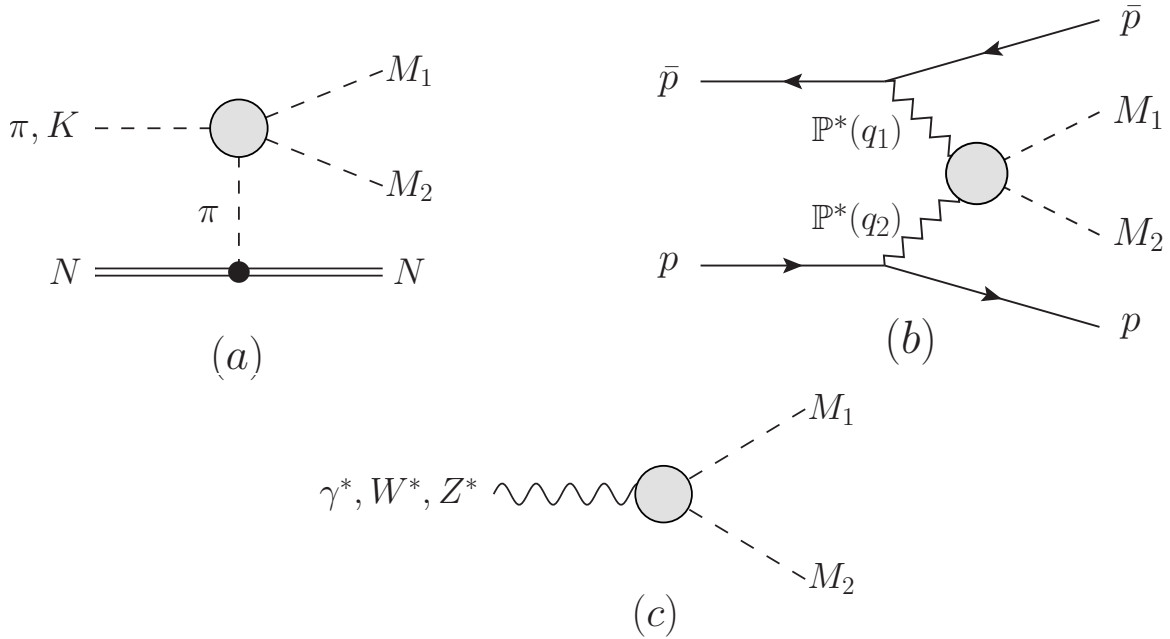


Figure 4: Examples how two-meson isolated systems can be produced for studies of their interactions: (a) one-pion-exchange mechanism to study $\pi\pi$ and $K\pi$ scattering amplitudes; (b) double-Pomeron production; (c) production of hadronic systems via an elementary gauge boson.

state photon radiation. Examples are radiative decays of neutral vector mesons directly produced in electron–positron annihilation, such as $\phi \rightarrow \pi^0\pi^0\gamma$ [37,38] or $J/\psi \rightarrow \pi^0\pi^0\gamma$ [39]. These radiative decays give access to meson systems with scalar quantum numbers, whose investigation was motivated by the search for a scalar glueball candidate in the 1 GeV range, and the quest for an understanding of the nature of the lowest-mass scalar mesons. The decay channels of such potentially exotic systems are essentially restricted to the $\pi\pi$ and $K\bar{K}$ final states. Radiative decays of quarkonia were advertised as an ideal place to search for bound states created in gluon–gluon fusion [40–44]. However, as it was pointed out by Au, Morgan and Pennington [45] any production process is very tightly related to scattering reactions, $\pi\pi \rightarrow \pi\pi$ and $\pi\pi \rightarrow K\bar{K}$, by unitarity. Therefore it cannot reveal effects that could not be seen in the scattering reactions, but it can act as a filter to suppress backgrounds and enhance the signal. Other examples are two-photon formation processes such as $\gamma\gamma \rightarrow \pi^+\pi^-$ as studied at Belle [46]. Electron–positron colliders are also sources of τ lepton pairs, which allow studies of hadronic weak decays like $\tau^- \rightarrow \pi^-\pi^0\nu_\tau$ or $\tau^- \rightarrow K^-\pi^0\nu_\tau$.

Another option is amplitude analyses of multi-meson decays. Such hadronic decays have large branching fractions and often provide “infinite” statistics, in the sense that the statistical uncertainties are negligible. In recent years there has been a lot of progress in the development of precision analysis tools for processes involving three and more hadrons in the final state. There is a trend to base the tools on sound conjectures such as the analytic properties of the transition matrix. Analyses of such reactions normally use two-meson interaction amplitudes as their building blocks. However, in case the amplitudes are not known sufficiently well, it is possible to validate or even extract information on the two-body meson processes. We will discuss three-meson decays in which the decaying particles are abundantly produced and easily tagged at electron–positron colliders. Some examples include multi-hadron decays: weak decays of τ leptons or K and D mesons as well as strong and radiative decays of mesons.

The scope of this review is limited to the interactions in systems of two and three stable mesons with invariant mass below ~ 2 GeV, i.e., below baryon–antibaryon pair production threshold. This choice is

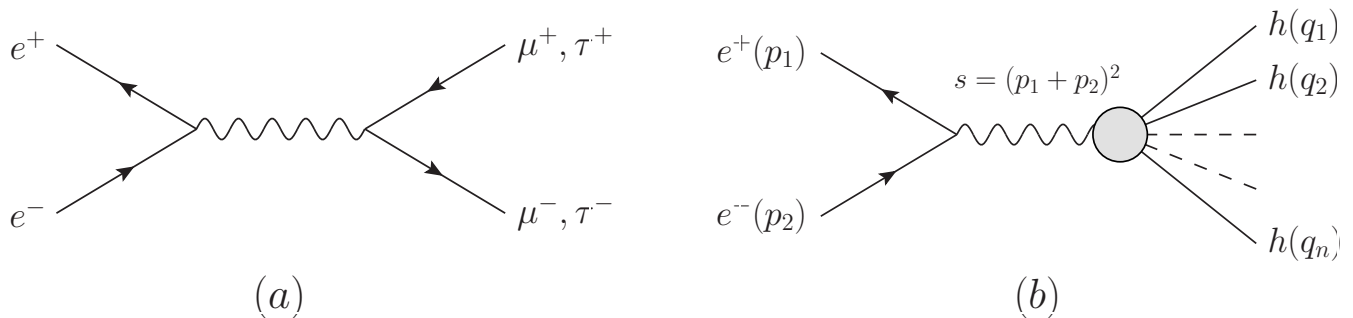


Figure 5: Lowest-order diagrams representing particle production in single-photon electron–positron annihilation: a) lepton–antilepton pairs $\mu^+\mu^-$ or $\tau^+\tau^-$; b) production of a multi-hadron system.

motivated by the applicability of the methods used for the analysis and extraction of meson interaction amplitudes (dispersive as well as based on chiral symmetry). For colliders with c.m. energies up to the charm–tau region, the main annihilation process into a lepton–antilepton or quark–antiquark pair proceeds via an intermediate photon. The leading order of such annihilation processes $e^+e^- \rightarrow \mu^+\mu^-$ or $\tau^+\tau^-$ is shown in Fig. 5(a). The contribution from Z or Z – γ interference in the propagator at these energies is negligible. However, with c.m. energies close to narrow vector resonances, one should consider hadronic vacuum polarization contributions in the propagator, as we will discuss in Sec. 2.3.2.

The main mechanism for the production of hadronic systems at electron–positron colliders is shown in Fig. 5(b). The electron–positron pair annihilates via a single virtual photon, and a hadronic system is produced. The system has therefore the same $J^{PC} = 1^{--}$ quantum numbers as the photon. The lightest hadronic system that can be created in such an annihilation is $\pi^+\pi^-$, with the c.m. electron–positron energies above $\sqrt{s} = 2m_\pi$. However, the lightest hadron, the π^0 meson, can be created in a higher-order radiative process $e^+e^- \rightarrow \pi^0\gamma$ already at $\sqrt{s} > m_{\pi^0}$, but the cross section is very low. For c.m. energies at which hadrons can be produced, the mass of the electron is negligible and the virtual photon has only helicities ± 1 (no 0 projection). The cross section of $e^+e^- \rightarrow$ hadrons is dominated by $e^+e^- \rightarrow \pi^+\pi^-$ and $e^+e^- \rightarrow \pi^+\pi^-\pi^0$ for the isospin states $I = 1$ and $I = 0$, respectively, at low energies. The contribution of the two channels to the total cross section is shown in Fig. 6. In addition, the final states $K^+K^-/K_S K_L$, $\eta\pi^+\pi^-$, and $\pi^+\pi^-\pi^+\pi^-/\pi^+\pi^-\pi^0\pi^0$ are included. The sum of these approximately saturates the total cross section up to 1.2 GeV. The result is not exact since for the exclusive data, we used an arbitrary parameterization included in the Phokara program [47].

When the concept of the electron–positron collider was first proposed (see Sec. 1.2), the main physics motivation was to study the time-like pion vector form factor directly accessible in the process $e^+e^- \rightarrow \pi^+\pi^-$. Precise studies of this process are still most relevant today in the context of the hadronic contribution to the muon anomalous magnetic moment [18]. The energy dependence of the total cross section for electron–positron annihilation into hadrons directly reveals the crucial role of the neutral vector mesons with quantum numbers $J^{PC} = 1^{--}$, identical to those of the photon. The production yield of hadronic systems is greatly enhanced at c.m. energies tuned to one of such resonances. Decays of the mesons represent one of the main approaches to study hadronic systems at low-energy electron–positron colliders discussed in the present review.

In more detail we will discuss processes where two and three pseudoscalar mesons are produced both in the continuum and at certain (narrow) resonances. A special case is when the produced vector meson decays in sequence, where the first step is a radiative two-body process involving narrow hadronic state like η , η' , or χ_{cJ} . Another important class is decays of K and D/D_s mesons, which are produced in single-photon processes as entangled pairs. Again the cross section is enhanced when the beams are at resonances such as the ϕ for $K\bar{K}$ or $\psi(3770)$ for $D\bar{D}$ production. Finally, the light-meson systems can be produced in decays of τ leptons, which are in turn produced via $e^+e^- \rightarrow \tau^+\tau^-$.

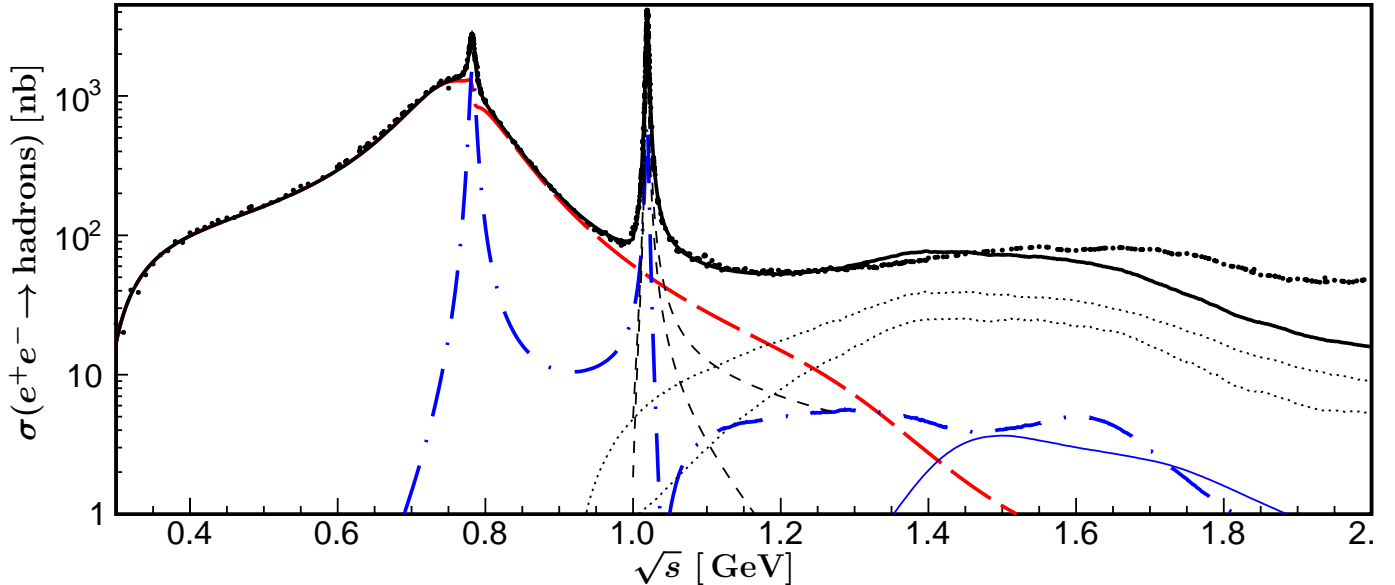


Figure 6: Cross sections for electron–positron annihilation to hadrons. Data points are from the Particle Data Group compilation [48]. Lines represent parameterizations of the individual contributions from the main final states from Phokara [47]. Included final states are: $\pi^+\pi^-$ (red long-dashed line), $\pi^+\pi^-\pi^0$ (blue dashed–dotted line), K^+K^- and $K_S K_L$ (black dashed lines), $\pi^+\pi^-\pi^+\pi^-$ and $\pi^+\pi^-\pi^0\pi^0$ (black dotted lines), and $\eta\pi^+\pi^-$ (blue solid line). The sum, shown as the black solid line, approximately saturates the total cross section up to 1.2 GeV.

1.2 Historical note

The concept of electron–positron colliders was triggered by technical developments in electron accelerators, the idea of colliding beams [49–51], and by discoveries of the first vector meson resonances in the beginning of the 1960s. The culmination of this first stage of development was the discovery of the J/ψ particle during the “November revolution” in 1974: at BNL [52] (November 12th) and at SLAC [53] (November 13th). A week after, the discovery was confirmed at Laboratori Nazionali di Frascati (LNF) Frascati [54] (November 18th). Two of the observations were made using electron–positron colliders, demonstrating the potential of the new machines.

We try to give a brief account of the crucial events before the November revolution [55–61]. The advantages of the center-of-mass collision scheme were well known in the mid-1950s [51], and by the end of the decade the idea of a particle collider was technically mature to be considered seriously. Gerard O’Neill had proposed an electron–electron storage ring collider at SLAC [50] and the plans were presented at CERN in June 1959. The physics motivation was high-precision experiments and tests of the predictions of Quantum Electrodynamics (QED), in particular tests of the space-like photon propagator [62]. This collider project was presented during a seminar at LNF in October 1959 by Pief Panofsky. One of the listeners was Bruno Touschek, who during the discussion reportedly asked the question [59]: “Why not try electrons against positrons?” Touschek’s vision was “that electron–positron annihilations—reactions proceeding through a state of well-defined quantum numbers—would be the pathway to new physics” [60]. For the collider concept the particle and antiparticle beams with opposite charges and the equal masses are particularly simple and appealing since they can be stored in one single ring, while the electron–electron collider requires two separate rings. This is considered to be the starting point of the chain of events leading to the first prototype electron–electron storage ring (AdA—Anello di Accumulazione) and further projects at LNF.

The question was what purpose such a machine could be used for. The first ideas were in fact

related to tests of the electron’s space-like propagator. To understand the emergence of the concept of the unique role of electron–positron colliders due to the “time-like one-photon channel dominating, to first order of Quantum Electrodynamics, the production of final states” [63], let us turn to the status of the theory of strong interactions at that time.

From the available data on pion production in pion-induced reactions above energies of 1 GeV it had become clear that a small momentum transfer to the nucleon is preferred. This was seen in the nucleon angular distributions, which are sharply peaked in the backward direction. These results suggested the importance of large-impact-parameter collisions in such processes. The simplest mechanism that could contribute is the beam pion colliding with a virtual (nearly real) pion emitted by the target nucleon. The quantitative aspects of such collisions were discussed by Chew and Low [64], as well as Salzman and Salzman [65], as means of extracting information on the $\pi\pi$ interactions from $\pi N \rightarrow \pi\pi N$ data [66].

On the other hand, experimental studies of elastic electron scattering off protons and deuterons, carried out by Hofstadter et al. [67], had raised the question of photon interactions with nucleons. It seemed logical to assume that also here the long-range domain would be dominated by the interaction with systems of the lightest hadrons—pions. The role of the photon–two-pion vertex for the explanation of the nucleons’ anomalous magnetic moments was investigated by G. F. Chew et al. [68] in 1958, using dispersion relations developed for the analyses of the pion–nucleon scattering. In a follow-up paper by P. Federbush et al. [69], the dispersive analysis was extended and the concept of the pion form factor $F_\pi^V(s)$ was introduced to represent the structure of the photon–two-meson vertex. An important part of the photon–nucleon interactions can be understood in this way via an isovector $\pi^+\pi^-$ pair, linking the isovector nucleon form factors to the pion form factor and $\pi\pi \rightarrow N\bar{N}$ P -wave amplitudes. This relation has been exploited repeatedly, with ever more accurate experimental input, in the following decades [70–74] (see also Ref. [75] for a broader review on nucleon form factors). The properties of the pion form factor $F_\pi^V(s)$ can in turn be related to $\pi^+\pi^-$ elastic rescattering using dispersion relations. With

$$F_\pi^V(s) = 1 + \frac{s}{\pi} \int_{4m_\pi^2}^{\infty} dx \frac{\text{Im} F_\pi^V(x)}{x(x-s-i\epsilon)}, \quad (5)$$

setting $F_\pi^V(s) = \exp\{i\varphi(s)\} |F_\pi^V(s)|$ and assuming the phase $\varphi(s)$ to be known, the expression for the form factor is

$$F_\pi^V(s) = P(s) \exp \left\{ \frac{s}{\pi} \int_{4m_\pi^2}^{\infty} dx \frac{\varphi(x)}{x(x-s-i\epsilon)} \right\}, \quad (6)$$

where $P(s)$ is an arbitrary polynomial. In case of elastic $\pi\pi$ rescattering, $\varphi(s) = \delta_1^1(s)$, the pion–pion P -wave phase shift of isospin $I = 1$. The paper points out that there was no experimental or theoretical information on the pion–pion scattering phase shifts. The phases δ_1^1 are real for $s < 16m_\pi^2$, i.e., below threshold for the production of two additional pions, since production of any odd number of pions is forbidden by G parity [76]. In February 1960, Cabibbo and Gatto proposed to use the reaction $e^+e^- \rightarrow \pi^+\pi^-$ to study the pion form factor in the time-like region [77]. Meanwhile the dispersive analyses were further extended and an isovector $\pi\pi$ resonance was proposed by Frazer and Fulco [70, 78]. Such a structure should be directly observed as a peak in electron–positron collisions. We will continue a detailed discussion of the properties of $F_\pi^V(s)$ in Sec. 3.1.

On the other hand, to explain the neutron charge structure emerging from the Hofstadter experiments, a strong coupling of the photon to an isoscalar hadronic current was required. The lightest such system consists of three pions $\pi^+\pi^-\pi^0$ in the $J^{PC} = 1^{--}$ state. Here, each pair of the pions is in a relative P -wave. The dispersive treatment of such three-body systems is much more complicated, but already in 1957 Nambu [79] speculated about the existence of an isoscalar three-pion bound state or a strongly decaying resonance (if the mass was sufficiently high). Such a state would be narrow and thus simplify the analysis of the isoscalar part of the electromagnetic current. The idea of both isovector and isoscalar $J^{PC} = 1^{--}$ mesons was then extended on $SU(3)$ flavor symmetry grounds to

include an additional neutral isoscalar vector meson by Sakurai in 1960 [80], leading to the concept of vector meson dominance (VMD). These three neutral vector mesons were discovered soon after. In 1961 a broad ρ^0 isovector vector resonance was observed by Erwin et al. [81], and an isoscalar ω meson by Maglic et al. [82]. In the following year in July 1962, the third meson $\phi(1020)$ was observed by Bertanza et al. [83] and confirmed in 1963 by two experiments [84, 85]. In parallel to these discoveries a comprehensive physics program for electron–positron colliding beam experiments was formulated by Cabibbo and Gatto in the so-called “Bible” [86].

The technological milestones towards electron–positron colliders can be summarized as follows. A proof-of-concept storage ring AdA at the LNF was proposed in February 1960 [87], with beam energies up to 250 MeV and a diameter of 1.3 m. The first electrons and positrons were accumulated in AdA in February 1961 [88, 89]. Tests continued in 1963 at the Orsay Laboratory where the ring was moved and resulted, e.g., in the discovery of the so-called Touschek effect [90, 91]. Soon after the AdA, research electron–positron colliders were proposed, both in the USA and in Europe, with higher energies and luminosities. At LNF the construction of ADONE with 1.5 GeV energy per beam was proposed as early as January 1961, ACO with 550 MeV beam energies at Orsay, and SPEAR [92] in the USA. Parallel independent efforts took place in the Soviet Union, where Gersch Budker and collaborators had been active in electron–electron colliders since the mid 1950s, and later in electron–positron collisions. A historic account of these events in Novosibirsk is given in Refs. [57, 93]. The first Novosibirsk e^+e^- collider VEPP-II with beam energies of 700 MeV began to produce physics data in 1966; shortly after ACO came into operation, and the first data at ADONE was taken in 1969. These physics topics and detectors of the early period of electron–positron accelerators are well described in a report from 1976 [94]. In some sense our review can be treated as a modern revision of the physics topics discussed there.

1.3 Meson resonances

The review focuses on interactions of stable mesons, i.e., mesons that do not decay strongly or whose strong decays are suppressed. These are in the first place pseudoscalar mesons from the ground state octet and the η' meson. They play a special role in the description of the low-energy domain of QCD. Among the few meson resonances with masses up to the $\phi(1020)$, see Fig. 7, there are only two narrow states the neutral vector mesons ω and ϕ . We try to treat the remaining light vector mesons $\rho(770)$ and $K^*(892)$, as well as the scalar states $f_0(500)$ (formerly known as σ), $f_0(980)$, and $a_0(980)$ as resonances in the systems of the pseudoscalar mesons, as they are much broader, and the narrow-width approximation much less reliable. Interactions between pairs of pseudoscalar mesons are a main source of information about the spectrum and structure of scalar mesons. From the perspective of the present review, the low-mass scalar meson spectrum is of interest as a probe of the interactions of the nonet of pseudoscalar mesons, since it allows us to test chiral perturbation theory and dispersive methods.

Above 1 GeV there are a large number of meson resonances. The spectrum of the flavor neutral states with masses below 2 GeV is shown in Fig. 8,¹ and the naming convention introduced by the Particle Data Group (PDG) given in Table 1. In this energy range, the lightest purely gluonic bound state, a *glueball*, is expected with scalar quantum numbers [95]. The observation of such a state would be the evidence that gluon self-interactions can generate a massive meson. Unfortunately, glueballs may mix with conventional quark bound states, making the interpretation of candidate resonances challenging. Despite the availability of a large amount of data on $\pi\pi$ and $K\bar{K}$ scattering in the low-mass region, the existence and characteristics of isoscalar scalar ($I^G J^{PC} = 0^+0^{++}$) and tensor (0^+2^{++}) states remain controversial [1]. This lack of understanding is due in part to the presence of broad, overlapping resonances, which are poorly described by most analytical methods. The PDG reports

¹All values for masses and widths of resonances as well as branching fractions in the review are taken from the Particle Data Group [48] unless otherwise stated.

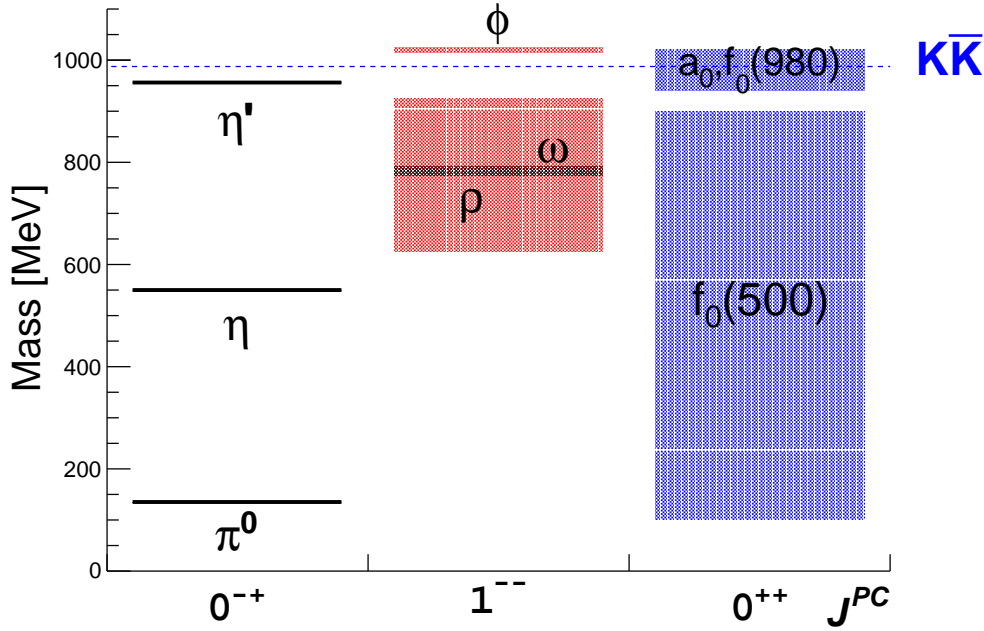


Figure 7: Spectrum of the flavor-neutral mesons with masses below 1 GeV. The masses and widths of the lightest states are represented schematically. In addition, the $K\bar{K}$ threshold for open strangeness is indicated explicitly.

Table 1: Naming convention for meson states according to Particle Data Group [48].

J	PC	$I = 1$	$I = 0$
$0, 2, \dots$	$-+$	π	η, η'
$1, 3, \dots$	$+-$	b	h, h'
$0, 1, 2, \dots$	$++$	a	f, f'
$1, 2, 3, \dots$	$--$	ρ	ω, ϕ

eight 0^+0^{++} mesons, which have widths between 100 and 450 MeV. Several of these states, including the $f_0(1370)$, are characterized only by ranges of values for their masses and widths.

For the energy region discussed in this review, the $s\bar{s}$ mesons, strangeonia, are also of relevance. In Fig. 9 the expected spectrum of the states with spin $J < 4$ predicted by the 3P_0 model [96, 97] is shown. Only seven states (indicated with the solid lines) have been assigned to the observed mesons and many members of the spectrum are still missing. The established states are $\eta'(954)$ [1^1S_0], ϕ [1^3S_1], $h_1(1380)$ [1^1P_1], $f_1(1420)$ [1^3P_1], $f'_2(1525)$ [1^3P_2], $\phi(1680)$ [2^3S_1], $\phi_3(1850)$ [1^3D_3]. Another possible strangeonium is the $\phi(2170)$, which can be either a 3^3S_1 or a 2^3D_1 state. It was first observed in the initial-state radiation (ISR) process $e^+e^- \rightarrow \gamma\phi f_0(980)$ [98] with a mass $m = 2175(18)$ MeV and width $\Gamma = 58(26)$ MeV. The poor experimental situation is due to the small production rates in low-energy hadronic processes, the large widths of the strangeonia since all states except for the η' are above $K\bar{K}$ threshold, and significant mixing with $u\bar{u}$ and $d\bar{d}$ states. High-statistics electron-positron machines in the charm region are especially well suited to study these states [99], since there is a significant fraction of $s\bar{s}$ states produced by the electromagnetic current (compare the discussion in Sec. 2.2).

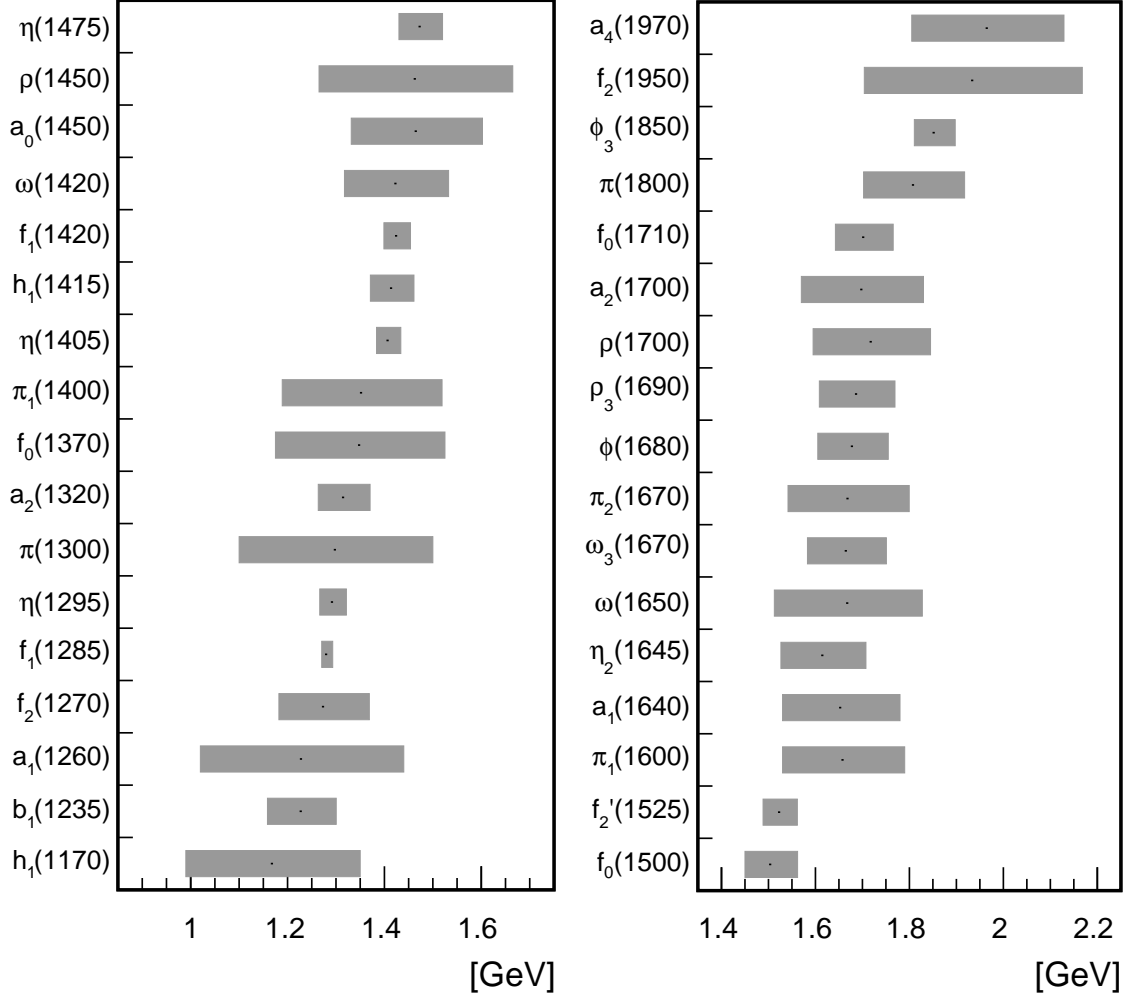


Figure 8: Spectrum of the well-established flavor-neutral meson resonances with masses in the range 1–2 GeV. The mass of a resonance is represented by the center of the shaded box, the decay width by its horizontal size.

1.4 Meson–meson scattering

Isospin and crossing symmetry allow us to relate amplitudes of different scattering processes of the π , K , and η mesons, such that all possible amplitudes can be expressed in terms of only eight independent ones. Pion–pion scattering in the isospin limit is strongly constrained by crossing symmetry, see Figs. 2(a) and 3(a). It can be expressed in terms of a single function $A(s, t, u)$ according to

$$M(\pi^a \pi^b \rightarrow \pi^c \pi^d) = \delta^{ab} \delta^{cd} A(s, t, u) + \delta^{ac} \delta^{bd} A(t, u, s) + \delta^{ad} \delta^{bc} A(u, s, t). \quad (7)$$

The amplitudes of definite isospin are given in terms of this by

$$\begin{aligned} T^{I=0} &= 3A(s, t, u) + A(t, u, s) + A(u, s, t), \\ T^{I=1} &= A(t, u, s) - A(u, s, t), \\ T^{I=2} &= A(t, u, s) + A(u, s, t). \end{aligned} \quad (8)$$

Kaon–pion scattering is obviously less symmetric, but similarly given in terms of a single function: crossing relates $K\pi \rightarrow K\pi$ to $K\bar{K} \rightarrow \pi\pi$. The possible isospin amplitudes $I = 1/2, 3/2$ and $I =$

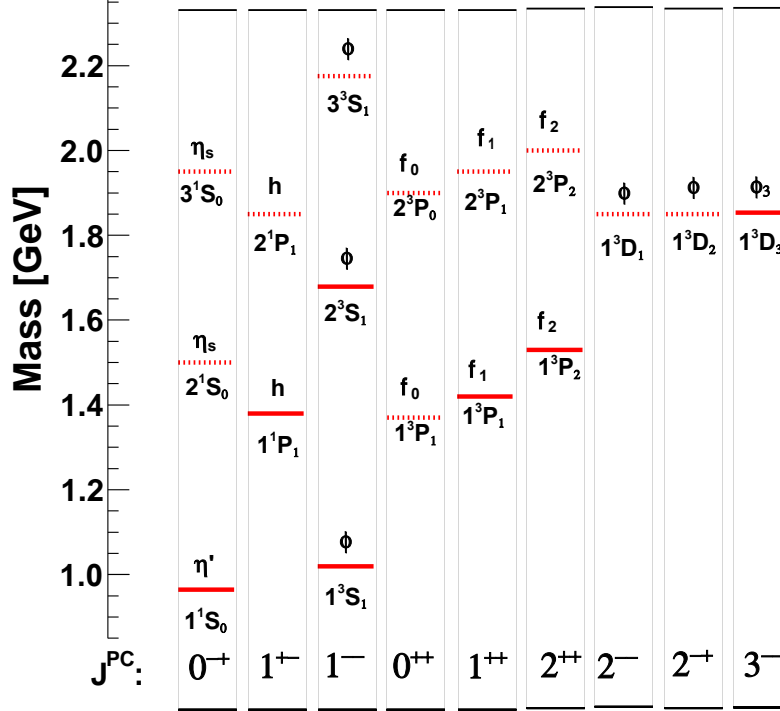


Figure 9: Spectrum of $s\bar{s}$ states with spin $J < 4$, predictions from Ref. [97]. Experimentally confirmed states are indicated by solid lines.

0, 1, respectively, can be expressed by one $I = 3/2$ amplitude corresponding to the $K^+\pi^+ \rightarrow K^+\pi^+$ process [100, 101]. $\bar{K}K$ scattering can be of total isospin $I = 0, 1$, which can be obtained as linear combinations of elastic K^+K^- as well as charge-exchange $K^+K^- \rightarrow K^0\bar{K}^0$ scattering [101]. The remaining processes involve just one isospin amplitude each: crossing symmetry relates $K\pi \rightarrow K\eta$ ($I = 1/2$) to $\bar{K}K \rightarrow \pi\eta$ ($I = 1$), $K\eta \rightarrow K\eta$ ($I = 1/2$) to $\bar{K}K \rightarrow \eta\eta$ ($I = 0$), and $\pi\eta \rightarrow \pi\eta$ ($I = 1$) to $\pi\pi \rightarrow \eta\eta$ ($I = 0$); the final process is $\eta\eta$ scattering.

Traditionally the experimental information about pseudoscalar meson scattering comes from πN and KN meson production experiments, where peripheral events are assumed to be dominated by the t -channel single-meson exchange. In particular phase shifts for $\pi\pi$ scattering for low partial waves were studied in detail in the past. A compilation of meson-meson scattering amplitudes $t_\ell^I(s)$ (related to phase shifts $\delta_\ell^I(s)$ and inelasticity parameters $\eta_\ell^I(s)$ via Eq. (4)) for $\sqrt{s} < 1.2$ GeV and $\ell = 0, 1$ from Ref. [101] is shown in Fig. 10. The theoretical curves shown for comparison are calculated using the inverse-amplitude method, which we will briefly introduce in Sec. 1.5.3. Here is an extensive caption of this figure:

- Amplitude $t_1^1(s)$, states $\pi\pi$ and $K\bar{K}$. In Fig. 10(a) data on the $\pi\pi$ scattering phase shift from Refs. [26] (squares) and [27] (triangles) is shown. This channel is completely dominated by the $\pi\pi$ state and the ρ resonance therein, and there is almost no inelasticity due to $K\bar{K}$ production below 1200 MeV; in fact, the inelasticity is rather dominated by 4π , especially clustered as $\pi\omega$ above its threshold [102]. The $(1 - |\eta_1^1|^2)/4$ points from Ref. [103] are shown in the lowest part of Fig. 10(d).
- Amplitude $t_0^0(s)$, states $\pi\pi$, $K\bar{K}$, and $\eta\eta$. By general consent, the coupling of the $\eta\eta$ state is believed to be rather weak, such that this amplitude is often described as a two-channel system $\pi\pi \leftrightarrow K\bar{K}$. In this case, there are three observables with several sets of data, which, as can be

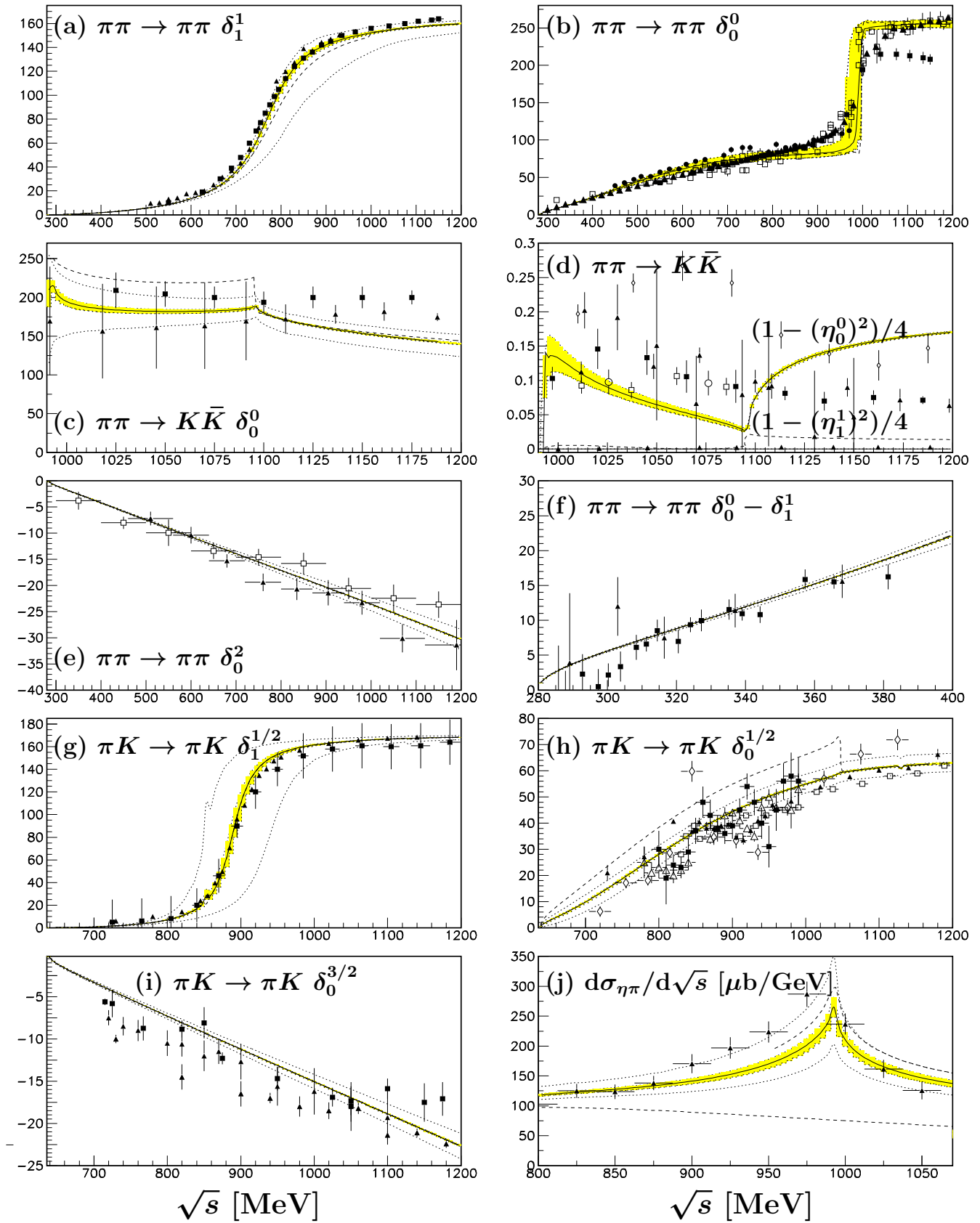


Figure 10: Compilation of experimental data on pseudoscalar meson–meson scattering amplitudes. See description in the text. Figure adapted from [101].

seen in Figs. 10(b), (c), and (d), are somewhat incompatible. For the $\pi\pi$ scattering phase shift δ_0^0 , see Fig. 10(b), the experimental data is from Refs. [29] (open squares), [26] (solid squares), [27] (solid triangles), and [104] (solid circles). Concerning the $\pi\pi \rightarrow K\bar{K}$ phase, the data in Fig. 10(c) corresponds to Refs. [103] (solid triangles) and [105] (solid squares); both are reasonably compatible. Figure 10(d) shows data for $(1 - |\eta_0^0|^2)/4$, which contains the information on the modulus of the $\pi\pi \rightarrow K\bar{K}$ amplitude. At higher energies, further inelastic channels become relevant, in particular 4π .

- Amplitude $t_0^2(s)$, state $\pi\pi$. In Fig. 10(e) the δ_0^2 phase shifts from Refs. [106] (open squares) and [107] (solid triangles) are displayed.
- Amplitude $t_1^{1/2}(s)$, states $K\pi$ and $K\eta$. The $K\pi$ P -wave resonating in the $K^*(892)$ couples very weakly to $K\eta$, which is usually ignored; the inelasticity at higher energies is rather due to $K\pi\pi$ intermediate states (see, e.g., Ref. [108]). Fig. 10(g) shows data on $\delta_1^{1/2}(s)$ from Refs. [109] (solid squares) and [110] (solid triangles). — The amplitude $t_1^{3/2}(s)$ ($K\pi$) is very weak and usually disregarded.
- Amplitude $t_0^{1/2}(s)$, states $K\pi$ and $K\eta$. Again, $K\eta$ is phenomenologically in fact not the most relevant inelasticity for the $K\pi$ S -wave, which is rather $K\eta'$ (at a much higher threshold) [111]. The data in Fig. 10(h) comes from Refs. [109] (solid squares), [112] (open triangles), [113] (open diamonds), [110] (solid triangles), and [114] (open squares).
- Amplitude $t_0^{3/2}(s)$, state $K\pi$. The data sets from [110] (solid squares) and [115] (solid triangles) are plotted in Fig. 10(i).
- Amplitude $t_1^1(s)$, states $\pi\eta$ and $K\bar{K}$. Fig. 10(j) shows the $\pi\eta$ effective-mass distribution from the $pp \rightarrow p(\eta\pi^+\pi^-)p$ reaction [116].

The extrapolations cause most of the deviations between the analyses, where a single data set can lead to contradictory results due to different assumptions and approximations. Some of the $K\pi \rightarrow K\pi$ production experiments are also limited by statistics.

Beyond the attempted “direct” access to meson scattering data, theoretical considerations provide very strong constraints on at least some of the meson scattering channels discussed above, and extremely accurate representations of the leading partial waves at low-to-moderate energies are available in particular for pion–pion [117–121] and kaon–pion [122–124] scattering. We will briefly sketch the principles behind those analyses in Sec. 1.5.4 on Roy equations.

In the course of this review, we will not so much discuss scattering reactions as such, but rather production reactions, in particular via electroweak currents, whose final-state interactions allow to infer detailed information on scattering phase shifts. A prime example for this are the decays $K \rightarrow \pi\pi l\nu_l$ (K_{l4}), which—according to the Pais–Treiman method [125]—allow to extract the $\pi\pi$ scattering phase shift difference $\delta_0^0 - \delta_1^1$ in a model-independent way. Corresponding data is shown in Fig. 10(f) from Ref. [126] (solid triangles) and, of higher precision, from Refs. [127, 128] (solid squares); yet more recent data from the NA48/2 collaboration [129] is not included. As these data are necessarily at very low energies ($\sqrt{s} < m_K$), K_{l4} decays fix the low-energy properties of the $\pi\pi$ scattering amplitude as predicted from chiral perturbation theory with high precision [130], which in turn, e.g., determines the position of the $f_0(500)$ resonance very accurately [131–133].

There are other examples of $\pi\pi$ scattering information extracted from production, most obviously the P -wave as constrained from data on the pion vector form factor [134–137]. Also, B -decay data has been used to extract the (strange) scalar pion form factors at energies up to 2 GeV, thereby also constraining the underlying S -matrix for isoscalar S -wave scattering [138].

For other meson pairs, production data is essentially the only access we have to their scattering phase shifts; this is, e.g., the case for $\pi\eta$ scattering, see Fig. 10(j). Modern parameterizations of the S -wave based on chiral constraints [139] have most recently been adjusted [140] to $\gamma\gamma \rightarrow \pi^0\eta$ data from Belle [141] (compare also Ref. [142] for a similar effort); a suggested similar extraction from B -decays has not been put into practice yet [143].

There are first results for meson–meson scattering from the lattice, where the status until 2017 is reviewed in Ref. [10]. Among more recent results we wish to emphasize studies of isovector pion–pion scattering and determinations of the ρ meson properties [144–146]; see also Ref. [147] for the link to chiral perturbation theory. This process is treated as a benchmark and recent developments are motivated by the goal to constrain hadronic contributions to $g - 2$ of the muon [18].

Traditionally, amplitude analyses at higher energies rely on modeling of the s -dependence of the meson–meson interaction as a coherent sum of resonant Breit–Wigner amplitudes $\text{BW}_k(s)$, described in Sec. 3.1:

$$t_\ell(s) = \sum_{k=1}^N c_k \text{BW}_k(s), \quad (9)$$

where c_k represent complex coupling parameters of the various contributions. Such modeling provides a practical way to parameterize the data accurately by including additional resonances until adequate agreement is achieved. However, this approach violates the relation between magnitude and phase of the amplitude based on unitarity and analyticity. This is particularly problematic for broad, overlapping resonances. Therefore, the extracted parameters lack direct correspondence to the underlying meson–meson amplitude and it is difficult to relate different experiments. In the K -matrix formalism [148], contributions from broad overlapping resonances can be combined preserving unitarity. Here the scattering amplitude is expressed as

$$t_\ell(s) = K(s) [1 - i\sigma(s)K(s)]^{-1}, \quad (10)$$

where $K(s)$ is a real function and $\sigma(s)$ the phase space factor including the branch cut for the corresponding channel. The K functions describing individual resonances can be combined as a sum, while unitarity will still be preserved. Scattering of two of the final-state particles to different coupled channels is described in this method by considering K -matrices representing the interactions between the channels. Such a K -matrix method allows one, e.g., to relate and constrain data from coupled channels like $\pi\pi \rightarrow \pi\pi$, $\pi\pi \rightarrow K\bar{K}$, and $K\bar{K} \rightarrow K\bar{K}$ channels in $I = 0$, $J = 0$ [45]. In Sec. 3.3, we will show some results for J/ψ radiative decays into $\pi\pi$, $K_S K_S$, and $\eta\eta$ coupled channels analyzed in such a way. An extended coupled-channel analysis using the K -matrix formalism has been performed using data from pion production, $p\bar{p}$ and $n\bar{p}$ annihilation, and $\pi\pi$ scattering [149], resulting in K -matrix amplitudes of the transitions into channels $\pi\pi$, $K\bar{K}$, $\eta\eta$, $\eta\eta'$, and 4π .

A special case of such a coupled-channel analysis is the $f_0(980)$ decay into $\pi\pi$ and $K\bar{K}$ final states. The resonance is located close to the $K\bar{K}$ threshold and the shape can be parameterized by the Flatté formula [150]:

$$f(s) = \frac{1}{m_{f_0}^2 - s - i[g_1\sigma_\pi(s) + g_2\sigma_K(s)]}, \quad (11)$$

where $\sigma_P(s) = 2q_P/\sqrt{s}$ is the phase space factor for each decay channel, with q_P the c.m. momentum in the resonance rest frame.

Once a set of strongly interacting particles is created in a production process, they will interact in the final state in the way dictated by the scattering phases. In general, to relate multiparticle final-state interactions to the two-body interactions, one has to solve complicated equations for which not all required input is available. If there are only two hadrons in the final state or the interaction for a certain pair of the final hadrons is much stronger, unitarity relations for two-particle system can be

used. They were first derived by Watson [151]. The amplitudes for such two-body processes can be represented as a product of a universal and a reaction-specific part. The universal part $\Omega(s)$ is given by the so-called Omnès function [152] describing final-state interactions between the mesons generated by the scattering phase.

1.5 Theory of low-energy strong interactions

1.5.1 Chiral perturbation theory

QCD, the theory of the strong interactions, is formulated in terms of fundamental quark and gluon fields, with local $SU(3)_c$ gauge symmetry related to color charge. The main parts of its Lagrangian are given by

$$\mathcal{L}_{\text{QCD}} = -\frac{1}{4}G_{\mu\nu}^a G^{a\mu\nu} + \sum_q \bar{q} (i\not{D} - m_q) q, \quad (12)$$

where the sum extends over all quark flavors q . $D_\mu = \partial_\mu + ig_s \lambda^a G_\mu^a/2$ is the covariant derivative, G_μ^a stands for the gluon field with strong coupling g_s , $G_{\mu\nu}^a = \partial_\mu G_\nu^a - \partial_\nu G_\mu^a - g_s f^{abc} G_\mu^b G_\nu^c$ is the gluon field strength tensor, and λ^a are the Gell-Mann matrices. We omit gauge-fixing terms etc. for simplicity.

A crucial feature of this nonabelian theory, as compared to QED, is the self-coupling of the gauge bosons, the gluons, which carry color charge themselves. As a consequence, the behavior of the strong coupling constant under the renormalization group, i.e., its change with the energy scale, is characteristically different: QCD shows asymptotic freedom, which means that the coupling strength becomes small, hence the theory as such perturbative, for large-momentum-transfer processes. This feature allows to calculate QCD processes at high energies using the well-known perturbative methods in the coupling constant $\alpha_s = g_s^2/(4\pi)$. At the other end, however, the running coupling grows at small energies, which is presumably related to the phenomenon of confinement of the quark and gluon degrees of freedom inside color-neutral hadronic states. In this regime, for low-momentum-transfer reactions, a large coupling in particular prohibits predicting static properties of hadrons and low-energy interactions using a perturbation expansion in α_s . There is no direct (analytic) link between QCD's fundamental degrees of freedom and the observed spectrum of hadrons.

The key concept to understand this energy regime is chiral symmetry. To illustrate this, we decompose the quark fields into their chiral components

$$q = \frac{1}{2}(1 - \gamma_5)q + \frac{1}{2}(1 + \gamma_5)q \equiv P_L q + P_R q \equiv q_L + q_R, \quad (13)$$

whereby we can rewrite the QCD Lagrangian Eq. (12) according to

$$\begin{aligned} \mathcal{L}_{\text{QCD}} &= \mathcal{L}_{\text{QCD}}^0 - \mathcal{L}_{\text{QCD}}^m + \dots, & \mathcal{L}_{\text{QCD}}^0 &= -\frac{1}{4}G_{\mu\nu}^a G^{\mu\nu,a} + i\bar{q}_L \not{D} q_L + i\bar{q}_R \not{D} q_R, \\ & & \mathcal{L}_{\text{QCD}}^m &= \bar{q}_L \mathcal{M} q_R + \bar{q}_R \mathcal{M}^\dagger q_L, \end{aligned} \quad (14)$$

where q now denotes a vector collecting the light quark flavors $q^T = (u, d, s)$, and $\mathcal{M} = \text{diag}(m_u, m_d, m_s)$ is the quark mass matrix. The ellipsis denotes the heavier quark flavors. We note that, besides the obvious symmetries like Lorentz invariance, $SU(3)_c$ gauge invariance, and the discrete symmetries P , C , T , \mathcal{L}_{QCD} displays a chiral symmetry in the limit of vanishing quark masses (which is hence called ‘‘chiral limit’’): $\mathcal{L}_{\text{QCD}}^0$ is invariant under chiral $U(3)_L \times U(3)_R$ flavor transformations,

$$(q_L, q_R) \longmapsto (Lq_L, Rq_R), \quad L, R \in U(3)_{L,R}. \quad (15)$$

As the masses of the three light quarks are small on the typical hadronic scale,

$$m_{u,d,s} \ll 1 \text{ GeV} \approx \Lambda_{\text{hadr}}, \quad (16)$$

there is hope that the real world is not too far from the chiral limit, such that one may invoke a perturbative expansion in the quark masses.

If we rewrite the symmetry group according to

$$U(3)_L \times U(3)_R = SU(3)_L \times SU(3)_R \times U(1)_V \times U(1)_A, \quad (17)$$

where we have introduced vector $V = L + R$ and axial vector $A = L - R$ transformations, and consider the Noether currents associated with this symmetry group, it turns out that the different parts of it are realized in very different ways in nature. The $U(1)_V$ current $V_\mu^0 = \bar{q}\gamma_\mu q$, the quark number or baryon number current, is a conserved current in the Standard Model; on the other hand, the $U(1)_A$ current $A_\mu^0 = \bar{q}\gamma_\mu\gamma_5 q$ is broken by quantum effects, the $U(1)_A$ anomaly, and is not a conserved current of the quantum theory. As far as the chiral symmetry group $SU(3)_L \times SU(3)_R$ and its conserved currents

$$V_\mu^a = \bar{q}\gamma_\mu\frac{\lambda^a}{2}q, \quad A_\mu^a = \bar{q}\gamma_\mu\gamma_5\frac{\lambda^a}{2}q, \quad \partial^\mu V_\mu^a = \partial^\mu A_\mu^a = 0, \quad a = 1, \dots, 8, \quad (18)$$

are concerned, they are certainly broken explicitly by the quark masses, but this is expected to be a small effect.

In nature, chiral symmetry is realized in the Goldstone mode, i.e., the symmetry is spontaneously broken: we find (approximate) $SU(3)_V$ multiplets, but no parity doubling is observed. The symmetry breaking pattern is

$$SU(3)_L \times SU(3)_R \xrightarrow{\text{SSB}} SU(3)_V. \quad (19)$$

Accordingly, the axial charges commute with the Hamiltonian, but do not leave the ground state invariant. As a consequence, massless excitations, so-called ‘‘Goldstone bosons’’ appear, which are noninteracting for vanishing energy. In the case at hand, the eight Goldstone bosons should be pseudoscalars, which the lightest hadrons in the spectrum indeed are, namely π^\pm , π^0 , K^\pm , K^0 , \bar{K}^0 , and η .

The task is therefore to construct a low-energy theory for these Goldstone bosons, and the first step to this end is to find a Lagrangian that fulfills all QCD symmetries. This can be constructed in terms of the matrix field [153, 154]

$$U = \exp\left(\frac{i\phi}{F_0}\right), \quad \phi = \sqrt{2} \begin{pmatrix} \frac{\pi^0}{\sqrt{2}} + \frac{\eta}{\sqrt{6}} & \pi^+ & K^+ \\ \pi^- & -\frac{\pi^0}{\sqrt{2}} + \frac{\eta}{\sqrt{6}} & K^0 \\ K^- & \bar{K}^0 & -\frac{2\eta}{\sqrt{6}} \end{pmatrix}, \quad (20)$$

that transforms according to $U \mapsto LUR^\dagger$ under chiral transformations, $L \in SU(3)_L$, $R \in SU(3)_R$, and F_0 is a dimensionful constant that can be identified with the pion decay constant (in the $SU(3)$ chiral limit), $F_0 \approx F_\pi = 92.2 \text{ MeV}$.² As we want to construct a low-energy effective theory, the guiding principle is to use the power of momenta or derivatives to order the importance of various possible terms. ‘‘Low energies’’ here refer to a scale well below 1 GeV, i.e., an energy region where the Goldstone bosons are the only relevant degrees of freedom. Lorentz invariance dictates that Lagrangian terms can only come in even powers of derivatives, hence \mathcal{L} is of the form

$$\mathcal{L} = \mathcal{L}^{(0)} + \mathcal{L}^{(2)} + \mathcal{L}^{(4)} + \dots \quad (21)$$

However, as U is unitary, $UU^\dagger = \mathbf{1}$, $\mathcal{L}^{(0)}$ can only be a constant. Therefore, in accordance with the Goldstone theorem, the leading term in the Lagrangian is $\mathcal{L}^{(2)}$, which already involves derivatives. It can be shown to consist of one single term,

$$\mathcal{L}^{(2)} = \frac{F_0^2}{4} \langle \partial_\mu U \partial^\mu U^\dagger \rangle, \quad (22)$$

²We have neglected the isospin-breaking effect of π^0 - η mixing in Eq. (20).

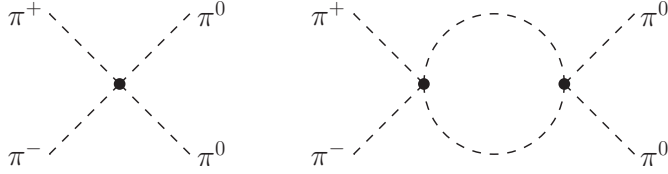


Figure 11: Pion–pion scattering in the current algebra approximation, i.e., in the lowest order of ChPT (left), as well as an example of a one-loop or next-to-leading-order (NLO) contribution (right).

where $\langle \dots \rangle$ denotes the trace in flavor space. Expanding U in powers of ϕ , we find the canonical kinetic terms

$$\mathcal{L}^{(2)} = \partial_\mu \pi^+ \partial^\mu \pi^- + \partial_\mu K^+ \partial^\mu K^- + \dots, \quad (23)$$

and indeed no mass terms: in the chiral limit, the Goldstone bosons are massless.

To render the theory more realistic, we need to reintroduce the quark mass matrix $\mathcal{M} = \text{diag}(m_u, m_d, m_s)$ as a perturbation. At leading order, i.e., to linear order in the quark masses and without any further derivatives, one finds exactly one term in the chiral Lagrangian, such that $\mathcal{L}^{(2)}$ is then of the complete form

$$\mathcal{L}^{(2)} = \frac{F_0^2}{4} \langle \partial_\mu U \partial^\mu U^\dagger + 2B_0(\mathcal{M}U^\dagger + \mathcal{M}^\dagger U) \rangle. \quad (24)$$

B_0 is an additional parameter that is related to the quark condensate in the chiral limit, $B_0 = -\langle 0 | \bar{u}u | 0 \rangle / F_0^2$. Expanding once more in powers of ϕ , we can read off the mass terms and find, e.g.,

$$m_{\pi^\pm}^2 = B_0(m_u + m_d), \quad m_{K^\pm}^2 = B_0(m_u + m_s), \quad m_{K^0}^2 = B_0(m_d + m_s). \quad (25)$$

This demonstrates why, in a common power counting scheme that assigns the generic order p to both energies/momenta and Goldstone boson masses, quark masses are counted as $\mathcal{O}(p^2)$.

Due to the nonlinear field representation in U , the Lagrangian $\mathcal{L}^{(2)}$ contains much more information than the masses, but also interaction terms. In particular, we can calculate the invariant amplitude $A(s, t, u)$ of pion–pion scattering, see Eq. (7), to be

$$A(s, t, u) = \frac{s - m_\pi^2}{F_0^2}, \quad (26)$$

a parameter-free prediction [155]. If we furthermore define the S -wave scattering lengths of definite isospin, proportional to the scattering amplitudes of Eq. (8) at threshold, $a_0^I = T^I(s = 4m_\pi^2, t = u = 0)/32\pi$, we find

$$a_0^0 = \frac{7m_\pi^2}{32\pi F_\pi^2} = 0.16, \quad a_0^2 = -\frac{m_\pi^2}{16\pi F_\pi^2} = -0.045. \quad (27)$$

Diagrammatically, this is represented by the tree-level diagram of Fig. 11(left).

The Lagrangian (24) as well as the relations (25), (26), and (27) are only the leading terms in a systematic approach called chiral perturbation theory (ChPT) [156–158], for which there are many comprehensive reviews available [159–166]. Equation (26) immediately renders the necessity of higher-order corrections obvious: the scattering amplitude is real, while the optical theorem (applied to partial waves t_ℓ^I) requires imaginary parts of the form

$$\text{Im } t_\ell^I = \sqrt{1 - \frac{4m_\pi^2}{s}} |t_\ell^I|^2. \quad (28)$$

It is well known from the Born series in quantum-mechanical scattering that the optical theorem links terms of different orders in perturbation theory to each other: if (the real part of) t_ℓ^I is of $\mathcal{O}(p^2)$, Eq. (28)

shows that $\text{Im} t_\ell^I$ will start at $\mathcal{O}(p^4)$, as a loop correction. Furthermore, all higher-order terms in the effective Lagrangian are allowed: they ought to be smaller at low energies, but for precision predictions and estimates of theoretical uncertainties, these corrections should be evaluated. In addition, the loop corrections entail divergences in the real parts of amplitudes, which have to be removed by appropriate counterterms. The theory is nonrenormalizable in the conventional sense: it contains interaction terms of negative mass dimension, and hence cannot be rendered finite to all orders by a finite number of counterterms: new operators have to be introduced at each order in perturbation theory. ChPT is however renormalizable, and therefore predictive, order by order in the low-energy expansion. The number of independent terms and corresponding free coupling constants increases rapidly at higher orders, with the $SU(3)$ version of it containing 2 (F_0, B_0), 10 [158], and 90 [167] terms at orders p^2 , p^4 , and p^6 , respectively.

As a perturbative expansion needs to proceed in powers of some dimensionless ratio p/Λ_χ , let us briefly discuss the size of the typical breakdown scale Λ_χ . From a renormalization-group-type of analysis, it can be shown that loop corrections are generically expected to generate a scale $\Lambda_\chi = 4\pi F_0$. On the other hand, we have to remember that we have constructed an effective theory for Goldstone bosons, which are the only dynamical degrees of freedom. The effective theory must fail once the energy reaches the resonance region, hence for momenta of the order of $\Lambda_\chi \approx m_{\text{res}}$. Both of these arguments hence point towards a breakdown scale of the order of 1 GeV.

The appearance of many unknown free Lagrangian parameters, usually called low-energy constants (LECs), at higher orders does not preclude the theory from making predictions. This is due to the fact that the same operators still contribute to various observables at the same time, and thus provide nontrivial relations between them. As an illustration for this principle, we briefly discuss the next-to-leading-order corrections to the pion–pion S -wave scattering length of isospin 0, a_0^0 (which is actually even known at next-to-next-to-leading order [168, 169]). An example for a loop diagram contributing therein is given in Fig. 11(right). The $\mathcal{O}(p^4)$ corrections are of the form [157]

$$a_0^0 = \frac{7m_\pi^2}{32\pi F_\pi^2} \left\{ 1 + \epsilon + \mathcal{O}(m_\pi^4) \right\}, \quad \epsilon = \frac{5m_\pi^2}{84\pi^2 F_\pi^2} \left(\bar{\ell}_1 + 2\bar{\ell}_2 + \frac{3}{8}\bar{\ell}_3 + \frac{21}{10}\bar{\ell}_4 + \frac{21}{8} \right). \quad (29)$$

Here, $\bar{\ell}_i$ refers to the renormalized, i.e., finite and scale-independent, LECs [157]. There are two different types of LECs in the expression (29). $\bar{\ell}_1$ and $\bar{\ell}_2$ come with structures containing four derivatives, i.e., they survive in the chiral limit and can be determined from the momentum dependence of the $\pi\pi$ scattering amplitude, namely from D -waves. $\bar{\ell}_3$ and $\bar{\ell}_4$ however are symmetry breaking terms that specify the quark mass dependence, therefore they cannot be determined from $\pi\pi$ scattering alone. The LEC $\bar{\ell}_3$ is particularly interesting as it determines the extent to which the pion mass is given by the leading term in the quark mass expansion, see Eq. (25):

$$m_\pi^2 = m^2 - \frac{m^4}{32\pi^2 F_\pi^2} \bar{\ell}_3 + \mathcal{O}(m^6), \quad (30)$$

where we have denoted the $\mathcal{O}(p^2)$ relation by $m^2 = 2B\hat{m} \equiv B(m_u + m_d)$ (and B is the $SU(2)$ analogue of B_0). The constant $\bar{\ell}_4$, on the other hand, is related to the scalar form factor of the pion $\Gamma(s)$,

$$\langle \pi^a(p)\pi^b(p') | \hat{m}(\bar{u}u + \bar{d}d) | 0 \rangle = \delta^{ab}\Gamma(s), \quad s = (p + p')^2. \quad (31)$$

At tree level, one has $\Gamma(s) = 2B\hat{m} = m_\pi^2 + \mathcal{O}(p^4)$ in accordance with the Feynman–Hellmann theorem [170, 171], $\Gamma(0) = \langle \pi | \hat{m} \bar{q}q | \pi \rangle = \hat{m} \partial m_\pi^2 / \partial \hat{m}$. At next-to-leading order, one defines the scalar radius $\langle r^2 \rangle_\pi^S$ according to

$$\Gamma(s) = \Gamma(0) \left\{ 1 + \frac{s}{6} \langle r^2 \rangle_\pi^S + \mathcal{O}(s^2) \right\}, \quad \langle r^2 \rangle_\pi^S = \frac{3}{8\pi^2 F_\pi^2} \left(\bar{\ell}_4 - \frac{13}{12} \right) + \mathcal{O}(m_\pi^2), \quad (32)$$

therefore the scalar radius is directly linked to $\bar{\ell}_4$. Although the scalar form factor is not directly experimentally accessible, one can analyze $\Gamma(s)$ in dispersion theory [172–175] and extract $\langle r^2 \rangle_\pi^S$ that way. These dispersively reconstructed scalar form factors are important for the phenomenology of S -wave pion–pion final-state interactions [138, 176], as well as for the description of hadronic matrix elements important in beyond-the-Standard-Model physics searches [177–180].

Traditionally, the relation laid out above have been utilized to determine the size of the quark condensate (via its relation to $\bar{\ell}_3$) through a determination of a_0^0 [130]. Both S -wave scattering lengths have been predicted to remarkable precision by combining their ChPT expansion with Roy equations, see Sec. 1.5.4, where they appear as subtraction constants [181]:

$$a_0^0 = 0.220(5), \quad a_0^2 = -0.0444(10). \quad (33)$$

Experimentally, these predictions have been tested most accurately by the NA48/2 collaboration, combining analyses of K_{e4} decays [129] and the cusp effect in $K^+ \rightarrow \pi^+ \pi^0 \pi^0$ [182], arriving at [129]

$$a_0^0 = 0.2210(47)_{\text{stat}}(40)_{\text{syst}}, \quad a_0^2 = -0.0429(44)_{\text{stat}}(28)_{\text{syst}}, \quad (34)$$

hence demonstrating remarkable agreement with Eq. (33). To arrive at this result, subtle radiative corrections need to be applied in the experimental analyses [183, 184]. We note that a_0^2 is very close to the leading-order ChPT prediction in Eq. (27), while a_0^0 is enhanced quite significantly: this sizable correction can be understood in terms of a chiral logarithm with a large coefficient contained already in the one-loop correction, see Eq. (29).

The coupling of the chiral Lagrangians to external vector (v_μ) and axial vector (a_μ) fields is rather straightforward: the ordinary derivative is replaced by a covariant one, $D_\mu U = \partial_\mu U - i[v_\mu, U] - i\{a_\mu, U\}$. Inserting the photon for the vector field, $v_\mu = eQ A_\mu$ with Q denoting the quark charge matrix, generates the couplings necessary to calculate, e.g., the electromagnetic form factor of the pion or pion Compton scattering at leading order. Higher orders in addition require the field strength tensor (with appropriate chiral transformation behavior) as a Lagrangian building block.

Now we consider the application of ChPT to the pion vector form factor $F_\pi^V(s)$,

$$\langle \pi^+(p) \pi^-(p') | j_\mu^{\text{em}}(0) | 0 \rangle = (p_\mu - p'_\mu) F_\pi^V(s), \quad (35)$$

where $j_\mu^{\text{em}} = 2/3 \bar{u} \gamma_\mu u - 1/3 \bar{d} \gamma_\mu d \pm \dots$ denotes the electromagnetic current. At $\mathcal{O}(p^4)$, there are loop diagrams contributing to $F_\pi^V(s)$ as well as a tree graph proportional to the low-energy constant $\bar{\ell}_6$. The full one-loop representation is given as [157]

$$F_\pi^V(s) = 1 + \frac{1}{6F_\pi^2} (s - 4m_\pi^2) \bar{J}(s) + \frac{s}{6} \left(\langle r^2 \rangle_\pi^V + \frac{1}{24\pi^2 F_\pi^2} \right),$$

$$\bar{J}(s) = \frac{1}{16\pi^2} \left\{ \sigma_\pi \log \frac{\sigma_\pi - 1}{\sigma_\pi + 1} + 2 \right\}, \quad \sigma_P = \sqrt{1 - \frac{4m_P^2}{s}}. \quad (36)$$

The (squared) electromagnetic radius $\langle r^2 \rangle_\pi^V$ is defined via the expansion for small s ,

$$F_\pi^V(s) = 1 + \frac{s}{6} \langle r^2 \rangle_\pi^V + \mathcal{O}(s^2), \quad \langle r^2 \rangle_\pi^V = \frac{1}{16\pi^2 F_\pi^2} (\bar{\ell}_6 - 1). \quad (37)$$

To understand the role of the LEC $\bar{\ell}_6$, we consider the contribution of the ρ resonance to this form factor, as shown in Fig. 12. Expanding the ρ propagator for $s \ll m_\rho^2$,

$$\frac{s}{m_\rho^2 - s} = \frac{s}{m_\rho^2} \left(1 + \frac{s}{m_\rho^2} + \dots \right), \quad (38)$$

Figure 12: The contribution of the ρ resonance to the pion vector form factor can, at small t , be represented by a point-like counterterm.

we find that identifying the leading term with the $\bar{\ell}_6$ contribution reproduces the empirical value for $\bar{\ell}_6$ nicely. This is a modern version of the VMD picture: where allowed by quantum numbers, the numerical values of LECs are dominated by the contributions of vector resonances [185, 186].

On the other hand, this connection also neatly demonstrates one of the central limitations of ChPT: it only parameterizes the low-energy tails of resonances in terms of approximate polynomials, but cannot, even at higher orders, reproduce the poles associated with resonant states. This failure is intimately linked to the fact that ChPT, as a low-energy effective theory, only fulfills unitarity perturbatively: Eq. (28) neatly illustrates that the imaginary part of a partial wave is necessarily suppressed relative to the real part within the range of applicability of the chiral power counting scheme, while near a resonance, $\text{Im } t_\ell^I \gg \text{Re } t_\ell^I$. The limited range of convergence of the perturbative ChPT expansion is therefore closely related to the violation of exact unitarity. As a consequence, there have been various attempts to extend the range of applicability of ChPT to higher energies by invoking unitarization in one way or the other. These therefore often rely on dispersion-theoretical methods, which are based on the underlying analytic properties of quantum field theories.

1.5.2 Dispersion relations; Omnès formalism

We have seen the first dispersion relation already in Eq. (5) for the pion vector form factor: in the spirit of the Kramers–Kronig relations from optics or electrodynamics, they allow to express a complex function (and specifically the real part thereof) in terms of an integral over its imaginary part. Dispersion relations rely on the fundamental quantum-field-theoretical properties of analyticity, the mathematical formulation of causality, and unitarity, the consequence of probability conservation (see Ref. [187] for the classic textbook and, e.g., Ref. [188] for a recent one including current applications). Analyticity allows to express complex functions such as form factors or scattering amplitudes in terms of contour integrals in the complex energy plane according to Cauchy’s integral formula. Unitarity dictates that this complex energy plane contains poles and cuts starting from certain branch points, dictated by single- or multi-particle intermediate states, respectively. The discontinuities along the branch cut are in many cases related to the imaginary parts in a straightforward way (following from Schwarz’ reflection principle), $\text{disc } f(s) = 2i \text{Im } f(s)$. This results, in the simplest case, in dispersion relations of the form

$$f(s) = \frac{1}{2\pi i} \int_{s_{\text{thr}}}^{\infty} ds' \frac{\text{disc } f(s')}{s' - s} = \frac{1}{\pi} \int_{s_{\text{thr}}}^{\infty} ds' \frac{\text{Im } f(s')}{s' - s}. \quad (39)$$

Here, s_{thr} denotes the branch point or outset of the unitarity cut, which in the simplest case—a two-particle intermediate state of equal masses m —is simply given by $s_{\text{thr}} = 4m^2$. If the integrals up to infinity in Eq. (39) do not converge, subtractions need to be introduced, which emphasizes the weight of the integrands at low energies (where the imaginary parts are typically known far better, as only few intermediate states are kinematically allowed), at the expense of introducing unknown parameters, the so-called subtraction constants, that need to be fixed from elsewhere.

The unitarity relation for a partial wave was already given in Eq. (28). Of particular interest in the context of this review is a form factor unitarity relation, as it links production (e.g., of a pair of mesons through an electroweak current) to scattering (the final-state interaction of said pair of mesons in the

given partial wave): e.g., the pion vector form factor obeys

$$\text{Im } F_\pi^V(s) = F_\pi^V(s) \sigma_\pi(s) [t_1^1(s)]^* \theta(s - 4m_\pi^2). \quad (40)$$

In the elastic regime, the partial wave $t_J^I(s)$ can be expressed in terms of the phase shift $\delta_J^I(s)$ according to

$$t_J^I(s) = \frac{e^{i\delta_J^I(s)} \sin \delta_J^I(s)}{\sigma_\pi(s)}, \quad (41)$$

which leads to the so-called Omnès solution already quoted in Eq. (6), as well as Watson's final-state theorem [151]: as long as elastic unitarity is fulfilled, the form factor phase $\arg F_\pi^V(s)$ is identical to the scattering phase shift $\delta_1^1(s)$.

Dispersion relations for four-point functions, such as scattering amplitudes or three-body systems in production mechanisms, are typically more complicated due to the presence of crossed-channel singularities: cuts in, say, the t - and u -channels of a scattering amplitude induce, when projected onto s -channel partial waves, additional cuts that extend from another branch point to $-\infty$. The latter necessitate the generalization of dispersion relations as in Eq. (39) to include a second integral over these so-called left-hand cuts.

1.5.3 Inverse-amplitude method

The partial-wave unitarity relation for $\pi\pi$ scattering (28), $\text{Im } t = \sigma_\pi |t|^2$ (omitting for simplicity isospin and angular momentum indices), has the immediate consequence that the imaginary part of the *inverse* partial wave is given by the phase space factor alone:

$$\text{Im } \frac{1}{t(s)} = -\sigma_\pi, \quad (42)$$

which leads to

$$t(s) = \frac{1}{\text{Re } t^{-1}(s) - i\sigma_\pi}. \quad (43)$$

Applying the next-to-leading-order chiral expansion $t = t^{(2)} + t^{(4)} + \dots$ to $\text{Re } t^{-1}$ as well as perturbative unitarity in the form $\text{Im } t^{(4)} = \sigma_\pi |t^{(2)}|^2$, one arrives at the expression

$$t(s) = \frac{[t^{(2)}(s)]^2}{t^{(2)}(s) - t^{(4)}(s)}, \quad (44)$$

which is the NLO inverse-amplitude method (IAM) expression for the partial wave $t(s)$ [101, 189–195]. Equation (44) has been extended to next-to-next-to-leading order, employing also the two-loop chiral representation of the $\pi\pi$ scattering amplitude [193, 195]. Special care has to be taken for the application of the IAM to S -waves to take zeros in the amplitudes into account (so-called Adler zeros) [101].

The important observation is that IAM representations of scattering partial waves fulfill unitarity exactly. In the elastic case, they can be derived rigorously based on dispersion theory, with only the crossed-channel singularities or left-hand cuts approximated according to the chiral expansion [192, 193]. In contrast to the strict chiral series, which contains essentially polynomials in the Mandelstam variables in addition to (perturbative) unitarity corrections, it is obvious that the series expansion in the inverse amplitude in Eq. (44) allows for the generation of poles for complex values of s , hence of resonances.

The generalization of the IAM to coupled channels, which turns Eq. (44) into a matrix relation, underlies the theoretical representation of the various phase shifts and inelasticities [101] shown in Fig. 10. These clearly show an at least reasonable reproduction of the lowest S - and P -wave resonances in $\pi\pi$ and $K\pi$ scattering. For the application of the IAM to form factors and associated production amplitudes, see, e.g., Ref. [196] and references therein.

1.5.4 Roy equations

Meson–meson phase shifts are central objects of interest for this review. The paradigm case for meson–meson scattering information that is known to excellent precision are the pion–pion phase shifts at low-to-moderate energies. As a lot of progress in the description of meson decays and production processes are based on the precision with which we nowadays know these, we here briefly recapitulate how these can be constrained rigorously by means of the so-called Roy equations [197].

Roy equations present a coupled system of partial-wave dispersion relations, which make maximal use of analyticity, unitarity, isospin, and crossing symmetry. The construction is based on a twice-subtracted dispersion relation for fixed Mandelstam variable t :

$$T(s, t) = c(t) + \frac{1}{\pi} \int_{4m_\pi^2}^{\infty} ds' \left\{ \frac{s^2}{s'^2(s' - s)} + \frac{u^2}{s'^2(s' - u)} \right\} \text{Im } T(s', t). \quad (45)$$

The two integrands correspond to the right- and left-hand cuts, respectively, and isospin indices are suppressed for simplicity. The t -dependent subtraction function $c(t)$ can be fixed using crossing symmetry. Partial-wave expanding the imaginary parts and projecting the resulting amplitude results in the schematic form [197]

$$t_J^I(s) = k_J^I(s) + \sum_{I'=0}^2 \sum_{J'=0}^{\infty} \int_{4m_\pi^2}^{\infty} ds' K_{JJ'}^{II'}(s, s') \text{Im } t_{J'}^{I'}(s'), \quad (46)$$

where we have reinstated the isospin dependence. The kernels $K_{JJ'}^{II'}(s, s')$ are analytically known; they contain a singular Cauchy kernel (diagonal in both isospin and angular momentum) as well as terms resulting from the left-hand cuts. The subtraction polynomial $k_J^I(s)$ can be expressed entirely in terms of the two $\pi\pi$ S -wave scattering lengths $a_0^{I=0,2}$. As long as elastic unitarity is fulfilled, the partial waves $t_J^I(s)$ can be expressed in terms of phase shifts $\delta_J^I(s)$, see Eq. (41), which turns Eq. (46) into a coupled set of integral equations for $\pi\pi$ phase shifts.

Roy equations can only be applied within a limited energy range, e.g., $s \leq s_{\text{max}} = (1.15 \text{ GeV})^2$ [198]. The phase shifts for the lowest partial waves (usually S and P) are therefore only solved for at low energies below a certain matching point s_m , above which experimental input is required. However, the low-energy $\pi\pi$ scattering phase shifts can still be determined with remarkable accuracy [117], and the matching of the subtraction constants, i.e., the S -wave scattering lengths, to ChPT further strengthens the constraints [118]. Alternative variants of the Roy equations with different subtraction schemes have also been used in fits to $\pi\pi$ scattering data [119, 199], resulting in similarly accurate parameterizations of phase shifts that have been widely used as input to dispersion-theoretical analyses of final-state interactions.

Roy equations can be adapted to other scattering reactions that are less symmetric under crossing. Such Roy–Steiner equations [200], making use of the relation between different crossed reactions, have been solved in particular for pion–kaon scattering [122–124], which is of high relevance in the context of this review, but also for pion Compton [201] as well as pion–nucleon scattering [202, 203].

1.6 Amplitude analyses for three-body decays

Amplitude analysis of multibody decays is a tool to study meson interactions gaining more importance in recent years. Often, the knowledge of two-body scattering amplitudes is assumed as a starting point to describe the decay dynamics. In some cases, especially when precise multidimensional data is available, one can try to extract information about meson interactions from such decays. We will illustrate the methods using mainly the simplest case of three-body decays. A pseudoscalar meson decay to three ground state pseudoscalar mesons is related to meson–meson scattering by crossing symmetry,

as discussed in Sec. 1.1. For a three-body decay $0 \rightarrow 1 + 2 + 3$ the Mandelstam variables are often denoted by

$$s_i \equiv (p_0 - p_i)^2, \quad (47)$$

where $i = 1, 2, 3$ and p_0, p_i are the four-momenta of the particles. The relation between the standard notation and s_i reads: $s \rightarrow s_3$, $u \rightarrow s_1$, $t \rightarrow s_2$. Alternatively one can use kinetic energies T_i of the decay particles in the rest frame of the particle “0”:

$$T_i = \frac{(m_0 - m_i)^2 - s_i}{2m_0}, \quad (48)$$

which are linearly related to the s_i . Energy conservation imposes the constraints

$$\sum_{i=1}^3 T_i = m_0 - \sum_{i=1}^3 m_i \equiv Q_0 \quad \text{and} \quad \sum_{i=1}^3 s_i = s + t + u = \sum_{i=0}^3 m_i^2. \quad (49)$$

The dynamical information on a three-body decay of scalar particles can be represented by a probability density function drawn in a plane defined by any two of the Mandelstam variables, the so-called Dalitz plot [204]. Examples of Dalitz plot boundaries are shown in Fig. 13 using Mandelstam variables expressed in units of squared pion masses, where the kinematical ranges for three-body decays of η and η' mesons are compared. The density distribution in the Dalitz plot is determined by the quantum numbers of the particles and by the interaction of the produced particles. The latter can be influenced by resonances or kinematical thresholds. A two-particle resonance will be seen as a band perpendicular to the corresponding s_i variable in the Dalitz plot if the mass is contained in the plot and the width is significantly less than the kinematical range. As we will discuss in Sec. 3.9, none of these conditions are fulfilled for $\eta \rightarrow 3\pi$ and $\eta' \rightarrow \eta\pi\pi$ decays presented in Fig. 13(a). The example of Fig. 13(b) shows the kinematic ranges for radiative decays of η and η' mesons into $\pi^+\pi^-\gamma$. The s_3 variable corresponds to the $\pi^+\pi^-$ invariant mass squared $M^2(\pi^+\pi^-)$. As we discuss in Sec. 3.4, the ρ^0 meson resonance is visible in the $\eta' \rightarrow \pi^+\pi^-\gamma$ decay. The peak position in the s_3 variable, corresponding to $m_\rho^2/m_\pi^2 \approx 33$ is indicated in the figure.

A virtue of the Dalitz plot representation using two of the Mandelstam variables or their linear combinations T_i is that the probability density function is directly proportional to the matrix element squared $|\mathcal{M}(s, t, u)|^2$:

$$d\Gamma = \frac{1}{(2\pi)^3} \frac{1}{8m_0} |\overline{\mathcal{M}}|^2 dT_1 dT_2 = \frac{1}{(2\pi)^3} \frac{1}{32m_0^3} |\overline{\mathcal{M}}|^2 ds_1 ds_2. \quad (50)$$

Sometimes it is useful to describe the three-body decay phase space in terms of sequential decays, i.e., processes $0 \rightarrow (1 + 2) + 3$, using helicity frames. This will, e.g., be the case when we discuss radiative decays into a meson–meson pair. One uses the invariant mass squared of the $(1 + 2)$ system s and the emission angle Ω_3 of particle “3” in the particle “0” rest frame, as well as Ω_1^* , the emission angle of particle “1” in the $(1 + 2)$ helicity system. The fully differential cross section (not spin averaged) is given by

$$d\Gamma = \frac{1}{(2\pi)^5} \frac{1}{16m_0^2} |\mathcal{M}|^2 \frac{|\mathbf{p}_3| |\mathbf{p}_1^*|}{\sqrt{s}} ds d\Omega_3 d\Omega_1^*, \quad (51)$$

where \mathbf{p}_3 and \mathbf{p}_1^* are the momenta of particle “3” and “1” in “0” and $(1 + 2)$ frames, respectively. If two of the particles are identical or are a particle–antiparticle pair the s variable corresponds to the invariant mass squared of the like particles. In this case one can represent the Dalitz plot using the following dimensionless variables:

$$x \equiv \frac{\sqrt{3}}{2} \frac{u - t}{m_0 Q_0}, \quad y \equiv \frac{3}{2} \frac{(m_0 - m_3)^2 - s}{m_0 Q_0} - 1. \quad (52)$$

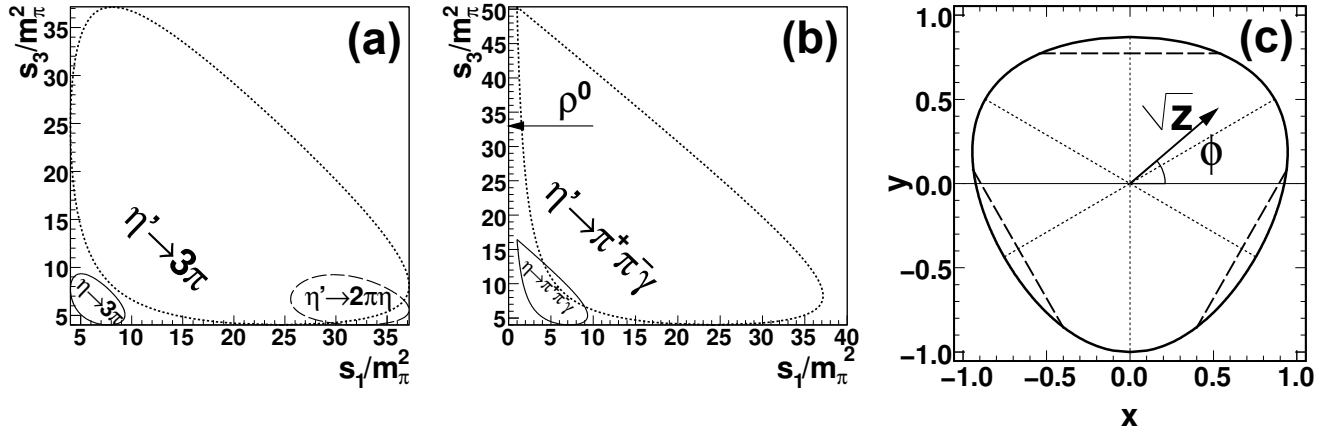


Figure 13: Dalitz plot boundaries for hadronic and radiative η and η' decays: (a) $\eta \rightarrow 3\pi$ — solid line, $\eta' \rightarrow 3\pi$ — dotted line, and $\eta' \rightarrow \eta\pi\pi$ — dashed line. The variables s_1, s_2 are expressed in units of the pion mass squared. (b) $\eta^{(\prime)} \rightarrow \pi^+\pi^-\gamma$. The vertical axis represents the invariant mass squared of the $\pi^+\pi^-$ system. The position of the ρ^0 meson in the dimensionless units is indicated by the arrow. (c) Example of a normalized Dalitz plot for three identical particles, the kinematic region for the decay $\eta \rightarrow 3\pi^0$ expressed in x and y variables. The dashed lines represent the thresholds for $\pi^+\pi^- \rightarrow \pi^0\pi^0$ rescattering.

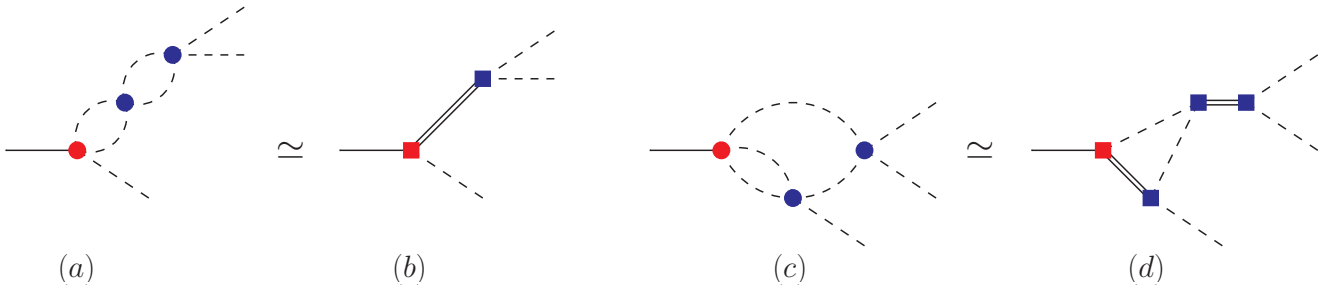


Figure 14: Rescattering effects in three-body decays. Two-body rescattering in the spectator approximation (a) is approximated by resonance (double line) exchange (b). The isobar model in its simplest form does not include rescattering between all three final-state particles (c) or sequential resonance exchanges in different two-body channels (d).

As an example the boundary of the Dalitz plot for $\eta \rightarrow 3\pi^0$ in the x and y variables is shown in Fig. 13(c). Decays into three identical particles are conveniently described using polar coordinates (\sqrt{z}, ϕ) in the (x, y) plane:

$$x = \sqrt{z} \sin \phi, \quad y = \sqrt{z} \cos \phi. \quad (53)$$

Such a Dalitz plot has a sextant symmetry and one can limit the range of the ϕ angle to $0^\circ \leq \phi < 60^\circ$. One example is $\eta^{(\prime)} \rightarrow 3\pi^0$ discussed in Sec. 3.9. The variable z is given by $z = x^2 + y^2$ and covers the range $0 \leq z \leq 1$.

The most common way to describe the matrix element of a decay is as a sum of interfering decay amplitudes, each proceeding through chains of resonant two-body decays. This is the so-called isobar model [205, 206]; see Fig. 14. The diagrams in this model would correspond to the tree contributions in a quantum field theory for the process if all the mass parameters in the propagators are taken to be real. However, in the isobar model the effect of final-state interactions is included by allowing the masses to be complex, i.e., by including finite widths. In this manner, however, the isobar model neglects more complicated rescattering effects between all three final-state particles; see Fig. 14(c) and (d). Below, in the context of reactions or decays of the type $e^+e^-, \omega, \phi \rightarrow \pi^+\pi^-\pi^0$, we will briefly describe the so-called

Table 2: Main parameters of the electron–positron colliders with c.m. energies in the range 0.3–5.0 GeV. Data taken from Ref. [48].

	VEPP-2M	VEPP-2000	BEPC	BEPC-II	DAΦNE
Physics start date	1974	2010	1989	2008	1999
Physics stop date	2000	–	2005	–	–
c.m. energy (GeV)	0.36–1.4	0.3–2.0	5.0	2.0–4.7	1.020
Delivered luminosity (fb^{-1})	0.1	0.125	0.11	20	10
Luminosity ($10^{31} \text{ cm}^{-2}\text{s}^{-1}$)	0.5	4	12	100	45
Circumference (m)	18	24	240	238	98
Crossing angle (m rad)	0	0	0	22	50
Interactions regions	2	2	1	1	1

Khuri–Treiman formalism [207] that takes more complete final-state interactions into account. Other theoretical approaches include the application of Bethe–Salpeter models [208, 209] or other formulations explicitly incorporating three-body unitarity [210, 211], all of which ought to be equivalent within their respective approximations [212] and describe the same physics.

2 Experiments at symmetric electron–positron colliders

2.1 Experimental facilities

The majority of the results presented in this review were obtained at low-energy symmetric electron–positron colliders in Frascati, Novosibirsk, and Beijing. The facilities and detectors are briefly described in this section. We do not include descriptions of earlier experiments like the CLEOc [213], which was a modification of an experiment originally running above $b\bar{b}$ threshold to carry out a physics program in the charm region. It had significantly lower luminosity than the facility in Beijing, but still several results persist as world-leading and are discussed in this review. Many findings that we will show come from the asymmetric electron–positron colliders PEP-II and KEKB designed to work in the $b\bar{b}$ region [214]. The attainable luminosities at these high energies are two orders of magnitude larger and allow the experiments to perform low-energy hadronic studies using higher-order electromagnetic processes such as initial-state radiation and two-photon fusion. These colliders have asymmetric configurations with electron and positron beams of different energies. In particular many results included in this review stem from the $\sim 0.5 \text{ ab}^{-1}$ of data collected by the BaBar collaboration [215] near the $\Upsilon(4S)$ resonance.

2.1.1 Frascati: DAΦNE and KLOE

DAΦNE at Frascati LNF-INFN is an electron–positron collider optimized to run at the c.m. energy corresponding to the ϕ meson mass. The visible ϕ peak cross section is about $3 \mu\text{b}$ and the decay width is $4.249(13) \text{ MeV}$, where the main decay modes are into K^+K^- [49.2(5)%] and K_LK_S [34.0(4)%]. During the KLOE experiment’s running period from 2001 to 2006, a total collected integrated luminosity of 2.5 fb^{-1} at the ϕ peak and about 250 pb^{-1} off peak were acquired. In 2008, DAΦNE was upgraded to be the first collider to implement the crab-waist interaction scheme [216]. At the same time, new

sub-detectors were added. From 2014 until March 2018, the new KLOE-2 detector collected 5.5 fb^{-1} at the ϕ resonance. The total KLOE and KLOE-2 data sets correspond to about 2.4×10^{10} ϕ -meson events. At present (2021), DAΦNE is used as a worldwide unique low-energy kaon–antikaon source, e.g., for kaonic atoms studies [217].

The KLOE detector consists of a large cylindrical drift chamber (DC) [218] surrounded by a hermetic electromagnetic calorimeter (ECAL) [219]. The detectors are placed inside a superconducting coil providing an axial magnetic field of 0.52 T. Having 4 m diameter and 3.3 m length the DC is the world’s largest of this type. The mechanical structure is of carbon fiber composite and consists of 12582 drift cells made of tungsten sense wires arranged in 58 stereo layers, a total of 52140 wires. A gas mixture of helium (90%) and isobutane (10%) is used. The position resolution is $150 \mu\text{m}$ in the transverse and 2 mm in the longitudinal directions with respect to the beams, and the relative transverse momentum resolution is $<0.4\%$ for large-angle tracks. The ECAL covers 98% of the solid angle and is divided into a barrel and two end caps with a total of 88 modules. Each module is built out of 1 mm diameter scintillating fibers embedded in 0.5 mm lead foils and the readout is made by photo-multipliers on both sides. The ECAL energy resolution is $\sigma(E)/E = 5.7\%/\sqrt{E(\text{GeV})}$ with excellent timing performance of $\sigma(t) = 54\text{ps}/\sqrt{E(\text{GeV})} \oplus 140 \text{ ps}$. The center of gravity of a cluster in the ECAL is measured with a resolution of 1.3 cm in the transverse and, by signal time difference, of $1.2 \text{ cm}/\sqrt{E(\text{GeV})}$ in the longitudinal direction relative to the fibers. Around the interaction point (IP), the beam pipe has spherical shape, with a radius of 10 cm, to allow K_S mesons to decay in vacuum. The beam pipe walls are made of a 60% beryllium/40% aluminum alloy 0.5 mm thick.

In the KLOE-2 upgrade a tracker device, a novel Inner Tracker (IT), was added. The IT consists of four concentric cylindrical gas electron multiplier detector (CGEM) layers [220] between the IP and the DC to improve the resolution on decay vertices close to the IP. Each layer consists of a triple-CGEM detector with an X-V strip readout. The X strips are placed along the beam axis while the V strips have on average 23° angle with respect to the beam axis. Both X and V strips have a $650 \mu\text{m}$ pitch. The CGEMs are filled with an argon-based gas mixture. A technology with low material budget (below 2% of the radiation length) was chosen, to minimize multiple scattering of low-momentum tracks, photon conversions, and kaon regeneration.

Reviews of the KLOE experimental results using data collected until 2005, including analyses finished until 2008, are given in Refs. [221,222], while the physics program for KLOE-2 was laid out in Ref. [223].

2.1.2 Beijing: BEPC and BES

The Beijing Spectrometer (BES) is a large general-purpose solenoidal detector [224] at the Beijing Electron–Positron Collider (BEPC) used for c – τ physics in the c.m. energy range of 2–5 GeV. The first version of the detector was completed in 1989 and was in operation for six years. Afterwards a major upgrade of the detector, called BESII, was installed [225] to improve its performance. At the same time BEPC was improved to increase the luminosity by a factor of 1.7–2 [226]. Several important results were obtained with BESII, e.g., a precision R -value measurement [227], or the observation of the $X(1835)$ [228]. The results were based on the data samples collected until 2005 at $6 + 85$ c.m. energies between 2 and 5 GeV, 5.8×10^7 J/ψ events, 1.4×10^7 ψ' events, and 20 pb^{-1} data at the peak of the $\psi(3770)$, which underlines the rich physics program in the τ -charm region, including light-hadron spectroscopy, the charmonium spectrum, charm meson decays, and τ physics.

To meet the challenge of precision c – τ physics, a major upgrade of the collider, now called BEPCII, was completed in 2008 together with the new BESIII detector. The collider has separate rings for the electron and positron beams with a single interaction region. The peak luminosity is $10^{33} \text{ cm}^{-2}\text{s}^{-1}$ at $\sqrt{s} = 3.773 \text{ GeV}$, i.e., 100 times larger than its predecessor. The BESIII detector is a large solid-angle magnetic spectrometer schematically shown in Fig. 15(b) and described in detail in Ref. [229]. The main

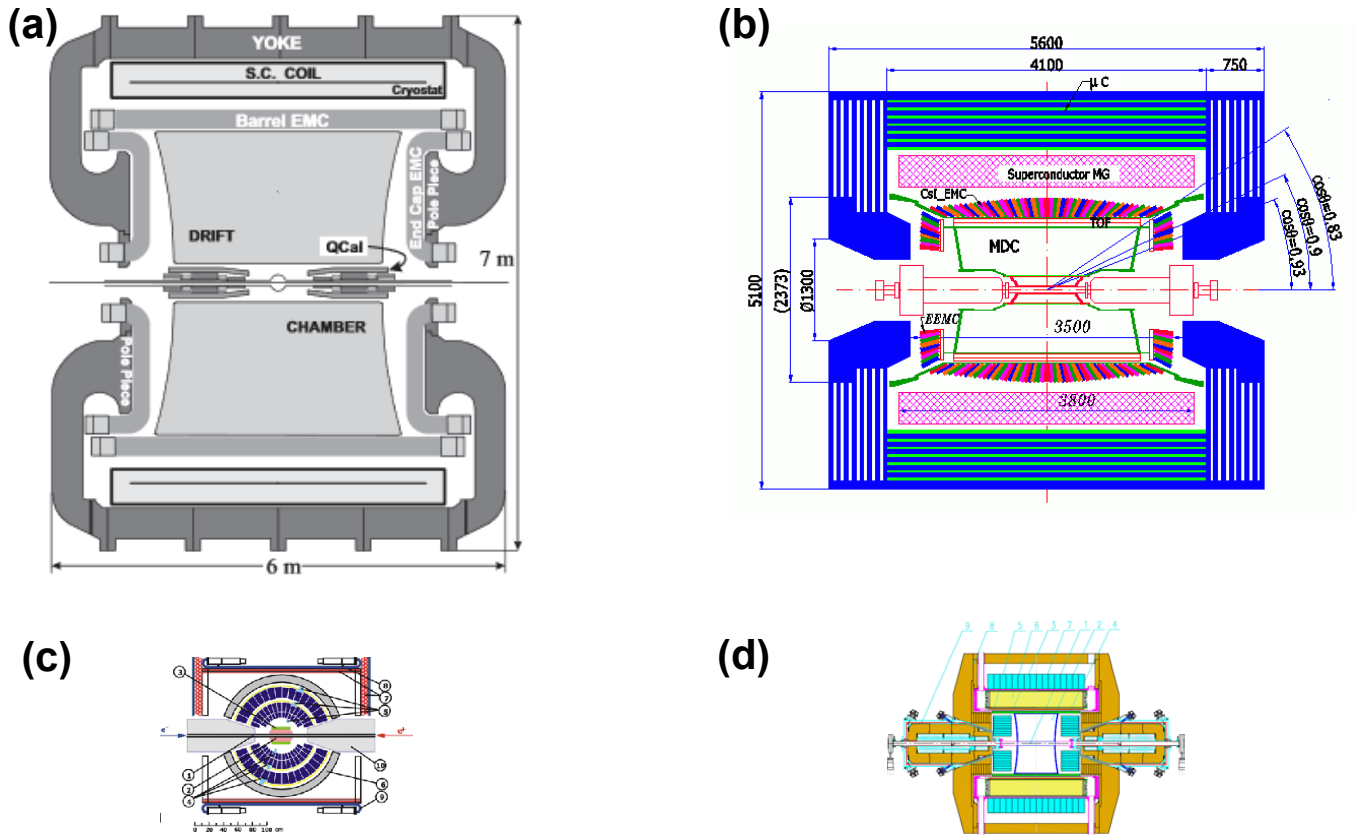


Figure 15: Detectors at the symmetric electron–positron colliders (a) KLOE, (b) BESIII, (c) SND, and (d) CMD-3. All detectors are drawn approximately in the same scale. We show schematic cross sections along the beam axes.

components are the superconducting solenoid magnet with a central field of 1 T, the main drift chamber (MDC), and a cesium iodide (CsI) electromagnetic calorimeter. Up to 2020 the BESIII detector has collected the world’s largest samples in the $c\text{-}\tau$ energy range including 10^{10} J/ψ events, 4.5×10^8 ψ' events, 2.9 fb^{-1} data at the $\psi(3770)$, and more than 15 fb^{-1} data above 4 GeV. Most of the results presented in the review for J/ψ decays use 1.31×10^9 events collected in the 2009 and 2012 runs. The physics accomplishments of the BES experiments are reviewed in the recent articles Refs. [230, 231].

2.1.3 Novosibirsk: VEPP and SND, CMD

The Institute of Nuclear Physics (INP) (currently the Budker Institute of Nuclear Physics) was one of the first research centers to build an electron–positron collider (see Sec. 1.2). The parameters of the second collider VEPP-2M operating with several generations of detectors until the end of the 1990s are given in Table 2 [93]. The c.m. energies ranged up to 1.4 GeV and it had two interaction points, allowing to collect data simultaneously by two detectors. The collected data on the hadronic cross sections by the two latest experiments CMD-2 [232, 233] and SND [234, 235] gives one of the most important contributions to the accuracy for the hadronic contributions to the muon $g - 2$. The purpose of the new successor collider VEPP-2000 is to study light hadrons using variable c.m. energies up to 2.0 GeV. The facility reuses the VEPP-2M buildings and its infrastructure. It uses a round beam to suppress beam–beam effects. Initially, until 2013, data were collected using the old injector system, which limited the luminosity at the highest energies. The two new detectors are CMD-3 and the upgraded SND [236] shown schematically in Fig. 15. The detectors are very compact, which is imposed by the size of the ring and the experimental hall.

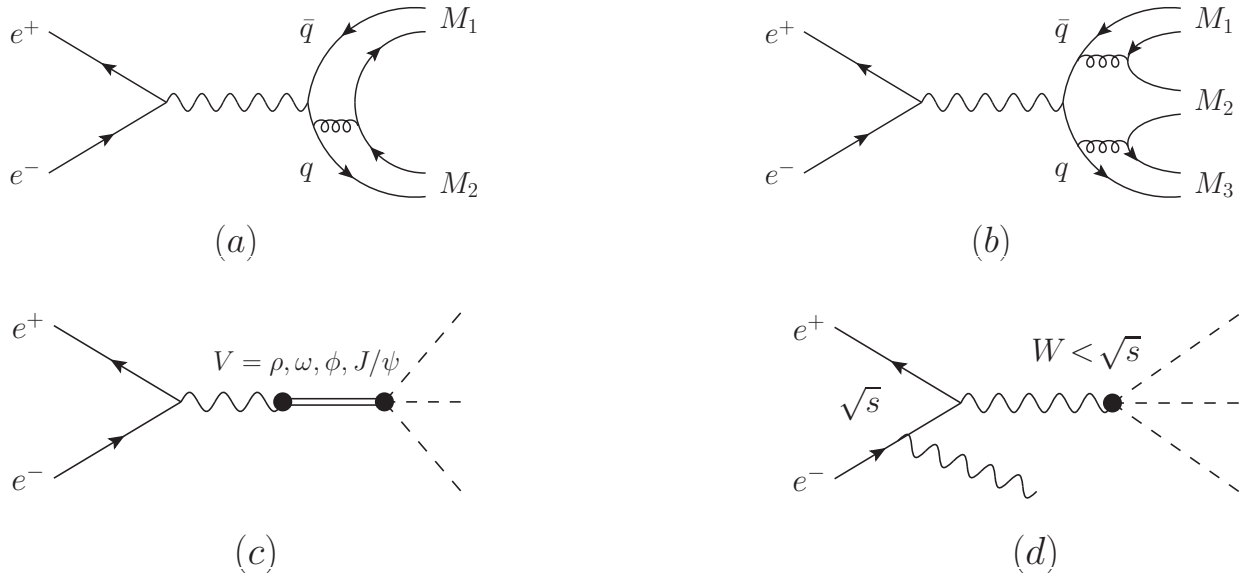


Figure 16: Mechanisms of hadron production in electron–positron annihilation: (a) a quark diagram for two-meson production; (b) a quark diagram for three-meson production; (c) a neutral-vector-meson-dominated process; (d) initial-state radiation production mechanism.

2.2 Production of hadronic systems

One can describe the ideal setup to study meson–meson interactions as a system without extra hadrons from the production process. The production mechanism should be well understood or easy to parameterize in a model-independent way. In addition, the invariant mass of the meson–meson system should be variable. Such conditions can be achieved, e.g., by changing the c.m. energy of the collider or having an extra photon, $l\bar{l}$, $l\bar{\nu}_l$, or ν_τ , which carry away part of the initial fixed energy. There are many sources of light-hadron systems at e^+e^- colliders. We consider only processes with sufficiently large cross sections to provide enough events for precision studies. In this section we introduce the main processes where systems of two or three light mesons in the final state can be produced.

2.2.1 Single-photon annihilation

The direct production of a meson system in the single-photon annihilation process $e^+e^- \rightarrow X$ exclusively produces states with quantum numbers $J^{PC} = 1^{--}$. We illustrate such production processes by simplified quark diagrams in Fig. 16(a) and (b) for meson–meson pairs and three-meson systems, respectively. The measurement of the total cross section for a pseudoscalar meson pair like $\pi^+\pi^-$ as a function of c.m. energy is directly related to the meson–meson interactions in the P -wave, and allows to extract vector form factors, $F_\pi^V(s)$ for the given example.

The differential rate for the production of a hadronic system via a single virtual photon, see Fig. 5(b), can be expressed as the product of leptonic and hadronic tensors, multiplied with the multihadron phase space element:

$$d\sigma = \frac{e^4}{8s^3} L_{\mu\nu} H^{\mu\nu} d\Phi_n(q_1, \dots, q_n), \quad (54)$$

where $s = (p_1 + p_2)^2$, and $d\Phi_n(q_1, \dots, q_n)$ denotes the n -body phase space with all statistical factors included. The leptonic tensor $L_{\mu\nu} = L_{\mu\nu}(p_1, p_2)$ is process-independent and for unpolarized beams given by the averages over lepton spins,

$$L_{\nu\mu}(p_1, p_2) = \frac{1}{4} \text{Tr}[\gamma_\nu \not{p}_1 \gamma_\mu \not{p}_2] = p_{1\nu} p_{2\mu} + p_{2\nu} p_{1\mu} - \frac{1}{2} s g_{\nu\mu}. \quad (55)$$

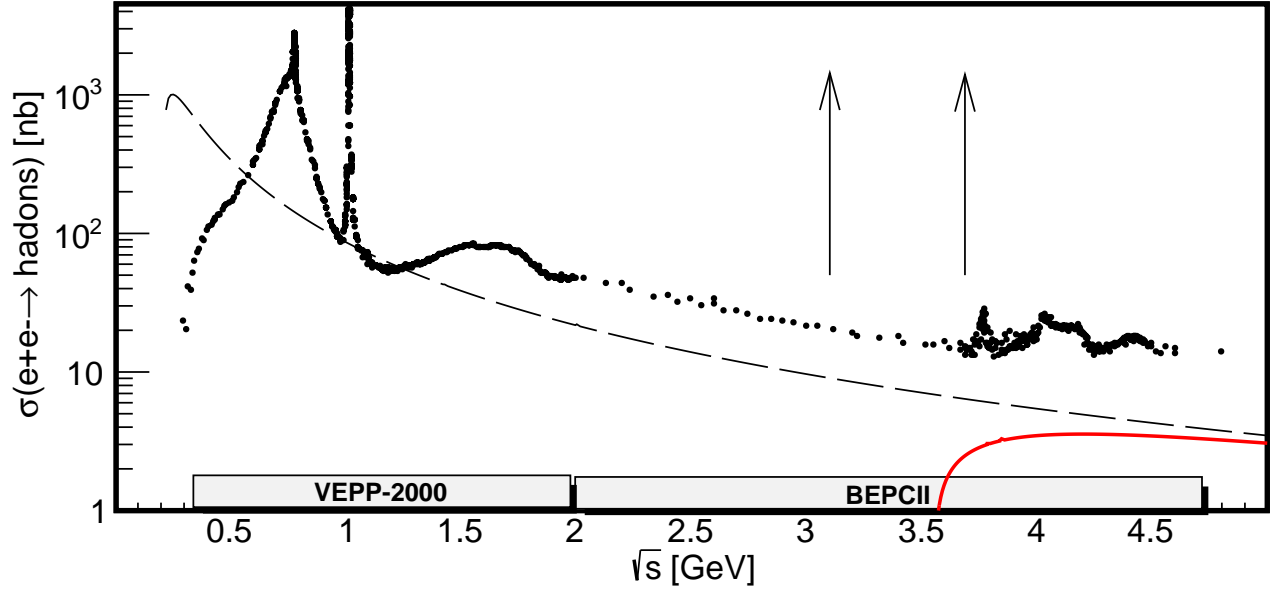


Figure 17: Total bare cross section of $e^+e^- \rightarrow \text{hadrons}$ as a function of center-of-mass energy from the compilation of Ref. [237]. The two vertical arrows indicate the positions of the J/ψ and ψ' peaks. The c.m. energy ranges of the VEPP-2000 and BEPCII colliders are also shown. Dashed and solid lines refer to $e^+e^- \rightarrow \mu^+\mu^-$ and $e^+e^- \rightarrow \tau^+\tau^-$ e.m. Born cross sections, respectively.

The leptonic tensor is symmetric, and hence it is only the real symmetric part of the hadronic tensor $H_{\mu\nu}$ that is relevant for the differential cross section. The hadronic tensor is defined via current matrix elements as [238]

$$H_{\mu\nu} = J_{\mu}^{\text{em}} (J_{\nu}^{\text{em}})^* , \quad (56)$$

where for the production of an n -particle hadronic final state, the matrix element of the hadronic current is

$$J_{\mu}^{\text{em}} \equiv J_{\mu}^{\text{em}}(q_1, \dots, q_n) \equiv \langle h(q_1), \dots, h(q_n) | j_{\mu}^{\text{em}} | 0 \rangle , \quad (57)$$

with the electromagnetic current at the quark level given by

$$j_{\mu}^{\text{em}} = \frac{2}{3} \bar{u}\gamma_{\mu}u - \frac{1}{3} \bar{d}\gamma_{\mu}d - \frac{1}{3} \bar{s}\gamma_{\mu}s + \frac{2}{3} \bar{c}\gamma_{\mu}c + \dots . \quad (58)$$

The quark electromagnetic current can be decomposed into an isospin singlet piece and a part transforming like the third component of an isospin triplet:

$$j_{\mu}^{\text{em}} = \frac{1}{\sqrt{2}} j_{\mu}^3 + \frac{1}{3\sqrt{2}} j_{\mu}^{I=0} - \frac{1}{3} \bar{s}\gamma_{\mu}s + \frac{2}{3} \bar{c}\gamma_{\mu}c + \dots , \quad (59)$$

where

$$j_{\mu}^3 = \frac{\bar{u}\gamma_{\mu}u - \bar{d}\gamma_{\mu}d}{\sqrt{2}} \quad \text{and} \quad j_{\mu}^{I=0} = \frac{\bar{u}\gamma_{\mu}u + \bar{d}\gamma_{\mu}d}{\sqrt{2}} . \quad (60)$$

The above expressions for the electromagnetic current give a qualitative picture of the annihilation process to the light-hadron systems. At the lowest energies, below the $K\bar{K}$ production threshold for open strangeness, the isovector systems should contribute with 90% to the total cross section, while above $c\bar{c}$ threshold this contribution is reduced to 45%. As two examples, which we will discuss in this review, we give the expressions for the hadronic currents for the dominant contributions to the isovector and the isoscalar processes $e^+e^- \rightarrow \pi^+\pi^-$ and $e^+e^- \rightarrow \pi^+\pi^-\pi^0$, respectively. For $e^+e^- \rightarrow \pi^+(q_+)\pi^-(q_-)$, the current matrix element

$$J_{\nu}^{\text{em},2\pi} = (q_+ - q_-)_{\nu} F_{\pi}^V(s) \quad (61)$$

is determined by only one scalar, dimensionless function, the pion vector form factor $F_\pi^V(s)$. We discuss properties of this form factor in Sec. 3.1. As we will show, there is a direct connection between F_π^V and pion–pion interactions in a P -wave. For the three-pion production $e^+e^- \rightarrow \pi^+(q_1)\pi^-(q_2)\pi^0(q_3)$, the current matrix element is restricted by negative parity to the form

$$J_\nu^{\text{em},3\pi} = \epsilon_{\nu\alpha\beta\gamma} q_1^\alpha q_2^\beta q_3^\gamma F_{3\pi}(s; s_1, s_2, s_3), \quad (62)$$

where $F_{3\pi}(s; s_1, s_2, s_3)$ is a scalar function of the total $s = (q_1+q_2+q_3)^2$ and the two-pion invariant masses $s_1 = (p_2 + p_3)^2$ (plus cyclic permutations). This function depends on three independent Mandelstam variables, as $s_1 + s_2 + s_3 = s + 3m_\pi^2$, and describes the interaction of three pions at a given c.m. energy. We discuss this process more closely in Sec. 3.7.

The basic observable measured at electron–positron colliders is the total cross section obtained by the integration of Eq. (54) over the kinematic variables defining the final state. In the case of two-body hadronic production as in $e^+e^- \rightarrow \pi^+\pi^-$, it is directly related to the pion dynamics via $|F_\pi^V(s)|^2$. An interesting question is to what extent we can infer information about meson–meson dynamics also from the cross section dependence in the case of three and more produced hadrons. A direct connection is established rather by studies of differential distributions via the multidimensional form factors such as $F_{3\pi}(s; s_1, s_2, s_3)$. However, the cross section is the first and often the only accessible observable as it requires the smallest amount of collected data. In case there is no interaction, $F_{3\pi} = \text{const.}$ and the cross section should follow three-body phase space or phase space restricted by angular momentum conservation and other symmetries. A strong interaction between a single pair of mesons would lead to the cross section dependence given by the corresponding two-body phase space. The effect is especially important close to threshold and can help to understand the dynamics of the process. We present examples of cross section measurements for three-body processes in Sec. 3.7.

2.2.2 Strong and radiative decays of vector mesons

A single-photon annihilation process into a hadronic system can be mediated by a narrow neutral vector meson [see Fig. 16(c)], like ω , ϕ , J/ψ , and ψ' , strongly enhancing the hadronic cross section at the c.m. energy corresponding to the resonance mass as shown in Fig. 17. One can therefore use the vector meson decays as an abundant source of light hadrons for precision studies of meson–meson interactions. The propagator of a neutral vector meson V with momentum $P = p_1 + p_2$ takes the form

$$\frac{i(-g_{\mu\nu} + P_\mu P_\nu/m_V^2)}{s - \Pi(s)}, \quad (63)$$

where m_V is the V mass and $\Pi(s)$ is the self-energy of the resonance, $\Pi(s) = m_V^2(s) + im_V(s)\Gamma_V(s)$. The absorptive part $\text{Im}\Pi(s) = m_V(s)\Gamma_V(s)$ is generated by intermediate states that can go on their mass shell, while the dispersive part $\text{Re}\Pi(s) = m_V^2(s)$ also obtains contributions from intermediate states that are virtual only (resonance propagation without decay). In general the function $\Pi(s)$ is very complicated and for hadronic resonances incalculable in a fundamental way. For a narrow resonance, it can be approximated as a constant $\Pi(s) \simeq m_V^2 + im_V\Gamma_V$, where Γ_V is the full decay width. Simple generalizations to energy-dependent widths take at least the corresponding decay phase spaces into account, thus avoiding imaginary parts below threshold. For a resonance produced through an intermediate photon, the contribution from the $P_\mu P_\nu$ term in the propagator vanishes and the matrix element is structurally identical to the nonresonant annihilation, provided we make the replacement

$$\frac{e^2}{s} \longrightarrow \frac{e_V e_X}{s - m_V^2 + im_V\Gamma_V}, \quad (64)$$

where e_V is the resonance coupling to the e^+e^- pair, determined from the leptonic decay width, and e_X is the coupling to the final state X .

Table 3: Estimate of the available η/η' data sets assuming 2.4×10^{10} ϕ events at KLOE/KLOE-2 and 10^{10} J/ψ events at BESIII.

Decay mode	\mathcal{B} ($\times 10^{-4}$) [48]	P_{cm} [MeV]	η/η' events
$\phi \rightarrow \gamma\eta$	130.3(2.5)	363	3.1×10^8
$\phi \rightarrow \gamma\eta'$	0.622(21)	60	1.5×10^6
$J/\psi \rightarrow \gamma\eta'$	52.1(1.7)	1400	5.2×10^7
$J/\psi \rightarrow \gamma\eta$	11.08(27)	1500	1.1×10^7
$J/\psi \rightarrow \phi\eta$	7.5(8)	1320	7.5×10^6
$J/\psi \rightarrow \phi\eta'$	4.6(5)	1192	4.6×10^6
$J/\psi \rightarrow \omega\eta$	17.4(2.0)	1394	1.7×10^7

In general, two types of experiments for meson–meson interactions are possible using decays of vector mesons. The first is direct production of hadronic systems in strong and radiative decays. To study dynamics in this case, three and more particles should be created, and the radiative decays with just two hadrons are particularly simple. We discuss these in Sec. 3.3. The data sets for ϕ , J/ψ , and ψ' mesons collected at KLOE and BESIII are huge, with at the order of 10^{10} events (see Sec. 2.1), and can be used for detailed studies of the interactions of the hadrons produced in the decays. In the second type of experiment a decay into a pair of stable particles (or narrow resonances) is used to tag a hadron to study its further decays. In particular radiative and strong hadronic decays of η and η' are well-known laboratories for precision studies of pion interactions. Radiative decays of ϕ and J/ψ are among the best sources of η and η' mesons since they have large branching fractions (\mathcal{B}) as shown in Table 3. The accompanying monochromatic radiative photon is in most cases well separated from the decay products. Huge numbers of ϕ and J/ψ collected at KLOE and BESIII were used for numerous precision studies of η and η' [239]. We show some examples in Secs. 3.4 and 3.9. Another option is the hadronic two-body processes with a narrow vector meson replacing the radiative photon, e.g., $J/\psi \rightarrow \omega\eta$, which allows for competitive study of ω decays as we discuss in Sec. 3.7. Furthermore, at a c - τ factory production of nonvector narrow charmonium resonances, e.g., η_c or χ_{cJ} , allows us to study their decays into light-hadron systems. At electron–positron colliders, these charmonia come from radiative decays of J/ψ and ψ' such as $J/\psi \rightarrow \eta_c\gamma$ with $\mathcal{B} \approx 1\%$ or $\psi' \rightarrow \gamma\chi_{cJ}$ with $\mathcal{B} \approx 10\%$.

2.2.3 Higher-order electromagnetic processes

With the modern high-luminosity colliders, hadron systems can be studied using higher-order electromagnetic processes like initial-state radiation $e^+e^- \rightarrow X\gamma$, shown in Fig. 16(d), and two-photon fusion $e^+e^- \rightarrow e^+e^-\gamma^*\gamma^* \rightarrow e^+e^-X$, Fig. 18(a). The invariant mass W of the produced hadronic system X can vary between threshold and the c.m. energy \sqrt{s} of the collider. There are recent extensive reviews covering these experimental techniques: Ref. [240] for the ISR method and Ref. [241] for the two-photon processes. In addition, such experiments benefit from highest luminosities or/and high energies available at B -factories.

Initial-state radiation processes The photon in the $e^+e^- \rightarrow X\gamma$ process can be radiated in the initial state from the electron or positron beams as shown in diagram Fig. 16(d). This corresponds to the

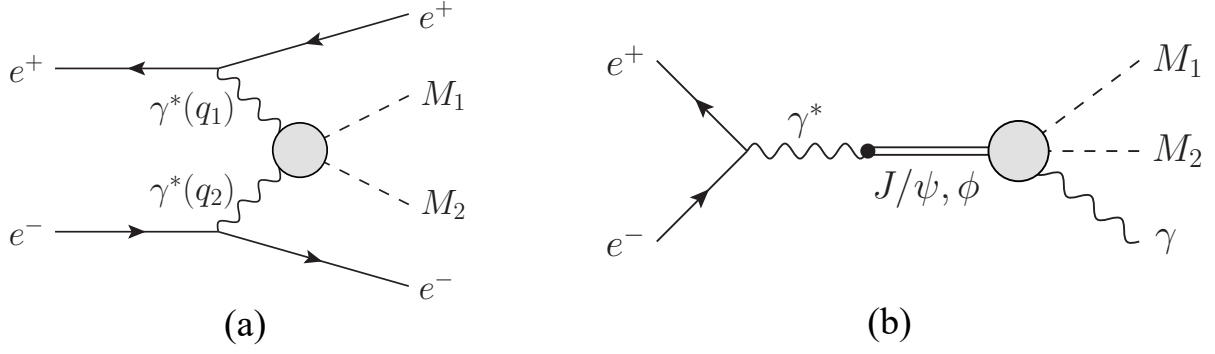


Figure 18: Production of parity-even meson systems ($M_1 M_2$) in (a) two-photon processes and (b) radiative decays of J/ψ or ϕ .

ISR mechanism, where the quantum numbers of the hadronic system X are $J^{PC} = 1^{--}$. Alternatively the photon can be radiated after annihilation took place, e.g., due to a radiative decay of a vector meson V as in diagram Fig. 18(b). This corresponds to final-state radiation (FSR) and the hadronic system is in an even charge conjugation eigenstate $C = +1$, but both spin and parity can have several values.

The general properties of an ISR process can be derived from QED and are given by the leptonic tensor $L_{\text{ISR}}^{\mu\nu}$, which is separated from the hadronic part. The main features of the ISR photon distribution are the infrared divergence for small energies of the radiated photon and collinear divergences for small emission angles with respect to the electron or positron beams. The ISR process allows one to extract continuum hadronic cross sections for invariant masses W of the hadronic system from threshold up to the c.m. energy \sqrt{s} of the colliding beams. It effectively converts a fixed energy, high-luminosity collider into a variable-energy machine [242]. The ISR technique was first applied at the KLOE experiment to study $e^+e^- \rightarrow \pi^+\pi^-$ [243]. Since then the production cross sections for many multihadron final states were measured using this method. Most of the results were obtained at the BaBar experiment, with accumulated data samples corresponding to the integrated luminosity of 0.5 ab^{-1} at the Υ resonances. In the context of our review, for light-meson dynamics, the application of the method is so far limited to studies of the total cross sections of meson systems. This might change in the future when statistics will be sufficient to study multidimensional differential distributions of the produced multihadron states.

The differential cross section for the ISR process $e^+(p_1) + e^-(p_2) \rightarrow \text{hadrons} + \gamma(k_1)$ can be written in terms of the leptonic and hadronic tensors as [244]

$$d\sigma = \frac{(4\pi\alpha)^2}{W^3 s^2} L_{\text{ISR}}^{\mu\nu} H_{\mu\nu} \frac{s - W^2}{64\pi^3} d\Phi_n(W; q_1, \dots, q_n) d\Omega dW, \quad (65)$$

where $\Phi_n(W; q_1, \dots, q_n)$ denotes the phase space volume of the hadronic system and Ω the scattering angle of the ISR photon. The general form of the ISR leptonic tensor is

$$L_{\text{ISR}}^{\mu\nu} = a_{00} g^{\mu\nu} + a_{11} \frac{p_1^\mu p_1^\nu}{s} + a_{22} \frac{p_2^\mu p_2^\nu}{s} + a_{12} \frac{p_1^\mu p_2^\nu + p_2^\mu p_1^\nu}{s} + i\pi a_{-1} \frac{p_1^\mu p_2^\nu - p_2^\mu p_1^\nu}{s}, \quad (66)$$

where the LO coefficients are

$$\begin{aligned} a_{00}^{(0)} &= \frac{2m^2 z^2 (1 - z^2)^2}{y_1^2 y_2^2} - \frac{2z^2 + y_1^2 + y_2^2}{y_1 y_2}, & a_{11}^{(0)} &= \frac{8m^2}{y_2^2} - \frac{4z^2}{y_1 y_2}, \\ a_{22}^{(0)} &= a_{11}^{(0)}(y_1 \leftrightarrow y_2), & a_{12}^{(0)} &= -\frac{8m^2}{y_1 y_2}, & a_{-1}^{(0)} &= 0, \end{aligned} \quad (67)$$

with

$$y_i = \frac{2k_1 \cdot p_i}{s}, \quad m^2 = \frac{m_e^2}{s}, \quad z = \frac{W}{\sqrt{s}}. \quad (68)$$

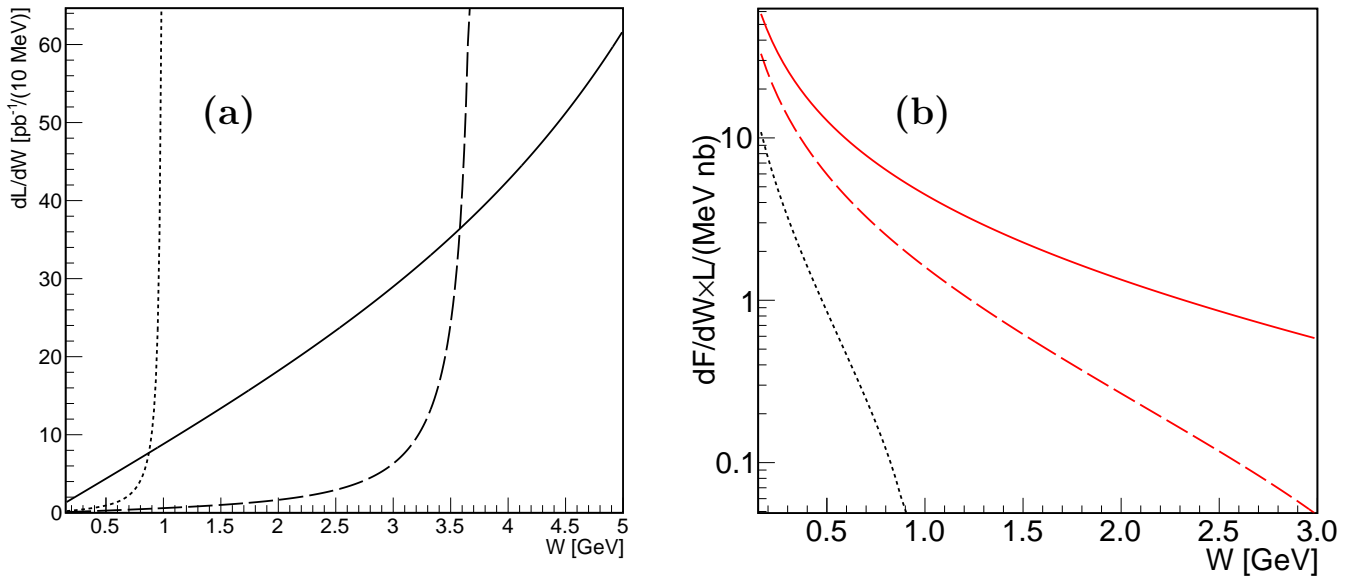


Figure 19: Indicative differential luminosities as a function of the hadronic system invariant mass W at the ϕ meson (dotted line), $c\text{-}\tau$ (dashed line), and B -factories (solid line) for (a) ISR processes (for $\mathcal{L} = 2 \text{ fb}^{-1}$, 10 fb^{-1} , and 1 ab^{-1} , respectively) and (b) $\gamma\gamma$ processes ($\mathcal{L} = 1 \text{ fb}^{-1}$).

The result of the integration of the cross section in Eq. (65) with respect to all variables but the invariant mass of the hadronic system W can be expressed in terms of the ISR luminosity L as

$$\frac{d\sigma}{dW} \approx \frac{\sigma_B(W)}{\mathcal{L}} \frac{dL}{dW}, \quad (69)$$

where \mathcal{L} is the integrated luminosity at the primary c.m. energy of the colliding electron–positron beams. The term dL/dW is given by a radiator function as discussed in Sec. 2.3. The ISR luminosity is compared for colliding beams with c.m. energies of 1 GeV, 3.77 GeV, and 10 GeV, approximately corresponding to the experiments at KLOE-2, BESIII, and B -factories, respectively, in Fig. 19(a). The plot was obtained using indicative values of the integrated luminosities \mathcal{L} for each facility: 2 fb^{-1} , 10 fb^{-1} , and 1 ab^{-1} . The ISR luminosity is a fast increasing function close to the c.m. energy of the collider. The cross section measurements using ISR processes have reached such statistical precision that they are often dominated by systematic effects. Therefore the ISR measurements at colliders with different c.m. energies provide complementary data sets with different experimental settings. The best example is given by the studies of the $e^+e^- \rightarrow \pi^+\pi^-$ process discussed in Sec. 3.1.

Two-photon processes Two-photon production of $C = +1$ hadronic systems in $e^-e^\pm \rightarrow e^-e^\pm\gamma^*\gamma^* \rightarrow e^-e^\pm X$ is given by the diagram illustrated in Fig. 18(a). The two photons are space-like with squared four-momenta $q_1^2, q_2^2 \leq 0$ and the process can be studied both in electron–positron and electron–electron collisions. The cross section increases as the logarithm of the c.m. energy of the colliding beams. Since it was realized in the 1970s that significant production rates could be achieved [245, 246], the two-photon processes have been investigated at most of the e^+e^- colliders with the limitations imposed by the rate of these subleading processes at the luminosity reached by past-generation colliders.

Three types of experiments are possible: untagged, where none of the leptons in the final state is recorded; single-tagged, with one lepton measured; and double-tagged, where the two leptons are

measured, meaning that the corresponding photon four-momenta are determined. If not tagged, the unmeasured photon distributions peak at $q_1^2(q_2^2) \approx 0$.

In the low-energy region the two γ^* can be considered quasi-real, so that only $J^{PC} = 0^{\pm\pm}, 2^{\pm\pm}$ quantum numbers are allowed [247]. If no cut is applied to the final-state leptons, the Weizsäcker–Williams or equivalent-photon approximation [246] can be used to understand the main qualitative features. Then the event yield, N_{eeX} , can be evaluated according to

$$N_{eeX} = \mathcal{L} \int \frac{dF}{dW} \sigma_{\gamma\gamma \rightarrow X}(W) dW, \quad (70)$$

where W is the invariant mass of the produced hadronic system, \mathcal{L} is the integrated luminosity, and dF/dW is the $\gamma\gamma$ flux,

$$\frac{dF}{dW} = \frac{1}{W} \left(\frac{2\alpha}{\pi} \right)^2 \left(\ln \frac{\sqrt{s}}{2m_e} \right)^2 f(z), \quad (71)$$

where \sqrt{s} is the c.m. energy of the collider and

$$f(z) = -(z^2 + 2)^2 \ln z - (1 - z^2)(3 + z^2) \quad \text{with} \quad z = \frac{W}{\sqrt{s}}. \quad (72)$$

Figure 19(b) shows the flux multiplied by an integrated luminosity $\mathcal{L} = 1 \text{ fb}^{-1}$, as a function of the W invariant mass for three different c.m. energies. This plot demonstrates the feasibility of the measurements of the final states $\pi^+\pi^-$, $\pi^0\pi^0$, or $\pi^0\eta$, whose cross sections are of the order of or larger than 1 nb, and of the identification of the resonances produced in these channels. Single pseudoscalar ($X = \pi^0, \eta$, or η') production is also accessible, which allows for the determination of the two-photon decay widths of these mesons and to measure the transition form factors $F_{X\gamma^*\gamma^*}(q_1^2, q_2^2)$ as a function of the momentum of the virtual photons, q_1^2 and q_2^2 .

In the present review we will give examples of the related radiative processes shown in Fig. 18(b). The radiative decays have usually much larger cross sections and precision differential experimental data is available. One can use dispersive methods to relate these processes to the two-photon form factors. A prominent example is the use of information from $e^+e^- \rightarrow \pi^+\pi^-$ and $e^+e^- \rightarrow \pi^+\pi^-\pi^0$ to deduce the π^0 transition form factor, i.e., the $\pi^0\gamma^*\gamma^*$ vertex [248–250].

2.2.4 Tau lepton decays

The purely leptonic initial state in τ decays involving two or three final-state hadrons and the τ neutrino represents one of the cleanest ways to study mesonic systems. The hadronic systems are produced by elementary currents. The accessible invariant masses of the produced system vary from threshold up to m_τ due to the energy taken by the emitted ν_τ .

Tau leptons are produced in the continuum electroweak process $e^+e^- \rightarrow \tau^+\tau^-$, see Fig. 5(a). The threshold $\sqrt{s_{\text{thr}}} = 2m_\tau$ is 132 MeV below the mass of the ψ' resonance. The differential cross section for a lepton–antilepton pair e.m. production process is

$$\frac{d\sigma}{d\Omega} = \frac{\alpha^2}{4s} \sqrt{1 - \frac{4m_\ell^2}{s}} \left[\left(1 + \frac{4m_\ell^2}{s} \right) + \left(1 - \frac{4m_\ell^2}{s} \right) \cos^2 \theta \right], \quad (73)$$

and the total Born cross section with perturbative photon propagator

$$\sigma = \frac{4\pi\alpha^2}{3s} \sqrt{1 - \frac{4m_\ell^2}{s}} \left(1 + \frac{2m_\ell^2}{s} \right). \quad (74)$$

The $e^+e^- \rightarrow \tau^+\tau^-$ e.m. Born cross section is shown in Fig. 17, where the maximum of 3.8 nb is reached at 4.2 GeV. The cross section in Eq. (74) should be multiplied by the lepton form factor

$|F_\ell(s)|^2$ accounting for vacuum polarization [251]. The effect of the form factor is that the production is enhanced at vector resonances such as the ψ' . We will discuss this effect in Sec. 2.3.2. So far the majority of the experimental studies of the τ lepton were done at high-energy electron–positron colliders such as LEP or B -factories. However, close-to-threshold production offers a cleaner environment. The direct scan at the $\tau^+\tau^-$ production threshold is also the best method to precisely measure the mass of the τ lepton, an important parameter of the Standard Model. The most precise recent results are from the KEDR [252] and BESIII experiments [253].

An important feature of the $e^+e^- \rightarrow \tau^+\tau^-$ process is that the $\tau^+\tau^-$ pair is produced in a spin-correlated state. We define τ^+ and τ^- polarization vectors in their respective rest frames with the same orientations of the spin quantization axes with the z direction along τ^- momentum in the overall c.m. system. The y direction is given by the vector product of the incoming electron and the outgoing τ^- momenta. The spin correlation matrix depends on the angle θ between the electron and the τ^- . At c.m. energies relevant to c - τ factories, the electron mass can be neglected and a single-photon annihilation process dominates. The spin correlation matrix for the e.m. process in the Born approximation is given as [254]

$$\frac{1}{1 + \eta \cos^2 \theta} \begin{pmatrix} \sin^2 \theta & 0 & \sqrt{1 - \eta^2} \sin \theta \cos \theta \\ 0 & -\eta \sin^2 \theta & 0 \\ \sqrt{1 - \eta^2} \sin \theta \cos \theta & 0 & \eta + \cos^2 \theta \end{pmatrix} \quad \text{with} \quad \eta = \frac{s - 4m_\tau^2}{s + 4m_\tau^2}. \quad (75)$$

Close to production threshold, $\eta \approx 0$ and the matrix includes x - z spin correlation terms. The $\tau^+\tau^-$ spin correlations are reflected in the multidimensional distribution of the daughter particles from the two leptons.

The matrix element for a semileptonic decay $\tau \rightarrow X\nu_\tau$ has the form

$$\mathcal{M} = \frac{G_F}{\sqrt{2}} \bar{u}(p_\nu) \gamma^\mu (1 - \gamma_5) u(p_\tau) J_\mu. \quad (76)$$

Since parity is maximally violated in τ decays, the hadronic current has both vector and axial-vector contributions, $J_\mu = \langle X | V_\mu - A_\mu | 0 \rangle$. The weak quark current is

$$j_\mu^- = \bar{d} \gamma_\mu (1 - \gamma_5) u \cos \theta_C + \bar{s} \gamma_\mu (1 - \gamma_5) u \sin \theta_C. \quad (77)$$

The general weak hadronic current contains four terms [254]:

$$J^\mu = \left[(F_1^\mu + iF_2^\mu) - (F_1^{5\mu} + iF_2^{5\mu}) \right] V_{ud} + \left[(F_4^\mu + iF_5^\mu) - (F_4^{5\mu} + iF_5^{5\mu}) \right] V_{us}. \quad (78)$$

In the limit of exact isospin symmetry, the weak vector current is conserved separately and is directly related to the electromagnetic current [255], i.e., the coupling of the W to the ρ meson is given by the replacement $e \rightarrow \sqrt{2}g \cos \theta_C$. The τ decays into two pseudoscalar mesons illustrated by the diagram in Fig. 20(left) are particularly clean systems to study meson–meson interactions. Branching fractions for some of such modes are listed in Table 4. In these decays the hadronic system can have spin-parity quantum numbers $J^P = 0^+$ or 1^- , and in the isospin limit the conserved-vector-current theorem forbids production of 0^+ nonstrange states in τ decays. Since there are two recent reviews dedicated to hadronic τ decays [256, 257] we will discuss only the direct connection between $e^+e^- \rightarrow \pi^+\pi^-$, $e^+e^- \rightarrow K\bar{K}$ and $\tau^- \rightarrow \pi^-\pi^0\nu_\tau$, $\tau^- \rightarrow K^-\bar{K}^0\nu_\tau$ in Sec. 3.1. The symmetric $V - A$ structure of the weak current implies that any differences between the two currents are generated by nonperturbative QCD effects. The axial vector current is dominated by $X = \pi^-\pi^+\pi^-$ with the $a_1(1260)$ resonance decaying (predominantly) to $\rho\pi$, which provides complementary information to the isoscalar vector current in the $e^+e^- \rightarrow \pi^-\pi^+\pi^0$ reaction.

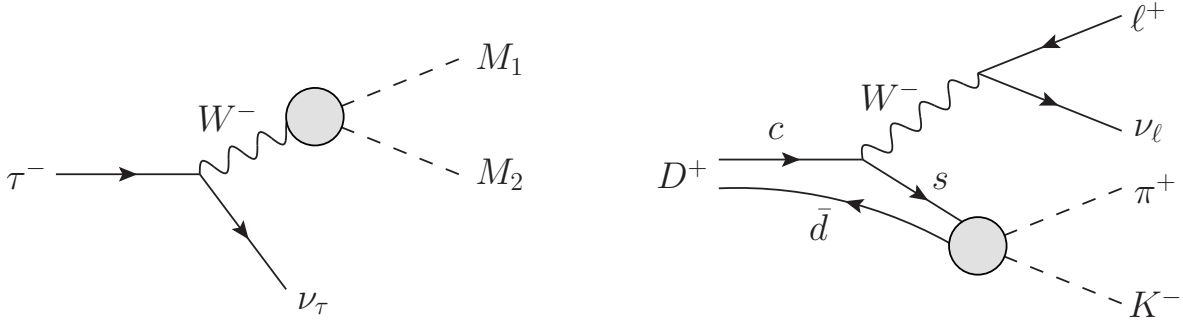


Figure 20: Tau and charmed-meson decays as a means to study meson interactions.

Table 4: Branching fractions for example decay modes of the τ lepton into two light mesons [48].

Decay mode	\mathcal{B}
$\tau \rightarrow \pi^- \pi^0 \nu_\tau$	25.49(9)%
$\tau \rightarrow K^- \pi^0 \nu_\tau$	$4.33(15) \times 10^{-3}$
$\tau \rightarrow K^- K^0 \nu_\tau$	$1.486(34) \times 10^{-3}$
$\tau \rightarrow \eta K^- \nu_\tau$	$1.55(8) \times 10^{-4}$
$\tau \rightarrow \phi \pi^- \nu_\tau$	$3.4(6) \times 10^{-5}$
$\tau \rightarrow \phi K^- \nu_\tau$	$4.4(16) \times 10^{-5}$
$\tau \rightarrow \omega \pi^- \nu_\tau$	$1.95(6) \times 10^{-2}$
$\tau \rightarrow \omega K^- \nu_\tau$	$4.1(6) \times 10^{-4}$

2.2.5 Weak decays of K and D mesons

The electron–positron colliders are also factories of exclusive quantum-correlated pairs of $K\bar{K}$ and $D\bar{D}$ mesons. The DAΦNE collider provides optimal conditions for the production of entangled kaon pairs close to threshold at the ϕ resonance, where the kaon–antikaon modes are the dominant contributions to the decay width: $\mathcal{B}(\phi \rightarrow K^+ K^-) = 49.2(5)\%$ and $\mathcal{B}(\phi \rightarrow K_L K_S) = 34.0(4)\%$. The main experimental advantage is the possibility to select a pure, kinematically well-defined K_S beam. Kaons from ϕ decays have low momenta of 110 MeV for neutral kaons. Due to the beams’ crossing angle, there is a transverse momentum component of 15 MeV in the detector reference system. The mean decay lengths of K_L and K_S are 3.4 m and 0.59 cm, respectively. For a detector with a radius of 2 m such as KLOE, this gives a geometrical efficiency of ca. 30% for the fiducial volume for the detection of the K_L decay vertex [221]. On the other hand, a fraction of the K_L interacts in the calorimeter, allowing the experiment to efficiently tag the K_S beam. However, from K_S decays, with the dominant contribution of two-pion decays, only limited information on meson interactions can be extracted. The more relevant K_L studies must be carried out at dedicated fixed-target facilities using hadronic production reactions and extracting K_L beams.

On the contrary, the potential for meson interaction studies in D and D_s decays at the c – τ colliders is huge. Both semileptonic $D \rightarrow X \ell \bar{\nu}_\ell$ shown in Fig. 20(right) and hadronic modes with at least three mesons can be investigated [258]. For D mesons the optimal production process is $e^+ e^- \rightarrow \psi(3770) \rightarrow D\bar{D}$ with cross sections $\sigma(e^+ e^- \rightarrow D^0 \bar{D}^0) = 3.6$ nb and $\sigma(e^+ e^- \rightarrow D^+ D^-) = 2.8$ nb [259]. The presently collected data sample by BESIII at the $\psi(3770)$ is 2.9 fb^{-1} . Also $D_s \bar{D}_s$ mesons are produced, with the

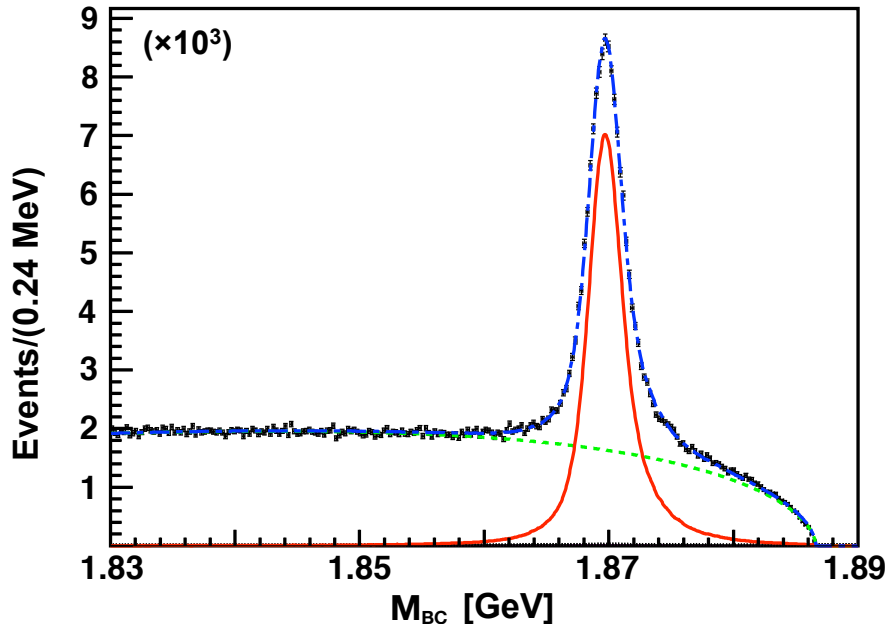


Figure 21: Beam-constrained mass M_{BC} distribution for the single-tag mode $D^+ \rightarrow K^- \pi^+ \pi^+ \pi^0$ from the BESIII analysis [259] (points with error bars). The lines represent the fit: background contribution (dashed line), signal (solid line), and the sum of the two (dashed-dotted line).

maximal yield within the range available for BESIII at c.m. energy of 4170 MeV, where the cross section is approximately 0.9 nb [260] and dominated by the $e^+e^- \rightarrow D_s^{*+} D_s^-$ intermediate state. The D_s^{*+} decays predominantly to $D_s^+ \gamma$, with $\mathcal{B}(D_s^{*+} \rightarrow D_s^+ \gamma) = 95.5(7)\%$.

The analyses of the D -meson decays benefit from a double-tag technique, pioneered by the Mark III collaboration [261, 262]. With this method one can select and reconstruct the complete kinematics for the data samples of D^+ and D^0 decays (or charge conjugated modes) with one missing particle. In the recent BESIII analysis [259] there are three tagging modes for \bar{D}^0 and six for D^- listed in Table 5. The criteria for choosing the tagging modes are: large signal yield (large product of \mathcal{B} and efficiency) and low background. In each event only one D candidate for a given tag mode is selected for D^+ and D^- separately. For each tag mode, one selects the signal region from distributions of beam-constrained mass $M_{BC} = \sqrt{E_{\text{beam}}^2 - |\mathbf{p}|^2}$, where \mathbf{p} is the three-momentum of the tag D^- candidate and E_{beam} is the beam energy in the c.m. system. An example of the M_{BC} distribution for $D^+ \rightarrow K^- \pi^+ \pi^+ \pi^0$ from BESIII is shown in Fig. 21. One can fit the M_{BC} distributions with Monte-Carlo-based signal shapes, and the background shape is well parameterized with an ARGUS function [263]. To select the tag, one requires $1863 \text{ MeV} < M_{BC} < 1877 \text{ MeV}$. Table 5 shows the number of selected events N_{tag} and reconstruction efficiencies ϵ_{tag} for each tag mode. In total, from the BESIII run at the $\psi(3770)$ more than 2×10^6 D^0/\bar{D}^0 and 1.5×10^6 D^+/D^- tagged events are available. This data sample in particular allows studies of semileptonic decays with two pseudoscalar mesons in the final state. Some examples are given in Sec. 3.5.

2.3 Radiative corrections

2.3.1 Initial-state-radiation corrections

In scan experiments, the goal is to determine the Born cross section σ_B for an exclusive process $e^+e^- \rightarrow X$, cf. Fig. 5(b). What is directly measured is the visible cross section σ_{vis} , which includes processes with extra ISR photons radiated, see Fig. 16(d). The observed cross section depends on the invariant mass $W < \sqrt{s}$ of the final state, as well as on the emission angle of the radiated photon. One obtains

Table 5: Channels used for D meson tagging in $e^+e^- \rightarrow D\bar{D}$ at the $\psi(3770)$ resonance. Single-tag efficiencies, ϵ_{tag} , are given. The efficiencies are corrected for $\mathcal{B}(K_S^0 \rightarrow \pi^+\pi^-)$. The number of events is for integrated luminosity of 2.9 fb^{-1} and c.c. is implied.

Tag mode	$N_{\text{tag}} (\times 10^3)$	$\epsilon_{\text{tag}} (\%)$	Tag mode	$N_{\text{tag}} (\times 10^3)$	$\epsilon_{\text{tag}} (\%)$
$\bar{D}^0 \rightarrow K^+\pi^-$	520	64	$D^- \rightarrow K^+\pi^-\pi^-$	798	51
$\bar{D}^0 \rightarrow K^+\pi^-\pi^-\pi^0$	1080	35	$D^- \rightarrow K^+\pi^-\pi^-\pi^0$	245	25
$\bar{D}^0 \rightarrow K^+\pi^+\pi^-\pi^-$	699	39	$D^- \rightarrow K_S^0\pi^-$	93	51
			$D^- \rightarrow K_S^0\pi^-\pi^0$	206	26
			$D^- \rightarrow K_S^0\pi^-\pi^-\pi^+$	110	27
			$D^- \rightarrow K^+K^-\pi^-$	68	40

the following relation between σ_B and σ_{vis} in the case the photon is not observed:

$$\sigma_{\text{vis}}(s) = \int_{M_{\text{th}}}^{\sqrt{s}} dW \frac{2W}{s} F(s, x) \sigma_B(W) := \sigma_B(s) \{1 + \delta(s)\}, \quad (79)$$

where M_{th} is the sum of the masses of the final particles for the process, $x \equiv 1 - W^2/s$, and $F(s, x)$ is the radiator function, which can be calculated in QED. It is necessary to go beyond the first order in α and sum all diagrams with soft multi-photon emission to avoid infrared divergences: both soft multiphoton emission and hard collinear bremsstrahlung in the leading logarithmic approximation have to be taken into account. To calculate the finite-order leading logarithmic correction, the structure function method was implemented in Ref. [264]. Up to order α^2 , the radiator function takes the form

$$F(s, x) = \beta x^{\beta-1} \Delta - \frac{\beta}{2}(2-x) + \frac{\beta^2}{8} \left\{ (2-x) [3 \ln(1-x) - 4 \ln x] - 4 \frac{\ln(1-x)}{x} - 6 + x \right\}, \quad (80)$$

where

$$\begin{aligned} \beta &= \frac{2\alpha}{\pi}(l-1), & \Delta &= 1 + \frac{\alpha}{\pi} \left(\frac{3}{2}l + \frac{1}{3}\pi^2 - 2 \right) + \left(\frac{\alpha}{\pi} \right)^2 \delta_2, & l &= 2 \ln \frac{\sqrt{s}}{m_e}, \\ \delta_2 &= \left(\frac{9}{8} - 2\zeta(2) \right) l^2 - \left(\frac{45}{16} - \frac{11}{2}\zeta(2) - 3\zeta(3) \right) l - \frac{6}{5}\zeta(2)^2 - \frac{9}{2}\zeta(3) - 6\zeta(2) \ln 2 + \frac{3}{8}\zeta(2) + \frac{57}{12}, \\ \zeta(2) &= \frac{\pi^2}{6}, & \zeta(3) &\approx 1.2020569, \end{aligned} \quad (81)$$

and ζ is the Riemann zeta function. In most cases the above representation of the radiator function up to second order is sufficient to determine the cross section, although contributions from $\mathcal{O}(\alpha^3)$ are known [265]. A detailed discussion of this important aspect of the cross section measurements at electron-positron colliders is found in the report by the Working Group on Radiative Corrections [266].

To give an illustration of the effect of the radiative corrections, we use a simplified form of the $e^+e^- \rightarrow \phi\eta$ reaction close to threshold (at $\sqrt{s} = 1.567\text{ GeV}$) inspired by the recent CMD-3 analysis using the scan method [267]. The energy dependence of the Born and visible cross sections is shown in Fig. 22(a). The process is dominated by the broad $\phi(1680)$ resonance and influenced by the threshold. In this example $\sigma_{\text{vis}}(s) < \sigma_B(s)$ for $\sqrt{s} < 1.8\text{ GeV}$. This is caused by two effects: the kinematical limit for the ISR photon energy due to the reaction threshold and the initially rising $\sigma_B(s)$. Eventually the

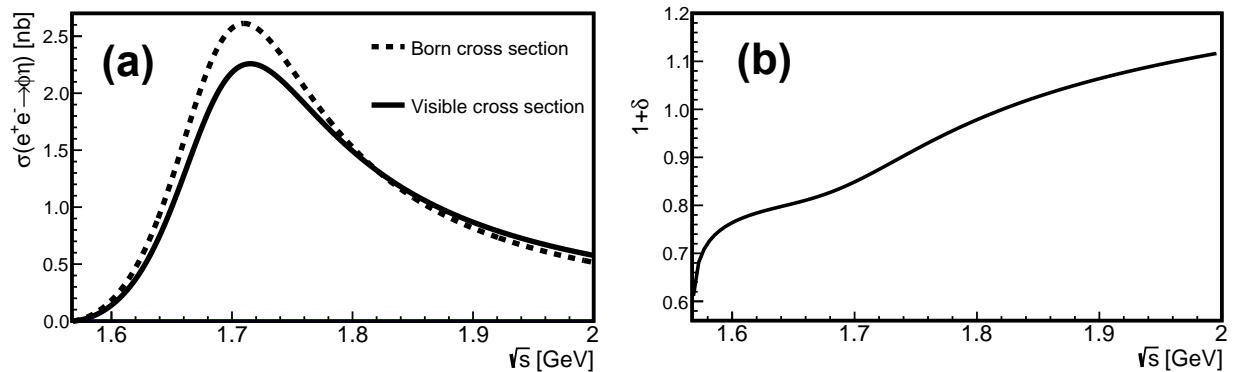


Figure 22: Radiative corrections for the $e^+e^- \rightarrow \phi\eta$ process close to threshold. (a) The Born cross section is shown by the dashed line and the visible cross section by the solid line. (b) The corresponding radiative correction term $1 + \delta(s)$.

contribution of the broad resonance compensates the two effects and $\sigma_{\text{vis}}(s) > \sigma_B(s)$. Figure 22(b) shows the corresponding ISR factor $1 + \delta(s)$. The radiative corrections are much larger (up to 20%) than what one would naïvely expect for an α suppressed process. Born cross sections measured by energy-scan experiments are obtained in the following way. At each c.m. energy point of the collider, N_i events consistent with a signal signature are selected and the background contribution B_i is estimated. The visible cross section is given as $\sigma_{\text{vis},i} = (N_i - B_i)/(\mathcal{L}_i \cdot \epsilon_i)$, where \mathcal{L}_i is the integrated luminosity and ϵ_i the detection efficiency. If the final state was selected using specific decay modes, the cross section is obtained by dividing by the product of branching fractions of all involved decays. The ISR correction is often performed by an iterative procedure using the measured $\sigma_{\text{vis},i}$ values directly or with the help of a cross section parameterization. The Born cross section is obtained by solving Eq. (79) iteratively. When dealing with the extracted Born cross sections using this method one should remember that the data points at different energies are correlated. Therefore the necessary practice of scan experiments is to provide information needed to calculate $\sigma_{\text{vis},i}$ and to list the determined $1 + \delta_i$ factors explicitly. In fact the Born cross sections might be reevaluated when new data sets are available. For analyses of line shapes close to narrow resonances, often only the visible cross section is shown and both radiative corrections and energy smearing are included in the fit function.

2.3.2 Hadronic vacuum polarization

Light-meson interactions also play an important role for precise descriptions of purely leptonic processes such as $e^+e^- \rightarrow \mu^+\mu^-$, via hadronic vacuum polarization (HVP) in the photon propagator and the contribution to the running of the fine structure constant α . The value of the QED coupling constant α is determined from the anomalous magnetic moment of the electron with the impressive accuracy of 0.37 parts per billion [268–271]. However, electromagnetic processes at nonzero momentum transfer squared, s , are described by an effective electromagnetic coupling $\alpha(s)$. The shift of the effective coupling involves low-energy nonperturbative hadronic effects, which affect the precision. These effects represent the largest uncertainty for electroweak precision tests such as the determination of $\sin^2 \theta_W$ at the Z pole or the Standard Model prediction of the muon $g - 2$ [272].

The effect of a vector meson V in lepton–antilepton pair production is obtained by combining contributions from the e.m. and the V propagators in Eq. (64). The Born cross section for the annihilation into a muon–antimuon pair $e^+e^- \rightarrow V \rightarrow \mu^+\mu^-$ close to m_V can be written as [273]

$$\sigma = \frac{4\pi\alpha^2}{s} \left| 1 + \frac{3s}{\alpha m_V} \frac{\sqrt{\Gamma_{ee}\Gamma_{\mu\mu}}}{s - m_V^2 + im_V\Gamma_V} \right|^2. \quad (82)$$

Table 6: Leptonic decay widths of narrow vector meson resonances (for $\ell = e, \mu$) [48].

V	$\mathcal{B}_{\ell\bar{\ell}}$	V	$\mathcal{B}_{\ell\bar{\ell}}$	$\mathcal{B}_{\tau\bar{\tau}}$
ω	7.4×10^{-5}	J/ψ	6×10^{-2}	–
ϕ	3×10^{-4}	ψ'	8×10^{-3}	3×10^{-3}

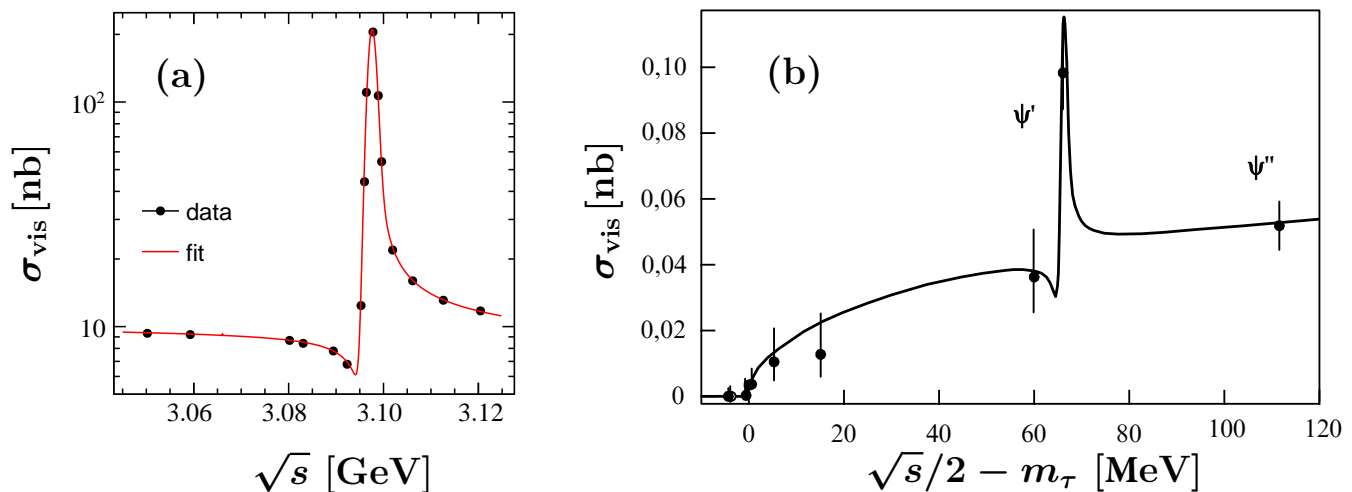


Figure 23: Visible cross section for lepton–antilepton pair production close to the J/ψ and ψ' resonances. (a) J/ψ scan data for $e^+e^- \rightarrow \mu^+\mu^-$ from BESIII [273]; (b) close-to-threshold $e^+e^- \rightarrow \tau^+\tau^-$ data from KEDR [252]. The curves are line shapes using the Born cross section from Eq. (82) convoluted with FSR and the beam energy spread.

At the peak, the squared modulus in Eq. (82) is equal to $|1 - 3i\mathcal{B}_{\ell\bar{\ell}}/\alpha|^2$, where the leptonic branching fractions $\mathcal{B}_{\ell\bar{\ell}}$ for narrow vector mesons are given in Table 6. One can see that the vector meson propagator dominates for J/ψ and ψ' , while for ω and ϕ it is at the percent level and will only be observed in the interference pattern. Figure 23(a) shows the observed $e^+e^- \rightarrow \mu^+\mu^-$ cross section in the vicinity of the J/ψ resonance. The effect is still large for $e^+e^- \rightarrow \tau^+\tau^-$ at the ψ' resonance close to $\tau^+\tau^-$ threshold as shown in Fig. 23(b).

The modulus in Eq. (82) can be treated as the effective e.m. running coupling constant $\alpha(s)/\alpha(0)$. The most precise method to determine the hadronic part of the s -dependence is to use a dispersion integral from a compilation of $e^+e^- \rightarrow$ hadrons [274, 275]. However, one can also see the $\alpha(s)$ variation in an $e^+e^- \rightarrow \mu^+\mu^-$ experiment for $s < 1$ GeV, where it is just a small correction. Such a study was performed by KLOE-2 [276] using the ISR method. The differential cross section for the process $e^+e^- \rightarrow \mu^+\mu^-\gamma(\gamma)$ was studied in the region $0.600 \text{ GeV} < W < 0.980 \text{ GeV}$, where W is the invariant mass of the $\mu^+\mu^-$ pair. The value of $|\alpha(s)/\alpha(0)|^2$ is extracted from the ratio of the experimental differential cross section to the corresponding cross section obtained from a Monte Carlo simulation, with $\alpha(s)$ set to the constant value of $\alpha(0)$.

A photon and two tracks of opposite curvature are required to identify a $\mu\mu\gamma$ event. Events are selected with an undetected photon emitted at small angle, i.e., within a cone of $\theta_\gamma < 15^\circ$ around the beamline, and the two charged muons are emitted at large polar angle, $50^\circ < \theta_\mu < 130^\circ$. The ISR $\mu^+\mu^-\gamma$ cross section is obtained from the observed number of events (N_{obs}) and the background

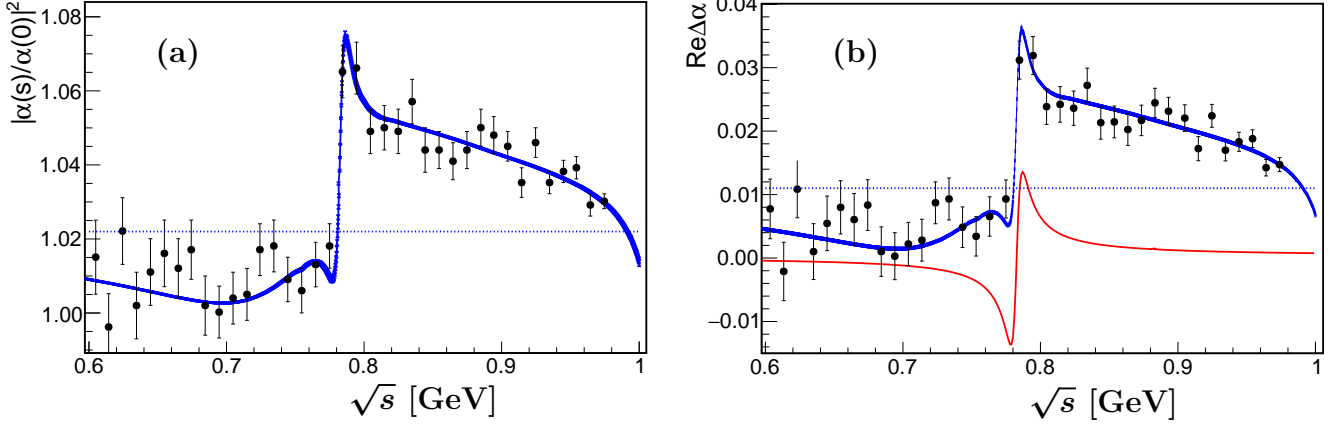


Figure 24: Hadronic vacuum polarization close to the masses of the ρ and ω mesons: (a) $|\alpha(s)/\alpha(0)|^2$ and (b) $\text{Re}\Delta\alpha$ as determined directly from the KLOE $e^+e^- \rightarrow \mu^+\mu^-$ data (points with statistical uncertainties only), compared to the result of a dispersive calculation (blue band) and the leptonic part (dotted line). In addition, the extracted contribution from the ω meson alone is shown (red solid line).

estimate (N_{bkg}) as

$$\frac{d\sigma(e^+e^- \rightarrow \mu^+\mu^-\gamma(\gamma))}{dW} = \frac{N_{\text{obs}} - N_{\text{bkg}}}{\Delta W} \cdot \frac{1 - \delta_{\text{FSR}}}{\epsilon(W) \cdot \mathcal{L}}, \quad (83)$$

where $\Delta W = 10 \text{ MeV}$ is the W bin width, ϵ is the efficiency, \mathcal{L} is the integrated luminosity, and $1 - \delta_{\text{FSR}}$ is the correction applied to remove the final-state radiation contribution. The extracted ratio $|\alpha(s)/\alpha(0)|^2$ is shown in Fig. 24(a) and compared both to the leptonic part from perturbative calculations and to the full combined hadronic and leptonic contributions, where the hadronic part is obtained from a dispersion integral over the $e^+e^- \rightarrow \text{hadrons}$ data [275]. The imaginary part of $\Delta\alpha \equiv 1 - \alpha(0)/\alpha(s)$, which can often be neglected [266], is related to the total cross section $\sigma(e^+e^- \rightarrow \gamma^* \rightarrow \text{anything})$: $\text{Im}\Delta\alpha = -\alpha/3R(s)$, with $R(s) = \sigma_{\text{tot}}/[4\pi|\alpha(s)|^2/(3s)]$. $R(s)$ includes leptonic and hadronic contributions: $R(s) = R_{\text{lep}}(s) + R_{\text{had}}(s)$. In the energy region around the ρ meson, the hadronic cross section can be approximated by the dominant 2π contribution:

$$R_{\text{had}}(s) = \frac{1}{4} \left(1 - \frac{4m_\pi^2}{s}\right)^{\frac{3}{2}} |F_\pi^V(s)|^2 \left|\frac{\alpha(0)}{\alpha(s)}\right|^2. \quad (84)$$

This information allows one to extract the real part for $\Delta\alpha$ as shown in Fig. 24(b).

The data on $\text{Re}\Delta\alpha$ can be used to determine the $\omega \rightarrow \mu^+\mu^-$ branching ratio. For this purpose we parameterize the hadronic contributions as a sum of $\rho(770)$, $\omega(782)$, and $\phi(1020)$, and a nonresonant term [266]. We use a Breit–Wigner description for the ω and ϕ resonances and a Gounaris–Sakurai parameterization [277] of the pion form factor for the ρ , where the interference with the ω and the higher ρ states can be neglected due to the statistical precision of the data. The dispersion integral for $\Delta\alpha_{\text{had}}$ reads

$$\Delta\alpha_{\text{had}} = -\frac{\alpha(0)s}{3\pi} \text{P.V.} \int_{4m_\pi^2}^{\infty} ds' \frac{R_{\text{had}}(s')}{s'(s' - s - i\epsilon)}, \quad (85)$$

where P.V. indicates the Cauchy principal value. The fit of $\text{Re}\Delta\alpha$ with fixed leptonic and ϕ parts shows a clear contribution of the ρ and ω resonances to the photon propagator, which results in a more than 5σ significance of the hadronic contribution to $\alpha(s)$. This is the strongest direct evidence achieved by a single experiment. The ω contribution to $\text{Re}\Delta\alpha$ obtained from the fit could be translated, assuming lepton universality, to the branching ratio value $\mathcal{B}(\omega \rightarrow \mu^+\mu^-) = 6.6(2.2) \times 10^{-5}$, to be compared to the only previous measurement of $9.0(3.1) \times 10^{-5}$ from ALEPH [278].

3 Example analyses

3.1 $e^+e^- \rightarrow P\bar{P}$

The only reactions in which two ground-state pseudoscalar mesons are produced in electron–positron annihilation are $e^+e^- \rightarrow \pi^+\pi^-$, K^+K^- , and K_LK_S , but together with $e^+e^- \rightarrow \pi^+\pi^-\pi^0$ they dominate the total low-energy cross section. The other neutral two-pseudoscalar systems are forbidden by charge conjugation conservation in the electromagnetic interactions. The hadronic current for the process can be written as in Eq. (61):

$$J_\mu^{\text{em},P} = (q_1 - q_2)_\mu F_P^V(s), \quad (86)$$

where q_1, q_2 are four-momenta of the produced pseudoscalar mesons and $F_P^V(s)$ is the elastic form factor of the meson P . The form factor is a scalar, dimensionless function with the constraint $F_P^V(0) = Q_P$, where Q_P denotes the meson’s charge (in units of e). The angular cross section is given as

$$\frac{d\sigma}{d\Omega} = \alpha^2 \frac{q_P^3}{s^{5/2}} \sin^2 \theta |F_P^V(s)|^2 = \frac{\alpha^2}{8s} \sigma_P^3 \sin^2 \theta |F_P^V(s)|^2, \quad (87)$$

where $q_P = \sqrt{s - 4m_P^2}/2$ is the momentum of a pion/kaon in the c.m. system and $\sigma_P = \sqrt{1 - 4m_P^2/s}$ the velocity. The total Born cross section is

$$\sigma = \frac{8\pi\alpha^2}{3s^{5/2}} q_P^3 |F_P^V(s)|^2 = \frac{\pi\alpha^2}{3s} \sigma_P^3 |F_P^V(s)|^2. \quad (88)$$

For the case of a produced pair of charged kaons the cross section close to threshold should be multiplied by the Sommerfeld–Gamov–Sakharov factor [279–281]

$$Z(s) = \frac{\pi\alpha}{\sigma_K} \frac{1 + \alpha^2/(4\sigma_K^2)}{1 - \exp(-\pi\alpha/\sigma_K)}, \quad (89)$$

obtained by solving the Schrödinger equation in a Coulomb potential for a P -wave final state. The normalized leading asymptotic s dependence of the pion and kaon form factors was calculated using perturbative QCD methods [282–284]:

$$F_P^V(s)_{s \rightarrow \pm\infty} = -\frac{64\pi^2 F_P^2}{(11 - 2n_f/3)s \ln|s|}, \quad (90)$$

where n_f is number of flavors and F_P is the pion (kaon) decay constant.

3.1.1 $e^+e^- \rightarrow \pi^+\pi^-$

The $e^+e^- \rightarrow \pi^+\pi^-$ process is the subject of many recent precision studies since it determines the by far most important individual hadronic contribution, both to the value and uncertainty, to the muon anomalous magnetic moment. A precision below 1% is required to match the expected uncertainty of the new muon $g - 2$ experiments [18], which has motivated several measurements of the $e^+e^- \rightarrow \pi^+\pi^-$ cross section: CMD2 [285, 286] and SND [287] using the scan technique, and KLOE [243, 288–290], BaBar [291, 292], and BESIII [293] using the ISR method. In addition to these electron–positron results, the time-like form factor was measured very close to threshold, in the range $0.101 \text{ GeV}^2 < s < 0.178 \text{ GeV}^2$, in the fixed-target NA7 experiment with a 100–175 GeV positron beam [294]. The pion form factor has been measured also in the space-like region $0.014 \text{ GeV}^2 < -s < 0.26 \text{ GeV}^2$ by scattering 300 GeV pions from the electrons of a liquid-hydrogen target. The long-standing issue with a high-precision evaluation of the HVP contribution of the $\pi^+\pi^-$ channel to $(g - 2)_\mu$ has been the fact that two precise individual experimental measurements, KLOE and BaBar, do not agree with each

other at a percent level in the most important energy region, that of the $\rho(770)$ resonance, but new experiments are expected to settle this issue soon. We refrain from discussing this data inconsistency here and instead refer to the recent review Ref. [18], where also the different approaches to account for it in the assessment of the resulting uncertainty in $(g-2)_\mu$ are presented in detail [136, 295–298].

At low s , the process is dominated by the contribution of the ρ^0 resonance. In Eq. (37) we have given the LO ChPT expression for $F_\pi^V(s)$. In general, the hadronic current can be rewritten by inserting a complete set of intermediate states X :

$$J_\mu^{\text{em}, 2\pi} = \sum_X \langle \pi^+ \pi^- | H | X \rangle \langle X | j_\mu^{\text{em}}(0) | 0 \rangle^* , \quad (91)$$

where the symbolic summation includes the integration over all kinematic variables. Equation (91) develops an imaginary part as soon as an intermediate state X can go on its mass shell, which, due to the optical theorem, happens for $s > 4m_\pi^2$. For energies $4m_\pi^2 < s < 16m_\pi^2$ (below four-pion production threshold), the intermediate X state can be only $\pi^+ \pi^-$, and we find the elastic unitarity relation for the imaginary part of the pion vector form factor as given in Eq. (40). We have discussed the ChPT one-loop representation in Sec. 1.5.1, however, we saw that this necessarily breaks down below the mass of the ρ meson. Here, we will describe approaches to describe $F_\pi^V(s)$ in the range $\sqrt{s} < 1 \text{ GeV}$ with percent precision as required by experiment.

Given the phase shifts $\delta_1^1(s)$, the form factor can be determined as

$$F_\pi^V(s) = R(s)\Omega(s) \quad (92)$$

up to energies where contribution of inelastic channels in $\pi\pi$ P -wave scattering become significant. Here the ambiguity of the solution allows $R(s)$ to be an arbitrary polynomial in s . The Omnès function $\Omega(s)$ is given by [152]

$$\Omega(s) = \exp \left\{ \frac{s}{\pi} \int_{4m_\pi^2}^{\infty} dx \frac{\delta_1^1(x)}{x(x-s-i\epsilon)} \right\} . \quad (93)$$

In modern applications, the function $R(s)$ is generalized to take into account intermediate states beyond two pions; most importantly three pions, which resonate at the mass of the narrow $\omega(782)$ and hence lead to an isospin-violating signal massively enhanced by a small energy denominator, see the discussion of ρ - ω mixing below. Furthermore, higher inelasticities are typically included in the form of a conformal polynomial. Such representations have been used to extract the pion–pion P -wave phase shift from form factor data with unprecedented precision [134–137, 299, 300].

In a VMD picture, one can represent the ρ^0 contribution to $F_\pi^V(s)$ as

$$F_\pi^V(s) = \frac{m_\rho^2}{m_\rho^2 - s - \text{Re } \mathcal{A}(s) - i \text{Im } \mathcal{A}(s)} , \quad (94)$$

where $\mathcal{A}(s)$ represents the 2π state insertion in the ρ -meson propagator [301]. The imaginary part of $\mathcal{A}(s)$ is normalized at $s = m_\rho^2$ to the ρ decay width Γ_ρ : $\text{Im } \mathcal{A}(m_\rho^2) = m_\rho \Gamma_\rho$. The simplest assumption for the \mathcal{A} amplitude is to take $\text{Im } \mathcal{A}(s) = m_\rho \Gamma_\rho = \text{const.}$ and to neglect the real part setting it to zero. This corresponds to the standard relativistic Breit–Wigner (BW) formula:

$$F_\pi^V(s) = \frac{m_\rho^2}{m_\rho^2 - s - i m_\rho \Gamma_\rho} \equiv \text{BW}_\rho(s) . \quad (95)$$

This approximation clearly fails for low s , as the imaginary part survives below $\pi\pi$ threshold (and even in the space-like region). A more refined assumption is therefore to consider a variable ρ decay width proportional to the volume of the P -wave phase space for the $\rho \rightarrow \pi\pi$ decay mode:

$$\text{Im } \mathcal{A}(s) = \sqrt{s} \Gamma_\rho \frac{m_\rho^2}{s} \frac{q_\pi^3(s)}{q_\pi^3(m_\rho^2)} \equiv \sqrt{s} \Gamma_\rho(s) . \quad (96)$$

This is equivalent to the assumption that the $\rho\pi\pi$ coupling is constant. There are two commonly used variants of parameterizations using this ansatz for the decay width. One is to neglect the real part as before, leading to the Kühn–Santamaria (KS) formula [302]

$$\text{BW}_\rho^{KS}(s) = \frac{m_\rho^2}{m_\rho^2 - s - i\sqrt{s}\Gamma_\rho(s)}. \quad (97)$$

In the Gounaris–Sakurai parameterization (GS) [277, 302], on the other hand, one determines the real part of $\mathcal{A}(s)$ from a dispersion relation with two subtractions at $s = 0$:

$$\mathcal{A}(s) = \mathcal{A}(0) + s\mathcal{A}'(0) + \frac{s^2}{\pi} \int_{4m_\pi^2}^{\infty} \frac{dx}{x^2} \frac{\text{Im} \mathcal{A}(x)}{x - s - i\epsilon}. \quad (98)$$

This is equivalent to the assumption of a generalized effective-range formula for $\ell = 1$ $\pi\pi$ scattering:

$$\left(\frac{q_\pi^3}{\sqrt{s}}\right) \cot \delta_1^1(s) = q_\pi^2 h(s) + a_1^1 + b_1^1 q_\pi^2, \\ h(s) = \frac{2}{\pi} \frac{q_\pi}{\sqrt{s}} \ln \left(\frac{\sqrt{s} + 2q_\pi}{2m_\pi} \right) \xrightarrow{s < 4m_\pi^2} -\frac{1}{\pi} \sqrt{\frac{4m_\pi^2}{s} - 1} \text{arccot} \left(\frac{s}{4m_\pi^2 - s} \right)^{1/2}, \quad (99)$$

where a_1^1 and b_1^1 are scattering length and effective range parameters³ determined assuming ρ meson dominance:

$$\cot \delta_1^1 \Big|_{s=m_\rho^2} = 0, \quad \frac{d \cot \delta_1^1}{ds} \Big|_{s=m_\rho^2} = \frac{1}{m_\rho \Gamma_\rho}. \quad (100)$$

For $s < 4m_\pi^2$, q_π is defined as $q_\pi(s) = i\sqrt{4m_\pi^2 - s}/2$. This ansatz leads to the following form of the form factor:

$$\text{BW}_\rho^{GS}(s) = \frac{m_\rho^2 + H(0)}{m_\rho^2 - s + H(s) - i\sqrt{s}\Gamma_\rho(s)}, \quad (101)$$

where

$$H(s) = \frac{\Gamma_\rho m_\rho^2}{q_\pi^3(m_\rho^2)} \left[q_\pi^2(s) (h(s) - h(m_\rho^2)) + q_\pi^3(m_\rho^2) h'(m_\rho^2) (m_\rho^2 - s) \right]. \quad (102)$$

In Fig. 25(a) the parameterizations are compared to the BaBar data [291, 292] in the range $\sqrt{s} < 1$ GeV. One immediately sees that isospin breaking due to the narrow ω resonance has to be included to describe the data. For the description of the data for $s < 1$ GeV² it is important to include $\rho^0 - \omega$ mixing, which in the GS parameterization can be achieved by

$$F_\pi^V(s) = \text{BW}_{\rho+\omega}^{GS}(s) \equiv \text{BW}_\rho^{GS}(s) \frac{1 + c_\omega \text{BW}_\omega(s)}{1 + c_\omega}, \quad (103)$$

where for the ω , given its small width, a simple Breit–Wigner function Eq. (95) is used, and c_ω has to be real to assure that the form factor is real below the two-pion threshold. In the Omnès parameterization, one replaces the polynomial $R(s)$ with a function explicitly including the ω pole [303]

$$R(s) = 1 + \alpha_V s + \lambda s^2 + \kappa \frac{s}{m_\omega^2} \text{BW}_\omega(s), \quad (104)$$

where the constants α_V , λ , and κ are real numbers.

³It is customary in the literature on pion–pion scattering to also refer to the leading terms in the near-threshold expansion of partial waves with nonvanishing angular momentum as “scattering lengths” and “effective ranges,” even though their dimensions would suggest otherwise.

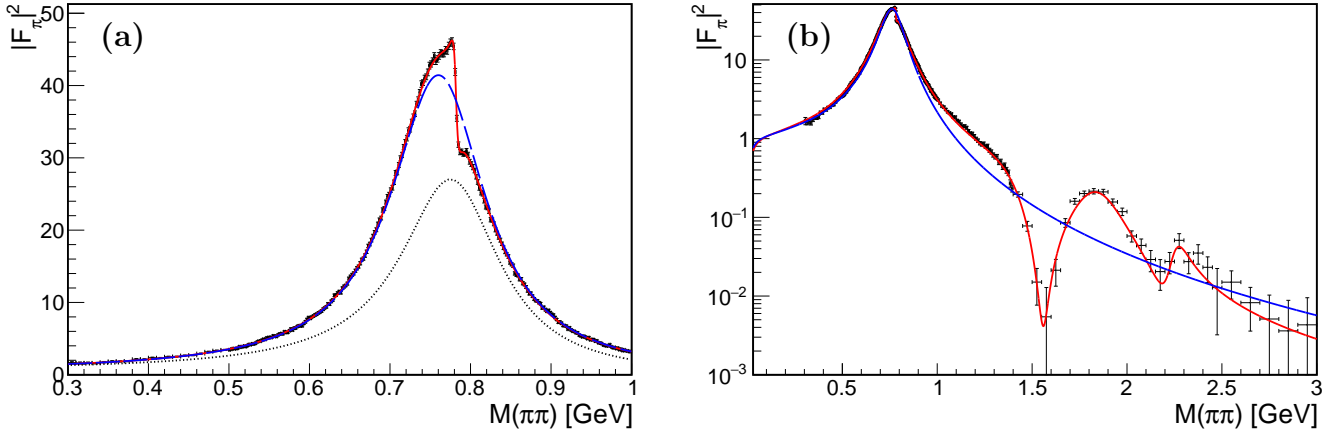


Figure 25: Pion form factor F_π^V illustrated using BaBar data [291, 292]. (a) Region $\sqrt{s} < 1$ GeV compared to the fixed-width Breit–Wigner Eq. (95) (dotted line), Omnès function (blue dashed line), and Omnès function multiplied by $R(s)$ including ρ – ω mixing as in Eq. (104) (red solid line). (b) Range up to 3 GeV compared to Gounaris–Sakurai parameterization with only ρ and ω (blue solid line) and including ρ' , ρ'' contributions Eq. (105) (red solid line).

For energies above 1 GeV, one has to include the effects of the inelastic resonances $\rho' = \rho(1450)$ and $\rho'' = \rho(1700)$ [302, 304]. In the GS parameterization this reads as

$$F_\pi^V(s) = \frac{\text{BW}_{\rho+\omega}^{GS}(s) + c_{\rho'} \text{BW}_{\rho'}^{GS}(s) + c_{\rho''} \text{BW}_{\rho''}^{GS}(s)}{1 + c_{\rho'} + c_{\rho''}}, \quad (105)$$

where $c_{\rho'}$ and $c_{\rho''}$ should be real numbers in order to assure the form factor has no imaginary part for $s < 4m_\pi^2$. This parameterization describes the $F_\pi^V(s)$ data in the range $2m_\pi < \sqrt{s} < 3$ GeV well as illustrated in Fig. 25(b) for the data collected by BaBar. For a unitary and analytic formalism that not only matches the Omnès formalism at low energies, but also includes the effects of ρ' and ρ'' above to describe the form factor data up to 2 GeV equally well, see Ref. [305].

The spectral function $v_1(s)$ for the $\tau^- \rightarrow \pi^- \pi^0 \nu_\tau$ decay is directly related to $F_\pi^V(s)$. It differs from the one measured in e^+e^- collisions by isospin-breaking effects, most prominently the absence of the ω resonance. The isospin corrections have been studied theoretically in quite some detail [306, 307] and subsequently applied with the goal to use τ -decay data to broaden the data basis for the two-pion HVP evaluation [308]. This has led to the puzzling observation that both do not seem to agree with each other very well, and that the significance of the $(g-2)_\mu$ discrepancy depends crucially on whether τ data are employed for the extraction of the pion form factor or not; see, e.g., Ref. [309]. While a phenomenological analysis based on a model for ρ – γ mixing has been able to reconcile e^+e^- and τ -decay data to a large extent [310], the current consensus seems to be that isospin breaking in the pion vector form factor is not yet sufficiently well understood to include τ data in the evaluation of $(g-2)_\mu$ reliably [18].

The spectral functions are obtained from the differential decay rate $d\Gamma/ds$, which up to electroweak radiative corrections can be written as [254, 311]

$$\frac{d\Gamma(\tau^- \rightarrow \pi^- \pi^0 \nu_\tau)}{ds} = \frac{G_F^2 |V_{ud}|^2}{32\pi^2 m_\tau^3} (m_\tau^2 - s)^2 (m_\tau^2 + 2s) v_1(s), \quad (106)$$

where s is the invariant mass squared of the $\pi^- \pi^0$ system, and $v_1(s)$ is the vector spectral function for the $\pi^- \pi^0$ system. The conserved vector current relates $v_1(s)$ to the isovector part of the pion vector

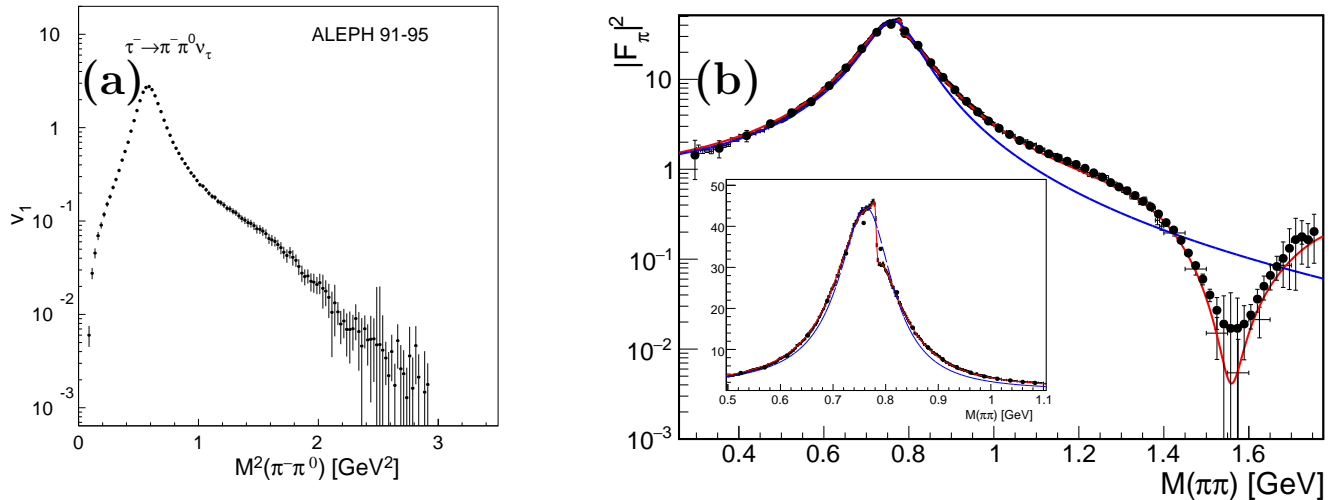


Figure 26: (a) Spectral function v_1 for $\tau^- \rightarrow \pi^- \pi^0 \nu_\tau$ from ALEPH [312]. (b) Comparison of pion vector form factor extracted from e^+e^- [BaBar data, see caption of Fig. 25(b)] and from τ decays data from Belle [313] (black circles). The insert shows the comparison close to the ρ peak.

form factor $F_\pi^V(s)$:

$$v_1(s) = \frac{1}{4\pi} \frac{\sigma_\pi^3}{3} |F_\pi^{V(I=1)}(s)|^2. \quad (107)$$

In Fig. 26(a) the spectral function v_1 from ALEPH [312] is shown. In the panel (b) of this figure the extracted pion form factor from Belle [313] is shown and compared to F_π^V from the BaBar experiment displayed in Fig. 25(b).

3.1.2 $e^+e^- \rightarrow K^+K^-$ and $e^+e^- \rightarrow K_L K_S$

The thresholds for the $e^+e^- \rightarrow K^+K^-$ and $e^+e^- \rightarrow K_L K_S$ reactions are just 32 MeV and 24 MeV below the ϕ mass, respectively. The dynamics of the process is described by the elastic form factors defined in Eq. (86). In the static limit, $s = 0$, they represent the electric charges: $F_{K^+}^V(s=0) = 1$ and $F_{K^0}^V(s=0) = 0$. The slope of the charged kaon form factor in the static limit, related to the electromagnetic radius $\langle r^2 \rangle_{K^+}^V$ defined in Eq. (37), was determined using the space-like kaon form factor from kaon–electron scattering experiments [314, 315]. Since the $K\bar{K}$ system is not an eigenstate of isospin, both form factors are the sum of isoscalar and isovector components, where [301]

$$F_{K^+}^{V(I=0)} = F_{K^0}^{V(I=0)} \quad \text{and} \quad F_{K^+}^{V(I=1)} = -F_{K^0}^{V(I=1)}. \quad (108)$$

In the $SU(3)$ flavor symmetry limit, $F_{K^+}^V(s) = F_\pi^V(s)$ and $F_{K^0}^V(s) = 0$. However, the near-threshold cross sections of $K_S K_L$ and $K^+ K^-$ in the ϕ meson region are almost the same, implying the isovector contribution to be very small there.

Precision scans of the cross sections around the ϕ peak were performed in Novosibirsk. The latest results are from CMD-3 for both $K_S K_L$ [316] and $K^+ K^-$ [317] in the energy range 1.0–1.06 GeV. The Born cross section for $e^+e^- \rightarrow K^+ K^-$ from the CMD-3 experiment is shown in Fig. 27(a) with the peak value of $2.23(2) \mu\text{b}$. This cross section exceeds the prior CMD-2 [286] result by about 10%, which is explained by a not-accounted-for systematic effect in the CMD-2 analysis. However, there is still a tension [18] with the BaBar measurement [318] obtained using the ISR method.

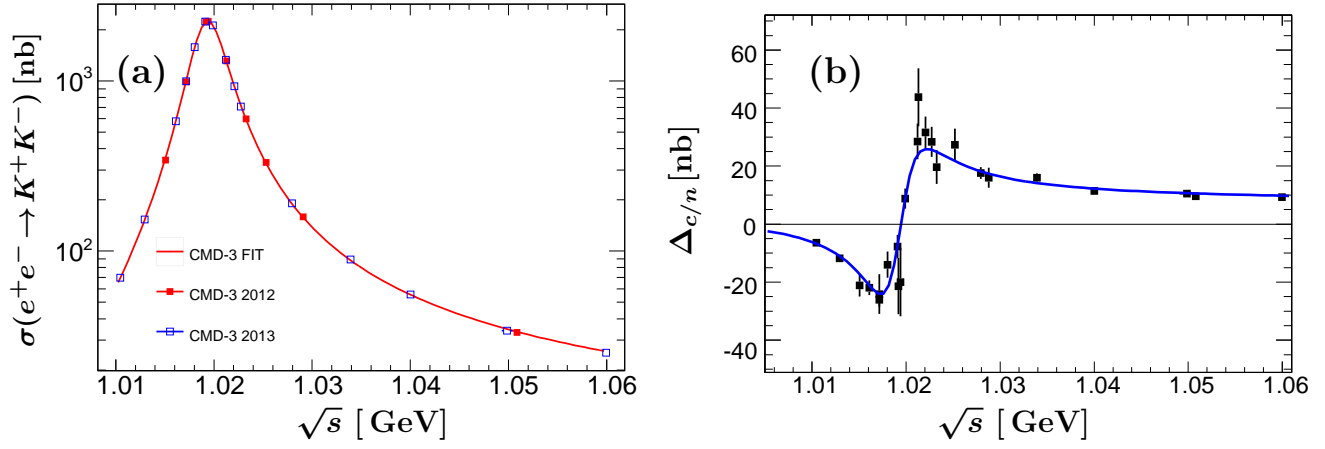


Figure 27: (a) Cross section for $e^+e^- \rightarrow K^+K^-$ in the vicinity of the ϕ meson. (b) The normalized difference of the charged and neutral cross sections $\Delta_{c/n}$ defined in Eq. (109). Only statistical uncertainties are shown. Data and fits (solid lines) are from the CMD-3 experiment [317].

The issue of isospin corrections for the two channels has received quite some theoretical attention [319–321]. Their cross sections are compared by plotting the following corrected difference:

$$\Delta_{c/n}(s) = \frac{q_{K^0}^3}{q_{K^\pm}^3} \frac{1}{Z(s)} \sigma(e^+e^- \rightarrow K^+K^-) - \sigma(e^+e^- \rightarrow K_S^0 K_L^0), \quad (109)$$

where $Z(s)$ is the Sommerfeld–Gamov–Sakharov factor defined in Eq. (89). Equation (109) is defined such that most of the common uncertainties cancel. The experimental value of $\Delta_{c/n}$ is shown in Fig. 27(b), where both cross section data sets are taken from CMD-3 [317]. The isovector contributions (nonresonant in the physical region) are dominated by the ρ and have opposite sign, see Eq. (108). The difference $\Delta_{c/n}$ probes interference of such contributions with the dominant ϕ pole mechanism. The magnitude of $\Delta_{c/n}$ in Eq. (109) is proportional to the ratio $g_{\rho K K} g_{\phi K K} / D_\phi(s) D_\rho(s)$ and allows us to determine the ρ contribution to K -meson production experimentally.

At slightly higher energies, the cross sections start to deviate significantly as shown in Fig. 28(b) for the \sqrt{s} region below 2 GeV. In particular, while the $\phi(1680)$ contribution is seen as a peak for $F_{K^0}^V$, for the $F_{K^+}^V$ it is seen only as a shoulder. This difference indicates strong interference between isoscalar and isovector amplitudes.

Measurements of the form factors in this energy range were performed by BaBar both for K^+K^- [318] and $K_S K_L$ [323], using the ISR method with the energy range from threshold up to 5 GeV. SND measured $e^+e^- \rightarrow K^+K^-$ in 2007 [324] in the range 1.04–1.38 GeV, and in 2016 [322] using two separate energy scans for c.m. energies 1.05–2.00 GeV. The results are consistent with the BaBar experiment and have a comparable or better accuracy, see Fig. 28(a). For $e^+e^- \rightarrow K_S K_L$, there are CMD-2 [325] and SND [326] measurements of the cross section in the energy range $\sqrt{s} = 1.04$ –1.38 GeV. For energies below 1.2 GeV, the cross section exceeds VMD model predictions when only $\rho(770)$, $\omega(782)$, and $\phi(1020)$ are taken into account. The measured cross section agrees well with BaBar.

Within the VMD model, a possible ansatz for the kaon form factors to cover the energy region up to 2 GeV is given by [301]

$$\begin{aligned} F_{K^+}^{V(I=1)}(s) &= \frac{1}{2} \{ c_\rho \text{BW}_\rho^{KS}(s) + c_{\rho'} \text{BW}_{\rho'}^{KS}(s) + c_{\rho''} \text{BW}_{\rho''}^{KS}(s) \}, \\ F_{K^+}^{V(I=0)}(s) &= \frac{1}{6} \{ c_\omega \text{BW}_\omega(s) + c_{\omega'} \text{BW}_{\omega'}(s) + c_{\omega''} \text{BW}_{\omega''}(s) \} + \frac{1}{3} \{ c_\phi \text{BW}_\phi(s) + c_{\phi'} \text{BW}_{\phi'}^{KS}(s) \}. \end{aligned} \quad (110)$$

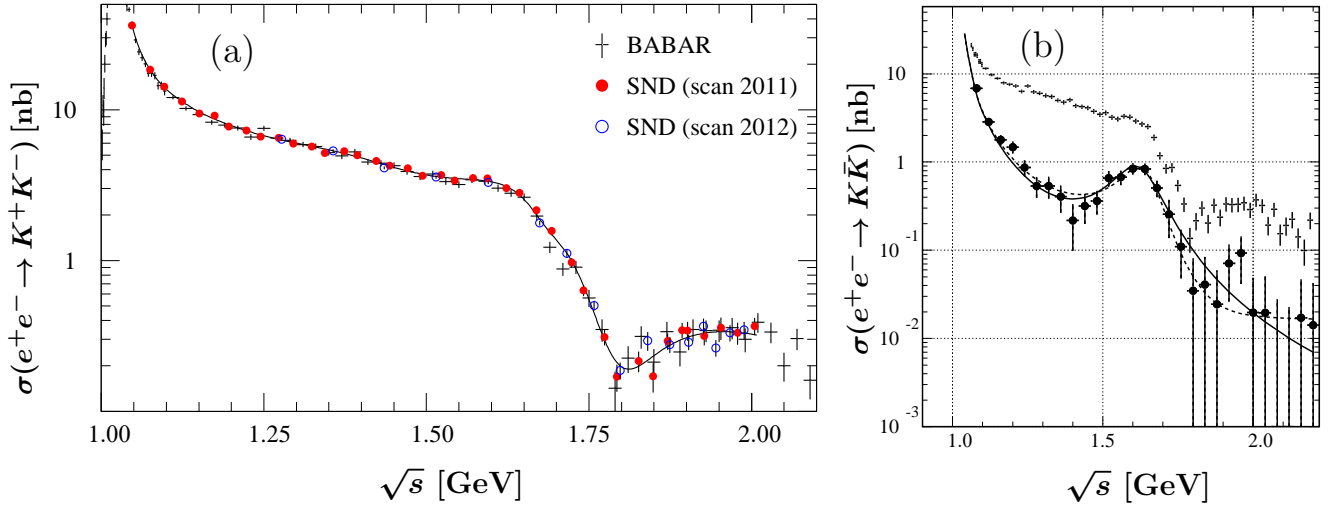


Figure 28: Born cross section for $e^+e^- \rightarrow K\bar{K}$. (a) $e^+e^- \rightarrow K^+K^-$ data from SND [322] and BaBar [318]. (b) Comparison of the $e^+e^- \rightarrow K^+K^-$ (crosses) [318] and $e^+e^- \rightarrow K_S K_L$ (black circles and lines representing VMD model parameterizations) [323] cross sections from BaBar.

See, e.g., Ref. [327] for a recent application of such a model in a combined fit to $e^+e^- \rightarrow K^+K^-$ and $e^+e^- \rightarrow K_S K_L$ together with the τ decay $\tau^- \rightarrow K^- K_S \nu_\tau$, see below.

Above 2 GeV, BESIII has measured the $e^+e^- \rightarrow K^+K^-$ cross section in a scan experiment at 22 energies between 2 GeV and 3.08 GeV [328], see Fig. 29(a). A resonant structure around 2.2 GeV is observed in the cross section line shape. A Breit–Wigner fit yields a mass of $M = 2239(13)$ MeV and a width of $\Gamma = 140(21)$ MeV. The structure seems to be distinct from the $\phi(2170)$ resonance. Since the kaon form factors include both isovector and isoscalar contributions, it is difficult to interpret the observed structure from a $e^+e^- \rightarrow K^+K^-$ cross section measurement only. For this reason, BaBar has carried out a more comprehensive analysis of several final states in Ref. [330], and the average $e^+e^- \rightarrow K_S K_L$ cross section in the energy range from 1.98 to 2.54 GeV is $4(7)$ pb, consistent with zero. The interference patterns observed in K^+K^- as well as $\pi^+\pi^-$, $\pi^+\pi^-\eta$, and $\omega\pi\pi$ channels in the resonance energy range, suggest an evidence for an isovector resonance $\rho(2230)$. — The measured K^+K^- form factor at 3 GeV and 7 GeV is 5.3 and 2.6 times larger than the LO asymptotic values, respectively [331], while the measured slope is consistent with the prediction.

Similarly to the case of $F_\pi^V(s)$, complementary information on the isovector part of the kaon form factor for \sqrt{s} below m_τ is obtained from τ decays, since the spectral function $v_1(s)$ in $\tau^- \rightarrow K^- K_S \nu_\tau$ is related in the same way to $|F_K^{V(I=1)}(s)|^2$ as given in Eq. (107) for the pion form factor. In Fig. 30, recent data on the spectral function v_1 from the BaBar experiment [329] is plotted and compared to the kaon form factor from the $e^+e^- \rightarrow K\bar{K}$ data [318, 323], using 4.3×10^8 $e^+e^- \rightarrow \tau^+\tau^-$ events produced at a c.m. energy around 10.6 GeV. As an example for a theoretical analysis dedicated specifically to the isovector kaon form factor, see Ref. [332].

3.2 $e^+e^- \rightarrow PV$

The next most important contribution to electron–positron annihilation is given by the final states with a vector and a pseudoscalar meson, $e^+e^- \rightarrow VP$, where V and P are members of the ground state nonets. We treat two of the vector resonances ω and ϕ separately as quasi-stable states and in this section focus on $e^+e^- \rightarrow \omega P$, ϕP , where the pseudoscalar meson has no electric charge. The remaining cases, with contributions from the broad nonisovector mesons $\rho(770)$ or $K^*(892)$, are discussed

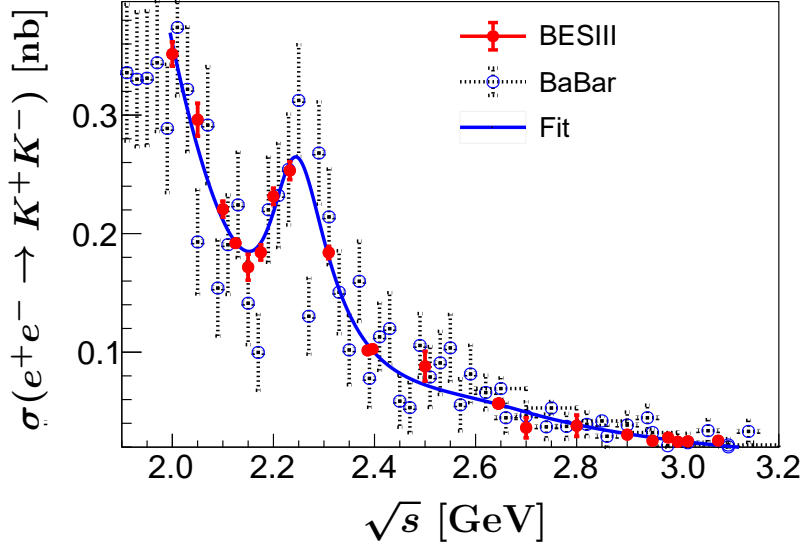


Figure 29: Born cross section for $e^+e^- \rightarrow K^+K^-$ in the 2–3 GeV range. Data is from BESIII [328] and BaBar [318].

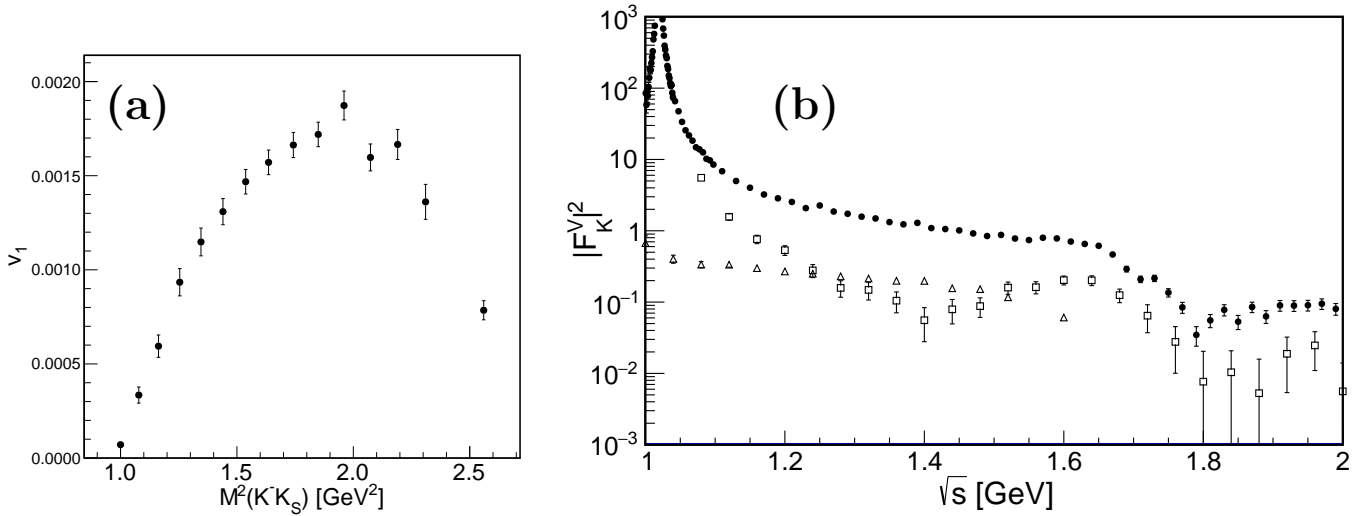


Figure 30: (a) Spectral function v_1 for $\tau^- \rightarrow K^- K_S \nu_\tau$ from BaBar [329]. (b) Comparison of the extracted kaon form factor $|F_K^{V(I=1)}(s)|^2$ (open triangles) with $|F_{K^0}^V(s)|^2$ from $e^+e^- \rightarrow K_S K_L$ [323] (open squares) and $|F_{K^+}^V(s)|^2$ from $e^+e^- \rightarrow K^+K^-$ [318] (black circles).

in the context of three-pseudoscalar production mechanisms in Sec. 3.7.

The Born cross section for a two-body production process $e^+e^- \rightarrow VP$ with narrow vector and pseudoscalar mesons is related to the transition form factor $F_{VP}(s)$ that represents the dynamics of the γ^*VP vertex shown in Fig. 31(a) and defined as [333, 334]

$$J_\mu^{\text{em},VP} = \epsilon_{\mu\nu\rho\sigma} \varepsilon^\nu q_1^\rho q_2^\sigma F_{VP}(s), \quad (111)$$

where ε^ν is the polarization vector of the corresponding vector meson.

Renewed and enforced interest in these transition form factors is not least motivated by their impact on the transition form factors of the light, flavor-neutral pseudoscalars $P = \pi^0, \eta, \eta'$, describing the couplings $P \rightarrow \gamma^*\gamma^*$: at low energies, their isoscalar spectral functions are entirely dominated by the

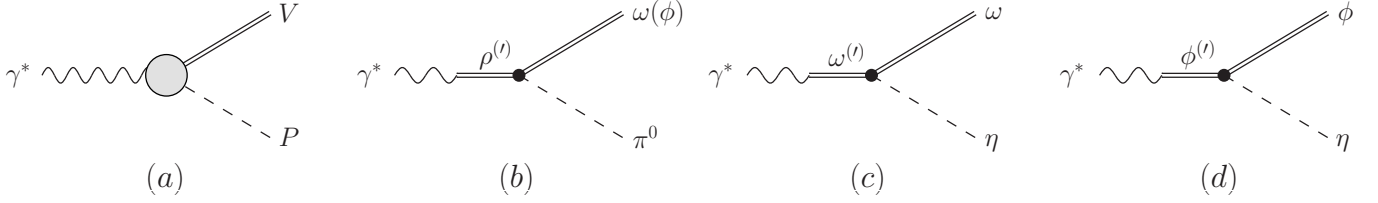


Figure 31: (a) Form factor $F_{VP}(s)$, as well as VMD-type contributions to the specific final states (b) $\omega(\phi)\pi^0$, (c) $\omega\eta$, and (d) $\phi\eta$. The final state $\phi\pi^0$ is OZI-suppressed; we also disregard the OZI-suppressed intermediate vector mesons for the $\omega\eta$ and $\phi\eta$ form factors. Note that we concentrate on *narrow* vector mesons in the final state and disregard those with a ρ , which are discussed separately as three-body continuum channels ($\pi^+\pi^-\pi^0$ and $\pi^+\pi^-\eta$) in Sec. 3.7.

Table 7: Transition form factor strengths for the $VP\gamma^*$ processes given by $F_{VP}(0)$, as extracted from the respective radiative decays. The remaining columns quote the upper limits of the decay regions and the thresholds for the production processes.

VP	Radiative decay	$F_{VP}(0)$ [GeV $^{-1}$]	Decay region $ m_V - m_P $ [GeV]	Production threshold $m_V + m_P$ [GeV]
$\omega\pi^0$	$\omega \rightarrow \pi^0\gamma$	2.31(3)	0.648	0.918
$\omega\eta$	$\omega \rightarrow \eta\gamma$	0.445(2)	0.235	1.331
$\omega\eta'$	$\eta' \rightarrow \omega\gamma$	0.41(1)	0.175	1.740
$\phi\pi^0$	$\phi \rightarrow \pi^0\gamma$	0.134(2)	0.884	1.154
$\phi\eta$	$\phi \rightarrow \eta\gamma$	0.691(7)	0.472	1.567
$\phi\eta'$	$\phi \rightarrow \eta'\gamma$	0.71(1)	0.062	1.977

narrow ω and ϕ resonances, and hence there is a close relation between $F_{VP}(s)$ and the pseudoscalar transition form factors with one virtuality fixed at the vector mass, $F_{P\gamma^*\gamma^*}(s, m_V^2)$, which has been exploited variously in dispersive analyses connected to light-by-light scattering [248, 335, 336].

Contrary to the elastic form factors such as $F_\pi^V(s)$, the transition form factors $F_{VP}(s)$ have dimension GeV $^{-1}$; they yield nontrivial information on the strength of the radiative transitions that is not constrained by gauge invariance. The value of the form factor at $s = 0$ is directly related to the decay width $\Gamma(V \rightarrow P\gamma)$ or $\Gamma(P \rightarrow V\gamma)$, depending on the sign of $m_V - m_P$:

$$\Gamma(V \rightarrow P\gamma) = \frac{\alpha}{3} E_\gamma^3 |F_{VP}(0)|^2, \quad \Gamma(P \rightarrow V\gamma) = \alpha E_\gamma^3 |F_{VP}(0)|^2, \quad (112)$$

where E_γ is the radiative photon energy. In Table 7, the values for the various $F_{VP}(0)$ are given, as well as the kinematic ranges for the time-like transition form factors discussed in this section. The cross section for $e^+e^- \rightarrow VP$ reads

$$\sigma(e^+e^- \rightarrow VP) = \frac{4\pi\alpha^2}{3s^{3/2}} |F_{VP}(s)|^2 P_f(s), \quad (113)$$

where the factor $P_f(s)$ describes the reaction energy dependence of the phase space of the final state. In the narrow-width approximation, $P_f(s) = p_V^3$, where p_V is the c.m. momentum in the final state. For $V = \omega$ or ϕ , the approximation is not valid close to threshold, where the phase space volume corrections

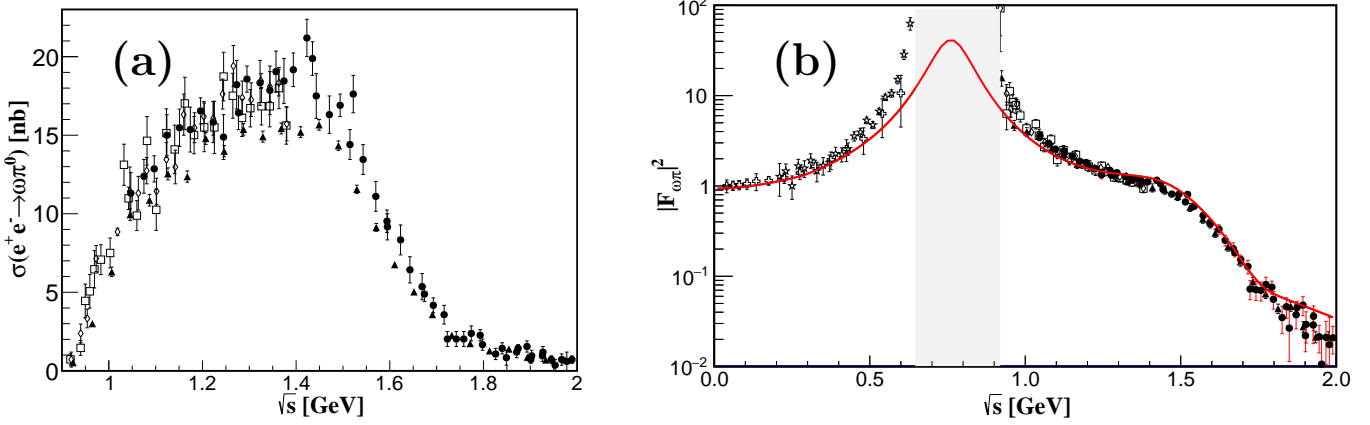


Figure 32: (a) Born cross section $e^+e^- \rightarrow \omega\pi^0$, data from SND [341, 342] (diamonds and circles), CMD2 [343] (squares), and BaBar [344] (triangles). (b) Form factor $|F_{\omega\pi}|^2$ in the two experimentally accessible kinematic regions $4m_e^2 < s < (m_\omega - m_\pi)^2$ and $s > (m_\omega + m_\pi)^2$. Form factor data in the decay region is taken from NA60 [345] (stars) and A2 [346] (crosses). The line is the VMD parameterization from Eq. (115).

for the specific V decays modes $V \rightarrow f$ should be included. The form factor can be studied in two separate kinematic regions. The $e^+e^- \rightarrow VP$ reaction covers the $\sqrt{s} > m_V + m_P$ region of the form factor. If $m_V > m_P$, the decay $V \rightarrow \ell^+\ell^-P$ covers the $2m_\ell < \sqrt{s} < m_V - m_P$ region, where \sqrt{s} is the invariant mass of the $\ell^+\ell^-$ system. In the contrary case, if $m_P > m_V$ the $P \rightarrow \ell^+\ell^-V$ decay covers the $2m_\ell < \sqrt{s} < m_P - m_V$ region.

Depending on the final state of the reaction, the virtual-photon contribution is either isovector or isoscalar, and the form factors will be dominated by the corresponding (excited) vector mesons. Figures 31(b)-(d) show the cases with narrow vector mesons that we will discuss in the present section. For illustration purposes the data will be compared with parameterizations using a naïve VMD model (photon couplings *solely* through vector mesons). The form factor $F_{VP}(s)$ is then given by [333]

$$F_{VP}(s) = \sum_{V'} \frac{g_{PV'V}}{g_{V'}} \text{BW}_{V'}(s). \quad (114)$$

The sum extends over the neutral vector mesons ($Q = S = 0$): ρ^0 , ω , ϕ , \dots ; $g_{PV'V}$ and g_V are their couplings to the VP meson pair and to the photon, respectively. The functions $\text{BW}_V(s)$ are given by the Breit–Wigner formula with fixed width from Eq. (95), for all vector resonances except for the $\rho(770)$. The contributing vector resonances are selected by isospin and the OZI rule for the specific reaction channel. The form factor has to be a real function below inelastic threshold, which is equal to $\sqrt{s_{in}} = 2m_\pi$ and $\sqrt{s_{in}} = 3m_\pi$ for the isovector and isoscalar virtual-photon contributions, respectively. Several studies that improve on simple VMD models have been performed using chiral Lagrangians including vector mesons, thus necessarily concentrating on decay kinematics [337–340].

$e^+e^- \rightarrow \omega\pi^0$ The process $e^+e^- \rightarrow \omega\pi^0$ was studied from threshold up to $\sqrt{s} = 2 \text{ GeV}$ by the SND [341, 342, 347, 348] and CMD-2 [343, 349] experiments, as well as by BaBar [344]. The measured cross section is shown in Fig. 32(a). The $F_{\omega\pi}(s)$ form factor should be dominated by a coherent contribution of isovector ρ resonances and is parameterized in VMD as

$$F_{\omega\pi}(s) = \frac{g_{\rho\omega\pi}}{g_\rho} (\text{BW}_\rho^{GS}(s) + c_1 \text{BW}_{\rho'}(s) + c_2 \text{BW}_{\rho''}(s) + \dots), \quad (115)$$

where for the $\rho(770)$ contribution a Gounari–Sakurai parameterization is used, while for ρ' and ρ'' fixed widths are assumed. Often the fits to the experimental data allow the coefficients c_1, c_2, \dots to be

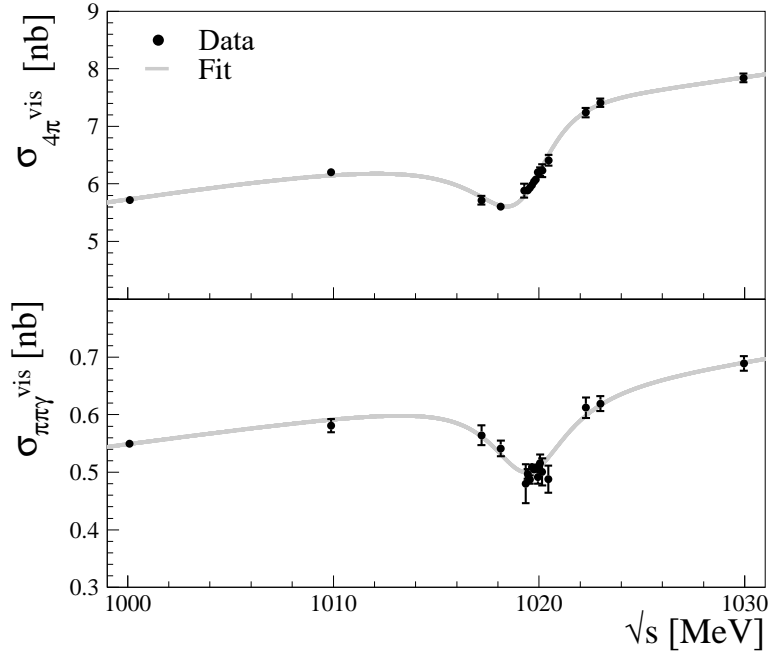


Figure 33: Visible cross section $\sigma(e^+e^- \rightarrow \pi^0\omega)$ close to the ϕ resonance as observed in $\omega \rightarrow \pi^0\pi^+\pi^-$ (upper) and $\omega \rightarrow \pi^0\gamma$ (lower panel) channels by the KLOE experiment [357].

complex numbers. However, the nonzero relative phases violate unitarity relations for the form factor, i.e., they have to be real below the inelastic threshold. The most recent and most precise data on $e^+e^- \rightarrow \omega\pi^0$ is from the SND experiment [342], from BaBar [344], and from BESIII above 2 GeV [350]. The description of the data in the c.m. energy range 1.05–2.00 GeV requires three ρ -like states. The extracted form factor is shown in Fig. 32(b). The data in the $2m_\ell < \sqrt{s} < m_\omega - m_\pi$ region for the form factor is obtained from $\omega \rightarrow \pi^0\ell^+\ell^-$ decays. The two most precise results from the NA60 [345] and A2 [346] experiments are included. In NA60, the ω mesons are produced in pp or p -nucleus collisions and the $\omega \rightarrow \pi^0\mu^+\mu^-$ decay is extracted from inclusive dimuon invariant-mass distributions. In the A2 experiment, ω mesons stem from the exclusive photoproduction process $\gamma p \rightarrow p\omega$, and the decay mode $\omega \rightarrow \pi^0e^+e^-$ is studied. The NA60 result for the form factor seems to be inconsistent with the VMD parameterization and the other data sets. In particular, more refined dispersion-theoretical analyses of the $\omega \rightarrow \pi^0\gamma^*$ transition form factor based on input for $\omega \rightarrow 3\pi$ and F_π^V fail to accommodate such a steep rise in the form factor towards the upper end of the decay region [351–354], and very general limits based on analyticity and unitarity exclude at least the NA60 data points at highest energies [355], in particular when combined with the information above $\omega\pi^0$ production threshold [356].

Dedicated studies of interference effects in $e^+e^- \rightarrow \omega\pi^0$ in the energy region close to $\sqrt{s} = m_\phi$ allow one to determine $\mathcal{B}(\phi \rightarrow \omega\pi^0)$, which is suppressed by the Okubo–Zweig–Iizuka (OZI) rule and G -parity. Such measurements were first performed at SND [358] and subsequently at KLOE [357]. The most precise KLOE data relies on 600 pb^{-1} collected at a few energy points between 1.00 and 1.03 GeV to extract the cross sections for $e^+e^- \rightarrow \pi^0\pi^0\pi^+\pi^-$ and $e^+e^- \rightarrow \pi^0\pi^0\gamma$. The dependence of the cross sections near the ϕ can be parameterized as

$$\sigma(s) = \sigma_0 + A \cdot (\sqrt{s} - m_\phi) \left| 1 - z \frac{\Gamma_\phi}{m_\phi} \cdot \text{BW}_\phi(s) \right|^2, \quad (116)$$

where z is a complex parameter describing the interference between the ϕ decay amplitude and non-resonant processes. In Fig. 33 the data points with the superimposed fit functions are shown for

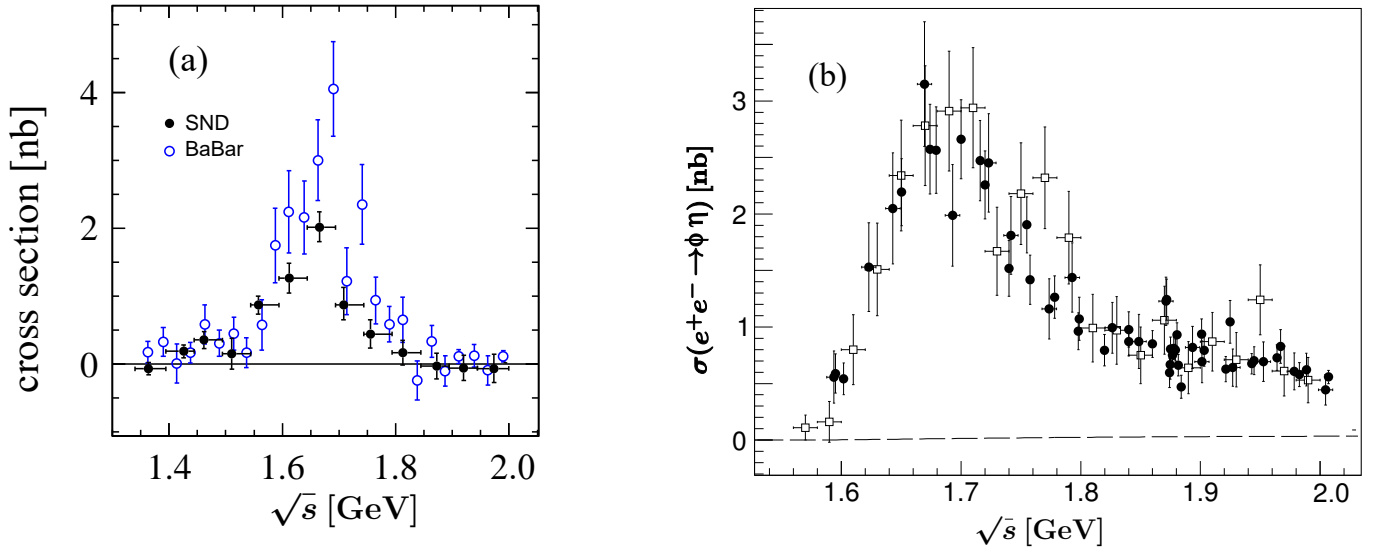


Figure 34: (a) The $e^+e^- \rightarrow \omega\eta$ cross sections from SND [359] and BaBar [360]. (b) The $e^+e^- \rightarrow \phi\eta$ cross section from BaBar [361] (open boxes) and CMD-3 [267] (filled circles).

both channels. By fitting the interference pattern for both final states, a ratio $\Gamma(\omega \rightarrow \pi^0\gamma)/\Gamma(\omega \rightarrow \pi^+\pi^-\pi^0) = 0.0897(16)$ was determined. This result improves the uncertainty by nearly a factor of four with respect to the previous measurement from SND [358], but the value is 1.9σ lower. The parameters σ_0 and z describing the $e^+e^- \rightarrow \pi^0\pi^0\pi^+\pi^-$ reaction allowed the experiment to extract $\mathcal{B}(\phi \rightarrow \omega\pi^0) = 4.4(6) \times 10^{-5}$.

$e^+e^- \rightarrow \omega\eta$ The most precise cross section measurements for the process $e^+e^- \rightarrow \omega\eta$ below 2.00 GeV are from SND [359] and CMD-3 [362], extracted using the $\omega \rightarrow \pi^+\pi^-\pi^0$ decay mode. There is a significant discrepancy between these results and the previous BaBar [360] measurement; see Fig. 34(a). The process is dominated by the effective contributions of $\omega(1650)$ and $\phi(1680)$, the fitted effective width of 110(20) MeV is smaller than the PDG value for the $\omega(1650)$ of 315(35) MeV, but consistent with 150(50) MeV for the $\phi(1680)$ resonance. The contribution of the $\omega(782)$ pole is neglected in the fits. The contribution from the $\omega(1420)$ is small, but necessary to describe the asymmetry in the peak in the measured distribution. In this channel, the recent BESIII measurement [350] indicates a resonance in the range $2 \text{ GeV} < \sqrt{s} < 2.5 \text{ GeV}$.

$e^+e^- \rightarrow \phi\eta$ and $e^+e^- \rightarrow \phi\eta'$ The process $e^+e^- \rightarrow \phi\eta$ was studied at BaBar using $K^+K^-\gamma\gamma$ [361] and $K_L K_S \gamma\gamma$ [365] final states for c.m. energies up to 4 GeV. Below 2 GeV it was studied at SND [366] and CMD-3 [267] with $\phi \rightarrow K^+K^-$. The resulting distributions from the three experiments are consistent with each other, as shown in Fig. 34(b). The close-to-threshold cross section is dominated by the $\phi(1680)$ resonance and well described with the simple ansatz

$$F_{\phi\eta}(s) = \frac{g_{\phi\phi\eta}}{g_\phi} \text{BW}_\phi(s) + \frac{g_{\phi'\phi\eta}}{g_{\phi'}} \text{BW}_{\phi'}(s) + \dots, \quad (117)$$

where ϕ' denotes the $\phi(1680)$. Complementary information about the form factor is given by the KLOE measurement of the Dalitz decay $\phi \rightarrow \eta e^+e^-$ [363]. The extracted form factor is shown in Fig. 35(a). The line assumes ϕ and ϕ' meson contributions.

The first measurement of $e^+e^- \rightarrow \phi\eta'$ by BESIII [364] shown in Fig. 35(b) has a similar qualitative behavior of the cross section close to threshold and is dominated by the apparent resonance with mass 2.180(20) GeV and width 149(18) MeV at c.m. energies below 3.08 GeV. This is likely the discussed

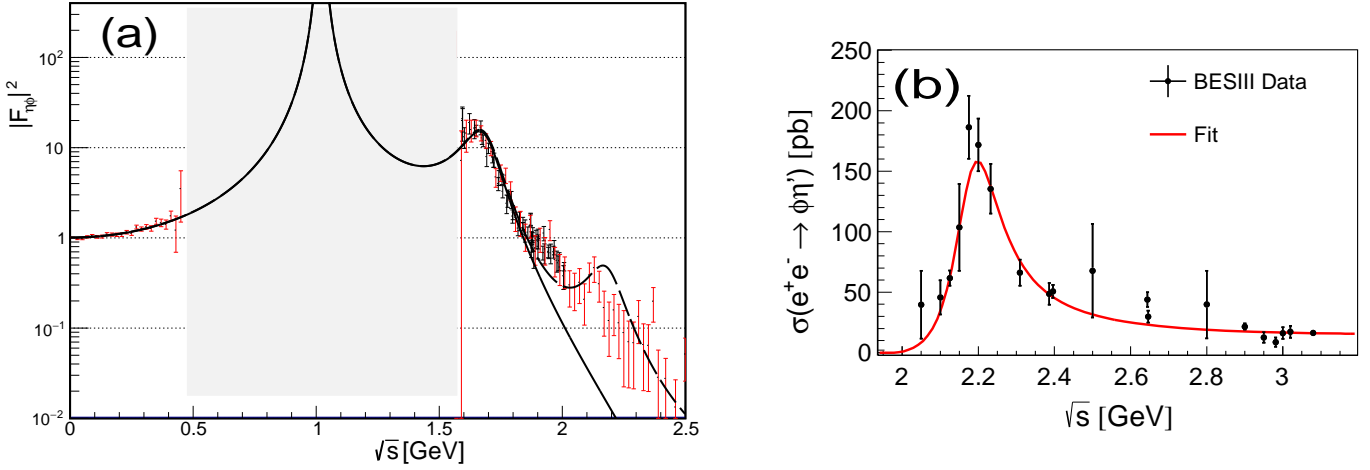


Figure 35: (a) Form factor $|F_{\phi\eta}|^2$ in two accessible kinematic regions (nonshaded areas). The data in the $\phi \rightarrow \eta e^+e^-$ region is from KLOE [363]. The data in the production region $e^+e^- \rightarrow \phi\eta$ is from BaBar [361] (red error bars) and CMD-3 [267] (black error bars in the range up to 2 GeV). The curves are the VMD model parameterization Eq. (117) with the ϕ and ϕ' contributions (solid line) and additionally with the $\phi(2170)$ state (dashed line). (b) Cross section for $e^+e^- \rightarrow \phi\eta'$ measured at BESIII [364].

strangeonium candidate, the $\phi(2170)$, observed in the ISR process $\rightarrow \gamma\phi f_0(980)$ at BaBar [98, 367] and Belle [368]. At BESII [369] and BESIII [370] it was observed in the $J/\psi \rightarrow \eta\phi f_0(980)$ decay. The discovery of the $\phi(2170)$ has triggered speculations that it might be an s -quark counterpart of the $Y(4260)$.

$e^+e^- \rightarrow \phi\pi^0$ The $e^+e^- \rightarrow \phi\pi^0$ process was measured at BaBar in $K^+K^-\pi^0$ [361] and $K_S K_L \pi^0$ [365], using the two main ϕ decay channels; cf. also Ref. [372] for a theoretical analysis. The cross section is shown in Fig. 36(b). The transition form factor $|F_{\phi\pi}|^2$ was also measured in the decay $\phi \rightarrow \pi^0 e^+e^-$ at KLOE [371]. The decay region (see the upper range in Table 7) is dominated by the ρ^0 contribution, which should be visible as a peak. More refined theoretical predictions have been obtained using dispersion relations in analogy to $F_{\omega\pi}$ [352, 353], based on an analysis of $\phi \rightarrow 3\pi$ Dalitz plot data [102, 373]. However, in the KLOE measurement, due to background from $\phi \rightarrow \pi\rho$, $\rho \rightarrow \pi\pi$ processes, it was only possible to study the form factor up to electron–positron invariant masses of 625 MeV. The KLOE result for the form factor is shown in Fig. 36(a). The curves correspond to the predictions from VMD and dispersive calculations [352, 353].

3.3 $V \rightarrow P_1 P_2 \gamma$

Amplitude analyses of two pseudoscalar mesons produced in radiative ϕ and J/ψ decays are particularly simple. Possible hadronic states have even angular momentum values with positive parity and charge conjugation quantum numbers ($J^{PC} = 0^{++}, 2^{++}, 4^{++}$, etc.). Systems such as $\pi^0\pi^0$, $\pi^+\pi^-$, K^+K^- , $K_S^0 K_S^0$, $\eta^{(\prime)}\eta^{(\prime)}$, and $\eta^{(\prime)}\pi^0$ can be produced. The branching fractions for the processes are listed in Table 8. The $K_L K_L$ final state is not included since due to the long lifetime, the K_L is difficult to register in the detectors used at electron–positron colliders. Also, no partial-wave analysis (PWA) of the processes $J/\psi \rightarrow \gamma\eta\pi^0$ has been performed yet since it was recently observed at BESIII [374].

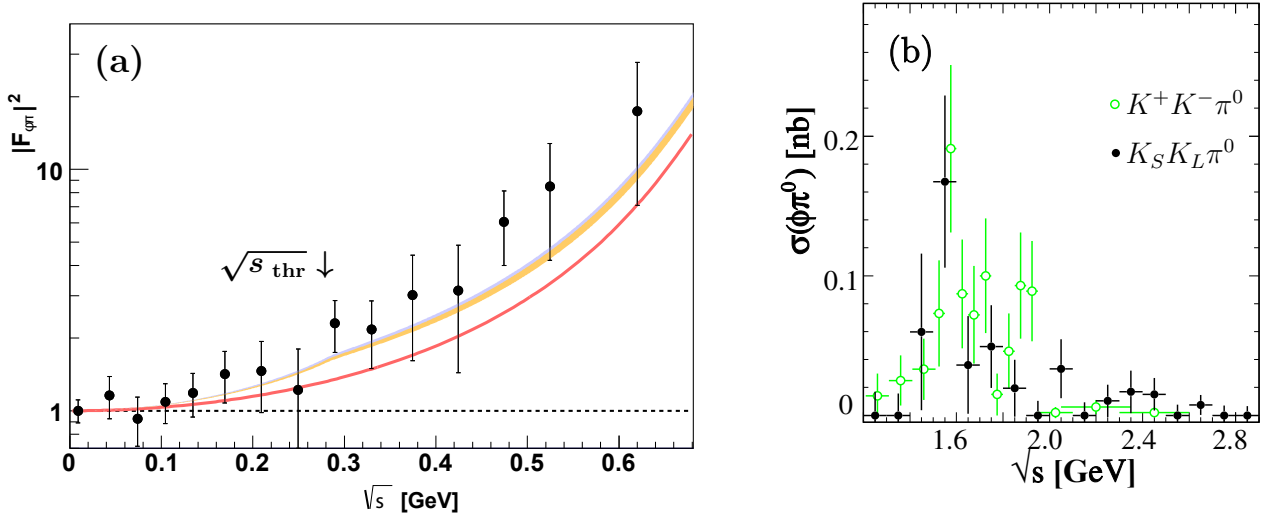


Figure 36: (a) Form factor $|F_{\phi\pi}|^2$ determined from the $\phi \rightarrow e^+e^-\pi^0$ decay at KLOE [371] (points), VMD predictions (solid line), and dispersive calculations [352, 353] (bands). (b) Born cross section for the $e^+e^- \rightarrow \phi\pi^0$ process, measured at BaBar using $K^+K^-\pi^0$ [361] and $K_S K_L \pi^0$ [365] final states.

The amplitude of a radiative decay $V \rightarrow P_1 P_2 \gamma$ is often presented assuming factorization [39],

$$\mathcal{M} = \sum_X \langle P_1 P_2 | H_S | X \rangle \langle X \gamma | H_{EM} | V \rangle, \quad (118)$$

where H_{EM} and H_S represent the electromagnetic transition $V \rightarrow \gamma X$ and the strong final-state interaction, respectively. However, since the strength of the two transitions might be comparable, this representation is only approximate, e.g., for $\phi \rightarrow \pi^0 \pi^0 \gamma$ there is a contribution from the $\phi \rightarrow \rho^0 \pi^0$ intermediate state with subsequent $\rho^0 \rightarrow \pi^0 \gamma$ decay. In helicity reference systems, the $e^+e^- \rightarrow V \rightarrow \gamma(X \rightarrow P_1 P_2)$ process is described by the mass squared s of the X system, radiative photon emission angle θ with respect to the incoming positron in the reaction's c.m. system, and the angle θ_1 of the meson P_1 in the $P_1 P_2$ helicity frame. The amplitude depends on the angular momentum j and helicity λ of the produced $P_1 P_2$ system as well as the helicity of the initial state $m = \pm 1$. Denoting the photon helicity by $\lambda_\gamma = \pm 1$, the amplitude for the radiative process at fixed invariant mass squared s of the $P_1 P_2$ system is

$$\langle s, \theta, \phi : \lambda, \lambda_\gamma | H | 1m \rangle = \sqrt{\frac{2j+1}{4\pi}} \mathcal{D}_{m, \lambda-\lambda_\gamma}^{1*}(\phi, \theta, 0) d_{\lambda, 0}^j(\theta_1) H_{\lambda, \lambda_\gamma}^j(s), \quad (119)$$

where $\mathcal{D}_{\lambda, \lambda'}^j(\phi, \theta, 0)$ and $d_{\lambda, 0}^j(\theta_1)$ are Wigner rotation functions. The hadronic system's helicity amplitudes $H_{\lambda, \lambda_\gamma}^j(s)$ depend on s and helicities λ and λ_γ . The amplitude can also be written in the radiative multipole basis:

$$H_{\lambda, \lambda_\gamma}^j(s) = \sqrt{\frac{2J_\gamma+1}{4\pi}} \langle J_\gamma - \lambda_\gamma; j \lambda | 1 \lambda - \lambda_\gamma \rangle \frac{\delta_{\lambda_\gamma, 1} + \delta_{\lambda_\gamma, -1} P(-1)^{J_\gamma-1}}{\sqrt{2}} T_{J_\gamma j}(s), \quad (120)$$

where J_γ is the photon angular momentum and P the parity of the meson pair. The amplitude $j = 0$ has only one component (E1) and $|H|^2$ from Eq. (119) can be written as

$$|H(\theta, s)|^2 \propto (1 + \cos^2 \theta) |T(s)|^2. \quad (121)$$

Any amplitude with $j > 0$ has three components, e.g., the 2^{++} amplitude has components related to E1, M2, and E3 radiative transitions.

Table 8: Branching fractions of radiative decays to a pair of pseudoscalar mesons.

	Final state	\mathcal{B}	Ref.
$\phi \rightarrow \gamma P_1 P_2$	$\gamma\pi^+\pi^-$	$4.1(1.3) \times 10^{-4}$	[375]
	$\gamma\pi^0\pi^0$	$1.09(6) \times 10^{-4}$	[37]
	$\gamma\pi^0\eta$	$7.06(22) \times 10^{-5}$	[376]
$J/\psi \rightarrow \gamma P_1 P_2$	$\gamma\pi^0\pi^0$	$1.15(5) \times 10^{-3}$	[39]
	$\gamma\pi^+\pi^-$	$2\mathcal{B}(J/\psi \rightarrow \gamma\pi^0\pi^0)$	inferred from Ref. [377]
	$\gamma\eta\pi^0$	$2.14(31) \times 10^{-5}$	[374]
	$\gamma\eta\eta$	$1.47(2) \times 10^{-4}$	excl. $\phi\eta$ [378]
	$\gamma K_S^0 K_S^0$	$8.1(4) \times 10^{-4}$	[379]
	$\gamma K^+ K^-$	–	

3.3.1 Radiative ϕ decays

First results for the ϕ radiative decays into pairs of pseudoscalar mesons were obtained at the SND and CMD-2 experiments: observations of $\phi \rightarrow \pi^0\pi^0\gamma$ [380], $\phi \rightarrow \pi^+\pi^-\gamma$ [375], and evidence for $\phi \rightarrow \eta\pi^0\gamma$ [381]. Further studies from the Novosibirsk experiments include Refs. [382, 383]. Here we focus on the most recent high-statistics data from KLOE.

The process $\phi \rightarrow \pi^0\pi^0\gamma$ was studied at KLOE [37] using a signal data sample of 2438(61) events. Later, a full Dalitz plot analysis was performed using a much larger data sample of 128530(660) events [38]. The $M(\pi^0\pi^0)$ spectrum from the first measurement is shown in Fig. 37(a). The dominant contribution to the processes is from the kaon-loop mechanism [385–388], where the main ingredients are the large direct coupling of the ϕ to the charged-kaon pair together with final-state radiation and the strong $K^+K^- \rightarrow \pi\pi$ rescattering. However, the decay distributions can also be described assuming structureless couplings of the ϕ meson to a scalar resonance and a photon [384], as the coherent sum of the $\phi \rightarrow f_0(500)\gamma$ and $\phi \rightarrow f_0(980)\gamma$ processes. The interference term between $f_0(500)$ and $f_0(980)$ amplitudes is destructive. The contribution of the crossed channel $\phi \rightarrow \rho^0\pi^0$ with $\rho^0 \rightarrow \pi^0\gamma$ is small and can be fixed from the known branching fractions.

Studies of the $e^+e^- \rightarrow \pi^+\pi^-\gamma$ reaction close to the ϕ peak require dedicated methods since it is dominated by the ISR mechanism, with the photon emitted at small angles with respect to the beams. The analysis at KLOE is based on 6.7×10^5 events collected at a c.m. energy around the ϕ mass [389]. The photon is not reconstructed but the ISR contribution is suppressed by requiring the polar angle θ_γ of the $\pi^+\pi^-$ momentum to be greater than 45° . In the selected sample, still the main contribution is from continuum $e^+e^- \rightarrow \pi^+\pi^-\gamma$ events with ISR photon, but a clear contribution from the intermediate process $\phi \rightarrow f_0(980)\gamma$ is observed in the $M(\pi^+\pi^-)$ spectrum shown in Fig. 38(a). An additional small contribution comes from the decay $\phi \rightarrow \rho^\pm\pi^\mp$ with $\rho^\pm \rightarrow \pi^\pm\gamma$. It contributes to the low-mass region, $400 \text{ MeV} < M(\pi^+\pi^-) < 600 \text{ MeV}$, with total branching fraction $\mathcal{B}(\phi \rightarrow \rho^\pm\pi^\mp) \times \mathcal{B}(\rho^\pm \rightarrow \pi^\pm\gamma) \approx 4 \times 10^{-5}$. Finally, the possibility to observe the decay chain $\phi \rightarrow f_0(500)\gamma \rightarrow \pi^+\pi^-\gamma$ should be considered. Each mechanism contributes to the $M(\pi^+\pi^-)$ invariant-mass spectrum in a characteristic way. The $\pi^+\pi^-$ pair is in a $J^{PC} = 0^{++}$ state for FSR and the scalar-mesons decays, while ISR produces them in $J^{PC} = 1^{--}$ quantum numbers. A sizable interference effect between FSR and f_0 decays is expected in the invariant-mass spectrum. On the other hand, interference terms between states with

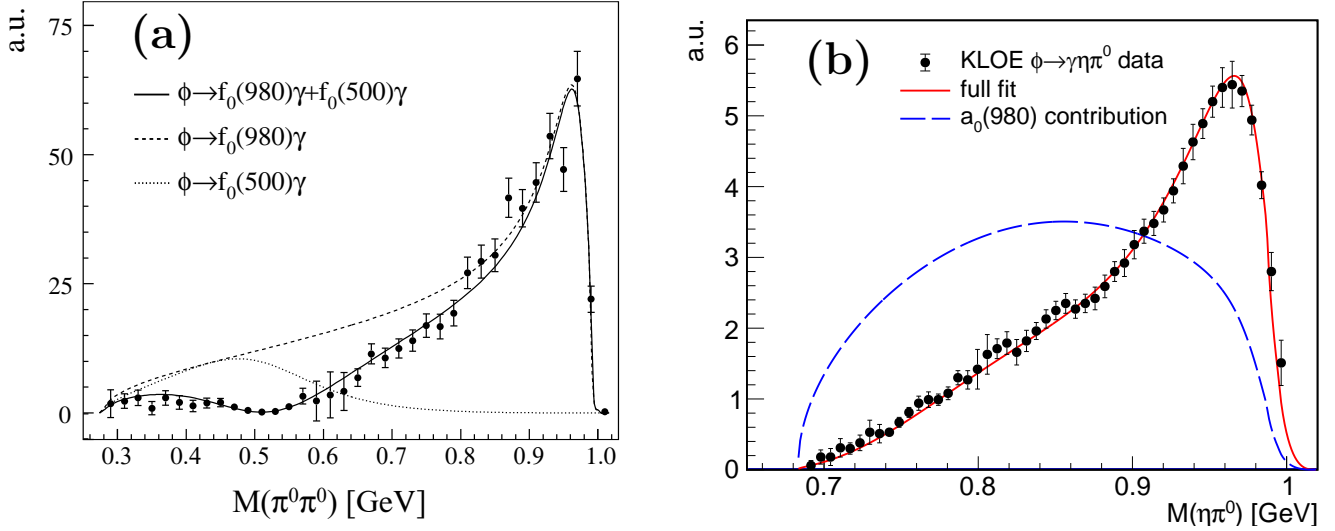


Figure 37: (a) $M(\pi^0\pi^0)$ spectrum from $\phi \rightarrow \pi^0\pi^0\gamma$ [37]. (b) $M(\eta\pi^0)$ spectrum from $\phi \rightarrow \eta\pi^0\gamma$ [376]. Both are unfolded and acceptance corrected distributions. The curves represent interfering contributions for the scalar amplitudes with structureless ϕ -scalar-resonance-photon couplings [384].

opposite C change sign when π^+ and π^- are interchanged and cancel in the $M(\pi^+\pi^-)$ distributions if symmetric cuts on θ_γ are used. However, a sizable forward-backward asymmetry for the π^+ angle θ_{π^+} defined with respect to the electron beam is expected and seen in the data.

The number of events N_i in a bin of the invariant-mass spectrum was described by the function

$$N_i = \mathcal{L}\epsilon_i \left(\Delta\sigma_{\text{ISR}} + \Delta\sigma_{\text{FSR}} + \Delta\sigma_{\rho\pi} + \Delta\sigma_{\text{scal}} \pm \Delta\sigma_{\text{scal+FSR}}^{\text{INT}} \right), \quad (122)$$

where \mathcal{L} is the integrated luminosity, ϵ_i is the selection efficiency, and the notation $\Delta\sigma$ represents the differential cross section $d\sigma/dm$ integrated over the i th bin range. The analytic expressions for the first and second terms, ISR and FSR, were obtained in Ref. [390], while the $\rho\pi$ term is given in Ref. [387]. For the ISR term, F_π^V was included in the KS parameterization [302]. Figure 38(b) shows the invariant-mass distribution with nonscalar (ISR, FSR, and $\rho\pi$) contributions subtracted. The data suggests destructive interference between the scalar-gamma and FSR amplitudes, which damps the low-mass tail of the $f_0(980)$ and no improvement in the quality of the kaon-loop fit is observed when the $f_0(500)$ is included.

The decay $\phi \rightarrow \eta\pi^0\gamma$ is dominated by $\phi \rightarrow a_0(980)\gamma$. Two analyses of this process were performed by KLOE. The first from 2002 [391], based on the same integrated luminosity as for $\phi \rightarrow \pi^0\pi^0\gamma$, yielded 802 candidate event. The second analysis with more than an order of magnitude larger statistics [376] used two η decay modes, $\eta \rightarrow \gamma\gamma$ with 13270(190) and $\eta \rightarrow \pi^+\pi^-\pi^0$ with 3602(70) events after background subtraction. The unfolded $M(\eta\pi^0)$ distribution is shown in Fig. 37(b). The solid curve represents the result of the fit of the $a_0(980)$ contribution interfering with other broad scalars represented using structureless ϕ -scalar-resonance-photon couplings [384]. The dashed line is the a_0 meson contribution.

3.3.2 Radiative J/ψ decays

The branching fraction for $J/\psi \rightarrow \gamma gg$ processes is relatively large, close to 10% [392], which makes radiative J/ψ decays a perfect place to study hadronic final states produced by two-gluon fusion. The radiative J/ψ decays to pion and kaon pairs were hence primarily motivated by the search for light glueballs [41–44].

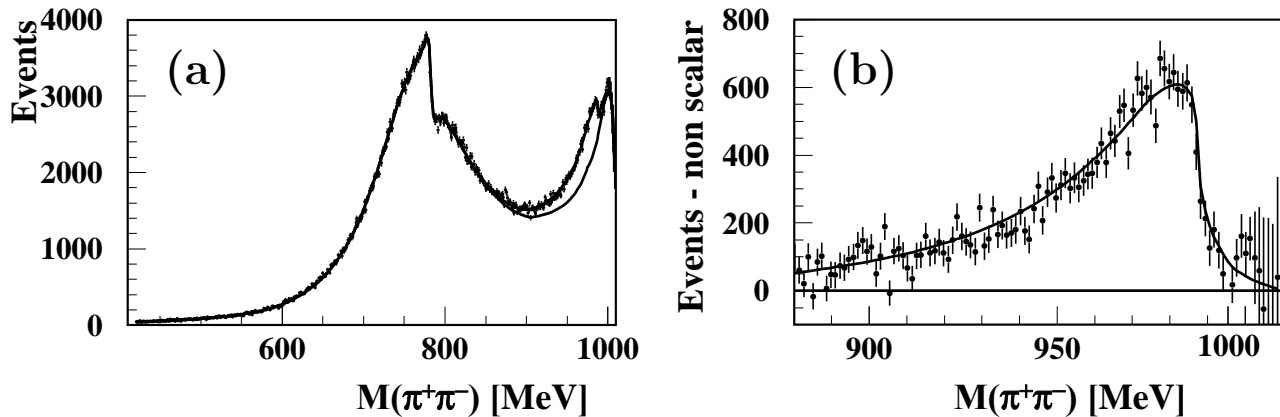


Figure 38: Invariant-mass distribution from $\phi \rightarrow \gamma\pi^+\pi^-$ decays. (a) Data spectrum compared with the fitting spectrum (upper curve following the data points) and with the estimated nonscalar part therein (lower curve); (b) the fitting function compared to the spectrum obtained subtracting the nonscalar part in the $f_0(980)$ region.

Using high-statistics data from BESIII, it is possible to extract information on meson systems in a model-independent way. First attempts of such analyses were performed at BESII, where radiative J/ψ decays to $\pi^+\pi^-$ and $\pi^0\pi^0$ were studied [377]. The Dalitz plots and invariant-mass spectra are shown in Fig. 39. The prominent features include the $f_0(1500)$, $f_0(1710)$, and $f_2(1270)$ resonances. The Dalitz plot for the $\pi^+\pi^-$ channel shows significant contributions of the $\rho\pi$ background. For the J/ψ radiative decays to K^+K^- and $K_S^0K_S^0$, a PWA was carried out in the 1–2 GeV mass range based on the same data sample, using both a mass-independent and a global analysis [393]. The process involves production of the $f_2'(1525)$ and $f_0(1710)$ resonances. The latter peaks at a mass of 1740(20) MeV with a width of 166(15) MeV. The scalar components dominate the spectrum. A comprehensive study of the two-pseudoscalar meson spectra from radiative J/ψ and ψ' decays was also performed using a 53 pb^{-1} data sample collected by CLEO-c [394] at c.m. energy $\sqrt{s} = 3.686 \text{ GeV}$. The aim of the analysis was the search for glueball states, and no full amplitude analysis was implemented.

With a much larger J/ψ data sample, the BESIII collaboration has performed two amplitude analyses for the channels $\pi^0\pi^0$ [39], 4.3×10^5 events, and $K_S K_S$ [379], 1.6×10^5 events. The neutral channels provide clean samples due to the lack of sizable backgrounds like $J/\psi \rightarrow \rho\pi$ for $\pi^+\pi^-$ [377] and $J/\psi \rightarrow K^+K^-\pi^0$ for K^+K^- . Since the initial studies suggest that contributions from $j \geq 4$ amplitudes are negligible, the goal is to extract the scalar and tensor components of the $\pi^0\pi^0$ and $K_S K_S$ systems as functions of the invariant masses squared s , while making minimal assumptions about the properties or number of poles in the amplitudes. Such model-independent descriptions allow one to integrate these results with other related analyses from complementary reactions, and to develop phenomenological models that can be used to directly fit experimental data to obtain parameters of interest. The amplitude components for $\pi\pi$ and $K_S K_S$ radiative decays are determined independently for many small ranges of the s variable. This allows one to reconstruct complex amplitudes $T_{J\gamma j}(s)$ independently for each region as the intensity $|T_{J\gamma j}|$ and the relative phase. Such a procedure makes minimal assumptions about the s -dependence of the $\pi\pi$ and $K_S K_S$ interactions, reduces potential systematic biases due to the amplitude model, and minimizes the risk for experimental artifacts. These results are easy to combine with those of similar reactions for a more comprehensive study of the light scalar and tensor meson spectra. These mass-independent analyses use the following general assumptions: the intensity and the phase difference for each amplitude are continuous functions of s , and each set of the $\pi^0\pi^0$ amplitudes with the same quantum numbers is constrained to have the same phase below

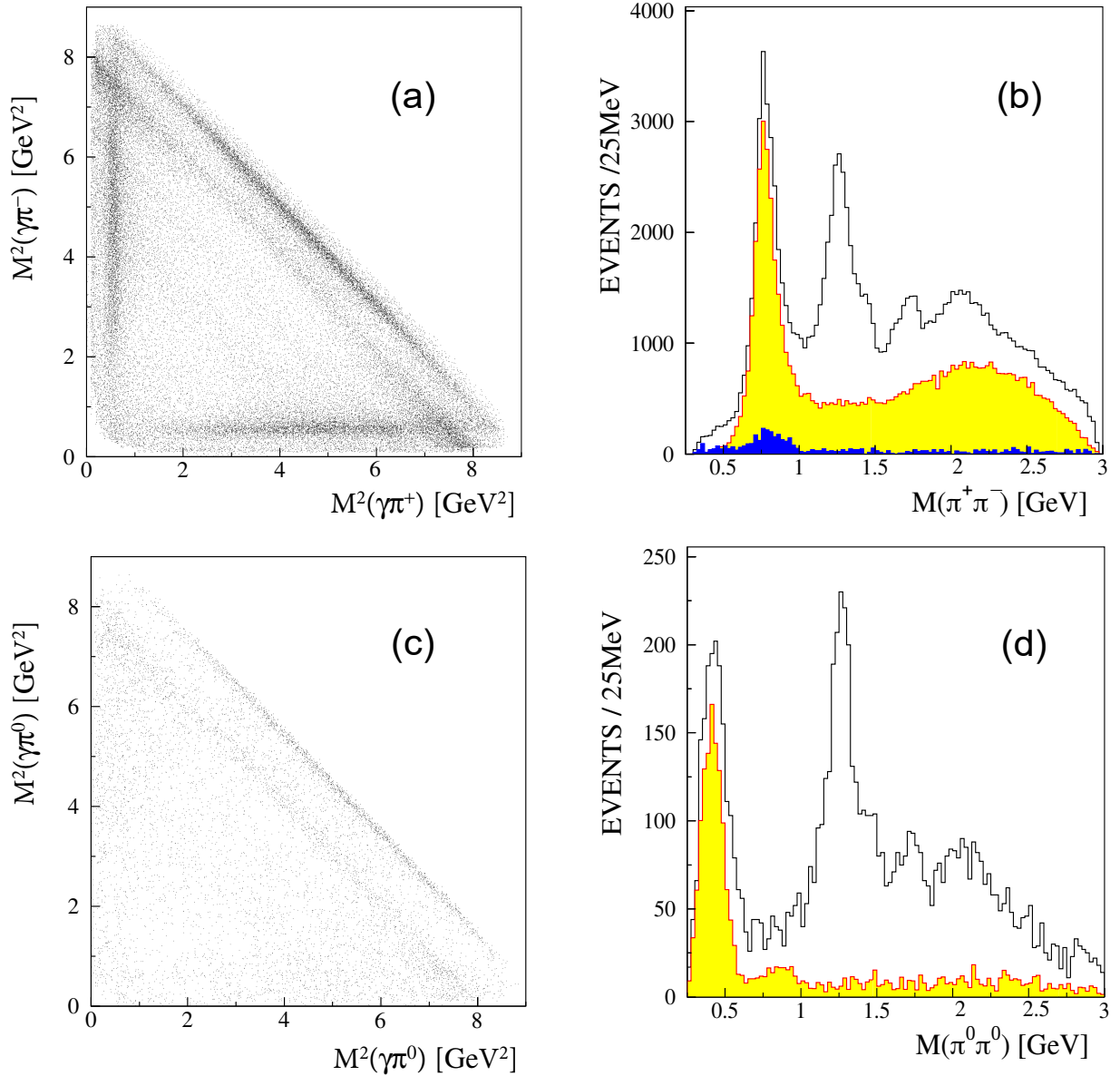


Figure 39: Radiative decays of J/ψ to $\pi^+\pi^-$ and $\pi^0\pi^0$ from the BESII experiment [377]. We show both Dalitz plots (left) and two-pion invariant-mass distributions (right) for $J/\psi \rightarrow \pi^+\pi^-\gamma$ (top) and $J/\psi \rightarrow \pi^0\pi^0\gamma$ (bottom).

the $K\bar{K}$ threshold (the vertex factors associated with the production process are purely real numbers unless additional channels are available). However, rescattering effects may become significant above the $K\bar{K}$ threshold and generate phase differences between the amplitudes of the same j^{PC} .

One should be aware of some drawbacks of this approach. First, in order to resolve the contribution of potentially narrow resonances, a large number of bins is needed and the result is a set of about a thousand parameters that describe the amplitudes, with no single parameter tied to an individual resonance of interest. Second, mathematical ambiguities result in multiple sets of optimal parameters in each bin. With only $j = 0$ and $j = 2$ resonances significant, there are two ambiguous solutions. In general, if one includes $j \geq 4$, the number of ambiguous solutions increases. Finally, in order to make the results manageable for subsequent analyses, an arbitrary assumption of Gaussian errors must be made.

The extracted intensities are shown in Fig. 40. The three dominating partial waves 0^{++} and

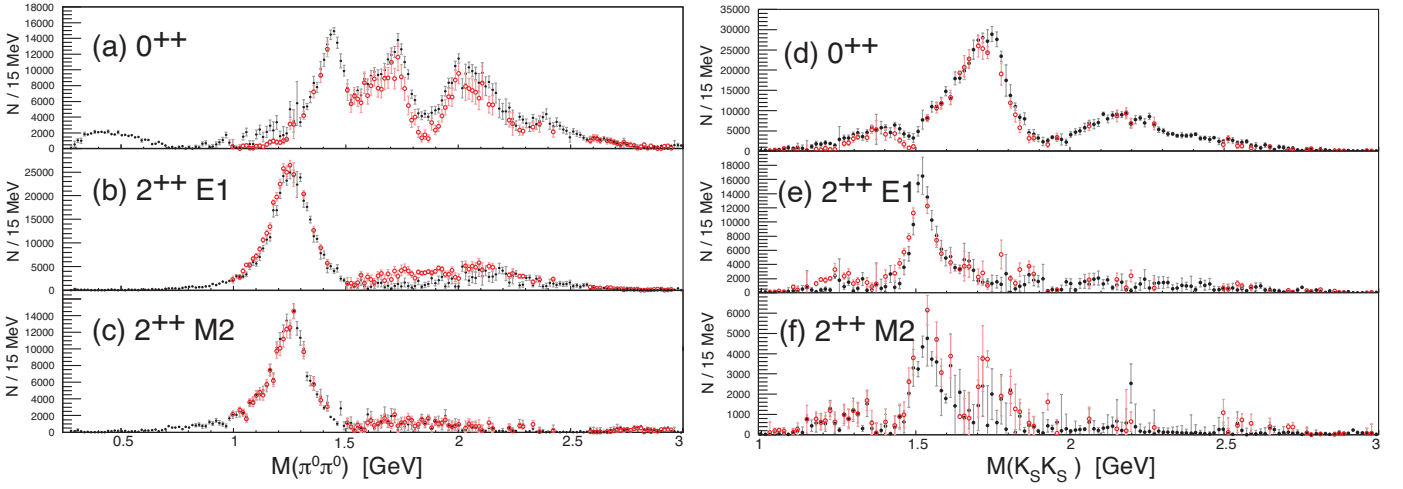


Figure 40: Intensities of the three dominating partial waves 0^{++} and $2^{++}(E1, M2)$ for (a)–(c) $J/\psi \rightarrow \pi^0 \pi^0 \gamma$ [39] and (d)–(f) $J/\psi \rightarrow K_S K_S \gamma$ [379] from BESIII. The solid and open markers represent the two possible solutions of the mass-independent fits.

$2^{++}(E1, M2)$ are shown for both reactions. The complex amplitudes thus determined include the relative phases with respect to the $2^{++}E1$ wave. For $\pi^0 \pi^0$ there are four significant structures: below 0.6 GeV likely $f_0(500)$; below 1.5 GeV and near 1.7 GeV, where one might expect $f_0(1370)$, $f_0(1500)$, and $f_0(1710)$; and near 2.0 GeV, which could be attributed to the $f_0(2020)$. In the 2^{++} amplitude, a dominant contribution of a structure consistent with the $f_2(1270)$ is seen. The remaining broad contribution is significantly different from the one assumed in the previous model-dependent analyses. The structures in the $K_S K_S$ channel are consistent with the $f'_2(1525)$ and $f_0(1710)$ resonances. The scalar contribution is stronger than the tensor one.

For the $K_S K_S$ system, in addition a model-dependent amplitude analysis was performed where the invariant-mass spectrum was parameterized as a coherent sum of Breit–Wigner line shapes, with the goal of extracting the resonance parameters of intermediate states. The mass-independent results are consistent with those of the model-dependent analysis.

$J/\psi \rightarrow \gamma \eta \eta$ A mass-dependent amplitude analysis of radiative J/ψ decays into $\eta \eta$, using a data sample of 5460 candidate events, was performed at BESIII using the relativistic covariant tensor amplitude method [378]. The scalar and tensor components from the fit to the data are shown in Fig. 41. The scalar spectrum is described by the contributions from the $f_0(1500)$, $f_0(1710)$, and $f_0(2100)$ states, while the tensor spectrum is dominated by the $f'_2(1525)$, $f_2(1810)$, and $f_2(2340)$ resonances.

3.4 $P \rightarrow \pi^+ \pi^- \gamma$

Radiative production of $\pi^+ \pi^-$ pairs is one of the main decay modes of the η and η' mesons, with branching fractions of 4.60(16)% and 29.1(5)%, respectively. Due to its odd intrinsic parity, the decay amplitude for the radiative decay of a pseudoscalar meson $P = \eta, \eta', \eta_c$ can be written in terms of a scalar amplitude $\mathcal{F}(s, t, u)$ as [395]

$$\langle \pi^+(q_+) \pi^-(q_-) \gamma(k, \epsilon) | H | P \rangle = i \epsilon_{\mu\nu\alpha\beta} \epsilon^\mu(k) q_+^\nu q_-^\alpha k^\beta \mathcal{F}(s, t, u), \quad (123)$$

where $s = (q_+ + q_-)^2$, $t = (q_- + k)^2$, and $u = (q_+ + k)^2$. One can express the amplitude in terms of two independent variables: s and the π^+ polar angle in the $\pi^+ \pi^-$ helicity system,

$$z \equiv \cos \theta_\pi = \frac{t - u}{\sigma_\pi(m_P^2 - s)}. \quad (124)$$

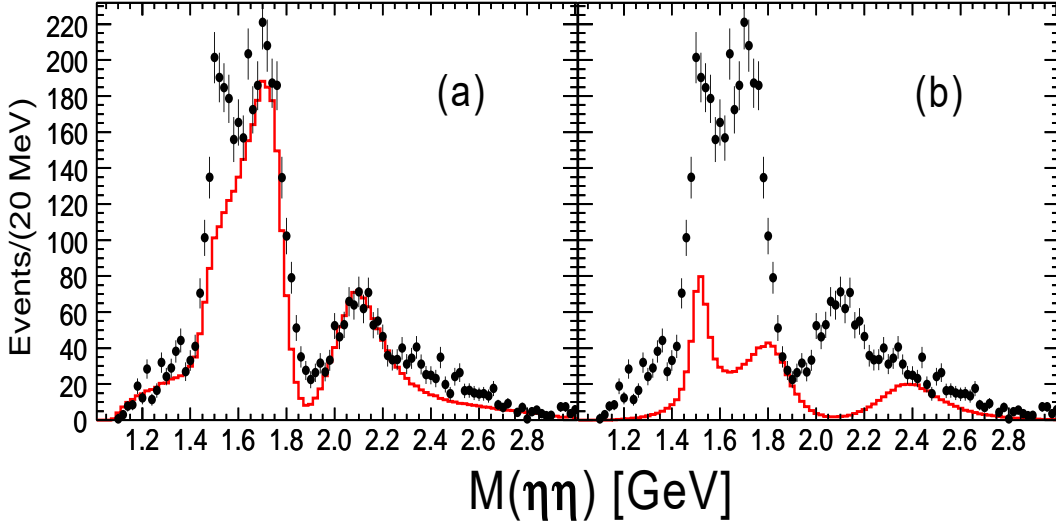


Figure 41: Invariant mass of the $M(\eta\eta)$ system from the analysis of J/ψ radiative decays at BESIII [378]. The figure shows the experimental data as well as extracted (a) scalar and (b) tensor amplitudes from the partial-wave analysis.

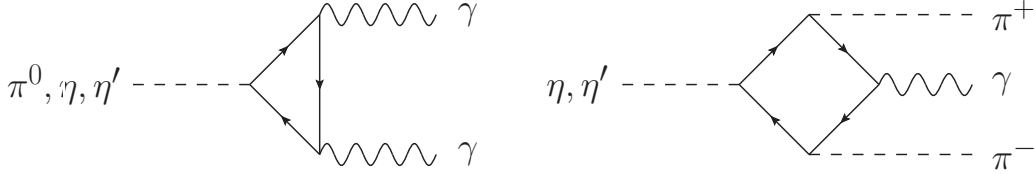


Figure 42: Triangle (left) and box (right) anomaly from the WZW Lagrangian.

The partial-wave expansion for the $\pi^+\pi^-$ system is given by

$$\mathcal{F}(s, t, u) = \sum_{\text{odd } l} P'_l(z) f_l(s) = f_1(s) + \sum_{\text{odd } l \geq 3} P'_l(z) f_l(s), \quad (125)$$

where only odd partial waves contribute due to C conservation. The decays of η and η' are completely dominated by the P -waves. In the limit of vanishing momenta and quark masses, the amplitude is fixed by the chiral anomaly of QCD, which has been incorporated in the Wess–Zumino–Witten (WZW) effective action [396, 397]. The relevant contribution of the Lagrangian to $\eta \rightarrow \pi^+\pi^-\gamma$ in the chiral limit is the box term describing the direct coupling of three pseudoscalar mesons and a photon, see Fig. 42(right). On the other hand in the VMD model the $\eta/\eta' \rightarrow \pi^+\pi^-\gamma$ decay is described by the $\rho^0\gamma$ intermediate state [398]:

$$f_1(s) = c_\rho \text{BW}_{\rho+\omega}^{GS}(s) + c_{\rho'} \text{BW}_{\rho'}^{GS}(s) + \dots \quad (126)$$

In the past, the dipion invariant-mass distribution for $\eta' \rightarrow \pi^+\pi^-\gamma$ was studied and interpreted within the VMD model by several experiments [399–404]. The distribution is given as

$$\sqrt{s} \frac{d\Gamma}{ds} = \frac{1}{12(8\pi m_{\eta'})^3} (m_{\eta'}^2 - s)^3 (s - 4m_\pi^2)^{3/2} |f_1(s)|^2. \quad (127)$$

The general conclusion was that the ρ^0 peak was shifted by about +20 MeV [405]. This discrepancy was attributed to the WZW box anomaly contribution, which was included as an extra nonresonant term in the decay amplitude, and it was suggested that fits to the dipion distribution would allow one to determine the fraction of the box contribution [406]. Evidence for the box anomaly using such a

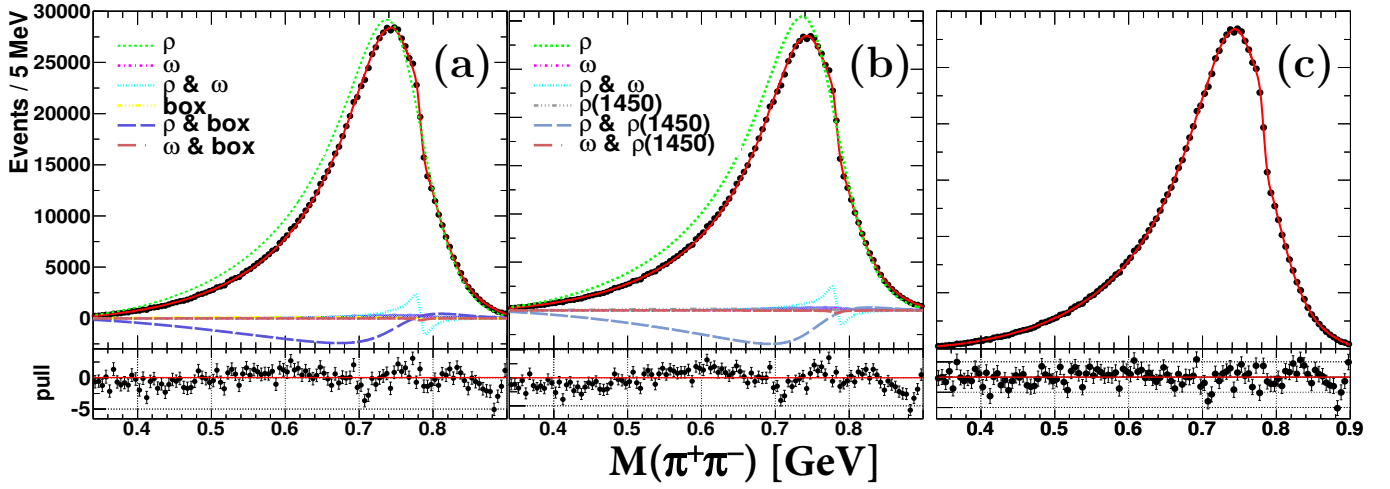


Figure 43: Two-pion invariant-mass distribution $M(\pi^+\pi^-)$ from $\eta' \rightarrow \pi^+\pi^-\gamma$ BESIII data [409]. The figure shows model-dependent fits to the $M(\pi^+\pi^-)$ spectrum with combinations of (a) ρ , ω , and box anomaly, as well as (b) ρ , ω , and ρ' . The results of the model-independent fit including ρ^0 - ω interference is shown in panel (c).

method was reported in 1997 by the Crystal Barrel experiment [407], using a sample of 7490(180) events, but this observation was not confirmed by the subsequent measurement by the L3 collaboration [408] with 2123(53) events. In the recent BESIII analysis [409], a low-background data sample of 9.7×10^5 $\eta' \rightarrow \gamma\pi^+\pi^-$ decays candidates was selected. The distribution of the dipion invariant mass, $M(\pi^+\pi^-)$, is displayed in Fig. 43. The $\rho^0 - \omega$ interference is clearly seen for the first time in this decay. However, the data cannot be described by the $\text{BW}_{\rho+\omega}^{GS}(s)$ function alone. The fit result is much improved by including a contact term from the box anomaly, see Fig. 43(a). However, a data description of similar quality can be obtained by replacing the box anomaly with a $\rho^0(1450)$ contribution, see Fig. 43(b).

Ultimately, the notion to separate additive contributions of a contact term/the box anomaly and resonance exchanges is misleading, as the universality of final-state interactions dictates all P -wave-produced pion pairs to undergo rescattering as encoded in an Omnès function $\Omega(s)$ built on the corresponding $\pi\pi$ phase shift δ_1^1 . A model-independent description of $\eta/\eta' \rightarrow \pi^+\pi^-\gamma$ decays therefore uses an approach closely resembling the one introduced in Eq. (92) for the pion vector form factor: $f_1(s) = P(s)\Omega(s)$ [410]. For the η' decay, the process-specific part denoted as $P(s)$ is given by [303]

$$P(s) = A(1 + \kappa s + \lambda s^2) + \frac{\xi}{m_\omega^2} \cdot \text{BW}_\omega(s), \quad (128)$$

where the normalization A can be matched to the chiral-limit value given by the WZW anomaly. The reaction-specific term $P(s)$ includes ρ^0 - ω mixing in first order in isospin violation as in the e.m. pion vector form factor $F_\pi^V(s)$. The fit to the BESIII $\eta' \rightarrow \pi^+\pi^-\gamma$ data is shown in Fig. 43(c), yielding $\kappa = 0.992(39) \text{ GeV}^{-2}$, $\lambda = -0.523(39) \text{ GeV}^{-4}$, and $\xi = 6.7(2) \times 10^{-3} \text{ GeV}^{-1}$. Since the fit to $|F_\pi^V(s)|^2$ results rather in linear slope parameters of the order of $\kappa \sim 0.1$, it is clear that the shape of the dipion distribution is different. The presence of a significant quadratic term is consistent with calculations including $\pi^\pm a_2^\mp$ crossed-channel contributions [395].

The reaction-specific part can be compared to the $\eta \rightarrow \pi^+\pi^-\gamma$ decay, which has a much smaller kinematic range and necessarily stays closer to the chiral limit, see Fig. 13(b). The parameters were determined experimentally by WASA-at-COSY [412] and KLOE [411]. The differential distributions in

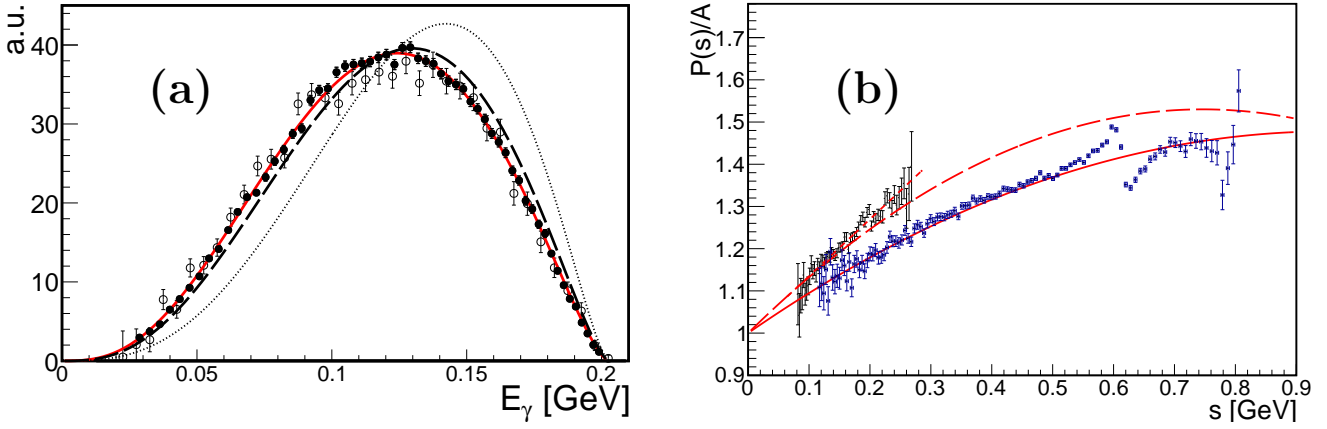


Figure 44: (a) The radiative photon energy distribution for $\eta \rightarrow \pi^+\pi^-\gamma$. Black data points are from KLOE [411] and open data points from WASA-at-COSY [412]. The dotted line is a pure P -wave matrix element $\mathcal{F}(s) \equiv 1$, the dashed line is an Omnès function only ($P(s) = 1$), and the (red) solid line is the fit with $\kappa = 1.32 \text{ GeV}^{-2}$. (b) The data points show the extracted reaction-specific part $P(s)/A$ for $\eta \rightarrow \pi^+\pi^-\gamma$ from KLOE-2 and $\eta' \rightarrow \pi^+\pi^-\gamma$ from BESIII. The dotted and solid lines are the polynomial part of the fits $1 + \kappa s + \lambda s^2$. In addition, the dashed line shows calculations including $\pi^\pm a_2^\mp$ crossed-channel contributions [395].

Fig. 44(a) are expressed in terms of the radiative photon energy E_γ in the η rest frame,

$$E_\gamma = \frac{m_\eta^2 - s}{2m_\eta}, \quad (129)$$

which is a linear function of the Mandelstam variable s . The distributions are compared to the pure P -wave matrix element and to an unmodified Omnès function. For the reaction-specific part, only the term linear in s is necessary, $\kappa = 1.32(13) \text{ GeV}^{-2}$, although crossed-channel contributions will likely induce curvature here, too, that only remains unnoticed due to the smaller kinematic range [395]. In Ref. [335] it was hypothesized that the reaction-specific part could be similar for the η and η' decays; the precise data for η and η' shows, however, that the linear coefficients differ. The reaction-specific parts for both processes are shown in Fig. 44(b).

3.5 $D \rightarrow P_1 P_2 \ell^+ \nu_\ell$

Semileptonic (SL) decays of charmed mesons are a valuable source of information for both the weak and strong interactions [258, 413]. The partial decay width is proportional to the square of the Cabibbo–Kobayashi–Maskawa (CKM) matrix elements $|V_{cs}|$ or $|V_{cd}|$, and the effect of the strong interaction in the initial and final hadrons is described by form factors. The SL decays into a meson pair $D \rightarrow P_1 P_2 \ell^+ \nu_\ell$ are potentially one of the best places to study isolated $P_1 P_2$ systems at c - τ factories. The form factors involved are related to $P_1 P_2$ scattering phases and inelasticities. As seen in Table 9, there is a variety of possible two-pseudoscalar-meson systems with relatively large branching ratios, allowing experiments to collect sufficient data samples. We have presented the double-tagging technique and examples of the available data sets at BESIII in Sec. 2.2. The matrix elements of $D \rightarrow P_1 P_2 \ell^+ \nu_\ell$ have the following form:

$$\langle P_1 P_2 | \bar{q} \gamma_\mu (1 - \gamma_5) c | D \rangle \bar{u}_\nu \gamma^\mu (1 - \gamma_5) v_\ell = \sum_J \langle P_1 P_2 | X^J \rangle \langle X^J | \bar{q} \gamma_\mu (1 - \gamma_5) c | D \rangle \bar{u}_\nu \gamma^\mu (1 - \gamma_5) v_\ell. \quad (130)$$

Table 9: Branching fractions \mathcal{B} for the main semileptonic D and D_s decays into pseudoscalar meson pairs. Unless marked otherwise, the branching fractions are taken from Ref. [48].

Decay	\mathcal{B}	Ref.
$D^0 \rightarrow K^- \pi^0 e^+ \nu_e$	$1.6^{(+1.3)}_{(-0.5)} \times 10^{-2}$	
$D^0 \rightarrow \bar{K}^0 \pi^- e^+ \nu_e$	$1.44(4) \times 10^{-2}$	[414]
$D^0 \rightarrow \pi^0 \pi^- e^+ \nu_e$	$1.45(7) \times 10^{-3}$	[415]
$D^0 \rightarrow \rho^- e^+ \nu_e$	$1.45(7) \times 10^{-3}$	[415]
$D^+ \rightarrow K^- \pi^+ e^+ \nu_e$	$4.02(18) \times 10^{-2}$	
$D^+ \rightarrow K^- \pi^+ \mu^+ \nu_\mu$	$3.65(34) \times 10^{-2}$	
$D^+ \rightarrow \eta \pi^0 e^+ \nu_e$	$1.7^{(+0.8)}_{(-0.7)} \times 10^{-4}$	
$D^+ \rightarrow \pi^+ \pi^- e^+ \nu_e$	$2.45(10) \times 10^{-3}$	[415]
$D^+ \rightarrow \rho^0 e^+ \nu_e$	$1.86(9) \times 10^{-3}$	[415]

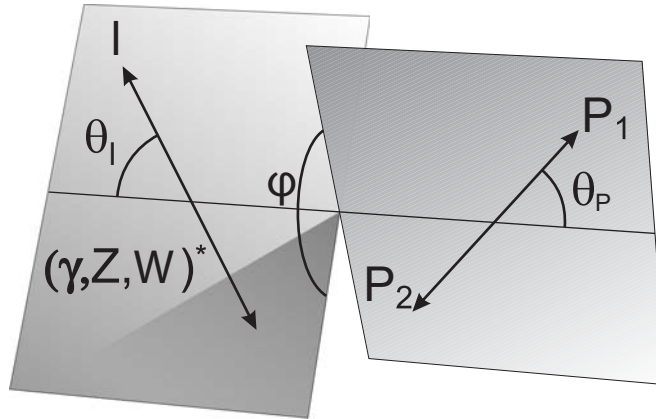


Figure 45: Definition of the kinematic variables used for the description of semileptonic weak decays and e.m. conversion decays.

Compared to strong and electromagnetic processes, there is no background from potential on-shell crossed channels. The goal is to extract the final-state interaction term $\langle P_1 P_2 | X^J \rangle$, possibly in a model independent way, in the range of the accessible invariant masses squared s . However, one should understand the hadronic initial-state interaction (ISI) term, which depends on the invariant mass squared q^2 of the $\ell^+ \nu_\ell$ system. The remaining three kinematic variables describing the decay are the angle between P_1 and the D direction in the X rest frame (θ_P), the angle between the ν_ℓ and the D direction in the $\ell^+ \nu_\ell$ rest frame (θ_ℓ), and the angle between the two decay planes (ϕ); see Fig. 45. The nontrivial dynamics depends only on three kinematic variables s , q^2 , and θ_P .

The formalism for the fully differential decay distribution is based on the description of $K \rightarrow \pi \pi \ell \nu_\ell$ ($K_{\ell 4}$) decays by Pais and Treiman [125]. The hadronic current in a semileptonic decay into a vector

state $X^1 \rightarrow P_1 P_2$ involves four form factors V , A_0 , A_1 , and A_2 [416]:

$$\begin{aligned}
\langle X^1(p_X, \varepsilon) | \bar{q} \gamma_\mu c | D \rangle &= 2 \frac{V(q^2)}{m_D + m_X} \epsilon_{\mu\nu\alpha\beta} p_D^\nu p_X^\alpha \varepsilon^\beta, \\
\langle X^1(p_X, \varepsilon) | \bar{q} \gamma_\mu \gamma_5 c | D \rangle &= i(m_D + m_X) \left(\varepsilon_\mu - \frac{\varepsilon \cdot q}{q^2} q_\mu \right) A_1(q^2) \\
&\quad - i \frac{\varepsilon \cdot q}{m_D + m_X} \left((p_D + p_X)^\mu - \frac{m_D^2 - m_X^2}{q^2} q^\mu \right) A_2(q^2) \\
&\quad + 2i m_X \frac{\varepsilon \cdot q}{q^2} q_\mu A_0(q^2),
\end{aligned} \tag{131}$$

where ε is the polarization of the intermediate state X^1 . The vector form factor V is dominated by vector-meson-resonance exchanges, A_0 is dominated by pseudoscalar-meson exchanges, and A_1 and A_2 are dominated by axial-meson exchanges. For decays into a scalar state X^0 one has

$$\langle X^0(p_X) | \bar{q} \gamma_\mu \gamma_5 c | D \rangle = -i F_+(q^2) \left((p_D + p_X)^\mu - \frac{m_D^2 - m_X^2}{q^2} q^\mu \right) - i F_0(q^2) \frac{m_D^2 - m_X^2}{q^2} q^\mu. \tag{132}$$

The differential decay width of $D \rightarrow P_1 P_2 e^+ \nu_e$ can be expressed as [417]

$$d^5 \Gamma = \frac{G_F^2 |V_{cq}|^2}{(4\pi)^6 m_D^2} p_X \sigma \mathcal{I}(s, q^2, \theta_P, \theta_\ell, \phi) ds dq^2 d \cos \theta_P d \cos \theta_\ell d \phi, \tag{133}$$

where $\sigma = 2p^*/m_X$, p_X is the momentum of the X system in the D rest frame, and p^* is the momentum of P_1 in the X rest frame. The dependence of the decay density \mathcal{I} for the cases with electrons/positrons, i.e., neglecting terms with the lepton mass, is given by

$$\begin{aligned}
\mathcal{I} &= \mathcal{I}_1 + \mathcal{I}_2 \cos 2\theta_\ell + \mathcal{I}_3 \sin^2 \theta_\ell \cos 2\phi + \mathcal{I}_4 \sin 2\theta_\ell \cos \phi + \mathcal{I}_5 \sin \theta_\ell \cos \phi \\
&\quad + \mathcal{I}_6 \cos \theta_\ell + \mathcal{I}_7 \sin \theta_\ell \sin \phi + \mathcal{I}_8 \sin 2\theta_\ell \sin \phi + \mathcal{I}_9 \sin^2 \theta_\ell \sin 2\phi,
\end{aligned} \tag{134}$$

where the functions $\mathcal{I}_{1,\dots,9}$ depend on s , q^2 , and θ_P and can be expressed in terms of three form factors, $\mathcal{F}_{1,2,3}$. The form factors can be expanded into partial waves including S -wave (\mathcal{F}_{10}), P -wave (\mathcal{F}_{i1}), and D -wave (\mathcal{F}_{i2}), to show their explicit dependencies on θ_P . So far, high-statistics analyses of the semileptonic decays (like $D^+ \rightarrow K^+ \pi^- e^+ \nu_e$) do not require a D -wave component and the form factors can be written as

$$\mathcal{F}_1 = \mathcal{F}_{10} + \mathcal{F}_{11} \cos \theta_P, \quad \mathcal{F}_2 = \frac{1}{\sqrt{2}} \mathcal{F}_{21}, \quad \mathcal{F}_3 = \frac{1}{\sqrt{2}} \mathcal{F}_{31}, \tag{135}$$

where \mathcal{F}_{11} , \mathcal{F}_{21} , and \mathcal{F}_{31} are related to the helicity basis form factors $H_{0,\pm}(q^2)$ [417, 418]. The helicity form factors can in turn be related to the two axial-vector form factors, $A_1(q^2)$ and $A_2(q^2)$, as well as the vector form factor $V(q^2)$. The $A_{1,2}(q^2)$ and $V(q^2)$ are all taken as the simple pole form $A_i(q^2) = A_{i,2}(0)/(1 - q^2/m_A^2)$ and $V(q^2) = V(0)/(1 - q^2/m_V^2)$, with pole masses $m_V = m_{D_s^*(1^-)} = 2.1121$ GeV and $m_A = m_{D_s^*(1^+)} = 2.4595$ GeV. The form factor $A_1(q^2)$ is common to all three helicity amplitudes. Therefore, it is natural to define two form factor ratios as $r_V = V(0)/A_1(0)$ and $r_2 = A_2(0)/A_1(0)$ at the dilepton momentum squared $q^2 = 0$.

The experimental determination of these ISI form factors is performed through the study of the differential decay width $d\Gamma/dq^2$. Dispersive representations [419] allow one to place constraints on the shapes of the form factors by exploiting their analytic properties, leading to polynomial expansions in certain conformal variables (instead of the Mandelstam variables themselves) that account for the lowest branch cuts. Specifically for the charm sector, only the $D \rightarrow \pi$ form factors have been discussed in detail

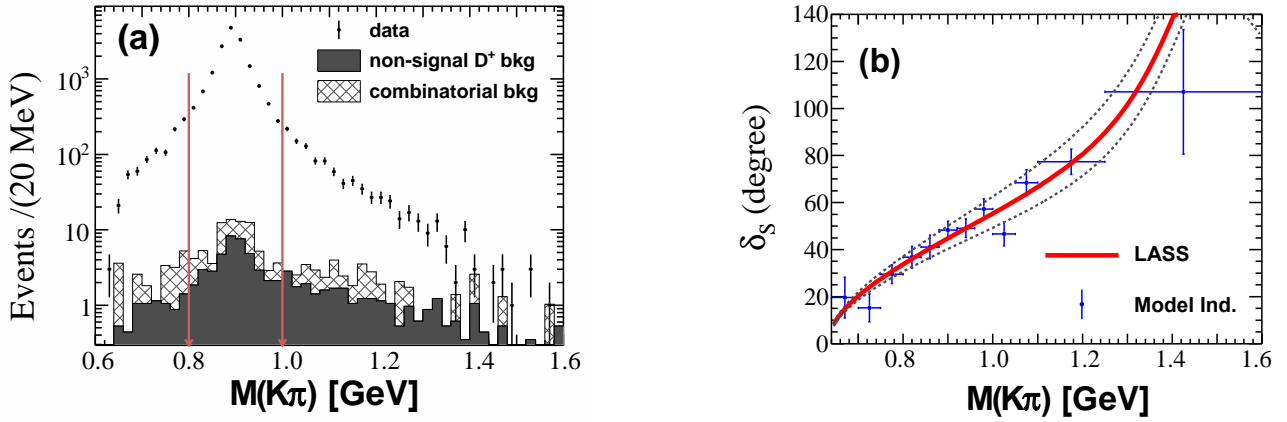


Figure 46: Study of the $K\pi$ system at BESIII in $D^+ \rightarrow K^-\pi^+e^+\nu_e$ [431]. (a) Distribution of the selected candidates with respect to the $K\pi$ invariant mass $M(K\pi)$. The range between the arrows corresponds to the K^* -dominated region. The dots with error bars represent data, the shadowed histogram and the hatched area show background contributions. (b) Dependence of the S -wave phase on $M(K\pi)$, assuming that the signal is composed of the S -wave and the $\bar{K}^*(892)^0$. The points with error bars correspond to the model-independent extraction; the solid line corresponds to the result based on the LASS parameterization; the dotted line shows the 1σ confidence band.

so far [420–422]. The most common model-dependent parameterization has been a single-pole form factor, where the pole is the lowest-mass resonance formed by the initial- and final-state hadron. The ISI form factor influences mainly the low $M(P_1P_2)$ region. In addition, there are already first calculations of the ISI form factors in lattice QCD [423]. A technique developed by the FOCUS experiment allows for the nonparametric determination of the form factors in $D^+ \rightarrow K^-\pi^+e^+\nu_e$ [424], later adopted also by the CLEO-c experiment [425], thus providing model-independent input for theoretical interpretation [426].

The SL decays are dominated by X^1 states of the meson pair. For instance, the semileptonic decays into $K\pi$ pairs are dominated by the $K^*(892)$, and those into $\pi\pi$ pairs by the $\rho(770)$ resonances. The unique possibility is to study the interference of parity-even amplitudes with these dominant and well-known contributions. The FOCUS experiment [427] was the first to report evidence for an even $K^-\pi^+$ amplitude interfering with the dominant \bar{K}^*0 component in the decay $D^+ \rightarrow K^-\pi^+\mu^+\nu_\mu$. CLEO-c [425] has seen the same effect in $D^+ \rightarrow K^-\pi^+e^+\nu_e$. These observations open prospects for exclusive charm semileptonic decays as a tool to measure phase-shift differences between the P - and S -waves [428]. Below, we give some examples using BESIII analyses that are based on 2.93 fb^{-1} of data collected at the c.m. energy of 3.773 GeV .

$K\pi$ system: $D^+ \rightarrow K^-\pi^+e^+\nu_e$ and $D^0 \rightarrow \bar{K}^0\pi^-e^+\nu_e$ Measurements of $\bar{K}\pi$ resonant and nonresonant amplitudes in the decay $D^+ \rightarrow K^-\pi^+e^+\nu_e$ have been reported by the CLEO [425, 429], BaBar [430], and BESIII [431] collaborations. In these studies, a nontrivial S -wave component is observed along with the dominant P -wave one. The BESIII analysis is based on a nearly background-free sample of 18262 double-tagged events (see Sec. 2.2.5). In Fig. 46(a) the invariant-mass distribution $M(K\pi)$ is shown and the K^* -dominated region is indicated. A PWA shows that this dominant component is accompanied by an S -wave contribution accounting for $6.1(3)\%$ of the total rate, while other components are negligible. The helicity form factors of the $\bar{K}^*(892)^0$ were studied in a model-independent way. The S -wave phase as a function of $M(K\pi)$, determined assuming that the signal is composed of the S -wave and the $\bar{K}^*(892)^0$, is shown in Fig. 46(b). The points with error bars correspond to the model-

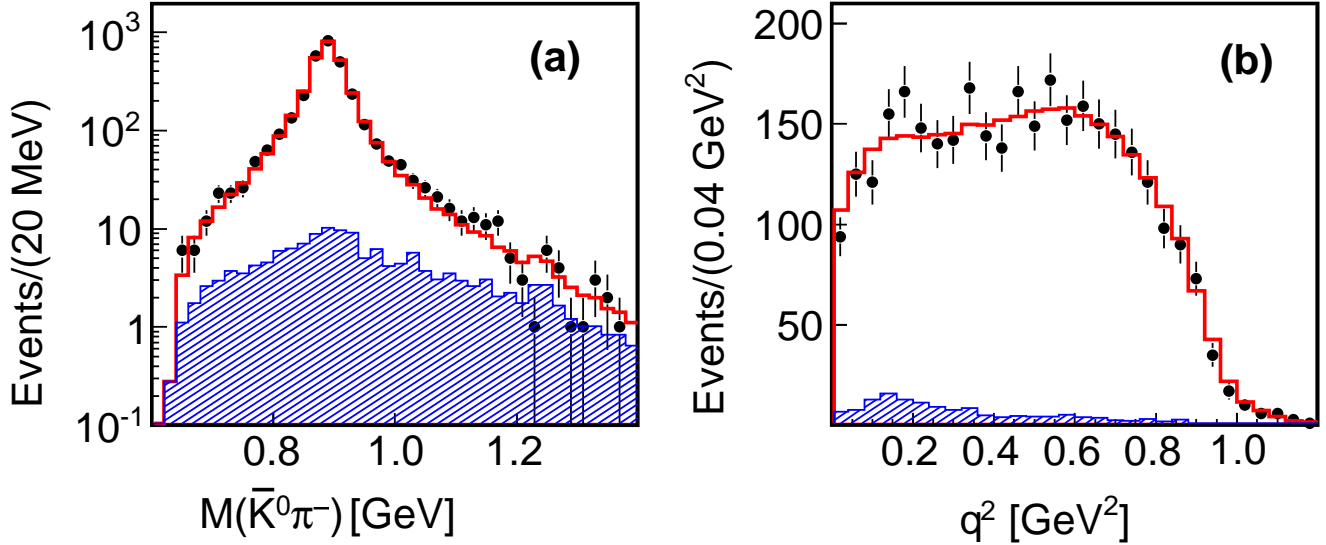


Figure 47: Study of the $K\pi$ system at BESIII in $D^0 \rightarrow \bar{K}^0\pi^-e^+\nu_e$ [414]. (a) Distribution of the selected candidates with respect to the $K\pi$ invariant mass $M(K\pi)$. (b) Distribution with respect to dilepton invariant mass squared q^2 . The dots with error bars represent data and the hatched area shows background contributions.

independent extraction and are compared to a parameterization of the $K\pi$ elastic scattering phase $\delta_0^{1/2}$ from the LASS experiment [114] shown in Fig. 10(h).

A study of the isospin-related mode $D^0 \rightarrow \bar{K}^0\pi^-e^+\nu_e$ provides complementary information on the $\bar{K}\pi$ system. Furthermore, the form factors in the $D \rightarrow Ve^+\nu_e$ transition, where V refers to a vector meson, have been measured in decays of $D^+ \rightarrow \bar{K}^{*0}e^+\nu_e$ and $D \rightarrow \rho e^+\nu_e$ [432], while no form factor in $D^0 \rightarrow K^*(892)^-e^+\nu_e$ has been studied yet. Therefore, the study of the dynamics in the decay $D^0 \rightarrow K^*(892)^-e^+\nu_e$ provides essential new information on the family of $D \rightarrow Ve^+\nu_e$ decays. A study of the decay $D^0 \rightarrow \bar{K}^0\pi^-e^+\nu_e$ was carried out at BESIII using 3112(64) double-tagged events [414]. This decay is dominated by the vector $K^*(892)^-$ contribution, as seen in the $M(K\pi)$ distribution in Fig. 47(a), and the determined $\bar{K}^0\pi^-$ S -wave component accounts for 5.5(1.2)% of the total decay rate. The hadronic form factor ratios $r_V = 1.46(7)$ and $r_2 = 0.67(6)$ were extracted from the distribution of the dilepton invariant mass squared shown in Fig. 47(b).

$\pi\pi$ system: $D^0 \rightarrow \pi^-\pi^0e^+\nu_e$ and $D^+ \rightarrow \pi^-\pi^+e^+\nu_e$ The two-pion SL decays are Cabibbo-suppressed by $|V_{cd}|^2$. BESIII has performed a partial-wave analysis of 1102(45) events of $D^0 \rightarrow \pi^-\pi^0e^+\nu_e$ and 1667(50) events of $D^+ \rightarrow \pi^-\pi^+e^+\nu_e$ [415]. The pion invariant-mass spectra are dominated by the ρ meson contribution as shown in Fig. 48(a) and (c). The narrow peak in the $M(\pi^-\pi^0)$ distribution in panel (a) and the removed region in the $M(\pi^+\pi^-)$ distribution in panel (c) correspond to backgrounds with kaons, where the K_S contribution from $D^+ \rightarrow K_S e^+\nu_e$ is particularly severe. An interesting feature is a hint at ρ^0 - ω interference seen as a narrow peak in the $M(\pi^+\pi^-)$ distribution close to the ω mass. The interference pattern is completely different from what we have seen in F_π^V , which can be understood from the different isospin structure of the transition that has the pion pair emerge effectively from a $\bar{d}\gamma_\mu d$ source; cf. the discussion in Ref. [176] for a related case. However, the most important conclusion of this analysis is the observation of a large $\pi^+\pi^-$ S -wave contribution of 26(2)% in the $D^+ \rightarrow \pi^-\pi^+e^+\nu_e$ decay, which is required to describe the data. The corresponding dilepton spectra related to the form factors are shown in Fig. 48(b) and (d).

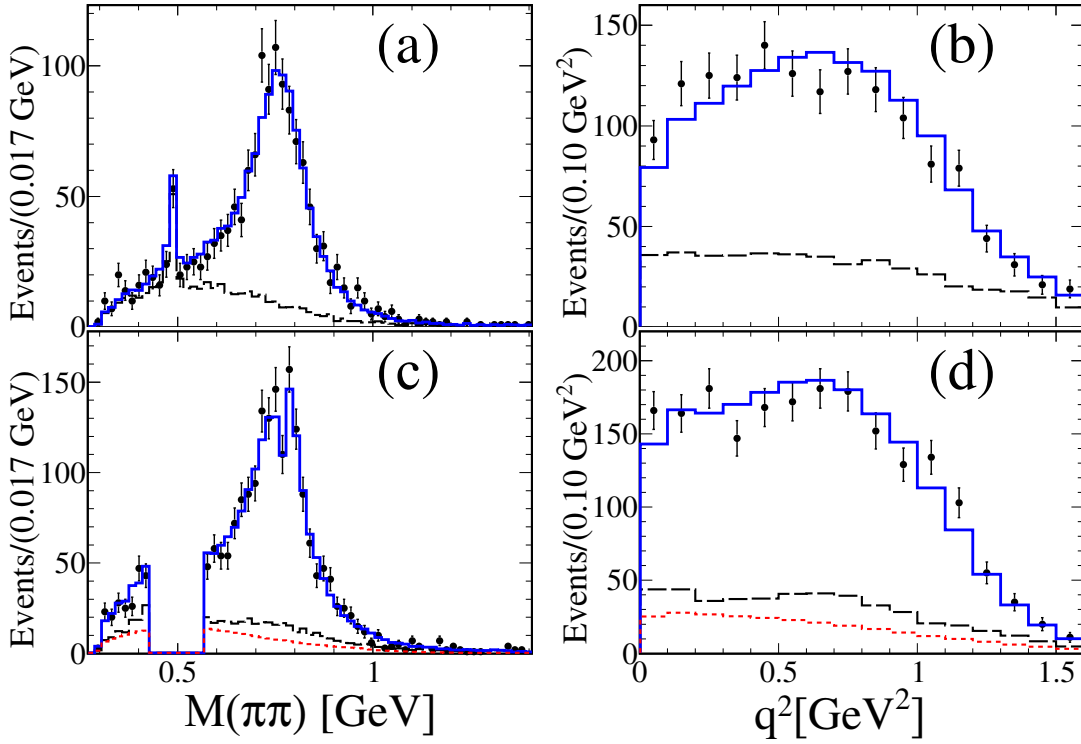


Figure 48: Dipion (left) and dilepton (right) invariant-mass distributions for $D^0 \rightarrow \pi^- \pi^0 e^+ \nu_e$ (top) and $D^+ \rightarrow \pi^- \pi^+ e^+ \nu_e$ (bottom), respectively. The lines are results of simultaneous PWA fit. The solid lines represent the fits, the dashed lines show the corresponding backgrounds, while the dotted lines in (c) and (d) show the scalar $D^+ \rightarrow f_0(500) e^+ \nu_e$ component.

$\eta\pi$ system: $D \rightarrow \eta\pi e^+ \nu_e$ The $D^0 \rightarrow \eta\pi^- e^+ \nu_e$ and $D^+ \rightarrow \eta\pi^0 e^+ \nu_e$ decays were studied at BESIII [433]. Since the isovector $\eta\pi$ system cannot originate from the vector current with positive G parity (as long as isospin is conserved), the reaction allows to study a clean signal of the $a_0(980)$ scalar contribution. The invariant mass $M(\eta\pi)$ spectra are shown in Fig. 49.

3.6 $V \rightarrow V' P_1 P_2$

In the context of our review, the J/ψ and ϕ' decays to a narrow vector meson V' and a system of two pseudoscalar mesons $P_1 P_2$ are tools to learn about the interaction of the pseudoscalar pair. The presence of the narrow vector meson in the final state of the strong decay is used as a spin/isospin/ $SU(3)_{\text{flavor}}$ filter, and the hope is it can be assumed to be a passive spectator in the reaction. We expect to be able to write the $V \rightarrow V' P_1 P_2$ amplitude in an analogous way as Eq. (118):

$$\mathcal{M} = \sum_X \langle P_1 P_2 | H_2 | X \rangle \langle X V' | H_1 | V \rangle, \quad (136)$$

where the two steps of the reaction proceed via strong interactions H_1, H_2 . In the case of isoscalar vector mesons V and V' the produced meson systems X will be isoscalar. Flavor filtering is illustrated in Fig. 50. Processes without a significant $s\bar{s}$ quark contribution in the meson state ($M_1 M_2$) are suppressed in decays to $\phi(M_1 M_2)$ due to double OZI suppression, since they require additional disconnected (i.e., producing separate hadrons) quark lines in the final state. This can be seen, e.g., from the comparison of the branching ratios

$$\frac{\mathcal{B}(J/\psi \rightarrow \omega\pi^+\pi^-)}{\mathcal{B}(J/\psi \rightarrow \omega K\bar{K})} \approx 3.8, \quad \frac{\mathcal{B}(J/\psi \rightarrow \phi\pi^+\pi^-)}{\mathcal{B}(J/\psi \rightarrow \phi K\bar{K})} \approx 0.53. \quad (137)$$

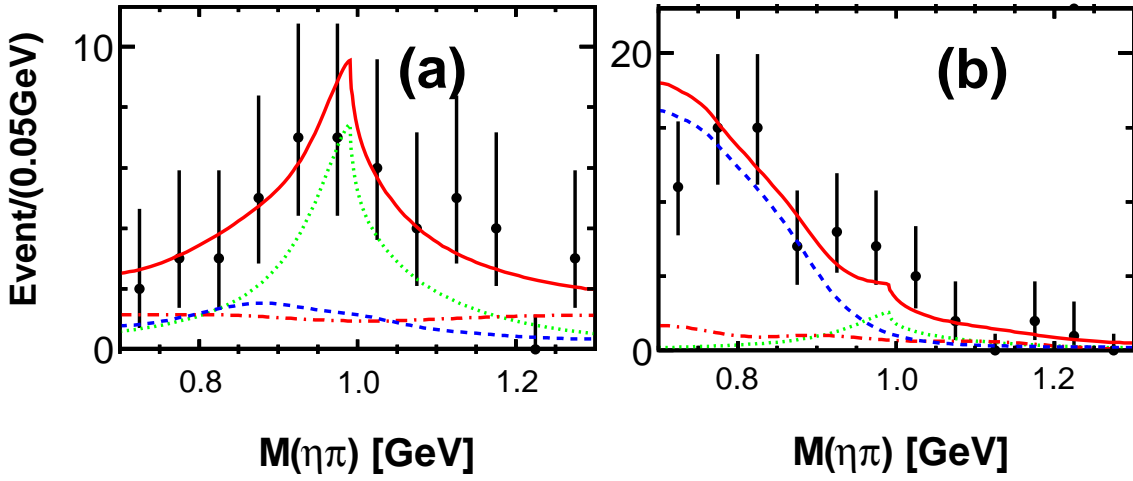


Figure 49: Invariant mass $M(\eta\pi)$ for (a) $D^0 \rightarrow a_0(980)^- e^+ \nu_e$ and (b) $D^+ \rightarrow a_0(980)^0 e^+ \nu_e$. The (red) solid curves are the overall fits, the dashed and dotted–dashed lines denote backgrounds, and the (green) dotted lines show the fitted signal shape.

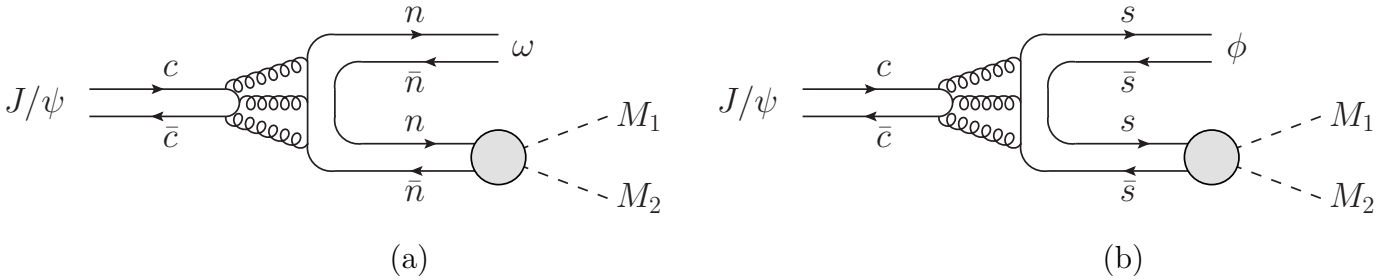


Figure 50: Production of parity-even meson systems ($M_1 M_2$) in (a) decay of J/ψ into $\omega(M_1 M_2)$ and (b) $\phi(M_1 M_2)$. The two processes select $\bar{n}n = (\bar{u}u + \bar{d}d)/2$ or $\bar{s}s$ ($M_1 M_2$) meson systems.

In some cases the assumption that the vector meson is a spectator is well founded, e.g., the $\phi\pi$ interaction is suppressed by the OZI rule in $J/\psi \rightarrow \phi\pi\pi$. In other cases, like $J/\psi \rightarrow \phi K \bar{K}$, the situation is not so clear as we will discuss later in this section. The high-statistics data of charmonium decays provides a new opportunity to extract information of meson–meson scattering, in particular scalar mesons. Nowadays the $f_0(500)$ is a well-established example of a resonance with its pole deep in the complex plane, which requires ChPT and dispersive methods to describe its properties [133]. The $f_0(500)$ state was first observed in $\pi\pi$ scattering and also in some production processes. It is needed in order to explain the $\pi\pi$ scattering phase shift data. The observation of clear bumps in charmonia decays at BESII such as in $J/\psi \rightarrow \omega\pi^+\pi^-$ was an important step towards general acceptance of the $f_0(500)$ resonance.

3.6.1 $\psi' \rightarrow J/\psi\pi\pi$

We start from the two $\psi' \rightarrow J/\psi\pi\pi$ processes, the main ψ' decay modes, see Table 10. Here, the assumptions leading to Eq. (136) should be well fulfilled, since crossed-channel $J/\psi\pi$ rescattering should be very weak, and no resonances are expected in the quark model. The advantages of this reaction to study quasi-isolated dipion systems in the low-mass region, $M(\pi\pi) < m_{\psi'} - m_{J/\psi}$, were pointed out already in 1975 [436, 437].

The dipion invariant-mass distribution in this process is strongly peaked towards its higher end, in

Table 10: Branching fractions for $V \rightarrow V' P_1 P_2$ decays. Unless marked otherwise, the branching fractions are taken from Ref. [48].

	Final state	\mathcal{B}	Ref.
$J/\psi \rightarrow V^0 P_1 P_2$	$\omega\pi^0\pi^0$	$3.4(8) \times 10^{-3}$	
	$\omega\pi^+\pi^-$	$7.2(1.0) \times 10^{-3}$	
	$\omega\pi^0\eta$	$3.4(1.7) \times 10^{-4}$	[434]
	$\omega K\bar{K}$	$1.9(4) \times 10^{-3}$	
	$\phi\pi^0\pi^0$	$5.0(1.0) \times 10^{-4}$	
	$\phi\pi^+\pi^-$	$9.4(1.5) \times 10^{-4}$	
	$\phi\eta\eta'$	$2.32(17) \times 10^{-4}$	[435]
	$\phi K\bar{K}$	$1.77(16) \times 10^{-3}$	
$\psi' \rightarrow J/\psi P_1 P_2$	$J/\psi\pi^+\pi^+$	0.3468(30)	
	$J/\psi\pi^0\pi^0$	0.1824(31)	

contrast to what is expected from phase space alone, and the angular distribution favors an S -wave state for the dipion system [438, 439]. Within a standard PWA approach, three main contributions have been considered: the $f_0(500)$ resonance, a D -wave term, and a contact term required by ChPT [440]: $A = A_0 + A_2 + A_{\text{contact}}$. The VPP production vertex is taken as a constant and the amplitudes $A_{0,2}$ are taken from the isobar model. The $M(\pi\pi)$ distribution from the BESII analysis [439], using a clean data sample of 40000 $\psi' \rightarrow \pi^+\pi^- J/\psi$ events with $J/\psi \rightarrow \mu^+\mu^-$, is shown in Fig. 51(a). It is compared to the results of the PWA with the above ansatz. Four different Breit–Wigner parameterizations for the mass dependence of the $f_0(500)$ resonance were tried. All fit the data well, but the solutions have strong destructive interference with the contact term, especially in the low $\pi\pi$ invariant-mass region. This effect is anticipated by chiral symmetry [436, 440]. The D -wave contribution amounts to only 0.3 to 1%. The extracted $f_0(500)$ pole parameters using different parameterizations are consistent with each other, and the average is $550(95) - i230(77)$. An alternative fit shown in Fig. 51(b) describes the VPP vertex using an effective Lagrangian and includes universal $\pi\pi$ S -wave rescattering in the final state [441], thus overcoming the violation of unitarity by naïvely employing contact term and $f_0(500)$ resonance (as an approximation to rescattering effects) additively. Here, the $f_0(500)$ -pole parameters are taken from Ref. [442], where they were determined from the $\pi\pi$ scattering data. The contribution of the contact term (LO ChPT) and the interference is small in this approach. The model does not include a D -wave, which might explain the slightly worse fit quality.

3.6.2 $J/\psi \rightarrow \omega(\pi^+\pi^-, K^+K^-)$ and $J/\psi \rightarrow \phi(\pi^+\pi^-, K^+K^-)$

In the BESII experiment, a sample of 58 million J/ψ events was used to study $J/\psi \rightarrow \omega\pi^+\pi^-$ [443], $J/\psi \rightarrow \omega K^+K^-$ [445], and $J/\psi \rightarrow \phi\pi^+\pi^-, \phi K^+K^-$ decays [444]. The vector mesons are reconstructed via their main decay modes $\omega \rightarrow \pi^+\pi^-\pi^0$ and $\phi \rightarrow K^+K^-$. Dalitz plots for all these channels are shown in Fig. 52. The prominent role of the resonances in the two-pseudoscalar-meson systems is seen from the predominantly anti-diagonal pattern of the plots, which indicates that the spectator assumption might be a reasonable approximation.

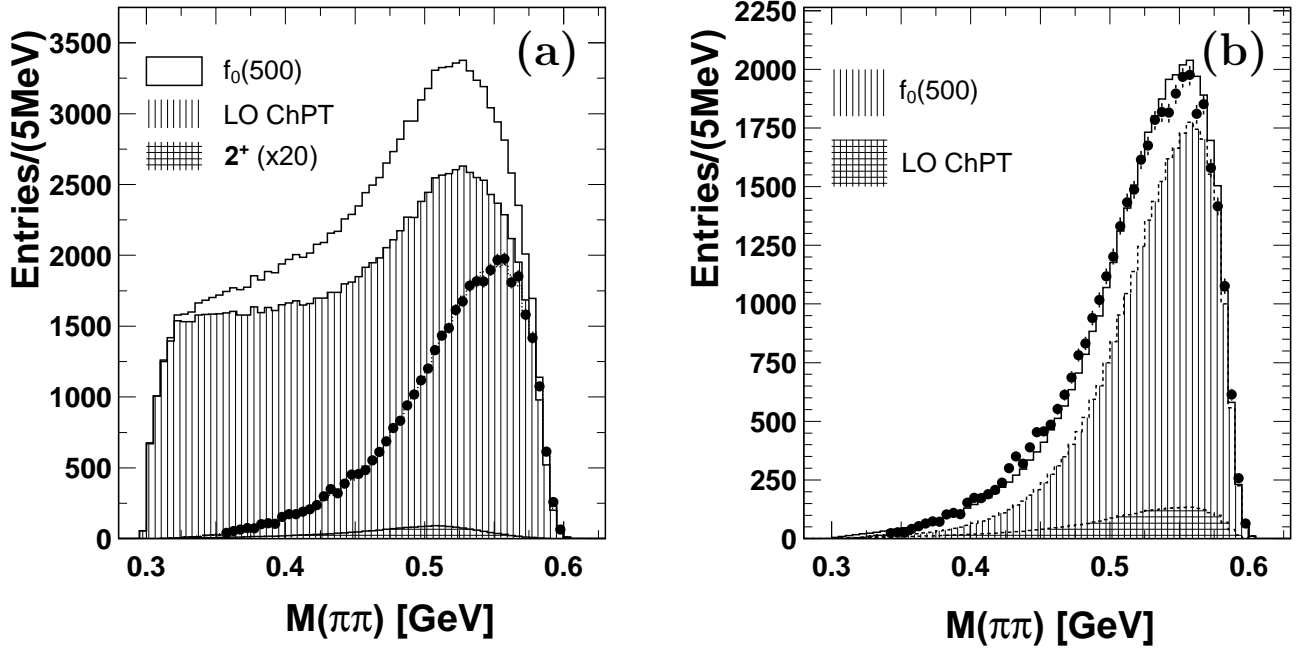


Figure 51: The $\pi^+\pi^-$ invariant-mass distribution in $\psi' \rightarrow J/\psi\pi^+\pi^-$ from BESII [439]. Panel (a) shows an isobar model fit, which includes the contributions from $f_0(500)$, D -wave term (enlarged by a factor of 20 in the figure), and contact term. The coherent sum of the contributions describes the data well. Panel (b) shows the invariant mass fitted by the chiral unitarity approach [441]. Dots with error bars are data, and the histograms are the fit results.

The standard approach to analyses of such reactions is a PWA using, e.g., the covariant tensor formalism [446]. In Ref. [443], in addition to the ω spectator scenario of Eq. (136) two crossed channels were considered for $J/\psi \rightarrow \omega\pi^+\pi^-$: $\rho(1450)\pi$ and $b_1(1235)\pi$ (the $b_1(1235)$ is a $J^{PC} = 1^{+-}$ state, see Table 1). However, the analysis does not include the sub-threshold channel $\rho(770)\pi$. In the spectator scenario, two isoscalar $\pi\pi$ waves were included: scalar 0^{++} and tensor 2^{++} . They were explicitly represented by the contributions from $f_0(500)$, $f_0(980)$, as well as $f_2(1565)$, $f_2(2240)$ resonances, respectively. Four different parameterizations of the $f_0(500)$ pole were tried in the analysis. The $f_0(500)$ contribution dominates the low-mass region of the $\pi\pi$ invariant mass, see Fig. 53(a), as a clear broad enhancement. The Monte Carlo (MC) study excluded a background and acceptance effects as the explanation. The extracted mass and width of the $f_0(500)$ resonance vary significantly depending on the parameterization. The variation was taken as a measure of the systematic uncertainty. The combined result for the pole position of the $f_0(500)$ is $541(39) - i 252(42)$ MeV.

The 2^{++} wave is dominated by the $f_2(1270)$ as shown in Fig. 54(a). The crossed-channel contribution, clearly visible as horizontal and vertical bands along the low-mass edges of the Dalitz plot in Fig. 52(a), is dominated by $b_1(1235)\pi$, see Fig. 54(b). Finally, in the 0^{++} wave, in addition to the $f_0(500)$, a small (1%) but significant contribution from the $f_0(980)$ is needed, see Fig. 53(a).

This picture is opposite for $J/\psi \rightarrow \phi\pi\pi$, where the $f_0(980)$ is the dominating contribution to $M(\pi\pi)$ below 1 GeV. The distorted line shape of the $f_0(980)$ is clearly seen in the $\pi\pi$ mass spectrum recoiling against the ϕ , which is shown in Fig. 53(c). The $f_0(980)$ is observed in both kaon-kaon channels, the $J/\psi \rightarrow \omega K^+K^-$ and $J/\psi \rightarrow \phi K^+K^-$ data sets (the dotted lines in Fig. 53(b) and 53(d)). In Ref. [444], the $\phi\pi^+\pi^-$ and ϕK^+K^- data are fitted simultaneously assuming common resonance masses in the two channels. Only the channels with spectator ϕ are considered. In the PWA, the $f_0(980)$ resonance is

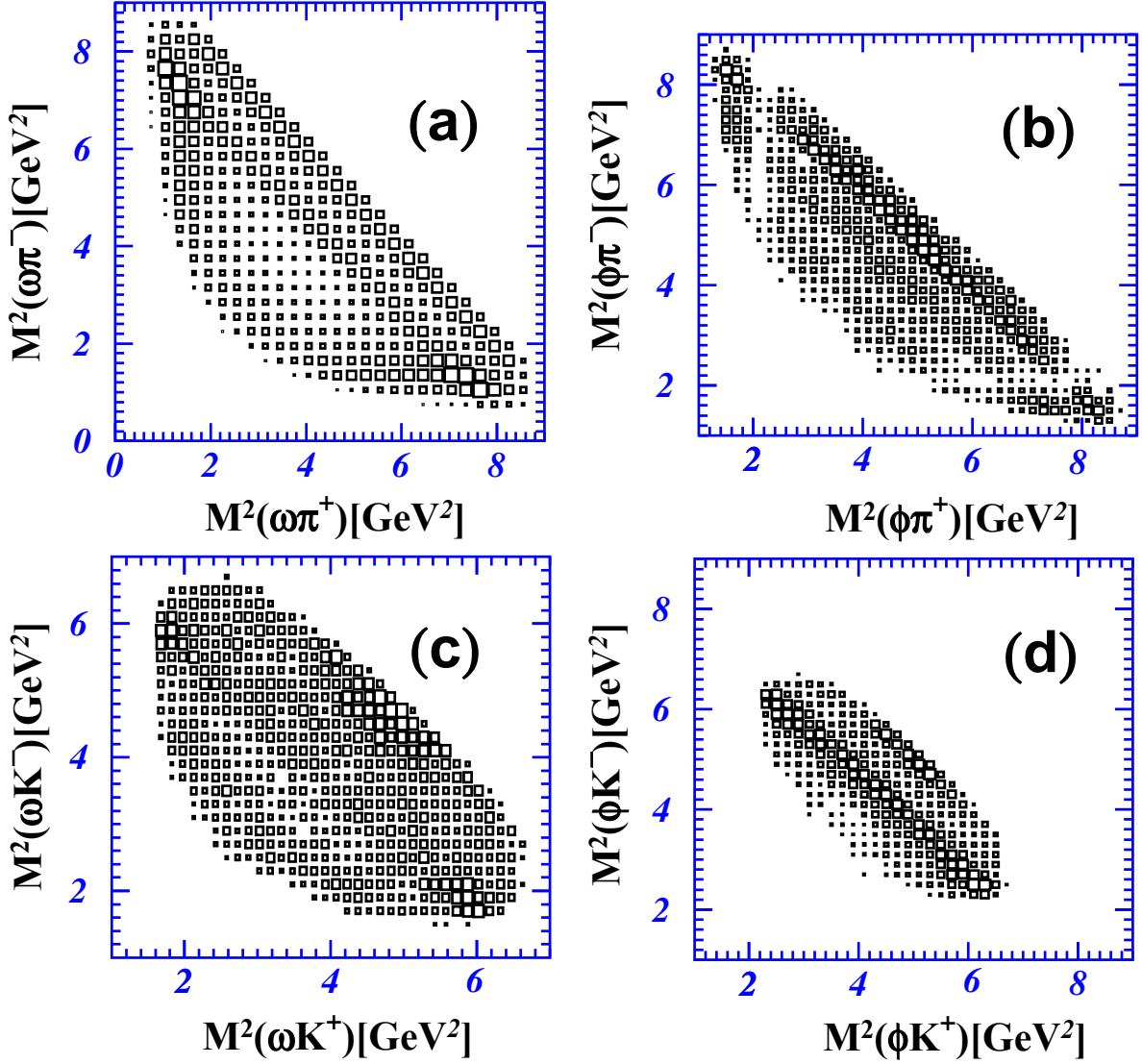


Figure 52: Dalitz plots for (a) $J/\psi \rightarrow \omega\pi^+\pi^-$ [443], (b) $J/\psi \rightarrow \phi\pi^+\pi^-$ (with removed $K^*(890)K\pi$ background) [444], (c) $J/\psi \rightarrow \omega K^+K^-$ [445], and (d) $J/\psi \rightarrow \phi K^+K^-$ [444].

parameterized by the Flatté formula Eq. (11) for the $\pi\pi$ and $K\bar{K}$ channels. The clean signal in the $\pi\pi$ mass spectrum offers a unique opportunity to determine the ratio of the couplings to the two channels, which is found to be $g_{KK}/g_{\pi\pi} = 4.21(33)$.

An additional state in the $\pi\pi$ system with mass 1790(35) MeV and width 270(45) MeV has likely spin 0, and we denote it as $f_0(1790)$. It is distinct from the $f_0(1710)$, since the branching fraction ratio $K\bar{K}/\pi\pi$ for the $f_0(1790)$ is an order of magnitude lower than for the $f_0(1710)$ [48]. This implies the existence of two states: the $f_0(1790)$ decaying dominantly into $\pi\pi$, and the $f_0(1710)$ dominantly into $K\bar{K}$. The $f_0(1790)$ is a natural candidate for the radial excitation of the $f_0(1370)$.

The $\phi K\bar{K}$ data contains a strong peak due to the $f_2'(1525)$. The shoulder on its upper side may be fitted assuming interference between $f_0(1500)$ and $f_0(1710)$. The data indicates a possible small contribution from the $f_0(1790)$ interfering with the $f_0(1500)$.

The $\phi\pi\pi$ data exhibits a broad peak in the $M(\pi\pi)$ spectrum centered at 1.33 GeV. It may be fitted with the $f_2(1270)$ and a dominant 0^+ signal made from $f_0(1370)$, interfering with a smaller $f_0(1500)$ component. There is evidence that the $f_0(1370)$ signal is resonant, from interference with the $f_2(1270)$.

Now we turn to alternative descriptions, motivated by unitarity, of the above four decay processes.

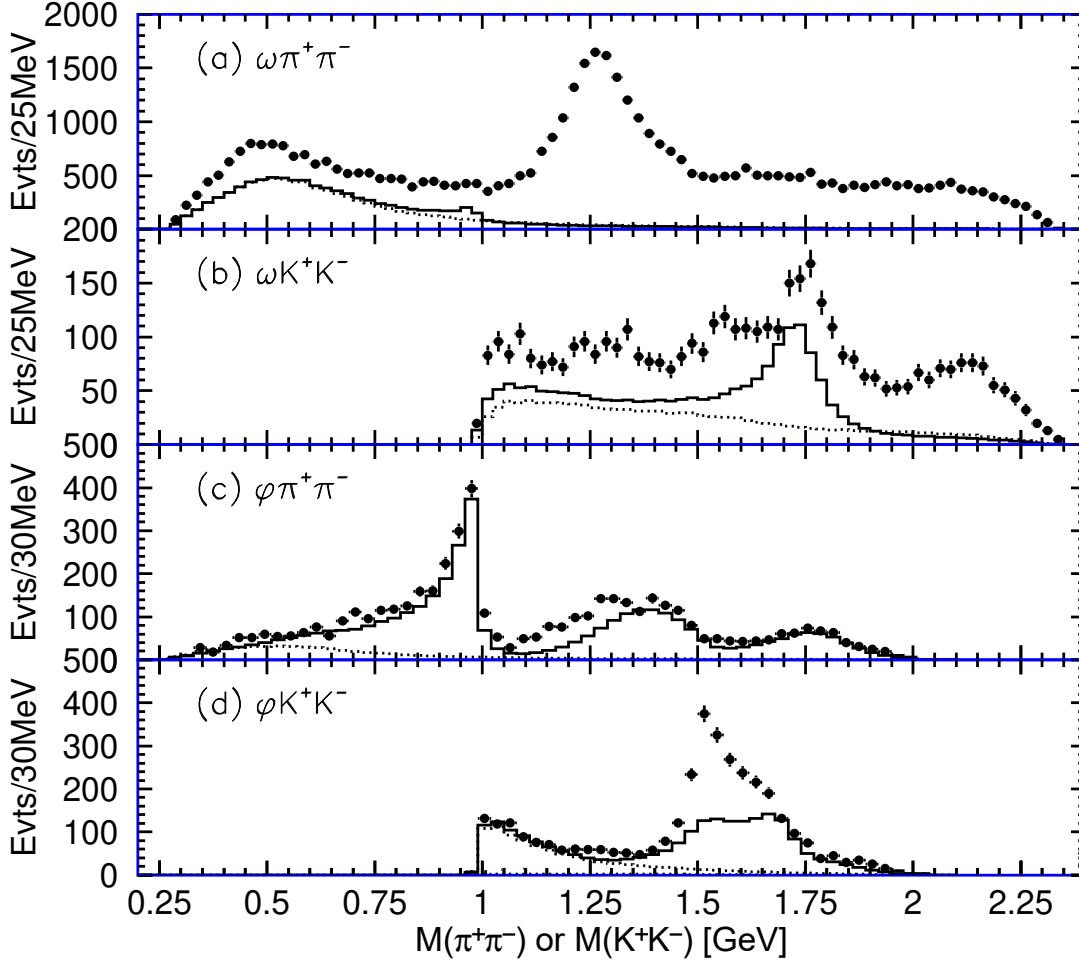


Figure 53: Invariant-mass distributions (uncorrected for acceptance) of pseudoscalar meson pairs recoiling against ω or ϕ in J/ψ decays measured at BESII. The solid-line histograms are the scalar contributions from the mass-dependent PWA. The dotted lines in (a) and (c) ($\pi^+\pi^-$ channels) denote the $f_0(500)$, and in (b) and (d) (K^+K^- channels) the $f_0(980)$.

At first we consider decay processes $J/\psi \rightarrow \phi\pi^+\pi^-$, ϕK^+K^- in the ϕ spectator approximation, where the meson pairs are in an S -wave. The two amplitudes are related to the $\pi\pi \leftrightarrow K\bar{K}$ coupled-channel meson-meson scattering amplitudes [447]:

$$F(J/\psi \rightarrow \phi\pi^+\pi^-) = \sqrt{\frac{2}{3}} [\alpha_1(s)t_{\pi\pi \rightarrow \pi\pi}(s) + \alpha_2(s)t_{K\bar{K} \rightarrow \pi\pi}(s)] , \quad (138)$$

$$F(J/\psi \rightarrow \phi K^+K^-) = \sqrt{\frac{1}{2}} [\alpha_1(s)t_{\pi\pi \rightarrow K\bar{K}}(s) + \alpha_2(s)t_{K\bar{K} \rightarrow K\bar{K}}(s)] , \quad (139)$$

where $\alpha_i = \kappa_i/(s - \lambda_i) + \gamma_{i0} + \gamma_{i1}s$ for $i = 1, 2$ are real functions of the couplings of J/ψ to the corresponding channels and are free parameters. This is an example of the K -matrix method in the zero-range approximation [448].

The S -waves in the J/ψ decays into ω and ϕ , accompanied by $\pi\pi$ and $K\bar{K}$ pairs, have also been analyzed in the framework of a chiral unitary approach [449, 450]. Here, the decay amplitudes are assumed to be proportional to appropriate mixtures of nonstrange and strange scalar form factors for pions and kaons; the latter, including various chiral low-energy constants, are extracted from a fit to data. While the gross features of the spectra up to slightly above 1 GeV, such as the contributions of $f_0(500)$ and $f_0(980)$, are reproduced, some properties of the extracted form factors are in conflict with

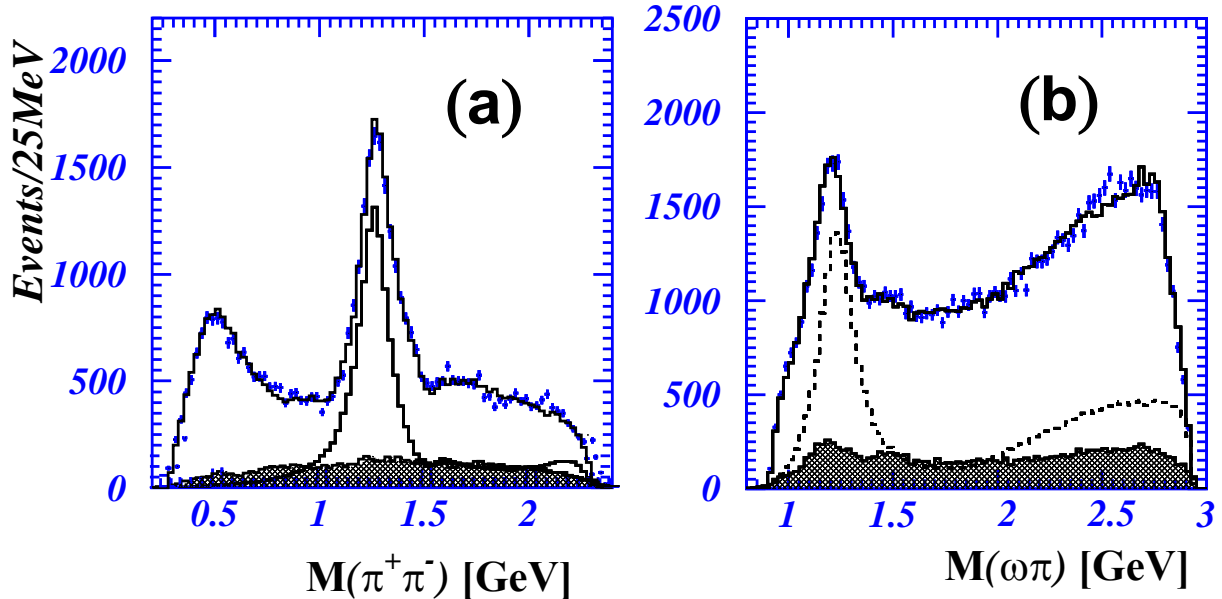


Figure 54: Invariant-mass distributions for $J/\psi \rightarrow \omega\pi^+\pi^-$ from BESIII [443]: (a) $M(\pi\pi)$ and (b) $M(\pi\omega)$. In panel (a) the PWA fit contribution from f_2 states is shown, while in panel (b) the dashed line shows the $b_1(1235)\pi$ contribution. The shaded areas represent the background estimated from sidebands.

constraints from low-energy QCD. This is likely due to the neglect of crossed-channel dynamics, which have been included in a similar framework in Refs. [451, 452]

3.6.3 Observation of $a_0^0(980) - f_0(980)$ mixing in $J/\psi \rightarrow \phi\eta\pi^0$

The neutral isovector $a_0^0(980)$ and the isoscalar $f_0(980)$ 0^{++} resonances can mix. The leading contribution to the isospin-violating transition amplitudes for $f_0 \leftrightarrow a_0^0$ can be shown to be due to the difference of the unitarity-cut contributions of charged and neutral $K\bar{K}$ pairs, arising due to the mass difference between the two. While away from thresholds, isospin breaking is expected to scale as a polynomial in the light quark mass difference or, accordingly, as $M_{K^\pm}^2 - M_{K^0}^2$, in the vicinity of both cuts this scaling is enhanced to $\sqrt{M_{K^\pm}^2 - M_{K^0}^2}$, and hence nonanalytic in the quark mass difference. As a consequence, a strong enhancement of the mixing signal is predicted between the charged and neutral $K\bar{K}$ thresholds, with the width of 8 MeV. The mixing amplitudes strongly depend on the couplings of a_0^0 and f_0 to $K\bar{K}$. Precise measurements of the mixing transitions are therefore important probes of the properties of these two scalar states and can give new insights into their nature [453–460]. Two kinds of mixing intensities ξ_{fa} and ξ_{af} for the $f_0 \rightarrow a_0^0$ and $a_0^0 \rightarrow f_0$ transitions, respectively, are accessible in charmonia decays [458, 460]:

$$\xi_{fa} = \frac{\mathcal{B}[J/\psi \rightarrow \phi(f_0 \rightarrow a_0^0 \rightarrow \eta\pi^0)]}{\mathcal{B}[J/\psi \rightarrow \phi(f_0 \rightarrow \pi\pi)]}, \quad \xi_{af} = \frac{\mathcal{B}[\chi_{c1} \rightarrow \pi^0(a_0^0 \rightarrow f_0 \rightarrow \pi^+\pi^-)]}{\mathcal{B}[\chi_{c1} \rightarrow \pi^0(a_0^0 \rightarrow \pi^0\eta)]}. \quad (140)$$

The branching ratio of the chain $J/\psi \rightarrow \phi f_0(980) \rightarrow \phi a_0^0(980) \rightarrow \phi\eta\pi^0$ is expected to be about $O(10^{-6})$ similar to the estimated total amount from two background reactions: the e.m. transition $J/\psi \rightarrow \gamma^* \rightarrow \phi a_0$ and $J/\psi \rightarrow K^*\bar{K} + c.c. \rightarrow \phi a_0$. However, the peak width from the $a_0(980)$ – $f_0(980)$ mixing is about 8 MeV, much smaller than that from other mechanisms [458].

The two processes were observed for the first time at BESIII and the two mixing parameters were extracted [461]. For $J/\psi \rightarrow \phi\eta\pi^0$ there is a significant electromagnetic contribution and ξ_{fa} is determined

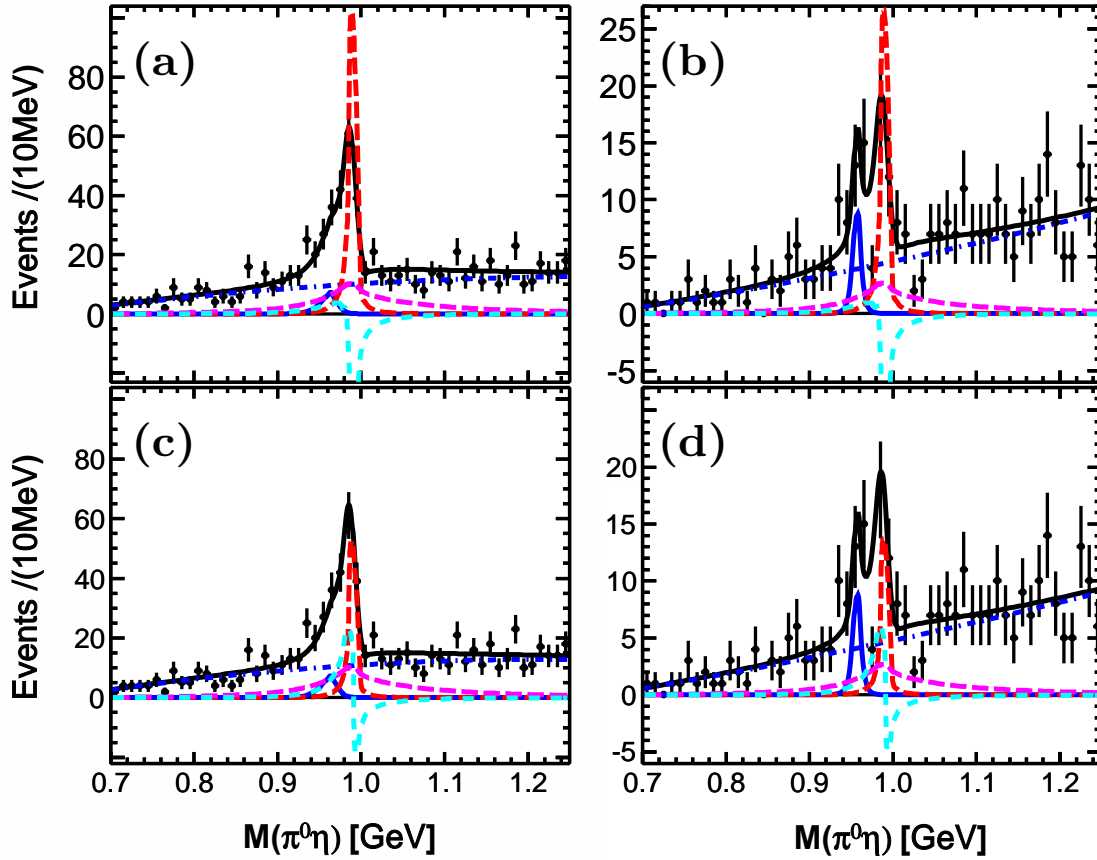


Figure 55: Fits to the $M(\pi^0\eta)$ spectra of the $J/\psi \rightarrow \phi\eta\pi^0$ decay for destructive (upper panels) and constructive (lower panels) interference between e.m. and $a_0 - f_0$ mixing contributions. The η meson is reconstructed via two decay channels: panels (a), (c) are for $\eta \rightarrow \gamma\gamma$ and (b), (d) for $\eta \rightarrow \pi^+\pi^-\pi^0$. The points are data, the (black) solid lines represent the fit result, the (red) dashed curves represent the $a_0 - f_0$ mixing signal, the (pink) dashed lines represent the e.m. processes, the (light-blue) dotted curves represent the interference, the (blue) solid lines show the η' background, and the (blue) dotted–dashed lines represent the continuum background.

from the interference signal observed in the $M(\pi^0\eta)$ distributions shown in Fig. 55. Two solutions are possible: $\xi_{fa} = 0.99(35)\%$ and $\xi_{fa} = 0.41(25)\%$. For $\chi_{c1} \rightarrow \pi^0\pi^+\pi^-$, the electromagnetic contribution is negligible and a signal of 42(7) events is observed, leading to $\xi_{af} = 0.40(17)\%$. In addition one can study the dependence of the mixing parameters ξ_{fa} and ξ_{af} on the recoil mass to ϕ and π^0 , respectively [460]. This allows one to determine bounds on the f_0 and a_0^0 couplings to $K\bar{K}$. The predicted value of the couplings is different for the quark model, multi-quark, and hadronic-molecule scenarios.

3.6.4 Search for isovector strangeonium-like states Z_s

The observation of isovector charmonium-like structures, like $Z_c^{\pm,0}(3900)$ in the $\pi J/\psi$ final states [462–465], has triggered extensive discussions of their nature, including interpretations as tetraquark, molecular, or hadroquarkonium states. This observation challenges also our initial assumption that J/ψ or ϕ act as spectators in the decays discussed in this section. It is possible to conceive a similar Z_s structure, where the $c\bar{c}$ pair is replaced by an $s\bar{s}$ pair. A plausible strategy to search for a Z_s is to use the $\phi(2170) \rightarrow \phi\pi\pi$ decay as the production process and to search for a peak in the $\phi\pi$ system. It is based on the analogy to $Y(4260) \rightarrow Z_c(3900)\pi$ since the $\phi(2170)$ is regarded as the strangeonium equivalent

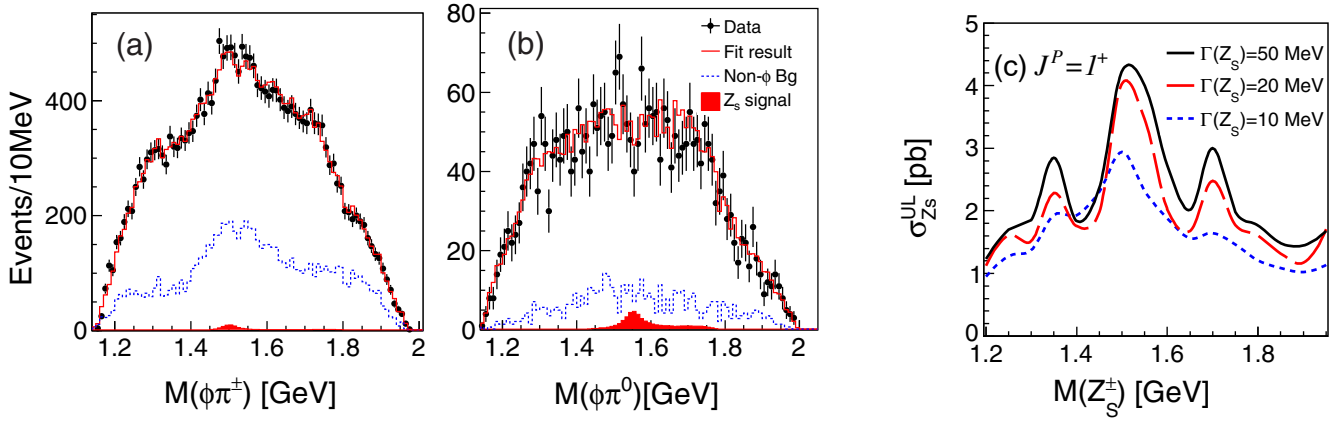


Figure 56: Invariant-mass distribution of the (a) $\phi\pi^\pm$ (b) $\phi\pi^0$ system. Panel (c) shows the determined upper limits for Z_c^\pm assuming $J^P = 1^+$ and different widths.

of the $Y(4260)$. Furthermore, as the narrow $Z_c(3900)$ state is located close to the $D^*\bar{D}$ threshold, the interesting range to search for a Z_s is around the $K^*\bar{K}$ threshold of 1.4 GeV [466], obviously complicated by the fact that the K^* width is nonnegligible.

Using a 108 pb^{-1} data sample taken at the center-of-mass energy of 2.125 GeV, a search for the Z_s in the process $e^+e^- \rightarrow \phi\pi\pi$ was carried out at BESIII [467]. No signal of a narrow Z_s is observed in the $\phi\pi$ invariant-mass spectra shown in Fig. 56(a)–(b). The corresponding upper limits on the Z_s production cross section at the 90% C.L. were determined for different mass and width hypotheses, as shown in Fig. 56(c) for the 1^+ spin-parity assignment. More data is needed to explore lower production cross sections or larger widths of the possible Z_s structure. A complementary analysis path is a complete amplitude analysis of the $J/\psi \rightarrow \phi\pi\pi$ process. Such an analysis is ongoing at BESIII, but the presence of many resonant structures in the $\pi\pi$ mass spectra poses a significant challenge.

3.7 $e^+e^- \rightarrow P_1P_2P_3$

3.7.1 Continuum cross sections

Production of three pseudoscalar mesons via single-photon e^+e^- annihilation for c.m. energies below 2 GeV is dominated by quasi-two-body processes involving a pair of one ground-state pseudoscalar and one vector meson. These processes include $e^+e^- \rightarrow \pi^+\pi^-\pi^0$ (dominated by the $\rho\pi$ intermediate state), $e^+e^- \rightarrow \pi^+\pi^-\eta$ ($\rho\eta$), $e^+e^- \rightarrow K\bar{K}\pi$ ($K\bar{K}^*$), and $e^+e^- \rightarrow K\bar{K}\eta$ (where the cross section is saturated by $\phi\eta$ [361]). They could be described approximately by the methods discussed in Sec. 3.2, using the VMD model of Eq. (114). However, the presence of broad vector resonances (as opposed to ω or ϕ) requires the inclusion of the proper phase space factors, and probably of a more elaborate understanding of the reaction dynamics.

$e^+e^- \rightarrow \pi^+\pi^-\pi^0$ A compilation of the cross section measurements for the most important process $e^+e^- \rightarrow \pi^+\pi^-\pi^0$ process is shown in Fig. 57. The low-energy region is totally dominated by contributions from narrow isoscalar resonances ω and ϕ . Above the ϕ , due to destructive interference with the nonresonant contribution the cross section has a narrow dip, reducing the cross section to almost zero:

$$\sigma(e^+e^- \rightarrow 3\pi)(s) = \frac{4\pi\alpha}{(s)^{3/2}} P_f(s) |\text{BW}_\omega(s) + c_1\text{BW}_\phi(s) + \dots|^2, \quad (141)$$

where $P_f(s)$ is a generalized phase space factor that depends on the final-state interactions in the three-pion system. The data using energy scans is from the SND(VEPP-2M) [469–471], SND(VEPP-

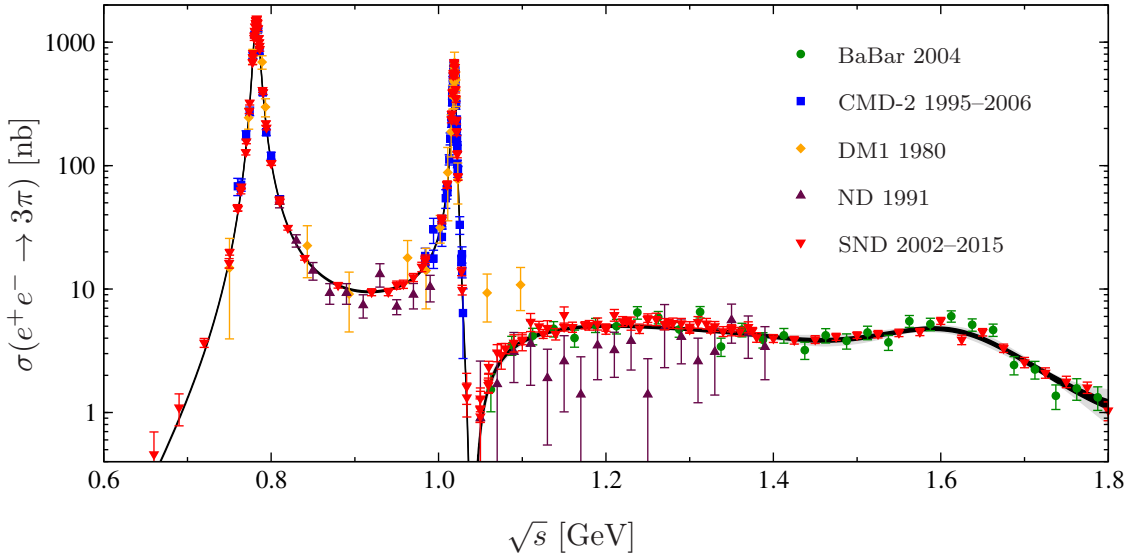


Figure 57: Compilation of $e^+e^- \rightarrow \pi^+\pi^-\pi^0$ data with dispersive $\gamma^* \rightarrow \pi^+\pi^-\pi^0$ amplitude parameterization [468].

2000) [472], and CMD-2 [285,473–475] experiments. For completeness, also earlier data from DM1 [476], DM2 [477], and ND [234] are shown. The ISR method data is from BaBar [478], and most recently from BESIII [479].

The starting point for a more elaborate description of three-pion final-state interactions is a dispersive representation of the $\gamma^* \rightarrow 3\pi$ amplitude $F_{3\pi}(s; s_1, s_2, s_3)$ defined in Eq. (62), which depends both on the two-pion invariant masses s_{1-3} and on the dilepton total energy squared s . The cross section is obtained therefrom via

$$\sigma_{e^+e^- \rightarrow 3\pi}(s) = \alpha^2 \int_{s_1^{\min}}^{s_1^{\max}} ds_1 \int_{s_2^{\min}}^{s_2^{\max}} ds_2 \frac{(s_1 - 4m_\pi^2) \lambda(s, m_\pi^2, s_1) \sin^2 \theta_{s_1}}{768 \pi s^3} |F_{3\pi}(s; s_1, s_2, s_3)|^2; \quad (142)$$

see Ref. [468] for details on the necessary kinematical relations. The amplitude $F_{3\pi}(s; s_1, s_2, s_3)$ has been constructed and studied in detail in the context of the π^0 transition form factor [248–250]. It is decomposed into symmetrized P -wave amplitudes that are calculated in a Khuri–Treiman framework [207], which consistently incorporates arbitrary pairwise rescattering to all orders; see also Sec. 3.7.2 below for additional details. The s -dependence is subsequently parameterized in terms of dispersively improved ω , ϕ , $\omega'(1420)$, and $\omega''(1650)$ resonances, supplemented by a conformal polynomial taking further inelasticities into account. As a side product, resonance pole parameters for ω and ϕ have been extracted from the cross section data fits with improved precision [480].

$e^+e^- \rightarrow \pi^+\pi^-\eta$ Recent results on the $e^+e^- \rightarrow \pi^+\pi^-\eta$ reaction include several Novosibirsk scan measurements: CMD-2 [481] with $\eta \rightarrow \pi^+\pi^-\pi^0$, SND(VEPP-2M) [482] with $\eta \rightarrow \gamma\gamma$, SND(VEPP-2000) with $\eta \rightarrow \gamma\gamma$ [483] and $\eta \rightarrow 3\pi^0$ [484], and CMD-3 with $\eta \rightarrow \gamma\gamma$ [485]. In addition the process was measured using the ISR method at BaBar with $\eta \rightarrow \pi^+\pi^-\pi^0$ [486], $\eta \rightarrow \gamma\gamma$ [487], and $\eta \rightarrow 3\pi^0$ [434]. A compilation of results in Fig. 58(b) shows that the data sets are largely consistent with each other. The energy dependence of the $e^+e^- \rightarrow \eta\pi^+\pi^-$ cross section has been fitted with a VMD model, where the main contribution comes from the $\eta\rho^0(770)$ intermediate state [488], and the total cross section has a large contribution from the $\rho(1450)$. In the narrow-width approximation for the $\rho(770)$, the cross section can be expressed in terms of a transition form factor $F_{\rho\eta}(s)$ for the $\gamma^*\rho\eta$ vertex, in a similar way as discussed in Sec. 3.2. Due to the large width of the ρ meson, the P -wave $\pi^+\pi^-$ two-body phase space has to be integrated out for each $M(\pi^+\pi^-)$ in the range $2m_\pi < M(\pi^+\pi^-) < \sqrt{s} - m_\eta$ [483,488]. A more

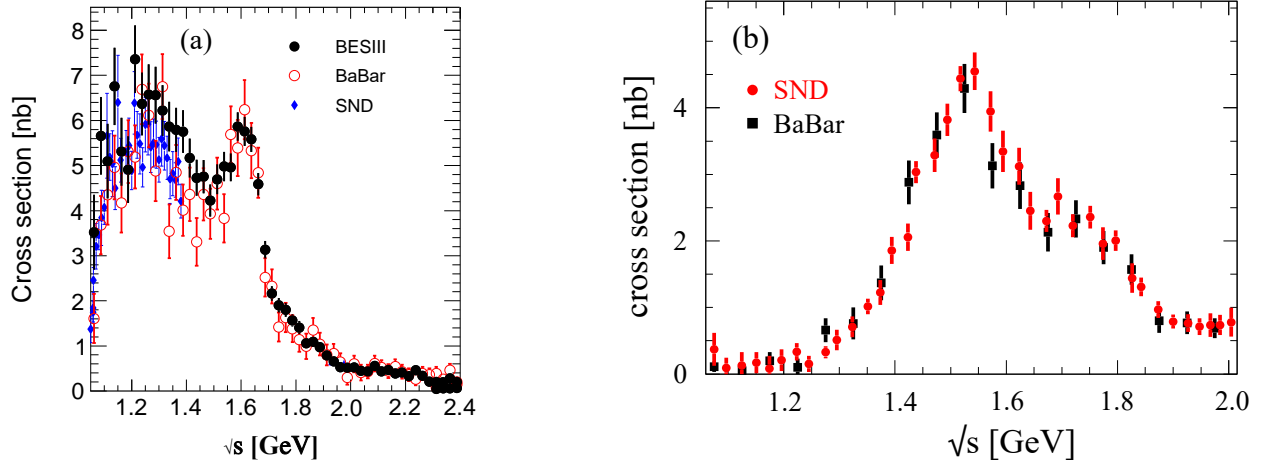


Figure 58: Data on three-pseudoscalar production cross sections in electron-positron annihilation for $\sqrt{s} > 1 \text{ GeV}$: (a) $e^+e^- \rightarrow \pi^0\pi^+\pi^-$ [470, 478, 479], (b) $e^+e^- \rightarrow \eta\pi^+\pi^-$ [484, 486].

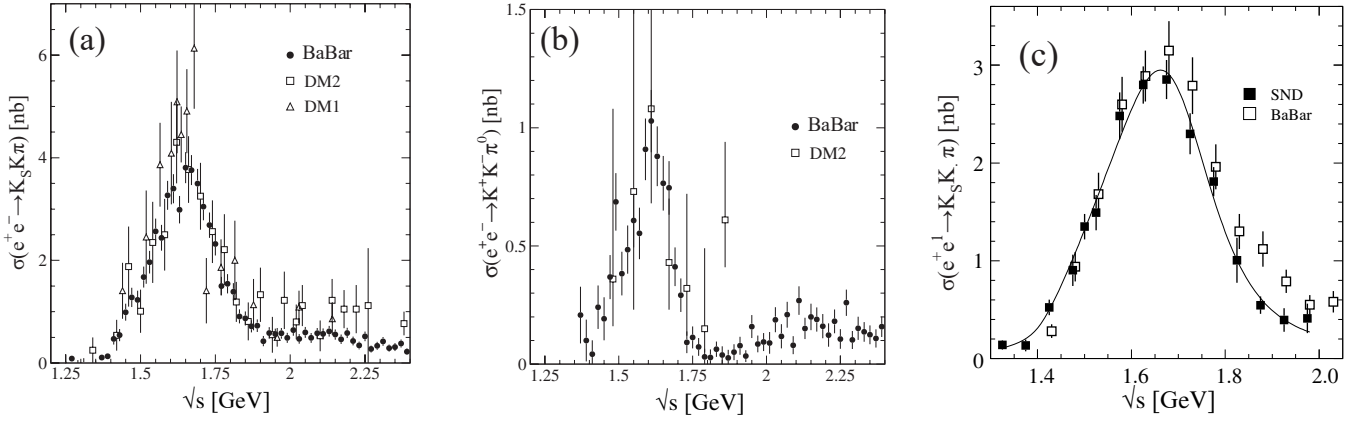


Figure 59: Cross sections of $e^+e^- \rightarrow K\bar{K}\pi$ processes: (a) $K_S K^\pm \pi^\mp$ [361, 495, 496], (b) $K^+ K^- \pi^0$ [361, 496], (c) $K_S K_L \pi^0$ [365, 497].

refined analysis of the $\pi\pi$ invariant-mass distribution and the influence of crossed-channel ($\pi\eta$) dynamics is of high interest [489], in particular with regard to its impact on dispersion-theoretical analyses of the η transition form factor [335, 395, 410]. Theoretical analyses using resonance chiral theory [490, 491] are constrained to isovector vector resonances ($\rho(770)$ and its radial excitations), but contain neither $\pi\eta$ interactions nor nontrivial three-body rescattering effects.

The obtained cross section data has also been used to test the conserved-vector-current hypothesis and make predictions for the corresponding τ decay $\tau^- \rightarrow \pi^- \pi^0 \eta \nu_\tau$ [492, 493]. The latter have similarly been studied in resonance chiral theory [494].

$e^+e^- \rightarrow K\bar{K}\pi$ For $e^+e^- \rightarrow K\bar{K}\pi$, there is data for three charge modes: $K^+K^-\pi^0$, $K_S K^\pm \pi^\mp$, and $e^+e^- \rightarrow K_S K_L \pi^0$. They give sizable contributions to the total annihilation cross section into hadrons in the c.m. range between 1.5 and 1.8 GeV. The processes are also important for the spectroscopy of excited ϕ mesons, since their main decay modes are expected to include kaon pairs. For example, the main decay mode for the $\phi(1680)$ is $K^*(890)\bar{K}$. In the analysis of the two $K\bar{K}\pi^0$ channels, the OZI-suppressed intermediate state $\phi\pi^0$ is analysed separately and we have discussed it in Sec. 3.2.

Measurements of all three channels were performed at BaBar using the ISR technique [361, 365]. In addition, SND at VEPP-2000 has measured the $e^+e^- \rightarrow K_S K_L \pi^0$ cross section by scanning the c.m.

Table 11: Branching fractions of neutral-vector-mesons decays into three pseudoscalar mesons. Unless marked otherwise, the branching fractions are taken from Ref. [48].

	Final state	\mathcal{B}	Ref.
$\omega \rightarrow P_1 P_2 P_3$	$\pi^+ \pi^- \pi^0$	89.3(6)%	
$\phi \rightarrow P_1 P_2 P_3$	$\pi^+ \pi^- \pi^0$	15.24(33)%	
$J/\psi \rightarrow P_1 P_2 P_3$	$\pi^+ \pi^- \pi^0$	2.10(8)%	
	$K^+ K^- \pi^0$	$2.88(12) \times 10^{-3}$	
	$K_S K_L \pi^0$	$2.06(27) \times 10^{-3}$	
	$K_S K^\pm \pi^\mp$	$5.6(5) \times 10^{-3}$	
	$K_S K_L \eta$	$1.44(34) \times 10^{-3}$	
	$\pi^+ \pi^- \eta$	$3.8(7) \times 10^{-4}$	
	$\pi^+ \pi^- \eta'$	$8.1(8) \times 10^{-4}$	[498]
$\psi' \rightarrow P_1 P_2 P_3$	$\pi^+ \pi^- \pi^0$	$2.01(17) \times 10^{-4}$	
	$\pi^+ \pi^- \eta'$	$1.9^{(+1.7)}_{(-1.2)} \times 10^{-5}$	[498]
	$K_S K_L \pi^0$	$< 3.4 \times 10^{-4}$	
	$K_S K_L \eta$	$1.3(5) \times 10^{-3}$	
	$K^+ K^- \pi^0$	$4.07(31) \times 10^{-5}$	
	$\pi^+ \pi^- (\rho) \eta$	$2.2(6) \times 10^{-4}$	

energy range $\sqrt{s} = 1.3\text{--}2.0$ GeV [497]. The results for the three channels are shown in Fig. 59. The cross sections are dominated by $K^*(892)\bar{K}$ intermediate states. The fraction of the $\phi\pi^0$ contribution in the neutral-pion channels at 1.7 GeV is about 1% [361].

3.7.2 Dynamics of three-pion final states

The decay distributions of three-pseudoscalar-meson decays of the narrow isoscalar vector mesons ω , ϕ , J/ψ , ψ' are particularly apt to study the dynamics of the final-state interactions in detail and with high precision, most prominently three-pion final states. An overview of the corresponding branching fractions is given in Table 11.

The matrix element of a vector meson decay into three pions $V(\varepsilon^\mu) \rightarrow \pi^+(q_+)\pi^-(q_-)\pi^0(q_0)$ can be written in exactly the same form as the three-pion hadronic current in Eq. (62),

$$\mathcal{M}(s, t, u) = \epsilon_{\mu\nu\alpha\beta} \varepsilon^\mu q_+^\nu q_-^\alpha q_0^\beta \mathcal{F}(s, t, u). \quad (143)$$

The matrix element squared of the $e^+e^- \rightarrow V \rightarrow \pi^+\pi^-\pi^0$ process can be represented as a product of the P -wave phase space $\mathcal{P}(s, t, u)$ (see, e.g., Refs. [102, 353, 499]) and the squared modulus of the scalar function $\mathcal{F}(s, t, u)$,

$$\sum_{\lambda=\pm 1} |\mathcal{M}_\lambda|^2 \propto \mathcal{P} |\mathcal{F}(s, t, u)|^2, \quad (144)$$

where λ is the helicity of the vector meson V , restricted in e^+e^- annihilations to $\lambda = \pm 1$. The \mathcal{P} term vanishes at the Dalitz plot boundary [500]. It can also account for kinematic isospin violation due to

the difference between the masses of the uncharged and charged pions. The scalar function $\mathcal{F}(s, t, u)$ can be decomposed into series of odd partial waves only, and is hence entirely dominated by P -waves. Neglecting F - and higher waves (or, more precisely, the discontinuities therein), it can be written as a sum of so-called single-variable functions, which themselves are free of cuts from crossed channels [102]:

$$\mathcal{F}(s, t, u) = \mathcal{F}(s) + \mathcal{F}(t) + \mathcal{F}(u). \quad (145)$$

The P -wave projection $f_1(s)$ in, e.g., the s -channel is hence given by the sum of two terms,

$$f_1(s) = \mathcal{F}(s) + \hat{\mathcal{F}}(s), \quad (146)$$

where the second term is due to the projection of $\mathcal{F}(t) + \mathcal{F}(u)$ onto the s -channel P -wave and contains the left-hand cuts in $f_1(s)$. The separation of right- and left-hand cuts in Eq. (146) allows us to translate a Watson-like unitarity relation for the partial wave into a discontinuity equation for the single-variable function,

$$\text{disc } \mathcal{F}(s) = 2i \left(\mathcal{F}(s) + \hat{\mathcal{F}}(s) \right) \theta(s - 4m_\pi^2) \sin \delta_1^1(s) \exp \{ -i\delta_1^1(s) \}. \quad (147)$$

In the absence of the so-called inhomogeneity $\hat{\mathcal{F}}(s)$, Eq. (147) is solved simply in terms of an Omnès function calculated from the $\pi\pi$ P -wave phase shift $\delta_1^1(s)$. The inclusion of the crossed-channel effects is interpreted intuitively as the inclusion of all pairwise rescattering effects in the final state. The solution has the form of so-called Khuri–Treiman equations [207], and their concrete form for the system (145) has by now been discussed in the literature many times [102, 353, 354, 501–503].

$\omega \rightarrow \pi^+\pi^-\pi^0$ Back in 1961, the ω meson’s spin and parity were determined by observing that the Dalitz plot of the main decay mode $\omega \rightarrow \pi^+\pi^-\pi^0$ is consistent with a P -wave phase space distribution [82]. This is a very good approximation due to the limited phase space volume for the three pions. Only recently, precision Dalitz plot analyses have shown there is a deviation from the P -wave phase space distribution [504, 505]. Given the small decay region and the lack of resonances within the kinematic limits, the deviation from P -wave phase space $|\mathcal{F}(s, t, u)|^2$ can be parameterized, in the isospin limit, using an expansion about the center of the Dalitz plot in the z and ϕ variables [102]:

$$|\mathcal{F}|^2 = \mathcal{N} \left(1 + 2\alpha z + 2\beta z^{3/2} \sin 3\phi + 2\gamma z^2 + \mathcal{O}(z^{5/2}) \right), \quad (148)$$

where α (quadratic slope parameter), β , and γ are Dalitz plot parameters. The WASA-at-COSY experiment using ω mesons produced in hadronic processes [504] has found the Dalitz plot consistent with $\alpha = 147(36) \times 10^{-3}$ and the remaining parameters equal to zero. The most precise study is from BESIII, using 2.6×10^5 $\omega \rightarrow \pi^+\pi^-\pi^0$ events tagged by the $J/\psi \rightarrow \omega\eta$ decay [505]. In the best fit, $\alpha = 120(8) \times 10^{-3}$ and there is evidence for the next term in the expansion Eq. (148) with $\beta = 29(10) \times 10^{-3}$.

The process is important as a cross check of three-body dispersive calculations using pion–pion phase shifts. In the absence of available Dalitz plot data at the time, Refs. [102, 353] employed a single subtraction constant in their amplitude representation, which amounts to an overall normalization and hence can be fixed from the partial width; the energy dependence of the Dalitz plot is then a parameter-free prediction. The BESIII result is consistent with dispersive calculations without crossed-channel rescattering: $\alpha = (125 \dots 135) \times 10^{-3}$, $\beta = (29 \dots 33) \times 10^{-3}$ [102] and $\alpha = 125 \times 10^{-3}$, $\beta = 30 \times 10^{-3}$ [353]. However, there seems to be tension when the full calculations including the effect of crossed-channel rescattering are compared to: $\alpha = (74 \dots 84) \times 10^{-3}$, $\beta = (24 \dots 28) \times 10^{-3}$ [102] and $\alpha = 84 \times 10^{-3}$, $\beta = 28 \times 10^{-3}$ [353]. Thus, the investigation of this decay’s dynamics with higher precision by analyzing the full J/ψ data sample of 10 billion events at BESIII is expected to clarify this issue.

As a consequence, a recent update has demonstrated that the experimental Dalitz plot parameters can be reproduced with a second (complex) subtraction constant, at the expense of reducing the high predictive power of the original formulation [354]. The projections on z and ϕ axes of the Dalitz plot density are shown and compared to the fit results and to P -wave phase space in Fig. 60.

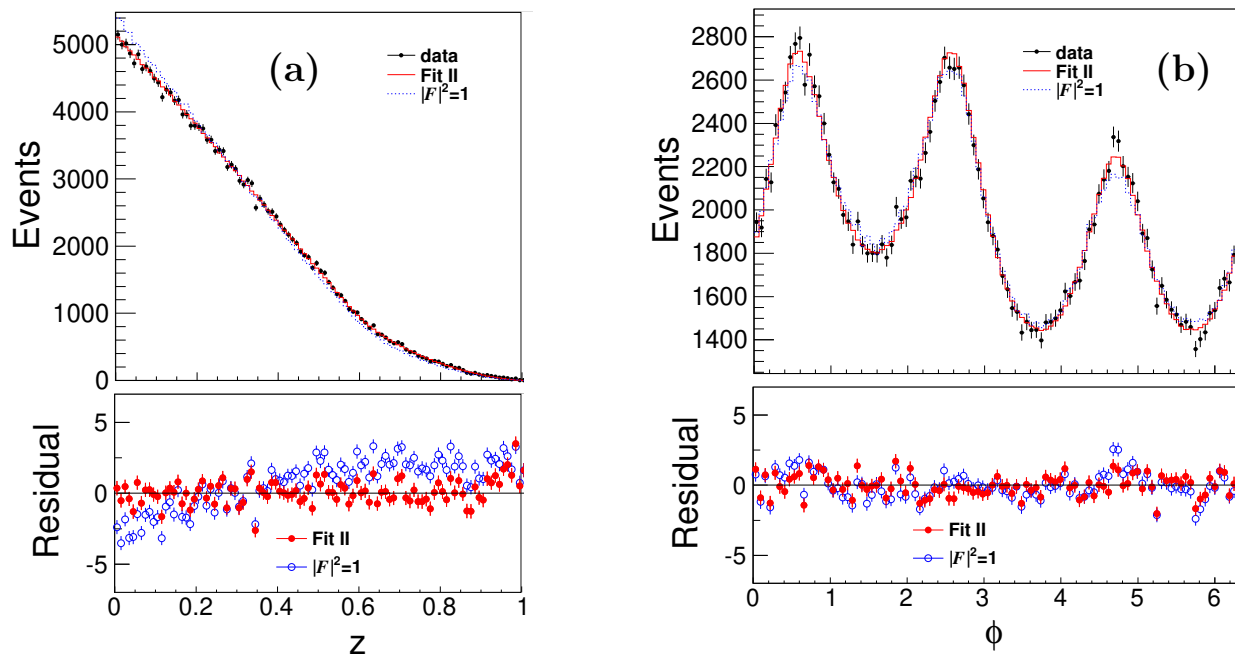


Figure 60: BESIII data on $\omega \rightarrow \pi^+\pi^-\pi^0$ compared to the best fit and the P -wave phase space for: (a) z and (b) ϕ distributions. The black points with error bars in the upper panels are data, the solid line is the fit, the dashed line the P -wave. The solid and hollow dots in the lower panels denote the residuals for the fit and the P -wave, respectively.

$\phi \rightarrow \pi^+\pi^-\pi^0$ The three-pion decay of the ϕ is one of its main decay modes despite OZI-rule suppression. Two amplitude analyses were performed by the CMD2 experiment: the first using 10790(110) events [474] and the second 78780(280) [475]. The most precise data on $\phi \rightarrow \pi^+\pi^-\pi^0$ is from KLOE [373], using 1.98×10^6 selected events. A theoretical fit of the Dalitz plot, divided by the phase space, is shown in Fig. 61, where bands due to the $\rho\pi$ intermediate states are clearly visible.

The description of the decay within the isobar model uses $\mathcal{F}(t)$ and $\mathcal{F}(u)$ as BW_ρ^{GS} or BW_ρ^{KS} form factors. For $\mathcal{F}(s)$, where $\rho^0\text{-}\omega$ mixing is expected, a $\text{BW}_{\rho+\omega}^{GS}$ form should be used to describe the precision data.⁴ In addition, a contact term has to be introduced, representing a direct coupling or an effect of a higher-mass ρ resonance like the $\rho(1450)$, which is outside the kinematic decay range. The use of a contact term (or the simple addition of a heavier resonance) without subsequent rescattering violates the universality of final-state interactions and should hence be discarded from a theoretical point of view.

The dispersive description of $\phi \rightarrow 3\pi$ is formally identical to the one of $\omega \rightarrow 3\pi$ discussed above, the only change being the mass of the decaying vector state. Interestingly enough, the nontrivial rescattering effects beyond the simple $\rho\pi$ picture do depend on the decay mass, and vary with it. It is observed that here, rescattering effects significantly improve on the KLOE Dalitz plot description [102]: the contact term employed in the model fit can be understood as an effective replacement of the final-state interactions that are incorporated in the Khuri–Treiman amplitudes, but omitted in the Breit–Wigner-type isobar model. To achieve a perfect fit of the high-statistics data, a second subtraction constant was used, which however only induced a very minor change in the Dalitz plot, in contrast to what seems to be required for $\omega \rightarrow 3\pi$ [354, 505].

⁴The ω features as a background effect via $e^+e^- \rightarrow \omega\pi^0$, with subsequent, isospin-violating, decay $\omega \rightarrow \pi^+\pi^-$, and does not necessarily appear as an actual decay product of the ϕ , which would be doubly isospin-suppressed.

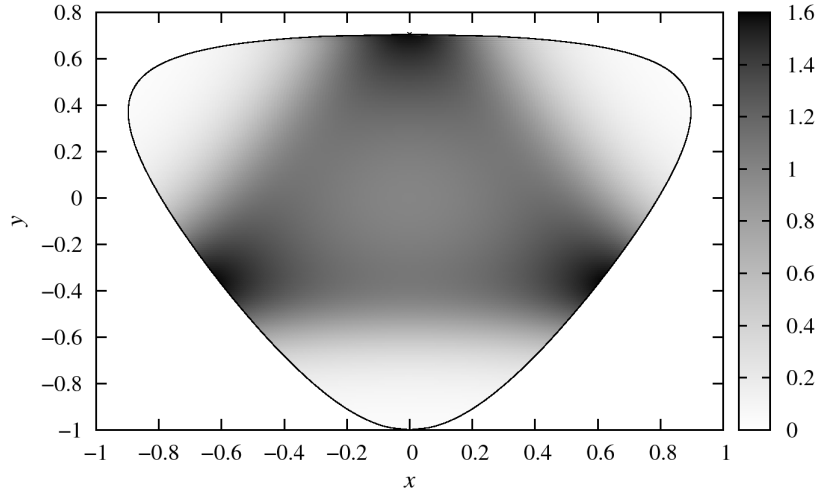


Figure 61: Dalitz plot distribution for $\phi \rightarrow \pi^+\pi^-\pi^0$ divided by P -wave phase space [102]. Three broad bands corresponding to the three ρ states are seen. The kinematical boundary is also shown.

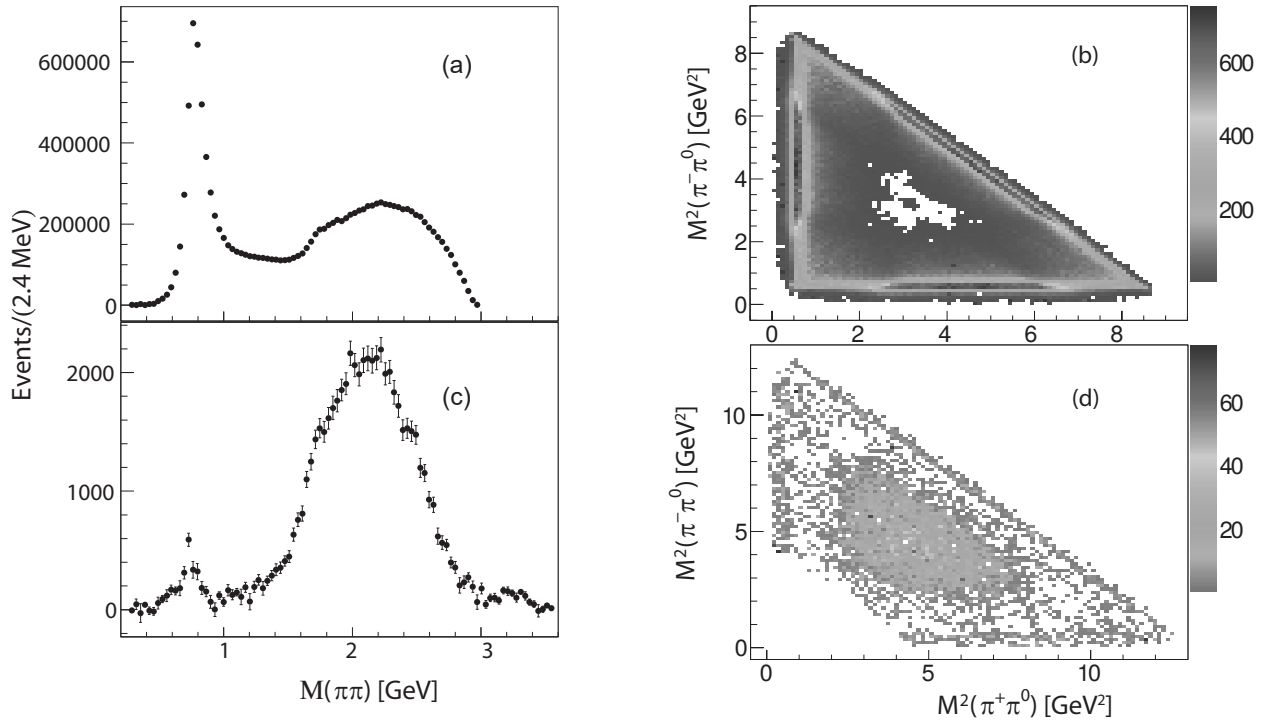


Figure 62: Results on three-pion decays of J/ψ and ψ' from BESIII [506]. Invariant-mass distributions $M(\pi\pi)$ (a) and (c) and Dalitz plots (b) and (d) with backgrounds subtracted and corrected for efficiency. The top and bottom panels are for the $J/\psi \rightarrow \pi^+\pi^-\pi^0$ and $\psi' \rightarrow \pi^+\pi^-\pi^0$ decays, respectively.

$J/\psi, \psi' \rightarrow \pi^+\pi^-\pi^0$ It is instructive to also consider and compare the three-pion decays of the vector charmonia. The decay $J/\psi \rightarrow \pi^+\pi^-\pi^0$, despite its huge phase space in principle allowing for the production of many ρ excited states, is entirely dominated by the $\rho(770)\pi$ intermediate state, see Fig. 62(b), with almost no events in the center of the Dalitz plot. The situation changes dramatically for the ψ' decay: the partial decay width of $\psi' \rightarrow \pi^+\pi^-\pi^0$ is only 3% of $J/\psi \rightarrow \pi^+\pi^-\pi^0$, and the Dalitz plot distribution is completely different; see Fig. 62(d). Here, the fraction of $\rho(770)\pi$ events is

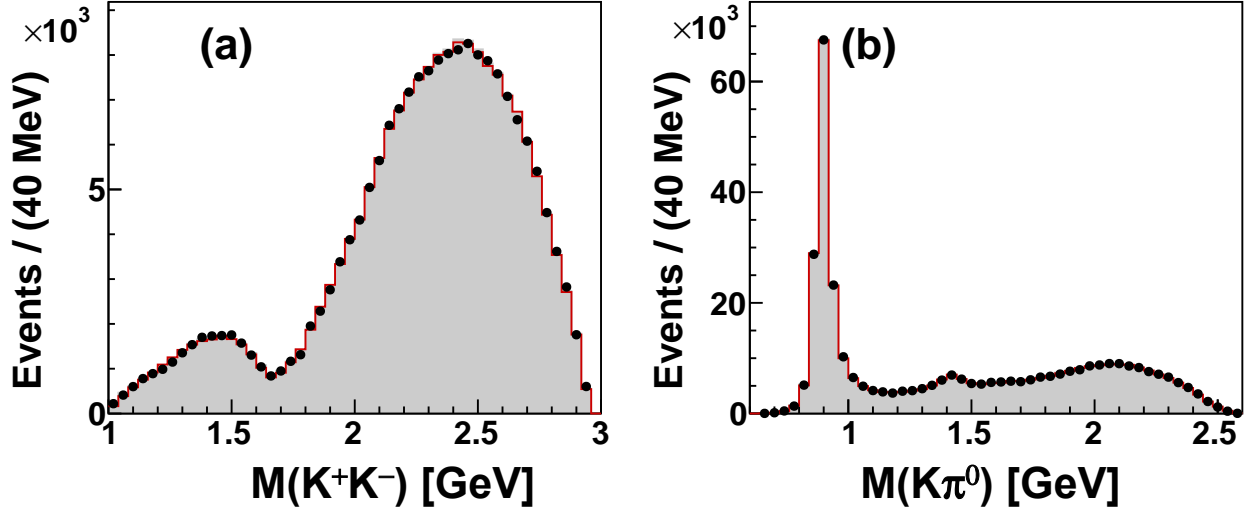


Figure 63: Invariant mass of the K^+K^- (a) and $K^\pm\pi^0$ (b) systems for $J/\psi \rightarrow K^+K^-\pi^0$ from BESIII [511] compared to two PWA solutions PWA solution I (shaded histograms) and the PWA solution II (solid line).

suppressed and pions are often produced with equal energies, populating the center of the Dalitz plot. This effect is known as the “ $\rho\pi$ puzzle,” which is difficult to explain.

Partial-wave analyses of both decays might shed some light on the puzzle. For $J/\psi \rightarrow \pi^+\pi^-\pi^0$, in addition to the BESIII data shown in Fig. 62 there is an amplitude analysis from BaBar using 19560(160) $J/\psi \rightarrow \pi^+\pi^-\pi^0$ events [507]. The isobar model analysis for J/ψ indicates a contribution of the $\rho(1450)\pi$ intermediate state (ca. 10%), which interferes destructively with the main $\rho(770)\pi$ contribution. An alternative is that $\rho(1450)\pi$ represents an effective contribution of excited ρ resonances as expected in the Veneziano model [508]. The $\psi' \rightarrow \pi^+\pi^-\pi^0$ Dalitz plot analysis was performed by BESII [509]. Here, the main contribution is from the $\rho(2150)$ resonance, where the mass and the width were fixed to 2.149 GeV and 363 MeV, respectively. The $\rho(770)\pi$ contribution is only 28%.

$J/\psi \rightarrow K\bar{K}\pi$ Amplitudes of the decays $J/\psi \rightarrow K^+K^-\pi^0$ and $J/\psi \rightarrow K_S^0K^\pm\pi^\mp$ have been studied at BES and BaBar. The processes are dominated by $K^*(892)\bar{K}$ and $K_2^*(1430)\bar{K}$ intermediate states. However, in 2005 BESII observed a broad structure in the K^+K^- invariant mass in $J/\psi \rightarrow K^+K^-\pi^0$ [510], dubbed $X(1575)$, using a data sample of 1000(100) events. The J/ψ decays to strangeonium states plus π^0 are doubly OZI suppressed and the branching fractions should be very small, e.g., $\mathcal{B}(J/\psi \rightarrow \phi\pi^0) < 10^{-5}$. Therefore the broad $X(1570)$ state triggered speculations on its nature, including multi-quark states and the interference between $\rho(1450)$ and $\rho(1700)$. Subsequently the Dalitz plot analysis using 2002(48) events performed by BaBar [507] attributed the broad structure to the presence of the $\rho(1450)$.

The most recent partial-wave analysis of the decay $J/\psi \rightarrow K^+K^-\pi^0$ has been performed at BESIII [511], using 181550(430) signal events. The invariant-mass distribution of both the K^+K^- and the $K^\pm\pi^0$ systems are shown in Fig. 63. In addition to the dominant $K^*(892)^\pm K^\mp$ and $K_2^*(1430)^\pm K^\mp$ channels, small contributions from $K_2^*(1980)^\pm K^\mp$ and $K_4^*(2045)^\pm K^\mp$ are also necessary to provide a good description of the data. The broad structure clearly observed in the K^+K^- mass spectrum cannot be described with a single state. The PWA solution cannot be saturated with the well-known states included as Breit–Wigner resonances and constant contributions in the lowest partial waves. At the same time, the “missing part” of the PWA solution cannot be reliably attributed to a single resonance and mainly manifests itself as a slowly changing background in the $J^{PC} = 3^{--}$ partial wave of the $K^\pm\pi^0$ pairs at high $K^\pm\pi^0$ masses.

Two solutions constructed with and without the smooth contribution in this partial wave were provided to demonstrate that the conclusions of this analysis are not strongly affected by the assumptions on the “missing part” of the PWA solution. For the first solution, one contribution is from a vector structure with $M = 1643(3)$ MeV and $\Gamma = 167(12)$ MeV as indicated in the Dalitz plot, which could be attributed to the $\rho(1700)$ or the $\omega(1650)$. The second contribution that can be reliably identified is a vector resonance with a mass of $2078(6)$ MeV and width of $149(21)$ MeV. However, to describe the data additional contributions are necessary. Tests including contributions from $\rho(770)$, $\rho_3(1690)$, $\rho(1450)$, as well as a smooth background in the $J^{PC} = 1^{--} K^+K^-$ partial wave, are all found to be significant.

For the second solution, a striking feature is the presence of a nonresonance component in the $J^P = 3^- K\pi^0$ partial waves, which cannot be clearly interpreted as an interference between Breit–Wigner states. A possible interpretation is that this component is the manifestation of nonresolved contributions present in the F -wave $K\pi$ scattering amplitude [114]. This may include the presence of several resonances, nonresonant production, and final-state particle rescattering effects. In this case, two $J^{PC} = 1^{--}$ states around 1.65 GeV and 2.04 GeV were introduced to describe the enhancement at low $M(K^+K^-)$ mass. The first state may be the 3D_1 isovector ground state, but at the same time its mass, width, and small relative contribution to the decay are reasonably consistent with the $\omega(1650)$ produced in J/ψ decays through a virtual photon. The second state can be interpreted as the $\rho(2150)$ or as another isovector vector state.

3.8 Other $J/\psi \rightarrow \gamma X$ and $J/\psi \rightarrow VX$ reactions

In this section, we discuss extensions of the methods for studies of the two-pseudoscalar-meson system X in $J/\psi \rightarrow \gamma X$ and $J/\psi \rightarrow VX$ presented in Secs. 3.3 and 3.6 to final states involving more particles. In the first place, the system X can decay to three pseudoscalar mesons. In radiative decays of J/ψ to three (and more) pseudoscalar mesons, hadronic systems X with $C = +1$ and a variety of J and P quantum numbers can be studied. For example, for $\pi^+\pi^-\eta$ all J^P values are possible: $0^-, 1^+, 1^-, 2^+, 2^-$, etc. An additional motivation for the studies of J/ψ radiative decays is the large fraction of two-gluon processes $J/\psi \rightarrow \gamma gg$, estimated to be 8(1)% [48]. They are therefore considered as promising modes to search for glueballs [512].

3.8.1 Observation and properties of the $X(1835)$ state

$J/\psi \rightarrow \gamma\pi^+\pi^-\eta'$ In 2005, the BESII experiment observed a structure in the invariant mass of the $\pi^+\pi^-\eta'$ system $M(\pi^+\pi^-\eta')$ produced in J/ψ radiative decay closely below nucleon–antinucleon threshold [513], see Fig. 64(a). This allows one to speculate about a relation to the threshold enhancement in radiative J/ψ decays to a $J^P = 0^+ p\bar{p}$ pair, observed by BESII in 2003 [228] and subsequently confirmed by BESIII [514]. This interesting structure, called $X(1835)$, attracted many theoretical interpretations, including a $p\bar{p}$ bound state, a glueball, a radial excitation of the η' meson, etc. [515–519].

Three structures, $X(1835)$, $X(2120)$, and $X(2370)$, were observed by the BESII and BESIII experiments in the invariant mass of the $\pi^+\pi^-\eta'$ system produced in J/ψ radiative decays [513, 520], see Fig. 64(b). The $X(1835)$ is probably the most interesting among those, due to its possible connection to the $p\bar{p}$ threshold, with many experimental findings pointing to this connection. The new BESIII analysis using 2012 data clearly shows that the shape of the $X(1835)$ is sharply affected by the $p\bar{p}$ threshold, see Fig. 64(c) [521]. The spin-parity of $X(1835)$ of $J^P = 0^+$ was determined by an amplitude analysis of the J/ψ radiative decay to $\eta K_S K_S$ [522]. Moreover, no evidence of the $X(1835)$ is found in $J/\psi \rightarrow \omega\eta'\pi^+\pi^-$ [523]. The state is observed in $J/\psi \rightarrow \gamma\gamma\phi$ together with the $\eta(1475)$ [524], indicating a sizable $s\bar{s}$ component.

The two higher-mass X structures were studied in the decay $J/\psi \rightarrow \gamma K\bar{K}\eta'$. The higher-mass state $X(2370)$ was found with statistical significance of 8.3σ [525]. In addition, the 90% C.L. upper limit for

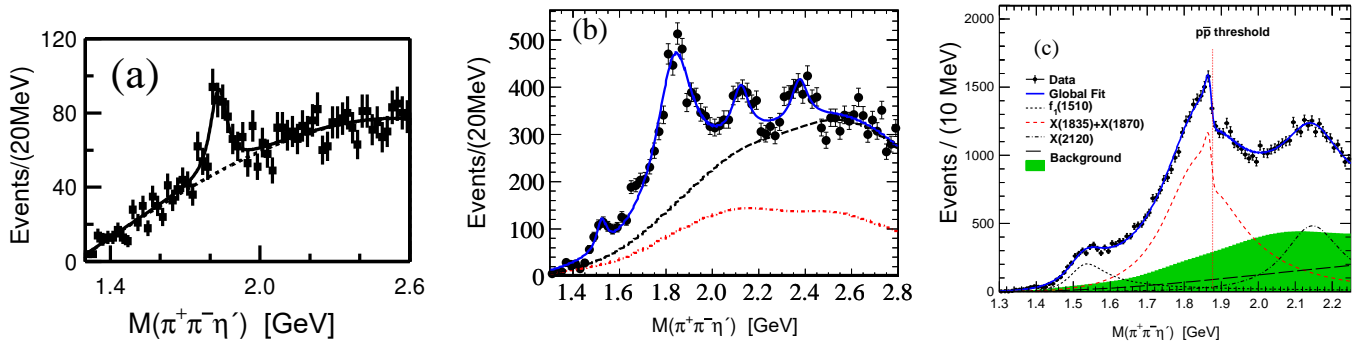


Figure 64: $X(1835)$ and other structures observed in the invariant mass of the $\pi^+\pi^-\eta'$ system $M(\pi^+\pi^-\eta')$ produced in J/ψ radiative decays. (a) First observation at BESII [513]; (b) BESIII 2009 data [520]; (c) BESIII 2009 and 2012 data [521].

the branching ratio of the decay chain $J/\psi \rightarrow \gamma X(2120) \rightarrow \gamma K \bar{K} \eta'$ was set at the 10^{-5} level.

The huge number of the accumulated J/ψ events allows BESIII to perform much more detailed studies of the $X(1835)$ and the other structures to understand their nature. Two decay modes of the η' , $\eta' \rightarrow \pi^+\pi^-\gamma$ and $\eta' \rightarrow \pi^+\pi^-\eta$, are used to reconstruct the η' , which helps to cross-check the measurement as well as to improve on the statistical precision. Figure 64 shows the $\pi^+\pi^-\eta'$ invariant-mass spectrum for the two η' decay modes combined. The $X(1835)$ structure with a width of $190(40)$ MeV is seen [520], cf. Fig. 64(b). In addition a little peak corresponding to the $f_1(1510)$ and two other unknown structures $X(2120)$ and $X(2370)$ are observed. The masses and widths of these states are for the $X(1835)$ $M = 1836(6)$ MeV, $\Gamma = 190(49)$ MeV; for the $X(2120)$ $M = 2122(8)$ MeV, $\Gamma = 83(35)$ MeV; and for the $X(2370)$ $M = 2376(10)$ MeV, $\Gamma = 83(47)$ MeV.

However, an anomalous shape of the structure around 1.85 GeV was observed in the $\pi^+\pi^-\eta'$ mass spectrum [521] that cannot be accommodated by an ordinary Breit–Wigner resonance function. Two example models for such a line shape are used to describe the data. The first model assumes the state couples to $p\bar{p}$ and the distortion reflects the opening of the $p\bar{p}$ decay channel. The fit result for this model yields a strong coupling between the broad structure and $p\bar{p}$. The pole nearest to the $p\bar{p}$ mass threshold of this state is located at $M_{\text{pole}} = 1909(19)$ MeV and $\Gamma_{\text{pole}} = 273(40)$ MeV. The second model assumes that the distortion reflects interference between the $X(1835)$ and another resonance with mass close to the $p\bar{p}$ mass threshold. A fit with this model uses a coherent sum of two interfering Breit–Wigner amplitudes and yields a narrow resonance below the $p\bar{p}$ mass threshold with $M = 1870(3)$ MeV and $\Gamma = 13.0(67)$ MeV. With present accuracy, both models fit the data well and both suggest the existence of a new state: either a broad one with strong couplings to $p\bar{p}$, or a narrow one just below the $p\bar{p}$ mass threshold. For the broad state above the $p\bar{p}$ mass threshold, its strong couplings to $p\bar{p}$ suggests the existence of a $p\bar{p}$ molecule-like state. On the other hand the narrow width of the state just below $p\bar{p}$ mass threshold suggests an unconventional meson, most likely a $p\bar{p}$ bound state. In order to further elucidate the nature of the states around 1.85 GeV, more data is needed to further study the $J/\psi \rightarrow \gamma \eta' \pi^+ \pi^-$ process together with an analysis of line shapes for other J/ψ decays near the $p\bar{p}$ mass threshold, including $J/\psi \rightarrow \gamma p\bar{p}$ and $J/\psi \rightarrow \gamma \eta K_S^0 K_S^0$ reactions.

$J/\psi \rightarrow \gamma K_S^0 K_S^0 \eta$ Further studies of the structures observed in $\pi^+\pi^-\eta'$ include searches for other decay modes like $K_S K_S \eta$. A BESIII study of $J/\psi \rightarrow \gamma K_S K_S \eta$ [522] with invariant masses $M(K_S K_S)$ in the $f_0(980)$ mass region, $M(K_S K_S) < 1.1$ GeV, a structure around 1.85 GeV is clearly seen, cf. Fig. 65(a). The performed partial-wave analysis allows one to determine the spin and parity to be $J^{PC} = 0^{-+}$ (pseudoscalar), the same as the $X(p\bar{p})$ structure [514]. The mass and width are $1844(22)$ MeV and $192(56)$ MeV, respectively, consistent with the $J/\psi \rightarrow \gamma \pi^+ \pi^- \eta'$ results.

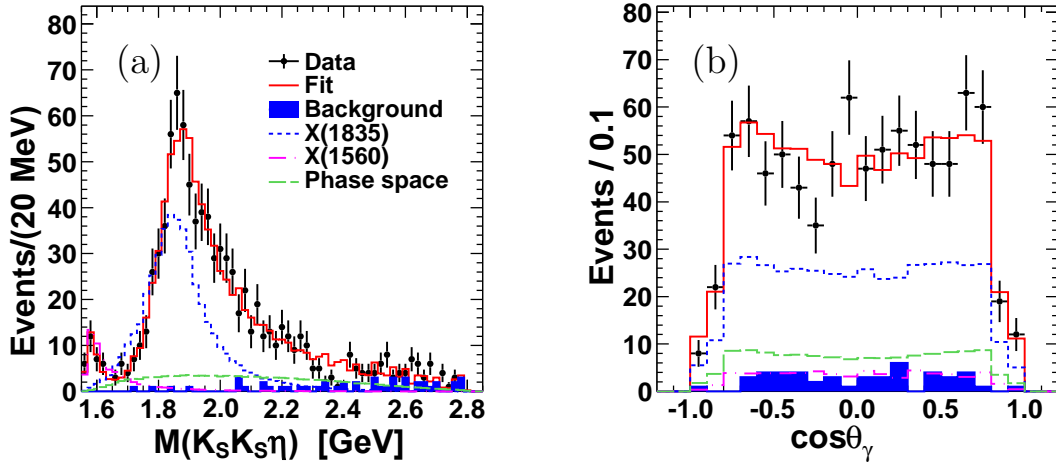


Figure 65: (a) $K_S K_S \eta$ invariant-mass spectrum for $J/\psi \rightarrow \gamma K_S^0 K_S^0 \eta$ events from BESIII with the requirement $M(K_S K_S) < 1.1$ GeV and (b) the angular distribution of the photon.

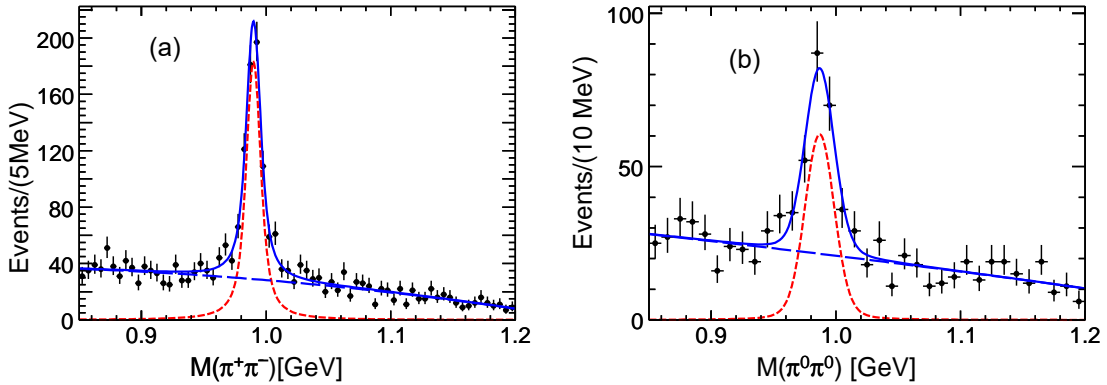


Figure 66: The $\pi^+\pi^-$ (a) and $\pi^0\pi^0$ (b) invariant-mass spectra with the $\pi^+\pi^-\pi^0$ and $3\pi^0$ systems in the $\eta(1405)$ mass region, respectively. The dotted curves are the $f_0(980)$ signals, while the dashed curves denote the background.

3.8.2 $J/\psi \rightarrow \gamma\pi^+\pi^-\pi^0(3\pi^0)$

Analyses of $J/\psi \rightarrow \gamma\pi^+\pi^-\pi^0$ and $J/\psi \rightarrow \gamma 3\pi^0$ at BESIII [526] can be used to study $\eta(1405) \rightarrow f_0(980)\pi^0$ with isospin violation. The apparent signatures of this $\eta(1405)$ decay mode in the final states are shown in Fig. 66. The ratio of $\mathcal{B}(\eta(1405) \rightarrow f_0(980)\pi^0 \rightarrow \pi^+\pi^-\pi^0)$ determined from this measurement to $\mathcal{B}(\eta(1405) \rightarrow a_0^0(980)\pi^0 \rightarrow \eta\pi^0\pi^0)$ [48] is 17.9(4.2)%, which is one order of magnitude larger than the $a_0^0(980) - f_0(980)$ mixing intensity (less than 1%) determined at BESIII previously [527]. In addition, the measured width of the $f_0(980)$ observed in the dipion mass spectra is anomalously narrow, 9 MeV, compared to the world average. There is also evidence for an enhancement around 1.3 GeV (likely from the $f_1(1285)$ or the $\eta(1295)$) in the charged mode.

3.9 Strong three-body decays of nonvector states

Nonvector states cannot be directly produced in e^+e^- collisions via single-photon processes,⁵ but as discussed in Sec. 2.2.2, they are abundantly produced in ϕ , J/ψ , and ψ' decays. The decays of η , η' , η_c ,

⁵Production via two-photon intermediate states is obviously strongly suppressed, but has been searched for, e.g., at the Novosibirsk experiments to put upper limits on $e^+e^- \rightarrow \eta'(958)$ [528, 529] or to establish the reaction $e^+e^- \rightarrow f_1(1285)$ [530].

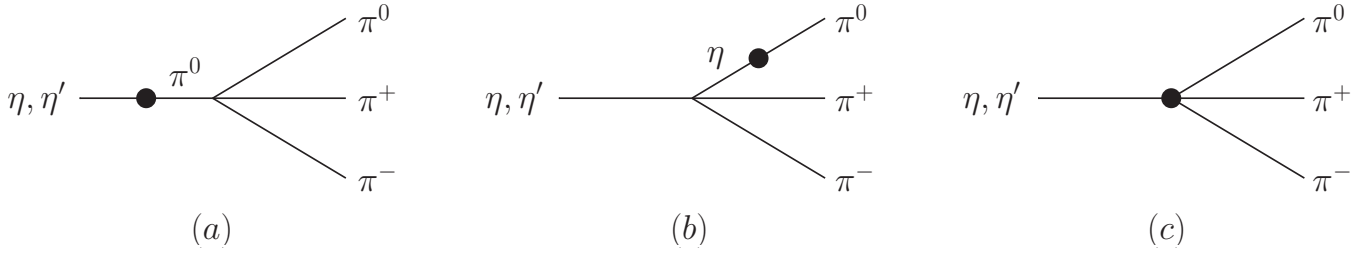


Figure 67: The isospin-violating decay $\eta^{(\prime)} \rightarrow \pi^+\pi^-\pi^0$ in leading-order ChPT (or current algebra) [538]: (a)+(b) $\eta^{(\prime)}-\pi^0$ mixing, (c) contact term.

χ_{cJ} ($J^{PC} = J^{++}$), and h_c ($J^{PC} = 1^{+-}$) into three pseudoscalars allow us to study the interactions in the configurations corresponding to the quantum numbers of the initial states. The special cases are those of η and η' decays, which only involve the pseudoscalar nonet. In the case of the η_c , the large decay width 32.0(7) MeV presents certain challenges for amplitude analyses: depending on the decay mode there may be significant contributions from interference with the nonresonant $J/\psi \rightarrow \gamma X$ decays to the identical final states [531–533]. Therefore a viable alternative, where the η_c is produced in two-photon processes, is discussed in this section.

$\eta \rightarrow 3\pi$ The η meson decays into three pions ($\eta \rightarrow \pi^+\pi^-\pi^0$ and $\eta \rightarrow 3\pi^0$) are two of the main decay modes (the branching ratios are 32.7% and 22.9%, respectively). They are isospin-violating decays; since the electromagnetic contribution is suppressed [534–537], the decay mechanism is instead driven by the light quark mass difference $m_u - m_d$. The lowest-order contributions [538] to the decay are shown in Fig. 67. The resulting decay amplitude for $\eta \rightarrow \pi^+\pi^-\pi^0$, $\mathcal{A}_c(s, t, u)$, is a linear function of the Mandelstam variable $s = (p_{\pi^+} + p_{\pi^-})^2$ in LO ChPT [538–540],

$$\mathcal{A}_c(s, t, u) = \mathcal{A}_c(x, y) \propto \frac{3s - 4m_\pi^2}{m_\eta^2 - m_\pi^2} = 1 - \frac{2m_\eta(m_\eta - 3m_\pi)}{m_\eta^2 - m_\pi^2}y, \quad (149)$$

where the Dalitz plot variables x and y are defined in Eq. (52). As $\mathcal{A}_c(s, t, u) \propto m_u - m_d$, the partial decay width can be formulated as a precise and sensitive probe of the light quark mass ratio $Q^2 = (m_s^2 - \hat{m}^2)/(m_d^2 - m_u^2)$ [541] and is used as a benchmark of ChPT and dispersive calculations. The need for the latter arises through the strong role played by final-state $\pi\pi$ rescattering [542], in particular in the isospin $I = 0$ S -wave: the perturbative chiral loop expansion converges only very slowly [540, 543]. For this reason, dispersive representations akin to the one we have briefly described earlier for $\omega/\phi \rightarrow 3\pi$, see Sec. 3.7.2, have been studied extensively in the literature [544–551]: rescattering is resummed in Khuri–Treiman-type representations, based on analyticity and unitarity and using precisely known $\pi\pi$ phase shifts as the essential input. The remaining free parameters in the form of subtraction constants can be obtained from fits to the experimental Dalitz plot distributions and subsequently matched to ChPT at a kinematical point where the chiral expansion works best. As these theoretical studies have recently been reviewed and summarized elsewhere [239], we refrain from describing them here in any detail.

For $\eta \rightarrow \pi^+\pi^-\pi^0$, a polynomial parameterization is often used to represent the Dalitz plot distribution,

$$|\mathcal{A}_c(x, y)|^2 \propto 1 + ay + by^2 + cx + dx^2 + exy + fy^3 + gx^2y + hx^3 + \dots, \quad (150)$$

where the coefficients of the polynomial in x and y are called Dalitz plot parameters. The LO result Eq. (149) results in $a = -1.04$, $b = a^2/4 = 0.27$, and all other parameters vanish. The terms with odd powers of the x variable, like c , e , h , \dots , are zero in the strong and electromagnetic interactions, as they imply charge conjugation violation. The observation of C-violating asymmetries is of significant interest

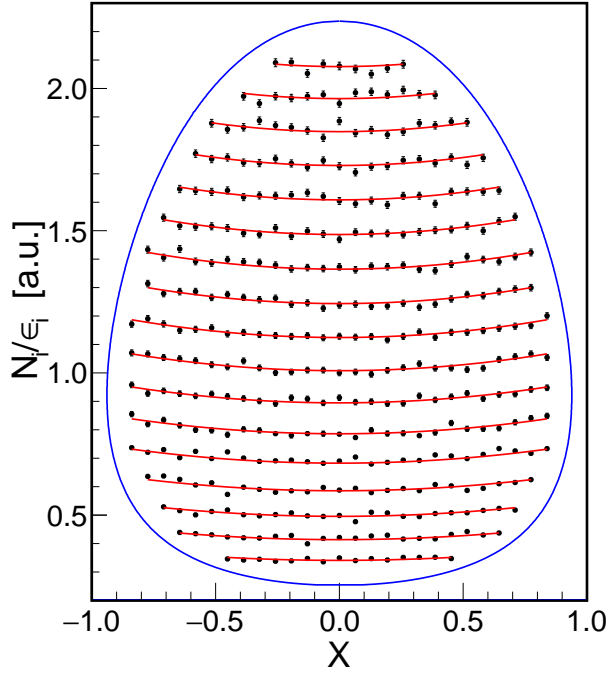


Figure 68: Acceptance corrected $\eta \rightarrow \pi^+\pi^-\pi^0$ Dalitz plot from KLOE [554] together with the result of the polynomial fit. Separate rows correspond to different y values, where the number of events decreases with increasing y .

for searches of physics beyond the Standard Model [239]; see Ref. [552] for an analysis of C-violating $\eta \rightarrow \pi^+\pi^-\pi^0$ amplitudes beyond polynomial parameters.

At $\mathcal{O}(m_u - m_d)$, the amplitudes for $\mathcal{A}_c(\eta \rightarrow \pi^+\pi^-\pi^0)$ and $\mathcal{A}_n(\eta \rightarrow 3\pi^0)$ are related by [500]

$$\mathcal{A}_n(s, t, u) = -\mathcal{A}_c(s, t, u) - \mathcal{A}_c(t, u, s) - \mathcal{A}_c(u, s, t). \quad (151)$$

Equation (151) is valid at leading order in isospin breaking; corrections to this relation have been investigated and found to be tiny [537, 553]. Therefore, Eq. (149) implies $\mathcal{A}_n(s, t, u)$ to be a constant at leading order.

The most precise result for the $\eta \rightarrow \pi^+\pi^-\pi^0$ Dalitz plot is from KLOE-2 [554], using 4.7×10^6 $\eta \rightarrow \pi^+\pi^-\pi^0$ candidate events from $e^+e^- \rightarrow \phi \rightarrow \eta\gamma$ with background admixture of less than one percent. The Dalitz plot distribution is constructed using 31 and 20 bins for the x and y ranges, respectively. The acceptance corrected data is presented in Fig. 68 and compared to the fit using the polynomial parameterization of Eq. (150). This presentation uses the fact that the y dependence is monotonic, and therefore each row of data points (the fit line) corresponds to the subsequent value of the y bin ranges. The lowest rows correspond to the largest y bin values. The results for the Dalitz plot parameters are $a = -1.095(4)$, $b = 0.145(6)$, $d = +0.081(7)$, $f = +0.141(11)$, and $g = -0.044(15)$. They are a factor of 2–3 more precise than previous measurements, and for the first time a statistically significant contribution of the $\propto gx^2y$ term is found. The data was used for the determination of the quark mass ratio by the Bern group [549, 550].

$\eta' \rightarrow \eta\pi\pi$ The combined branching fraction of the two main hadronic decays of the η' , $\eta' \rightarrow \eta\pi^+\pi^-$ and $\eta' \rightarrow \eta\pi^0\pi^0$, is nearly 2/3. The ratio $\Gamma(\eta' \rightarrow \eta\pi^+\pi^-)/\Gamma(\eta' \rightarrow \eta\pi^0\pi^0)$ should be exactly two in the isospin limit. The decays involve both η and pions in the final state and therefore are sensitive to the largely unknown $\pi\eta$ interactions (dominantly in the S -wave). However, the excess energy of the processes is relatively small: 131 MeV and 140 MeV for $\eta\pi^+\pi^-$ and $\eta\pi^0\pi^0$, respectively. This means

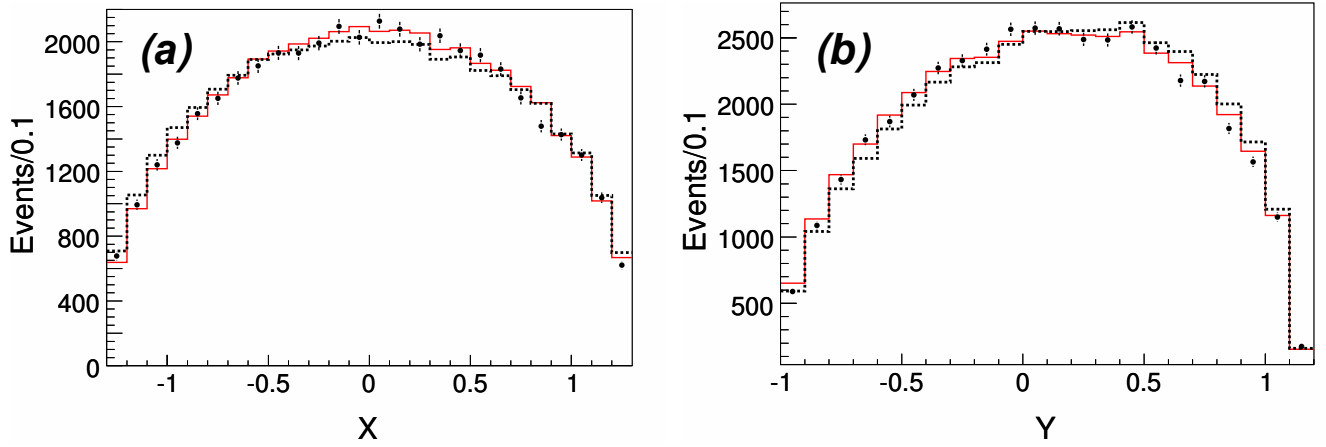


Figure 69: Projections on the Dalitz plot variables x and y from the BESIII measurement of $\eta' \rightarrow \eta\pi^+\pi^-$ [555]. The dashed histograms are for the MC events generated with constant matrix element. The solid histograms are the result of the fit of the polynomial parameterization Eq. (150).

that precision high-statistics experimental data on the Dalitz plots together with the appropriate theory framework are needed to understand the dependence on $\pi\eta$ phase shifts.

There are two recent measurements of these decays from the BESIII [555] and A2 [556] experiments. The A2 measurement uses a photoproduction reaction on a proton target and considers only the $\eta' \rightarrow \eta\pi^0\pi^0$ channel, with a signal of 1.2×10^5 events. The BESIII analysis includes both channels simultaneously, using 3.5×10^5 $\eta' \rightarrow \eta\pi^+\pi^-$ and 5.6×10^4 $\eta' \rightarrow \eta\pi^0\pi^0$ events. The general feature of the Dalitz plots is that the deviation from a uniform distribution is small, as illustrated for the $\eta' \rightarrow \eta\pi^+\pi^-$ data in Fig. 69. Therefore, a polynomial parameterization analogous to the one for $\eta \rightarrow \pi^+\pi^-\pi^0$, see Eq. (150), is frequently employed, with the similar restriction that terms odd in x are forbidden either by C -conservation (for charged pions) or Bose symmetry (neutral). The BESIII data is not consistent with the previous measurement from VES [557] and the predictions within the $U(3)$ chiral effective Lagrangian combined with a relativistic coupled-channel treatment of the final-state interactions [558]; this holds in particular for the Dalitz plot coefficient a , where the discrepancies are about four standard deviations. For $\eta' \rightarrow \eta\pi^0\pi^0$, the results are in general consistent with previous measurements and the predictions within uncertainties. A discrepancy of 2.6 standard deviations for the parameter a between the $\eta' \rightarrow \eta\pi^+\pi^-$ and $\eta' \rightarrow \eta\pi^0\pi^0$ modes is seen. The significance is not sufficient to conclusively establish isospin violation. Effects like radiative corrections [559] and the π^+/π^0 mass difference should be considered consistently to study isospin conservation at the amplitude level; cf. Ref. [560]. More recent theoretical analyses of these decays, based on unitarized versions of ChPT [561, 562] or dispersion theory with free subtraction constants [560], all require experimental Dalitz plot information as input to fix various parameters.

The most prominent isospin-violating feature occurs in the $\eta' \rightarrow \eta\pi^0\pi^0$ Dalitz plot and is due to $\pi^+\pi^- \rightarrow \pi^0\pi^0$ S -wave rescattering, which produces a cusp at the $\pi^+\pi^-$ threshold [559]. This effect is analogous to the one observed with very high precision in $K^+ \rightarrow \pi^+\pi^0\pi^0$ decays, where it has been used to extract a combination of pion-pion scattering lengths [182], based on a nonrelativistic EFT framework [183, 563, 564] (cf. also Refs. [565, 566]). A search for the cusp in $\eta' \rightarrow \eta\pi^0\pi^0$ is performed by inspecting the $\pi^0\pi^0$ invariant-mass spectrum close to $2m_{\pi^+}$. The A2 collaboration [556] reports evidence for the cusp with statistical significance of $\sim 2.5\sigma$, while BESIII [555] does not observe a statistically significant effect. A simultaneous direct fit of the dispersive amplitudes from Ref. [560] to the Dalitz plot data for the two decay modes would provide more precise information and in particular an improved prediction for the cusp effect.

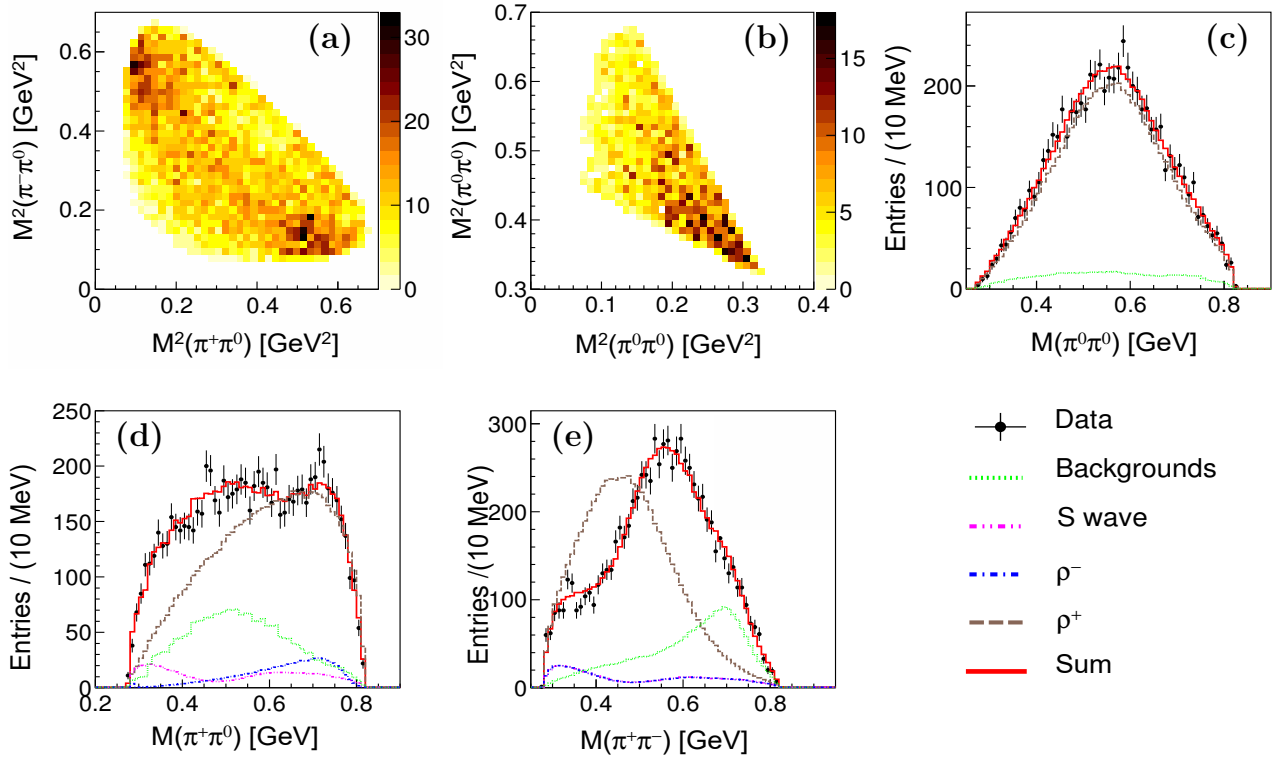


Figure 70: Dalitz plots for (a) $\eta' \rightarrow \pi^+\pi^-\pi^0$ and (b) $\eta' \rightarrow 3\pi^0$ from the BESIII analysis [569]. Two-pion invariant-mass distributions for (c) $\eta' \rightarrow 3\pi^0$ and (d)+(e) $\eta' \rightarrow \pi^+\pi^-\pi^0$ are also shown. The experimental distributions are compared to the projections of the amplitude fit. The solid line is the sum of all contributions. The dotted, dashed, dashed-dotted, and dashed-dot-dotted histograms show the contributions from background, S -wave, ρ^- , and ρ^+ , respectively.

$\eta' \rightarrow 3\pi$ The Sutherland theorem [534, 535] that ensures the suppression of electromagnetic effects as the source of isospin breaking in $\eta \rightarrow 3\pi$ is equally applicable in the analogous decay $\eta' \rightarrow 3\pi$, which therefore depends similarly on the light quark mass difference $m_u - m_d$. It was hypothesized early [567] that the decay amplitude for $\eta' \rightarrow \pi^+\pi^-\pi^0$ may be understood in terms of the dominating $\eta' \rightarrow \pi^+\pi^-\eta$ mode, followed by π^0 - η mixing. This would offer a straightforward possibility for an independent quark mass determination from the branching fraction ratio of the two processes. However, the theoretical assumptions underlying such a picture are far too simplistic [568], in particular the one of “essentially constant” decay amplitudes across the Dalitz plot; the decays $\eta' \rightarrow 3\pi$ are strongly affected by resonances in the final state.

The Dalitz plot for $\eta' \rightarrow \pi^+\pi^-\pi^0$ constructed from BESIII data shows clear P -wave contributions, with $\eta' \rightarrow \rho^\pm\pi^\mp$ visible as the two clusters in Fig. 70(a). The first amplitude analysis of the decays $\eta' \rightarrow \pi^+\pi^-\pi^0$ and $\eta' \rightarrow 3\pi^0$ was performed at BESIII using an isobar model [569]. The fit results are illustrated by the invariant-mass spectra of $\pi^+\pi^-$, $\pi^+\pi^0$, and $\pi^-\pi^0$ in Fig. 70(d)–(e). A significant P -wave contribution from $\eta' \rightarrow \rho^\pm\pi^\mp$ in $\eta' \rightarrow \pi^+\pi^-\pi^0$ is needed. In addition to a nonresonant S -wave, the resonant $\pi\pi$ S -wave with a pole at $512(15) - i188(12)$ MeV, interpreted as the broad $f_0(500)$ meson, plays an essential role in the description of the $\eta' \rightarrow 3\pi$ decays. The (unphysical) separation of the nonresonant and resonant S -wave contributions is hindered by the large interference between the two. A consistent dispersion-theoretical interpretation with universal $\pi\pi$ final-state interactions is still in progress [570].

The Dalitz plot for $\eta' \rightarrow 3\pi^0$ is shown in Fig. 70(b) (due to the symmetry only one hexagonal section is shown) and a projection of the amplitude fit is displayed in Fig. 70(c). A significant resonant S -wave

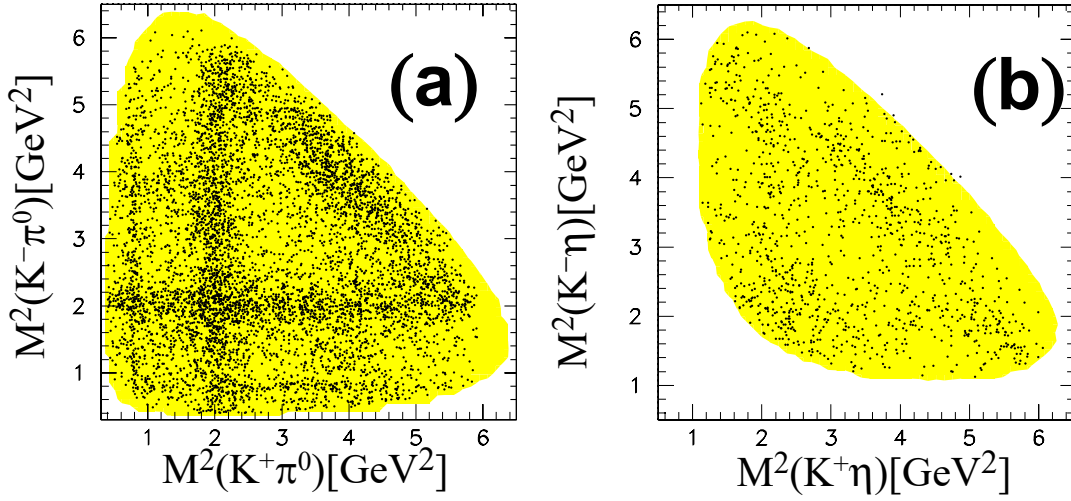


Figure 71: Dalitz plots for (a) $\eta_c \rightarrow K^+K^-\pi^0$ and (b) $\eta_c \rightarrow K^+K^-\eta$ [572].

contribution is necessary to provide an explanation for the negative slope parameter $\alpha = -0.640(66)$ of the $\eta' \rightarrow 3\pi^0$ Dalitz plot [571]. The value deviates significantly from zero, which implies that final-state interactions play an important role. The ratio between the S -wave components of the two decay modes, $\mathcal{B}(\eta' \rightarrow 3\pi^0)/\mathcal{B}(\eta' \rightarrow \pi^+\pi^-\pi^0)_S$, is determined to be $0.94(32)$, where the common systematics cancel.

$\eta_c \rightarrow K\bar{K}\pi$ and $\eta_c \rightarrow K^+K^-\eta$ The BaBar analysis of the $K^+K^-\eta$ and $K\bar{K}\pi$ systems originating from η_c decays [572, 573] is an interesting example of the use of the two-photon production mechanism to study meson dynamics at electron–positron colliders, with data samples of 4520(140) events for $\eta_c \rightarrow K^+K^-\pi^0$, 8260(110) for $\eta_c \rightarrow K_S K^\pm \pi^\mp$, and 1145(44) for $\eta_c \rightarrow K^+K^-\eta$ (combined $\eta \rightarrow \gamma\gamma$ and $\eta \rightarrow \pi^+\pi^-\pi^0$ channels). The Dalitz plots are shown in Fig. 71. In particular, a contribution of the $K_0^*(1430) \rightarrow K\eta$ decay is observed. Dalitz plot analyses of the two final states were performed using a model-independent partial-wave approach for the $I = 1/2$ $K\pi$ S -wave amplitude from Ref. [574]. In such analyses all other channels and partial waves are expressed as in the isobar-model approach. The model-independent component is extracted for each $M(K\pi)$ invariant-mass bin as a complex number represented by the intensity and phase. The results are shown in Fig. 72. A comparison with the LASS experiment indicates similar behavior for the phase up to a mass of 1.5 GeV. In contrast, the intensities show marked differences. The data requires the presence of a new $a_0(1950)$ resonance with parameters $m = 1931(26)$ MeV and $\Gamma = 271(36)$ MeV.

χ_{c1} decays Other nonvector states that are useful for the study of meson dynamics in three-body decays are χ_{cJ} states produced in radiative decays of the ψ' at BESIII. In $\chi_{c1} \rightarrow \eta'K^+K^-$ [575], 529(26) events are observed and used for an amplitude analysis. Intermediate processes $\chi_{c1} \rightarrow \eta'f_0(980)$, $\chi_{c1} \rightarrow \eta'f_0(1710)$, $\chi_{c1} \rightarrow \eta'f_2'(1525)$, and $\chi_{c1} \rightarrow K_0^*(1430)^\pm K^\mp$ ($K_0^*(1430)^\pm \rightarrow \eta'K^\pm$) are observed with statistical significances larger than 5σ . The decay $\chi_{c1} \rightarrow \eta\pi^+\pi^-$ was studied using 32920(180) events [576]. The dominant two-body structure is $a_0(980)^\pm\pi^\mp$ ($a_0(980)^\pm \rightarrow \eta\pi^\pm$). The $a_0(980)$ line shape is modeled using a dispersive approach, and a significant nonzero $a_0(980)$ coupling to the $\eta'\pi$ channel is measured for the first time. The ratio of the couplings of $a_0(980) \rightarrow \eta'\pi$ and $a_0(980) \rightarrow \eta\pi$ is expected to be large, since it is driven by η – η' mixing. In the Dalitz plot projection shown in Fig. 73(a), the effect of the $\eta'\pi$ coupling is seen as a shoulder at $(m_{\eta'} + m_\pi)^2$. In addition, a $\chi_{c1} \rightarrow a_2(1700)\pi$ subprocess is identified.

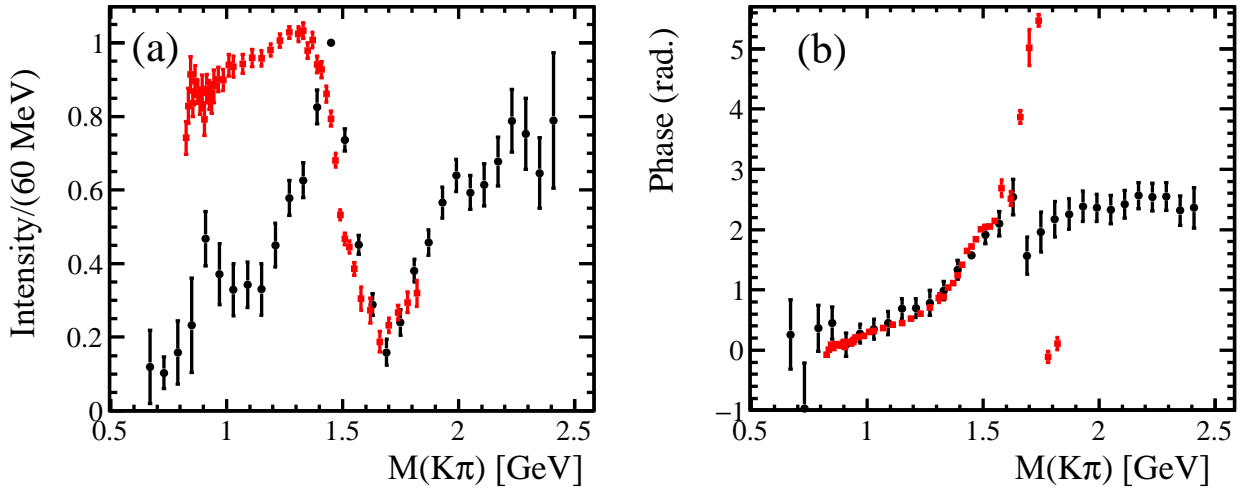


Figure 72: The $I = 1/2$ $K\pi$ S -wave amplitude extracted from the $\eta_c \rightarrow K_S K^\pm \pi^\mp$ BaBar Dalitz plot analysis [573] compared to the results from the LASS experiment [114].

Table 12: Example decay modes of the τ lepton into three light pseudoscalars (+ neutrino) [48].

Decay mode	\mathcal{B}
$\tau^- \rightarrow \pi^- \pi^0 \pi^0 \nu_\tau$	$9.26(10) \times 10^{-2}$
$\tau^- \rightarrow \pi^- \pi^+ \pi^- \nu_\tau$	$9.31(5) \times 10^{-2}$
$\tau^- \rightarrow \pi^- \bar{K}^0 \pi^0 \nu_\tau$	$3.82(13) \times 10^{-3}$
$\tau^- \rightarrow K^- \pi^+ \pi^- \nu_\tau$	$3.45(7) \times 10^{-3}$
$\tau^- \rightarrow K^- K^0 \pi^0 \nu_\tau$	$1.50(7) \times 10^{-3}$
$\tau^- \rightarrow \pi^- K^0 \bar{K}^0 \nu_\tau$	$1.55(24) \times 10^{-3}$
$\tau^- \rightarrow \pi^- K^+ K^- \nu_\tau$	$1.496(33) \times 10^{-3}$
$\tau^- \rightarrow \eta \pi^- \pi^0 \nu_\tau$	$1.39(7) \times 10^{-3}$

3.10 Weak decays $D \rightarrow P_1 P_2 P_3$ and $\tau \rightarrow P_1 P_2 P_3 \nu_\tau$

We have already argued that τ decays provide a unique place to study the dynamics of light mesons. This is especially the case for decay modes into three pseudoscalars. Some of the branching fractions for these decays are given in Table 12. The hadronic systems not accessible in single-photon processes are produced by the elementary $V - A$ current, and the invariant-mass dependence can be studied just in one experiment due to the presence of the ν_τ , which carries away part of the energy. The three-pion decay modes probe the axial-vector-meson spectrum and are dominated by the $a_1(1260)$ meson, with the subsequent decay dominantly into $\rho\pi$ [254]. The two final channels $\pi^+\pi^-\pi^-$ and $\pi^0\pi^0\pi^-$ add up to 20% of all τ decays. The decay rate $d\Gamma/ds$ in $\tau^- \rightarrow \pi^- \pi^+ \pi^- \nu_\tau$ is expressed using the axial-vector spectral function $a_1(s)$, related by the same kinematic prefactor as in Eq. (106). In Fig. 74, the $a_1(s)$ spectral function from the ALEPH experiment [312] is shown. The peak is almost exclusively due to the $a_1(1260)$ meson contribution. The most recent results on the dynamics in the three-meson decays of τ leptons are from the Belle [577] and BaBar [578] experiments. Theoretical analyses have been performed both using chiral Lagrangians with resonances [579, 580] and models based on unitarity [581, 582].

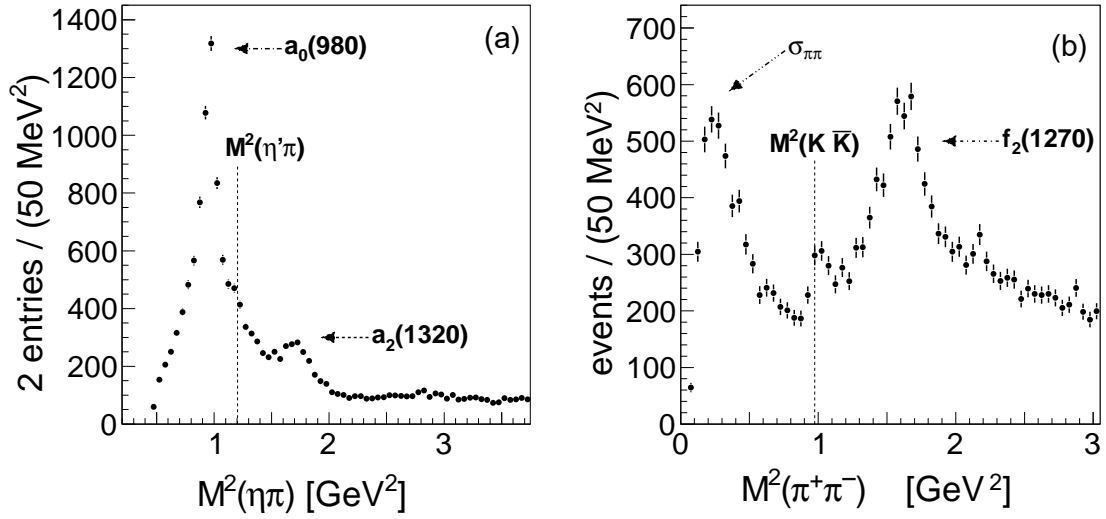


Figure 73: Dalitz plot projections for $\chi_{c1} \rightarrow \eta\pi^+\pi^-$: (a) $M^2(\eta\pi)$; (b) $M^2(\pi\pi)$. The relevant thresholds are indicated and the main contributions to the spectrum listed.

Weak three-body decays of D mesons $D \rightarrow P_1 P_2 P_3$ are so far much better explored at $c\text{-}\tau$ factories. In the isobar model the amplitude for the weak decay $D \rightarrow P_1 P_2 P_3$ can be written as

$$\begin{aligned} \langle P_1 P_2 P_3 | H_{S+W} | D \rangle = & \sum_{R_1} \langle P_2 P_3 | H_S | R_1 \rangle \langle R_1 P_1 | H_W | D \rangle + \sum_{R_2} \langle P_1 P_3 | H_S | R_2 \rangle \langle R_2 P_2 | H_W | D \rangle \\ & + \sum_{R_3} \langle P_1 P_2 | H_S | R_3 \rangle \langle R_3 P_3 | H_W | D \rangle, \end{aligned} \quad (152)$$

where H_W and H_S refer to a weak and a strong transition, respectively. R_1 represents a meson resonance in the $P_2 P_3$ system etc. However, the model does not include the most general form of final-state interactions between the three pseudoscalars.

The two $D^+ \rightarrow \bar{K}\pi\pi^+$ decays demonstrate why rescattering beyond the simplest isobar model leads to essential additional insights: $D^+ \rightarrow K^-\pi^+\pi^+$ and $D^+ \rightarrow K_S^0\pi^+\pi^0$ are coupled to each other by charge exchange, and the various subamplitudes obey isospin symmetry; however, only the latter includes direct contributions of resonances in the $\pi\pi$ system (most prominently the $\rho(770)$), while $\pi^+\pi^+$ in the former necessarily has isospin 2 and is hence nonresonant.

The extensive data base on $D^+ \rightarrow K^-\pi^+\pi^+$ by E791 [574], FOCUS [583, 584], and CLEO [585] has spurred several theoretical analyses, many of them focusing on the $K\pi$ S -wave amplitudes therein [586–588]. In Refs. [589, 590], nontrivial rescattering effects beyond two-body interactions were considered theoretically, using a loop model and Faddeev equations, respectively. A dispersion-theoretical approach based on Khuri–Treiman equations has been worked out in Ref. [591], and subsequently applied to a simultaneous analysis of $D^+ \rightarrow K^-\pi^+\pi^+$ with the BESIII Dalitz plot data on $D^+ \rightarrow K_S^0\pi^+\pi^0$ [592] in Ref. [593]. The number of partial waves and subtraction constants, as well as the heightened importance of inelastic effects in the two-body subsystems in parts of the Dalitz plots (which are not included in the theoretical formalism), make the dispersive representation and the control of the various phase motions not quite as strict as in the low-energy decays such as $\eta, \omega, \phi \rightarrow 3\pi$ or $\eta' \rightarrow \eta\pi\pi$ described earlier. However, Refs. [591, 593] still demonstrate that three-body rescattering effects induce additional phase motion that, e.g., make the $K\pi$ $I = 1/2$ S -wave rise more steeply than the corresponding elastic phase shift. This has been observed in experimental analyses before [574, 584], but does not violate Watson’s theorem: the presence of the third meson taking part in the final-state interactions allows us to explain these modifications.

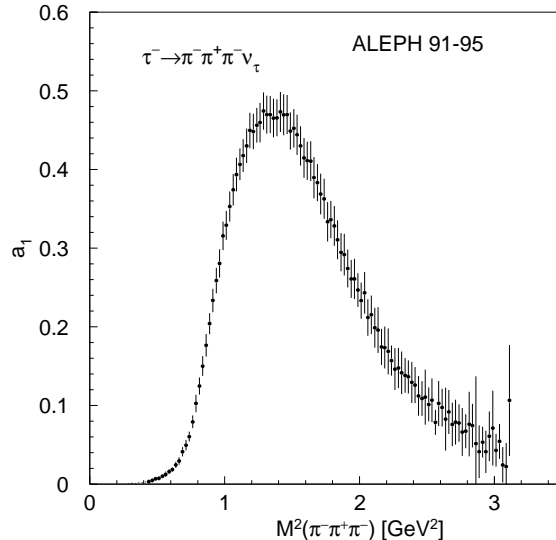


Figure 74: Spectral function a_1 for $\tau^- \rightarrow \pi^- \pi^+ \pi^- \nu_\tau$ from ALEPH [312].

In the long run, the efforts to develop physically sound descriptions of D -decay Dalitz plots are motivated by future studies of CP violation in the charm sector, where the hope is that the resonance-rich environment of three-body decays with rapid, but ultimately controllable strong phase variation may (locally) enhance the supposedly very small weak CP phases from the CKM matrix.

4 Summary and perspectives

To date, about seven decades since the discovery of the first light mesons (the pion and the kaon), studies of light-meson interactions continue to provide opportunities for a variety of physics at low energy scales, including precision tests of effective theoretical models, investigations of the quark structure of the light mesons, tests of fundamental symmetries, and searches for new physics beyond the Standard Model. With the advantages of high production rates and the excellent performance of the detectors, in this review we have tried to give a broad overview of the existing data from e^+e^- colliders, which can be used to investigate systems of light mesons. The massive progress in precision studies in recent years is driven to a large extent by the need to understand hadronic backgrounds for low-energy tests of the Standard Model and for the interpretation of the many new exotic states. Meanwhile, the theoretical advancement of rigorous tools, such as those based on dispersion-theoretical methods and effective field theories, for providing a good description of experimental data are highlighted.

In order to better understand and appreciate the progress in the field, it is illuminating to compare the physics focus of the present review to the snapshot of the physics at electron-positron colliders in 1976, as described in Ref. [94]. This was the time after the discoveries of the first charmonium states, with some observations hinting at the existence of charmed mesons and the τ lepton. In the beginning of the 1990s, the J/ψ factories were motivated mainly by the search for QCD exotics, more specifically for gluonium states [594]. The physics of light mesons was described in terms of VMD and quark models.

Some of the strongest motivation for, and strongest impact of, the high-precision, high-statistics data taken at e^+e^- data taken in the new millennium has been on precision observables: hadronic contributions to $(g-2)_\mu$ are the most obvious example, with the almost direct determination of hadronic vacuum polarization contributions, and the new strategies to constrain hadronic light-by-light scattering therefrom [18]. Maybe less obvious is the strong role of Dalitz plot studies of unprecedented accuracy,

which in the case of $\eta \rightarrow 3\pi$ has lead to the most precise phenomenological determination of the ratios of the light quark masses [550,554]. Both of these examples have pushed the development of theoretical precision tools to describe form factors and scattering amplitudes, using combinations of dispersion-theoretical methods and QCD constraints as embodied in ChPT. These developments allow us, in turn, to improve on the input for many of these dispersive studies, the elementary meson–meson phase shift information: the pion vector form factor measurements provide the sharpest experimental information available on the pion–pion P -wave phase shift, thanks to the universal relation between scattering and production [136]. Precisely in $\pi\pi$ P -wave systems, the modification of the spectral form of the $\rho(770)$ is now well understood, e.g., in radiative η' decays [303,409], using the same dispersive techniques, and thus paving the way towards a consistent high-precision extraction of ρ -pole properties from many different reactions [48]. The two-meson radiative decays of ϕ , J/ψ , and ψ' may take a similar role for even partial waves of pairs of light pseudoscalars in the future; they have already provided crucial arguments for the modern interpretation of the scalar states.

Clearly, the theoretical progress varies a lot, depending on the specific processes: many-body interactions, scattering beyond the ground-state pseudoscalars, and inelastic reactions including many coupled channels still pose severe challenges to a truly rigorous theoretical treatment. But also here, new efforts and developments are being triggered by new high-precision data. The collider data allowed for the development and implementation of dispersive methods for three-pion final states discussed in Secs. 3.7 and 3.9, due to the relatively simple partial-wave structure. These may be extended to more complicated three-pion systems in the future [595,596]. Also, form factors traditionally thought to be described sufficiently well using VMD approaches, such as vector–pseudoscalar transition form factors, now show deviations from such a simplistic picture and require more advanced theoretical tools; see Sec. 3.2. An increasing number of modern theory approaches to describe light-meson interactions includes frameworks to estimate uncertainties and to improve calculations in a systematic way. And while several of the abovementioned problems are still out of reach for present-day lattice QCD calculations, we observe a rapid development of methods and algorithms for vastly improved ab initio studies of meson–meson interactions.

Despite this impressive progress, light-hadron physics is still a rich field to be explored and there remains considerable room for improvement of experimental precision. With the abundant and clean event samples accumulated at the e^+e^- colliders, light-meson interactions will continue to be studied at facilities such as CMD-3, KLOE-2, BESIII, and SND. Taking BESIII for example, a data sample of 10^{10} J/ψ events is now available, eight times larger than the one used in the present publications, which offers great additional opportunities for research in light-meson decays, especially for pseudoscalar and vector mesons, with unprecedented precision. Moreover, the presently operating facilities BEPCII and VEPP2000 have plans for new data to be collected. Particularly interesting from our perspective is BESIII: 20 fb^{-1} at $\psi(3770)$ for $D\bar{D}$ production and the full data set of 10^9 ψ' resonance events. The physics goals and plans for the further BESIII experiments are discussed in Refs. [597,598]. These experiments require at most minor improvements in the accelerator or in the detector and will be carried out in the coming few years. In addition, the huge data samples at the new B factory, Belle-II, at SuperKEKB will also support investigations of light-meson interactions with the different opportunities of ISR and two-photon production techniques. In general, more surprises are expected to be produced at these precision experiments, which will further strengthen our present paradigms of light-hadron physics. Complementary measurements are possible in experiments at hadron and photon beam machines: not only MAMI at Mainz university [599], CLAS [600], GlueX [601], and the planned KLF [602] experiments at JLab, LHCb [603] and COMPASS [596] experiments at CERN, but also HESR at FAIR [15], J-PARC at KEK [604], and others.

Experimentally, the future investigations of light-meson interactions, in particular the search for new physics, demand the creation of new-generation facilities that have excellent performance and can obtain experimental data of much higher statistics and precision. Indeed, in recent years there are discussions

to construct super τ -charm factories (SCTFs) in Novosibirsk [605] and in China [606] to extensively explore the τ -charm physics, such as charmonium decays, charm-meson physics, hadron spectroscopy, and the so-called XYZ particles. Naturally, these main goals of the experimental programs are connected with studies of light-hadron physics as we perform them at the data-taking experiments of BESIII and Belle-II. With the advantages of high luminosity, about two orders of magnitude larger than BEPCII, and other new techniques such as polarization of beams and an energy spread compensation scheme, the SCTFs will give access to previously unexplored regions and bring the study of light-meson interactions into a very-high-precision era. Many new precision tests of the Standard Model in the s - and c -quark systems will be possible. Examples for (open or hidden) strangeness systems are η , η' , and hyperon decays. For c -quarks, entangled systems of $D\bar{D}$ mesons and ground-state charmed baryons are of high interest. In addition, for the SCTF projects electron beam polarization of up to 80% is considered. The polarization can be utilized in τ -decay studies for the determination of structure functions [607] and for CP symmetry tests [608]. These new experimental activities in the low-energy region also strongly call for more detailed theoretical studies in this area, which will play an important role in the developments of chiral effective field theory and lattice QCD, and make significant contributions to our understanding of hadron physics in the nonperturbative regime.

Acknowledgements

This publication is part of a project that has received funding from the European Union’s Horizon 2020 research and innovation programme under grant agreement STRONG-2020 – No 824093. This project has received funding from the National Natural Science Foundation of China (NSFC) and the Deutsche Forschungsgemeinschaft (DFG) through the funds provided to the Sino–German Collaborative Research Center CRC 110 “Symmetries and the Emergence of Structure in QCD” (DFG – Project-ID 196253076 – TRR 110), and by the Munich Institute for Astro- and Particle Physics (MIAPP), which is funded by the DFG under Germany’s Excellence Strategy – EXC-2094 – 390783311. This work is also supported in part by the NSFC under Contracts No. 11735014 and No. 11675184. AK acknowledges a grant of the Chinese Academy of Science President’s International Fellowship Initiative (PIFI) for Visiting Scientists. We thank our colleagues for sharing the results that were included in this review, and apologize for all those that could not be discussed any more.

References

- [1] E. Klempt, A. Zaitsev, Glueballs, Hybrids, Multiquarks. Experimental facts versus QCD inspired concepts, Phys. Rept. 454 (2007) 1–202. [arXiv:0708.4016](#).
- [2] H.-X. Chen, W. Chen, X. Liu, S.-L. Zhu, The hidden-charm pentaquark and tetraquark states, Phys. Rept. 639 (2016) 1–121. [arXiv:1601.02092](#).
- [3] A. Esposito, A. Pilloni, A. D. Polosa, Multiquark Resonances, Phys. Rept. 668 (2017) 1–97. [arXiv:1611.07920](#).
- [4] R. F. Lebed, R. E. Mitchell, E. S. Swanson, Heavy-Quark QCD Exotica, Prog. Part. Nucl. Phys. 93 (2017) 143–194. [arXiv:1610.04528](#).
- [5] A. Ali, J. S. Lange, S. Stone, Exotics: Heavy Pentaquarks and Tetraquarks, Prog. Part. Nucl. Phys. 97 (2017) 123–198. [arXiv:1706.00610](#).
- [6] S. L. Olsen, T. Skwarnicki, D. Zieminska, Nonstandard heavy mesons and baryons: Experimental evidence, Rev. Mod. Phys. 90 (2018) 015003. [arXiv:1708.04012](#).

- [7] M. Karliner, J. L. Rosner, T. Skwarnicki, Multiquark States, *Ann. Rev. Nucl. Part. Sci.* 68 (2018) 17–44. [arXiv:1711.10626](#).
- [8] F.-K. Guo, C. Hanhart, U.-G. Meißner, Q. Wang, Q. Zhao, B.-S. Zou, Hadronic molecules, *Rev. Mod. Phys.* 90 (2018) 015004. [arXiv:1705.00141](#).
- [9] S. Aoki, et al. [Flavour Lattice Averaging Group], FLAG Review 2019, *Eur. Phys. J. C* 80 (2020) 113. [arXiv:1902.08191](#).
- [10] R. A. Briceño, J. J. Dudek, R. D. Young, Scattering processes and resonances from lattice QCD, *Rev. Mod. Phys.* 90 (2018) 025001. [arXiv:1706.06223](#).
- [11] M. T. Hansen, S. R. Sharpe, Lattice QCD and Three-particle Decays of Resonances, *Ann. Rev. Nucl. Part. Sci.* 69 (2019) 65–107. [arXiv:1901.00483](#).
- [12] R. Aaij, et al., Physics case for an LHCb Upgrade II – Opportunities in flavour physics, and beyond, in the HL-LHC era (2018). [arXiv:1808.08865](#).
- [13] W. Altmannshofer, et al. [Belle-II], The Belle II Physics Book, *PTEP* 2019 (2019) 123C01, [Erratum: *PTEP* 2020, 029201 (2020)]. [arXiv:1808.10567](#).
- [14] J. Dudek, et al., Physics Opportunities with the 12 GeV Upgrade at Jefferson Lab, *Eur. Phys. J. A* 48 (2012) 187. [arXiv:1208.1244](#).
- [15] M. F. M. Lutz, et al., Physics Performance Report for PANDA: Strong Interaction Studies with Antiprotons (2009). [arXiv:0903.3905](#).
- [16] G. W. Bennett, et al. [Muon $g-2$], Final Report of the Muon E821 Anomalous Magnetic Moment Measurement at BNL, *Phys. Rev. D* 73 (2006) 072003. [arXiv:hep-ex/0602035](#).
- [17] F. Jegerlehner, A. Nyffeler, The Muon $g-2$, *Phys. Rept.* 477 (2009) 1–110. [arXiv:0902.3360](#).
- [18] T. Aoyama, et al., The anomalous magnetic moment of the muon in the Standard Model, *Phys. Rept.* 887 (2020) 1–166. [arXiv:2006.04822](#).
- [19] E. Pallante, A. Pich, Strong enhancement of ϵ'/ϵ through final state interactions, *Phys. Rev. Lett.* 84 (2000) 2568–2571. [arXiv:hep-ph/9911233](#).
- [20] V. Cirigliano, G. Ecker, H. Neufeld, A. Pich, J. Portoles, Kaon Decays in the Standard Model, *Rev. Mod. Phys.* 84 (2012) 399. [arXiv:1107.6001](#).
- [21] A. J. Buras, J.-M. Gerard, Final state interactions in $K \rightarrow \pi\pi$ decays: $\Delta I = 1/2$ rule vs. ϵ'/ϵ , *Eur. Phys. J. C* 77 (2017) 10. [arXiv:1603.05686](#).
- [22] H. Gisbert, A. Pich, Direct CP violation in $K^0 \rightarrow \pi\pi$: Standard Model Status, *Rept. Prog. Phys.* 81 (2018) 076201. [arXiv:1712.06147](#).
- [23] H.-Y. Cheng, C.-K. Chua, A. Soni, Final state interactions in hadronic B decays, *Phys. Rev. D* 71 (2005) 014030. [arXiv:hep-ph/0409317](#).
- [24] I. Bediaga, I. I. Bigi, A. Gomes, G. Guerrer, J. Miranda, A. C. dos Reis, On a CP anisotropy measurement in the Dalitz plot, *Phys. Rev. D* 80 (2009) 096006. [arXiv:0905.4233](#).
- [25] R. Aaij, et al. [LHCb], Amplitude analysis of the $B^+ \rightarrow \pi^+\pi^+\pi^-$ decay, *Phys. Rev. D* 101 (2020) 012006. [arXiv:1909.05212](#).

- [26] S. D. Protopopescu, M. Alston-Garnjost, A. Barbaro-Galtieri, S. M. Flatté, J. H. Friedman, T. A. Lasinski, G. R. Lynch, M. S. Rabin, F. T. Solmitz, $\pi\pi$ Partial Wave Analysis from Reactions $\pi^+p \rightarrow \pi^+\pi^-\Delta^{++}$ and $\pi^+p \rightarrow K^+K^-\Delta^{++}$ at 7.1 GeV/c, Phys. Rev. D 7 (1973) 1279.
- [27] P. Estabrooks, A. D. Martin, $\pi\pi$ Phase Shift Analysis Below the $K\bar{K}$ Threshold, Nucl. Phys. B 79 (1974) 301–316.
- [28] G. Grayer, et al., High Statistics Study of the Reaction $\pi^-p \rightarrow \pi^-\pi^+n$: Apparatus, Method of Analysis, and General Features of Results at 17 GeV/c, Nucl. Phys. B 75 (1974) 189–245.
- [29] B. Hyams, et al., $\pi\pi$ Phase Shift Analysis from 600 MeV to 1900 MeV, Nucl. Phys. B 64 (1973) 134–162.
- [30] T. Akesson, et al. [Axial Field Spectrometer], A Search for Glueballs and a Study of Double Pomeron Exchange at the CERN Interacting Storage Rings, Nucl. Phys. B 264 (1986) 154–184.
- [31] D. Barberis, et al. [WA102], A Partial wave analysis of the centrally produced $\pi^0\pi^0$ system in pp interactions at 450 GeV/c, Phys. Lett. B 453 (1999) 325–332. [arXiv:hep-ex/9903044](#).
- [32] D. Barberis, et al. [WA102], A Partial wave analysis of the centrally produced $\pi^+\pi^-$ system in pp interactions at 450 GeV/c, Phys. Lett. B 453 (1999) 316–324. [arXiv:hep-ex/9903043](#).
- [33] R. Bellazzini, et al. [GAMS], A partial wave analysis of the centrally produced $\pi^0\pi^0$ system in pp interactions at 450 GeV/c, Phys. Lett. B 467 (1999) 296–302.
- [34] M. G. Albrow, T. D. Coughlin, J. R. Forshaw, Central Exclusive Particle Production at High Energy Hadron Colliders, Prog. Part. Nucl. Phys. 65 (2010) 149–184. [arXiv:1006.1289](#).
- [35] J. R. Batley, et al. [NA48/2], New high statistics measurement of K_{e4} decay form factors and $\pi\pi$ scattering phase shifts, Eur. Phys. J. C 54 (2008) 411–423.
- [36] N. Cabibbo, A. Maksymowicz, Angular Correlations in K_{e4} Decays and Determination of Low-Energy $\pi\pi$ Phase Shifts, Phys. Rev. 137 (1965) B438–B443, [Erratum: Phys. Rev. 168 (1968) 1926].
- [37] A. Aloisio, et al. [KLOE], Study of the decay $\phi \rightarrow \pi^0\pi^0\gamma$ with the KLOE detector, Phys. Lett. B 537 (2002) 21–27. [arXiv:hep-ex/0204013](#).
- [38] F. Ambrosino, et al. [KLOE], Dalitz plot analysis of $e^+e^- \rightarrow \pi^0\pi^0\gamma$ events at $\sqrt{s} \simeq M_\phi$ with the KLOE detector, Eur. Phys. J. C 49 (2007) 473–488. [arXiv:hep-ex/0609009](#).
- [39] M. Ablikim, et al. [BESIII], Amplitude analysis of the $\pi^0\pi^0$ system produced in radiative J/ψ decays, Phys. Rev. D 92 (2015) 052003, [Erratum: Phys. Rev. D 93 (2016) 039906]. [arXiv:1506.00546](#).
- [40] K. Koller, T. Walsh, Gluons in Quarkonium Decay, Nucl. Phys. B 140 (1978) 449–467.
- [41] J. Becker, et al. [Mark-III], Radiative Decays of the J/ψ Into $\gamma\pi^+\pi^-$ and γK^+K^- , Phys. Rev. D 35 (1987) 2077.
- [42] J. E. Augustin, et al. [DM2], Measurement of the Radiative J/ψ Decays in $K\bar{K}$ States, Phys. Rev. Lett. 60 (1988) 2238.
- [43] J. Z. Bai, et al. [BES], Studies of $\xi(2230)$ in J/ψ radiative decays, Phys. Rev. Lett. 76 (1996) 3502–3505.

- [44] J. Z. Bai, et al. [BES], Experimental study of J/ψ radiative decay to $\pi^0\pi^0$, Phys. Rev. Lett. 81 (1998) 1179–1182.
- [45] K. L. Au, D. Morgan, M. R. Pennington, Meson Dynamics Beyond the Quark Model: A Study of Final State Interactions, Phys. Rev. D 35 (1987) 1633.
- [46] T. Mori, et al. [Belle], High statistics study of $f_0(980)$ resonance in $\gamma\gamma \rightarrow \pi^+\pi^-$ production, Phys. Rev. D 75 (2007) 051101. [arXiv:hep-ex/0610038](https://arxiv.org/abs/hep-ex/0610038).
- [47] G. Rodrigo, H. Czyż, J. H. Kühn, M. Szopa, Radiative return at NLO and the measurement of the hadronic cross-section in electron positron annihilation, Eur. Phys. J. C 24 (2002) 71–82. [arXiv:hep-ph/0112184](https://arxiv.org/abs/hep-ph/0112184).
- [48] P. A. Zyla, et al. [Particle Data Group], Review of Particle Physics, PTEP 2020 (2020) 083C01.
- [49] R. Wideroe, Anordnung zur Herbeiführung von Kernreaktionen, Deutsches Patentamt, Patentschrift No. 876279, Klasse 21g, Gruppe 36, Mai 11 (1953).
- [50] G. K. O’Neill, Storage-Ring Synchrotron: Device for High-Energy Physics Research, Phys. Rev. 102 (1956) 1418–1419.
- [51] D. W. Kerst, F. T. Cole, H. R. Crane, L. W. Jones, L. J. Laslett, T. Ohkawa, A. M. Sessler, K. R. Symon, K. M. Terwilliger, N. V. Nilsen, Attainment of very high-energy by means of intersecting beams of particles, Phys. Rev. 102 (1956) 590–591.
- [52] J. J. Aubert, et al. [E598], Experimental Observation of a Heavy Particle J , Phys. Rev. Lett. 33 (1974) 1404–1406.
- [53] J. E. Augustin, et al. [SLAC-SP-017], Discovery of a Narrow Resonance in e^+e^- Annihilation, Phys. Rev. Lett. 33 (1974) 1406–1408, [Adv. Exp. Phys.5 (1976) 141].
- [54] C. Bacci, et al., Preliminary Result of Frascati (ADONE) on the Nature of a New 3.1 GeV Particle Produced in e^+e^- Annihilation, Phys. Rev. Lett. 33 (1974) 1408, [Erratum: Phys. Rev. Lett. 33 (1974) 1649].
- [55] T. H. Bauer, R. D. Spital, D. R. Yennie, F. M. Pipkin, The Hadronic Properties of the Photon in High-Energy Interactions, Rev. Mod. Phys. 50 (1978) 261, [Erratum: Rev. Mod. Phys. 51 (1979) 407].
- [56] Bruno Touschek Memorial Lectures, in: M. Greco, G. Pancheri (Eds.), Frascati Physics Series, Vol. XXXIII, 2005, pp. 1–133.
URL <http://www.lnf.infn.it/sis/frascatiseries/Volume33/volume33.pdf>
- [57] V. N. Baier, Forty years of acting electron–positron colliders (2006). [arXiv:hep-ph/0611201](https://arxiv.org/abs/hep-ph/0611201).
- [58] L. Bonolis, G. Pancheri, Bruno Touschek: Particle physicist and father of the e^+e^- collider, Eur. Phys. J. H 36 (2011) 1–61. [arXiv:1103.2727](https://arxiv.org/abs/1103.2727).
- [59] C. Bernardini, G. Pancheri, C. Pellegrini, Bruno Touschek: From Betatrons to Electron–Positron Colliders, Rev. Accel. Sci. Tech. 08 (2015) 269–290. [arXiv:1510.00933](https://arxiv.org/abs/1510.00933).
- [60] G. Pancheri, L. Bonolis, The path to high-energy electron–positron colliders: from Wideroe’s betatron to Touschek’s AdA and to LEP (2017). [arXiv:1710.09003](https://arxiv.org/abs/1710.09003).

- [61] V. Shiltsev, F. Zimmermann, Modern and Future Colliders, *Rev. Mod. Phys.* 93 (1) (2021) 15006. [arXiv:2003.09084](#).
- [62] L. M. Brown, F. Calogero, Effects of Pion–Pion Interaction in Electromagnetic Processes, *Phys. Rev. Lett.* 4 (1960) 315–317.
- [63] C. Bernardini, Bruno Touschek and AdA, in: V. Valente (Ed.), *Frascati Physics Series, Vol. VIII*, 1997, p. 1.
- [64] G. F. Chew, F. E. Low, Unstable particles as targets in scattering experiments, *Phys. Rev.* 113 (1959) 1640–1648.
- [65] F. Salzman, G. Salzman, Pion Production from π^-p Collisions in the Long-Range Interaction Model, *Phys. Rev.* 120 (1960) 599–608.
- [66] C. Goebel, Determination of the $\pi\pi$ Interaction Strength from πN Scattering, *Phys. Rev. Lett.* 1 (1958) 337–339.
- [67] R. Hofstadter, Electron scattering and nuclear structure, *Rev. Mod. Phys.* 28 (1956) 214–254.
- [68] G. F. Chew, R. Karplus, S. Gasiorowicz, F. Zachariasen, Electromagnetic Structure of the Nucleon in Local-Field Theory, *Phys. Rev.* 110 (1958) 265.
- [69] P. Federbush, M. L. Goldberger, S. B. Treiman, Electromagnetic Structure of the Nucleon, *Phys. Rev.* 112 (1958) 642–665.
- [70] W. R. Frazer, J. R. Fulco, Effect of a Pion–Pion Scattering Resonance on Nucleon Structure. II, *Phys. Rev.* 117 (1960) 1609–1614.
- [71] G. Höhler, E. Pietarinen, I. Sabba Stefanescu, F. Borkowski, G. G. Simon, V. H. Walther, R. D. Wendling, Analysis of Electromagnetic Nucleon Form-Factors, *Nucl. Phys. B* 114 (1976) 505–534.
- [72] P. Mergell, U.-G. Meißner, D. Drechsel, Dispersion theoretical analysis of the nucleon electromagnetic form-factors, *Nucl. Phys. A* 596 (1996) 367–396. [arXiv:hep-ph/9506375](#).
- [73] M. A. Belushkin, H.-W. Hammer, U.-G. Meißner, Novel evaluation of the two-pion contribution to the nucleon isovector form-factors, *Phys. Lett. B* 633 (2006) 507–511. [arXiv:hep-ph/0510382](#).
- [74] M. Hoferichter, B. Kubis, J. Ruiz de Elvira, H.-W. Hammer, U.-G. Meißner, On the $\pi\pi$ continuum in the nucleon form factors and the proton radius puzzle, *Eur. Phys. J. A* 52 (2016) 331. [arXiv:1609.06722](#).
- [75] S. Pacetti, R. Baldini Ferroli, E. Tomasi-Gustafsson, Proton electromagnetic form factors: Basic notions, present achievements and future perspectives, *Phys. Rept.* 550-551 (2015) 1–103.
- [76] T. D. Lee, C.-N. Yang, Charge Conjugation, a New Quantum Number G , and Selection Rules Concerning a Nucleon–Antinucleon System, *Nuovo Cim.* 10 (1956) 749–753.
- [77] N. Cabibbo, R. Gatto, Pion Form Factors from Possible High-Energy Electron-Positron Experiments, *Phys. Rev. Lett.* 4 (1960) 313–314.
- [78] W. R. Frazer, J. R. Fulco, Effect of a pion pion scattering resonance on nucleon structure, *Phys. Rev. Lett.* 2 (1959) 365.
- [79] Y. Nambu, Possible existence of a heavy neutral meson, *Phys. Rev.* 106 (1957) 1366–1367.

- [80] J. J. Sakurai, Theory of strong interactions, *Annals Phys.* 11 (1960) 1–48.
- [81] A. R. Erwin, R. March, W. D. Walker, E. West, Evidence for a $\pi\pi$ Resonance in the $I = 1, J = 1$ State, *Phys. Rev. Lett.* 6 (1961) 628–630.
- [82] B. Maglich, L. W. Alvarez, A. H. Rosenfeld, M. L. Stevenson, Evidence for a $T = 0$ Three Pion Resonance, *Phys. Rev. Lett.* 7 (1961) 178–182, [*Adv. Exp. Phys.* 5 (1976) 106].
- [83] L. Bertanza, et al., Possible Resonances in the $\Xi\pi$ and $K\bar{K}$ Systems, *Phys. Rev. Lett.* 9 (1962) 180–183.
- [84] P. E. Schlein, W. E. Slater, L. T. Smith, D. H. Stork, H. K. Ticho, Quantum Numbers of a 1020 MeV $K\bar{K}$ Resonance, *Phys. Rev. Lett.* 10 (1963) 368.
- [85] P. L. Connolly, et al., Existence and Properties of the ϕ Meson, *Phys. Rev. Lett.* 10 (1963) 371–376.
- [86] N. Cabibbo, R. Gatto, Electron Positron Colliding Beam Experiments, *Phys. Rev.* 124 (1961) 1577–1595.
- [87] C. Bernardini, G. F. Corazza, G. Ghigo, B. Touschek, The Frascati storage ring, *Il Nuovo Cimento (1955-1965)* (1960) 136–138.
- [88] C. Bernardini, U. Bizzarri, G. F. Corazza, G. Ghigo, R. Querzoli, B. Touschek, Progress report on AdA (Frascati storage ring), *Il Nuovo Cimento (1955-1965)* (1962) 202–207.
- [89] C. Bernardini, AdA: The first electron–positron collider, *Phys. Perspect.* 6 (2004) 156–183.
- [90] C. Bernardini, G. F. Corazza, G. Di Giugno, G. Ghigo, R. Querzoli, J. Haissinski, P. Marin, B. Touschek, Lifetime and beam size in a storage ring, *Phys. Rev. Lett.* 10 (1963) 407–409.
- [91] C. Bernardini, G. F. Corazza, G. Giugno, J. Haissinski, P. Marin, R. Querzoli, B. Touschek, Measurements of the rate of interaction between stored electrons and positrons, *Nuovo Cim.* 34 (1964) 1473–1493.
- [92] B. Richter, The Stanford Storage Ring – SPEAR, *Kerntechnik.* 12 (1970) 531.
- [93] E. B. Levicev, A. N. Skrinisky, G. M. Tumaikin, Y. M. Shatunov, Electron–positron beam collision studies at the Budker Institute of Nuclear Physics, *Phys. Usp.* 61 (2018) 405–423.
- [94] J. P. Perez-y Jorba, F. M. Renard, The physics of electron–positron colliding beams, *Phys. Rept.* 31 (1977) 1–157.
- [95] C. J. Morningstar, M. J. Peardon, The Glueball spectrum from an anisotropic lattice study, *Phys. Rev. D* 60 (1999) 034509. [arXiv:hep-lat/9901004](https://arxiv.org/abs/hep-lat/9901004).
- [96] S. Godfrey, N. Isgur, Mesons in a Relativized Quark Model with Chromodynamics, *Phys. Rev. D* 32 (1985) 189–231.
- [97] T. Barnes, N. Black, P. R. Page, Strong decays of strange quarkonia, *Phys. Rev. D* 68 (2003) 054014. [arXiv:nuc1-th/0208072](https://arxiv.org/abs/nuc1-th/0208072).
- [98] B. Aubert, et al. [BaBar], A Structure at 2175 MeV in $e^+e^- \rightarrow \phi f_0(980)$ Observed via Initial-State Radiation, *Phys. Rev. D* 74 (2006) 091103. [arXiv:hep-ex/0610018](https://arxiv.org/abs/hep-ex/0610018).

- [99] P.-L. Liu, S.-s. Fang, X.-C. Lou, Strange Quarkonium States at BESIII, *Chin. Phys. C* 39 (2015) 082001. [arXiv:1505.03061](#).
- [100] J. L. Petersen, Meson–meson scattering, *Phys. Rept.* 2 (1971) 155–252.
- [101] A. Gómez Nicola, J. R. Peláez, Meson meson scattering within one loop chiral perturbation theory and its unitarization, *Phys. Rev. D* 65 (2002) 054009. [arXiv:hep-ph/0109056](#).
- [102] F. Niecknig, B. Kubis, S. P. Schneider, Dispersive analysis of $\omega \rightarrow 3\pi$ and $\phi \rightarrow 3\pi$ decays, *Eur. Phys. J. C* 72 (2012) 2014. [arXiv:1203.2501](#).
- [103] A. D. Martin, E. N. Ozmütlu, Analyses of $K\bar{K}$ Production and Scalar Mesons, *Nucl. Phys. B* 158 (1979) 520–545.
- [104] C. D. Froggatt, J. L. Petersen, Phase Shift Analysis of $\pi^+\pi^-$ Scattering Between 1.0 GeV and 1.8 GeV Based on Fixed Momentum Transfer Analyticity. 2., *Nucl. Phys. B* 129 (1977) 89–110.
- [105] D. H. Cohen, D. S. Ayres, R. Diebold, S. L. Kramer, A. J. Pawlicki, A. B. Wicklund, Amplitude Analysis of the K^-K^+ System Produced in the Reactions $\pi^-p \rightarrow K^-K^+n$ and $\pi^+n \rightarrow K^-K^+p$ at 6 GeV/c, *Phys. Rev. D* 22 (1980) 2595.
- [106] W. Hoogland, et al., Measurement and Analysis of the $\pi^+\pi^+$ System Produced at Small Momentum Transfer in the Reaction $\pi^+p \rightarrow \pi^+\pi^+n$ at 12.5 GeV, *Nucl. Phys. B* 126 (1977) 109–123.
- [107] M. J. Losty, V. Chaloupka, A. Ferrando, L. Montanet, E. Paul, D. Yaffe, A. Zieminski, J. Alitti, B. Gandois, J. Louie, A Study of $\pi^-\pi^-$ scattering from $\pi - p$ interactions at 3.93 GeV/c, *Nucl. Phys. B* 69 (1974) 185–204.
- [108] B. Moussallam, Analyticity constraints on the strangeness changing vector current and applications to $\tau \rightarrow K\pi\nu_\tau$, $\tau \rightarrow K\pi\pi\nu_\tau$, *Eur. Phys. J. C* 53 (2008) 401–412. [arXiv:0710.0548](#).
- [109] R. Mercer, et al., $K\pi$ scattering phase shifts determined from the reactions $K^+p \rightarrow K^+\pi^-\Delta^{++}$ and $K^+p \rightarrow K^0\pi^0\Delta^{++}$, *Nucl. Phys. B* 32 (1971) 381–414.
- [110] P. Estabrooks, R. K. Carnegie, A. D. Martin, W. M. Dunwoodie, T. A. Lasinski, D. W. G. S. Leith, Study of $K\pi$ Scattering Using the Reactions $K^\pm p \rightarrow K^\pm\pi^+n$ and $K^\pm p \rightarrow K^\pm\pi^-\Delta^{++}$ at 13 GeV/c, *Nucl. Phys. B* 133 (1978) 490–524.
- [111] M. Jamin, J. A. Oller, A. Pich, Strangeness changing scalar form factors, *Nucl. Phys. B* 622 (2002) 279–308. [arXiv:hep-ph/0110193](#).
- [112] H. H. Bingham, et al., A New analysis of $K\pi$ scattering as observed in $K^+p \rightarrow K^+\pi^0\Delta^{++}$ from 3 GeV/c to 13 GeV/c, *Nucl. Phys. B* 41 (1972) 1–34.
- [113] S. L. Baker, et al., A Study of $K^+\pi^-$ Elastic Scattering in the Reaction $K^+n \rightarrow K^+\pi^-p$ Between 2.0 GeV/c and 3.0 GeV/c, *Nucl. Phys. B* 99 (1975) 211.
- [114] D. Aston, et al., A Study of $K^-\pi^+$ Scattering in the Reaction $K^-p \rightarrow K^-\pi^+n$ at 11 GeV/c, *Nucl. Phys. B* 296 (1988) 493–526.
- [115] D. Linglin, et al., $K^-\pi^-$ elastic scattering cross-section measured in 14.3 GeV/c K^-p interactions, *Nucl. Phys. B* 57 (1973) 64–76.

- [116] T. A. Armstrong, et al. [WA76, Athens-Bari-Birmingham-CERN-College de France], Study of the $\eta\pi^+\pi^-$ system centrally produced in the reaction $pp \rightarrow p(f)(\eta\pi^+\pi^-)p(s)$ at 300 GeV/c, *Z. Phys. C* 52 (1991) 389–396.
- [117] B. Ananthanarayan, G. Colangelo, J. Gasser, H. Leutwyler, Roy equation analysis of $\pi\pi$ scattering, *Phys. Rept.* 353 (2001) 207–279. [arXiv:hep-ph/0005297](#).
- [118] G. Colangelo, J. Gasser, H. Leutwyler, $\pi\pi$ scattering, *Nucl. Phys. B* 603 (2001) 125–179. [arXiv:hep-ph/0103088](#).
- [119] R. García-Martín, R. Kamiński, J. R. Peláez, J. Ruiz de Elvira, F. J. Ynduráin, The Pion-pion scattering amplitude. IV: Improved analysis with once subtracted Roy-like equations up to 1100 MeV, *Phys. Rev. D* 83 (2011) 074004. [arXiv:1102.2183](#).
- [120] I. Caprini, G. Colangelo, H. Leutwyler, Regge analysis of the $\pi\pi$ scattering amplitude, *Eur. Phys. J. C* 72 (2012) 1860. [arXiv:1111.7160](#).
- [121] J. R. Peláez, A. Rodas, J. Ruiz de Elvira, Global parameterization of $\pi\pi$ scattering up to 2 GeV, *Eur. Phys. J. C* 79 (2019) 1008. [arXiv:1907.13162](#).
- [122] P. Büttiker, S. Descotes-Genon, B. Moussallam, A new analysis of πK scattering from Roy- and Steiner-type equations, *Eur. Phys. J. C* 33 (2004) 409–432. [arXiv:hep-ph/0310283](#).
- [123] J. R. Peláez, A. Rodas, $\pi\pi \rightarrow K\bar{K}$ scattering up to 1.47 GeV with hyperbolic dispersion relations, *Eur. Phys. J. C* 78 (2018) 897. [arXiv:1807.04543](#).
- [124] J. R. Peláez, A. Rodas, Dispersive $\pi K \rightarrow \pi K$ and $\pi\pi \rightarrow K\bar{K}$ amplitudes from scattering data, threshold parameters and the lightest strange resonance κ or $K_0^*(700)$ (10 2020). [arXiv:2010.11222](#).
- [125] A. Pais, S. B. Treiman, Pion Phase-Shift Information from $K_{\ell 4}$ Decays, *Phys. Rev.* 168 (1968) 1858–1865.
- [126] L. Rosselet, et al., Experimental Study of 30,000 K_{e4} Decays, *Phys. Rev. D* 15 (1977) 574.
- [127] P. Truoel, New results on rare and forbidden semileptonic K^+ decays, *Frascati Phys. Ser.* 20 (2001) 49–63. [arXiv:hep-ex/0012012](#).
- [128] S. Pislak, et al. [BNL-E865], A new measurement of K_{e4}^+ decay and the s -wave $\pi\pi$ scattering length a_0^0 , *Phys. Rev. Lett.* 87 (2001) 221801, [Erratum: *Phys. Rev. Lett.* 105 (2010) 019901]. [arXiv:hep-ex/0106071](#).
- [129] J. R. Batley, et al. [NA48/2], Precise tests of low energy QCD from K_{e4} decay properties, *Eur. Phys. J. C* 70 (2010) 635–657.
- [130] G. Colangelo, J. Gasser, H. Leutwyler, The Quark condensate from K_{e4} decays, *Phys. Rev. Lett.* 86 (2001) 5008–5010. [arXiv:hep-ph/0103063](#).
- [131] I. Caprini, G. Colangelo, H. Leutwyler, Mass and width of the lowest resonance in QCD, *Phys. Rev. Lett.* 96 (2006) 132001. [arXiv:hep-ph/0512364](#).
- [132] R. García-Martín, R. Kamiński, J. R. Peláez, J. Ruiz de Elvira, Precise determination of the $f_0(600)$ and $f_0(980)$ pole parameters from a dispersive data analysis, *Phys. Rev. Lett.* 107 (2011) 072001. [arXiv:1107.1635](#).

- [133] J. R. Peláez, From controversy to precision on the sigma meson: a review on the status of the non-ordinary $f_0(500)$ resonance, Phys. Rept. 658 (2016) 1. [arXiv:1510.00653](#).
- [134] J. F. de Trocóniz, F. J. Ynduráin, Precision determination of the pion form factor and calculation of the muon $g - 2$, Phys. Rev. D 65 (2002) 093001. [arXiv:hep-ph/0106025](#).
- [135] J. F. de Trocóniz, F. J. Ynduráin, The hadronic contributions to the anomalous magnetic moment of the muon, Phys. Rev. D 71 (2005) 073008. [arXiv:hep-ph/0402285](#).
- [136] G. Colangelo, M. Hoferichter, P. Stoffer, Two-pion contribution to hadronic vacuum polarization, JHEP 02 (2019) 006. [arXiv:1810.00007](#).
- [137] G. Colangelo, M. Hoferichter, P. Stoffer, Constraints on the two-pion contribution to hadronic vacuum polarization, Phys. Lett. B 814 (2021) 136073. [arXiv:2010.07943](#).
- [138] S. Ropertz, C. Hanhart, B. Kubis, A new parametrization for the scalar pion form factors, Eur. Phys. J. C 78 (2018) 1000. [arXiv:1809.06867](#).
- [139] M. Albaladejo, B. Moussallam, Form factors of the isovector scalar current and the $\eta\pi$ scattering phase shifts, Eur. Phys. J. C 75 (2015) 488. [arXiv:1507.04526](#).
- [140] J. Lu, B. Moussallam, The $\pi\eta$ interaction and a_0 resonances in photon–photon scattering, Eur. Phys. J. C 80 (2020) 436. [arXiv:2002.04441](#).
- [141] S. Uehara, et al. [Belle], High-statistics study of $\eta\pi^0$ production in two-photon collisions, Phys. Rev. D 80 (2009) 032001. [arXiv:0906.1464](#).
- [142] I. Danilkin, O. Deineka, M. Vanderhaeghen, Theoretical analysis of the $\gamma\gamma \rightarrow \pi^0\eta$ process, Phys. Rev. D 96 (2017) 114018. [arXiv:1709.08595](#).
- [143] M. Albaladejo, J. T. Daub, C. Hanhart, B. Kubis, B. Moussallam, How to employ $\bar{B}_d^0 \rightarrow J/\psi(\pi\eta, \bar{K}K)$ decays to extract information on $\pi\eta$ scattering, JHEP 04 (2017) 010. [arXiv:1611.03502](#).
- [144] M. Werner, et al. [Extended Twisted Mass], Hadron-Hadron Interactions from $N_f = 2 + 1 + 1$ Lattice QCD: The ρ -resonance, Eur. Phys. J. A 56 (2020) 61. [arXiv:1907.01237](#).
- [145] F. Erben, J. R. Green, D. Mohler, H. Wittig, Rho resonance, timelike pion form factor, and implications for lattice studies of the hadronic vacuum polarization, Phys. Rev. D 101 (2020) 054504. [arXiv:1910.01083](#).
- [146] M. Fischer, B. Kostrzewa, M. Mai, M. Petschlies, F. Pittler, M. Ueding, C. Urbach, M. Werner, The ρ -resonance with physical pion mass from $N_f = 2$ lattice QCD (6 2020). [arXiv:2006.13805](#).
- [147] M. Niehus, M. Hoferichter, B. Kubis, J. Ruiz de Elvira, Two-Loop Analysis of the Pion Mass Dependence of the ρ Meson, Phys. Rev. Lett. 126 (10) (2021) 102002. [arXiv:2009.04479](#).
- [148] I. J. R. Aitchison, K -matrix formalism for overlapping resonances, Nucl. Phys. A 189 (1972) 417–423.
- [149] V. V. Anisovich, A. V. Sarantsev, K matrix analysis of the $(IJ^{PC} = 00^{++})$ -wave in the mass region below 1900 MeV, Eur. Phys. J. A 16 (2003) 229–258. [arXiv:hep-ph/0204328](#).
- [150] S. M. Flatté, Coupled-Channel Analysis of the $\pi\eta$ and $K\bar{K}$ Systems Near $K\bar{K}$ Threshold, Phys. Lett. B 63 (1976) 224–227.

- [151] K. M. Watson, The Effect of final state interactions on reaction cross-sections, *Phys. Rev.* 88 (1952) 1163–1171.
- [152] R. Omnès, On the Solution of certain singular integral equations of quantum field theory, *Nuovo Cim.* 8 (1958) 316–326.
- [153] S. R. Coleman, J. Wess, B. Zumino, Structure of phenomenological Lagrangians. 1., *Phys. Rev.* 177 (1969) 2239–2247.
- [154] C. G. Callan, Jr., S. R. Coleman, J. Wess, B. Zumino, Structure of phenomenological Lagrangians. 2., *Phys. Rev.* 177 (1969) 2247–2250.
- [155] S. Weinberg, Pion scattering lengths, *Phys. Rev. Lett.* 17 (1966) 616–621.
- [156] S. Weinberg, Phenomenological Lagrangians, *Physica A*96 (1979) 327–340.
- [157] J. Gasser, H. Leutwyler, Chiral Perturbation Theory to One Loop, *Annals Phys.* 158 (1984) 142.
- [158] J. Gasser, H. Leutwyler, Chiral Perturbation Theory: Expansions in the Mass of the Strange Quark, *Nucl. Phys. B* 250 (1985) 465–516.
- [159] J. Bijnens, G. Ecker, J. Gasser, Chiral perturbation theory, in: 2nd DAPHNE Physics Handbook, 1994, pp. 125–144. [arXiv:hep-ph/9411232](#).
- [160] G. Ecker, Chiral perturbation theory, *Prog. Part. Nucl. Phys.* 35 (1995) 1–80. [arXiv:hep-ph/9501357](#).
- [161] A. Pich, Chiral perturbation theory, *Rept. Prog. Phys.* 58 (1995) 563–610. [arXiv:hep-ph/9502366](#).
- [162] A. V. Manohar, Effective field theories, *Lect. Notes Phys.* 479 (1997) 311–362. [arXiv:hep-ph/9606222](#).
- [163] S. Scherer, Introduction to chiral perturbation theory, *Adv. Nucl. Phys.* 27 (2003) 277. [arXiv:hep-ph/0210398](#).
- [164] J. Gasser, Light quark dynamics, *Lect. Notes Phys.* 629 (2004) 1–35. [arXiv:hep-ph/0312367](#).
- [165] V. Bernard, U.-G. Meißner, Chiral perturbation theory, *Ann. Rev. Nucl. Part. Sci.* 57 (2007) 33–60. [arXiv:hep-ph/0611231](#).
- [166] S. Scherer, M. R. Schindler, *A Primer for Chiral Perturbation Theory*, Vol. 830, Springer, 2012.
- [167] J. Bijnens, G. Colangelo, G. Ecker, The Mesonic chiral Lagrangian of order p^6 , *JHEP* 02 (1999) 020. [arXiv:hep-ph/9902437](#).
- [168] J. Bijnens, G. Colangelo, G. Ecker, J. Gasser, M. E. Sainio, Elastic $\pi\pi$ scattering to two loops, *Phys. Lett. B* 374 (1996) 210–216. [arXiv:hep-ph/9511397](#).
- [169] J. Bijnens, G. Colangelo, G. Ecker, J. Gasser, M. E. Sainio, Pion-pion scattering at low energy, *Nucl. Phys. B* 508 (1997) 263–310, [Erratum: *Nucl. Phys. B* 517 (1998) 639]. [arXiv:hep-ph/9707291](#).
- [170] H. Hellmann, *Einführung in die Quantenchemie*, F. Deuticke, 1937.
- [171] R. P. Feynman, Forces in Molecules, *Phys. Rev.* 56 (1939) 340–343.

- [172] J. F. Donoghue, J. Gasser, H. Leutwyler, The Decay of a Light Higgs Boson, Nucl. Phys. B 343 (1990) 341–368.
- [173] B. Moussallam, N_f dependence of the quark condensate from a chiral sum rule, Eur. Phys. J. C 14 (2000) 111–122. [arXiv:hep-ph/9909292](#).
- [174] S. Descotes-Genon, Zweig rule violation in the scalar sector and values of low-energy constants, JHEP 03 (2001) 002. [arXiv:hep-ph/0012221](#).
- [175] M. Hoferichter, C. Ditsche, B. Kubis, U.-G. Meißner, Dispersive analysis of the scalar form factor of the nucleon, JHEP 06 (2012) 063. [arXiv:1204.6251](#).
- [176] J. T. Daub, C. Hanhart, B. Kubis, A model-independent analysis of final-state interactions in $\bar{B}_{d/s}^0 \rightarrow J/\psi\pi\pi$, JHEP 02 (2016) 009. [arXiv:1508.06841](#).
- [177] J. T. Daub, H. K. Dreiner, C. Hanhart, B. Kubis, U.-G. Meißner, Improving the Hadron Physics of Non-Standard-Model Decays: Example Bounds on R-parity Violation, JHEP 01 (2013) 179. [arXiv:1212.4408](#).
- [178] A. Celis, V. Cirigliano, E. Passemar, Lepton flavor violation in the Higgs sector and the role of hadronic τ -lepton decays, Phys. Rev. D 89 (2014) 013008. [arXiv:1309.3564](#).
- [179] A. Monin, A. Boyarsky, O. Ruchayskiy, Hadronic decays of a light Higgs-like scalar, Phys. Rev. D 99 (2019) 015019. [arXiv:1806.07759](#).
- [180] M. W. Winkler, Decay and detection of a light scalar boson mixing with the Higgs boson, Phys. Rev. D 99 (2019) 015018. [arXiv:1809.01876](#).
- [181] G. Colangelo, J. Gasser, H. Leutwyler, The $\pi\pi$ S -wave scattering lengths, Phys. Lett. B 488 (2000) 261–268. [arXiv:hep-ph/0007112](#).
- [182] J. R. Batley, et al., Determination of the S -wave $\pi\pi$ scattering lengths from a study of $K^\pm \rightarrow \pi^\pm\pi^0\pi^0$ decays, Eur. Phys. J. C 64 (2009) 589–608. [arXiv:0912.2165](#).
- [183] M. Bissegger, A. Fuhrer, J. Gasser, B. Kubis, A. Rusetsky, Radiative corrections in $K \rightarrow 3\pi$ decays, Nucl. Phys. B 806 (2009) 178–223. [arXiv:0807.0515](#).
- [184] G. Colangelo, J. Gasser, A. Rusetsky, Isospin breaking in K_{l4} decays, Eur. Phys. J. C 59 (2009) 777–793. [arXiv:0811.0775](#).
- [185] G. Ecker, J. Gasser, A. Pich, E. de Rafael, The Role of Resonances in Chiral Perturbation Theory, Nucl. Phys. B 321 (1989) 311–342.
- [186] J. F. Donoghue, C. Ramirez, G. Valencia, The Spectrum of QCD and Chiral Lagrangians of the Strong and Weak Interactions, Phys. Rev. D 39 (1989) 1947.
- [187] R. J. Eden, P. V. Landshoff, D. I. Olive, J. C. Polkinghorne, The analytic S-matrix, Cambridge Univ. Press, Cambridge, 1966.
- [188] J. A. Oller, A Brief Introduction to Dispersion Relations, SpringerBriefs in Physics, Springer, 2019.
- [189] T. N. Truong, Chiral Perturbation Theory and Final State Theorem, Phys. Rev. Lett. 61 (1988) 2526.

- [190] A. Dobado, M. J. Herrero, T. N. Truong, Unitarized Chiral Perturbation Theory for Elastic Pion–Pion Scattering, *Phys. Lett. B* 235 (1990) 134–140.
- [191] T. N. Truong, Remarks on the unitarization methods, *Phys. Rev. Lett.* 67 (1991) 2260–2263.
- [192] A. Dobado, J. R. Peláez, A Global fit of $\pi\pi$ and πK elastic scattering in ChPT with dispersion relations, *Phys. Rev. D* 47 (1993) 4883–4888. [arXiv:hep-ph/9301276](#).
- [193] A. Dobado, J. R. Peláez, The Inverse amplitude method in chiral perturbation theory, *Phys. Rev. D* 56 (1997) 3057–3073. [arXiv:hep-ph/9604416](#).
- [194] F. Guerrero, J. A. Oller, $K\bar{K}$ scattering amplitude to one loop in chiral perturbation theory, its unitarization and pion form factors, *Nucl. Phys. B* 537 (1999) 459–476, [Erratum: *Nucl. Phys. B* 602 (2001) 641]. [arXiv:hep-ph/9805334](#).
- [195] J. Nieves, M. Pavón Valderrama, E. Ruiz Arriola, The Inverse amplitude method in $\pi\pi$ scattering in chiral perturbation theory to two loops, *Phys. Rev. D* 65 (2002) 036002. [arXiv:hep-ph/0109077](#).
- [196] Y.-J. Shi, C.-Y. Seng, F.-K. Guo, B. Kubis, U.-G. Meißner, W. Wang, Two-Meson Form Factors in Unitarized Chiral Perturbation Theory, *JHEP* 04 (2021) 086. [arXiv:2011.00921](#).
- [197] S. M. Roy, Exact integral equation for pion–pion scattering involving only physical region partial waves, *Phys. Lett. B* 36 (1971) 353–356.
- [198] S. M. Roy, Pion–pion scattering, *Helv. Phys. Acta* 63 (1990) 627–659.
- [199] R. Kamiński, J. R. Peláez, F. J. Ynduráin, The pion–pion scattering amplitude. III. Improving the analysis with forward dispersion relations and Roy equations, *Phys. Rev. D* 77 (2008) 054015. [arXiv:0710.1150](#).
- [200] G. E. Hite, F. Steiner, New dispersion relations and their application to partial-wave amplitudes, *Nuovo Cim. A* 18 (1973) 237–270.
- [201] M. Hoferichter, D. R. Phillips, C. Schat, Roy–Steiner equations for $\gamma\gamma \rightarrow \pi\pi$, *Eur. Phys. J. C* 71 (2011) 1743. [arXiv:1106.4147](#).
- [202] C. Ditsche, M. Hoferichter, B. Kubis, U.-G. Meißner, Roy–Steiner equations for pion–nucleon scattering, *JHEP* 06 (2012) 043. [arXiv:1203.4758](#).
- [203] M. Hoferichter, J. Ruiz de Elvira, B. Kubis, U.-G. Meißner, Roy–Steiner-equation analysis of pion–nucleon scattering, *Phys. Rept.* 625 (2016) 1–88. [arXiv:1510.06039](#).
- [204] R. H. Dalitz, On the analysis of τ -meson data and the nature of the τ -meson, *Phil. Mag. Ser. 7* 44 (1953) 1068–1080.
- [205] R. M. Sternheimer, S. J. Lindenbaum, Extension of the Isobaric Nucleon Model for Pion Production in Pion–Nucleon, Nucleon–Nucleon, and Antinucleon–Nucleon Interactions, *Phys. Rev.* 123 (1961) 333–376.
- [206] D. Herndon, P. Soding, R. J. Cashmore, A Generalized Isobar Model Formalism, *Phys. Rev. D* 11 (1975) 3165.
- [207] N. N. Khuri, S. B. Treiman, Pion–Pion Scattering and $K^\pm \rightarrow 3\pi$ Decay, *Phys. Rev.* 119 (1960) 1115–1121.

- [208] M. Mai, B. Hu, M. Doring, A. Pilloni, A. Szczepaniak, Three-body Unitarity with Isobars Revisited, *Eur. Phys. J. A* 53 (2017) 177. [arXiv:1706.06118](#).
- [209] D. Sadasivan, M. Mai, H. Akdag, M. Döring, Dalitz plots and lineshape of $a_1(1260)$ from a relativistic three-body unitary approach, *Phys. Rev. D* 101 (2020) 094018. [arXiv:2002.12431](#).
- [210] A. Jackura, C. Fernández-Ramírez, V. Mathieu, M. Mikhasenko, J. Nys, A. Pilloni, K. Saldaña, N. Sherrill, A. P. Szczepaniak [JPAC], Phenomenology of Relativistic $\mathbf{3} \rightarrow \mathbf{3}$ Reaction Amplitudes within the Isobar Approximation, *Eur. Phys. J. C* 79 (2019) 56. [arXiv:1809.10523](#).
- [211] M. Mikhasenko, Y. Wunderlich, A. Jackura, V. Mathieu, A. Pilloni, B. Ketzer, A. P. Szczepaniak, Three-body scattering: Ladders and Resonances, *JHEP* 08 (2019) 080. [arXiv:1904.11894](#).
- [212] A. W. Jackura, S. M. Dawid, C. Fernández-Ramírez, V. Mathieu, M. Mikhasenko, A. Pilloni, S. R. Sharpe, A. P. Szczepaniak, Equivalence of three-particle scattering formalisms, *Phys. Rev. D* 100 (2019) 034508. [arXiv:1905.12007](#).
- [213] R. Poling, CLEO-c hot topics, eConf C060409 (2006) 005. [arXiv:hep-ex/0606016](#).
- [214] A. J. Bevan, et al. [BaBar, Belle], The Physics of the B Factories, *Eur. Phys. J. C* 74 (2014) 3026. [arXiv:1406.6311](#).
- [215] B. Aubert, et al. [BaBar], The BaBar detector, *Nucl. Instrum. Meth. A* 479 (2002) 1–116. [arXiv:hep-ex/0105044](#).
- [216] M. Zobov, et al., Test of crab-waist collisions at DAΦNE Φ factory, *Phys. Rev. Lett.* 104 (2010) 174801.
- [217] D. Sirghi, et al., Studies of kaonic atoms at the DAΦNE collider: from SIDDHARTA to SIDDHARTA-2, *J. Phys. Conf. Ser.* 1526 (2020) 012023.
- [218] M. Adinolfi, et al., The tracking detector of the KLOE experiment, *Nucl. Instrum. Meth. A* 488 (2002) 51–73.
- [219] M. Adinolfi, et al., The KLOE electromagnetic calorimeter, *Nucl. Instrum. Meth. A* 482 (2002) 364–386.
- [220] A. Balla, et al., Construction and test of the cylindrical-GEM detectors for the KLOE-2 Inner Tracker, *Nucl. Instrum. Meth. A* 732 (2013) 221–224.
- [221] P. Franzini, M. Moulson, The Physics of DAΦNE and KLOE, *Ann. Rev. Nucl. Part. Sci.* 56 (2006) 207–251. [arXiv:hep-ex/0606033](#).
- [222] F. Bossi, E. De Lucia, J. Lee-Franzini, S. Miscetti, M. Palutan [KLOE], Precision Kaon and Hadron Physics with KLOE, *Riv. Nuovo Cim.* 31 (2008) 531–623. [arXiv:0811.1929](#).
- [223] G. Amelino-Camelia, et al., Physics with the KLOE-2 experiment at the upgraded DAΦNE, *Eur. Phys. J. C* 68 (2010) 619–681. [arXiv:1003.3868](#).
- [224] J. Z. Bai, et al. [BES], The BES detector, *Nucl. Instrum. Meth. A* 344 (1994) 319–334.
- [225] J. Z. Bai, et al. [BES], The BES upgrade, *Nucl. Instrum. Meth. A* 458 (2001) 627–637.
- [226] Y.-N. Guo, Status and upgrade of BEPC/BES, *Nucl. Instrum. Meth. A* 379 (1996) 349–353.

- [227] J. Z. Bai, et al. [BES], Measurement of the total cross-section for hadronic production by e^+e^- annihilation at energies between 2.6 GeV–5 GeV, Phys. Rev. Lett. 84 (2000) 594–597. [arXiv:hep-ex/9908046](#).
- [228] J. Z. Bai, et al. [BES], Observation of a near threshold enhancement in the $p\bar{p}$ mass spectrum from radiative $J/\psi \rightarrow \gamma p\bar{p}$ decays, Phys. Rev. Lett. 91 (2003) 022001. [arXiv:hep-ex/0303006](#).
- [229] M. Ablikim, et al. [BESIII], Design and Construction of the BESIII Detector, Nucl. Instrum. Meth. A 614 (2010) 345–399. [arXiv:0911.4960](#).
- [230] R. A. Briere, F. A. Harris, R. E. Mitchell, Physics Accomplishments and Future Prospects of the BES Experiments at the Beijing Electron–Positron Collider, Ann. Rev. Nucl. Part. Sci. 66 (2016) 143–170. [arXiv:1603.09431](#).
- [231] C.-Z. Yuan, S. L. Olsen, The BESIII physics programme, Nature Rev. Phys. 1 (2019) 480–494. [arXiv:2001.01164](#).
- [232] R. R. Akhmetshin, et al. [CMD-2], Status of experiments and recent results from CMD-2 detector at VEPP-2M, Nucl. Phys. A 675 (2000) 424C–431C.
- [233] V. M. Aulchenko, B. O. Baibusinov, A. E. Bondar, A. S. Kuzmin, L. A. Leontev, V. S. Okhapkin, L. V. Pestsov, V. P. Smakhtin, A. I. Sukhanov, B. A. Shwartz, CMD-2 barrel calorimeter, Nucl. Instrum. Meth. A 336 (1993) 53–58.
- [234] S. I. Dolinsky, et al., Summary of experiments with the neutral detector at the e^+e^- storage ring VEPP-2M, Phys. Rept. 202 (1991) 99–170.
- [235] M. N. Achasov, et al., Spherical neutral detector for VEPP-2M collider, Nucl. Instrum. Meth. A 449 (2000) 125–139. [arXiv:hep-ex/9909015](#).
- [236] B. Khazin, Physics and detectors for VEPP-2000, Nucl. Phys. B Proc. Suppl. 181-182 (2008) 376–380.
- [237] V. V. Ezhela, S. B. Lugovsky, O. V. Zenin, Hadronic part of the muon $g - 2$ estimated on the $\sigma_{\text{tot}}^{2003}(e^+e^- \rightarrow \text{hadrons})$ evaluated data compilation (2003). [arXiv:hep-ph/0312114](#).
- [238] H. Czyż, J. H. Kühn, Four pion final states with tagged photons at electron positron colliders, Eur. Phys. J. C 18 (2001) 497–509. [arXiv:hep-ph/0008262](#).
- [239] L. Gan, B. Kubis, E. Passemar, S. Tulin, Precision tests of fundamental physics with η and η' mesons (7 2020). [arXiv:2007.00664](#).
- [240] V. P. Druzhinin, S. I. Eidelman, S. I. Serednyakov, E. P. Solodov, Hadron Production via e^+e^- Collisions with Initial State Radiation, Rev. Mod. Phys. 83 (2011) 1545. [arXiv:1105.4975](#).
- [241] I. Danilkin, C. F. Redmer, M. Vanderhaeghen, The hadronic light-by-light contribution to the muon’s anomalous magnetic moment, Prog. Part. Nucl. Phys. 107 (2019) 20–68. [arXiv:1901.10346](#).
- [242] S. Binner, J. H. Kühn, K. Melnikov, Measuring $\sigma(e^+e^- \rightarrow \text{hadrons})$ using tagged photon, Phys. Lett. B 459 (1999) 279–287. [arXiv:hep-ph/9902399](#).
- [243] A. Aloisio, et al. [KLOE], Measurement of $\sigma(e^+e^- \rightarrow \pi^+\pi^-\gamma)$ and extraction of $\sigma(e^+e^- \rightarrow \pi^+\pi^-)$ below 1 GeV with the KLOE detector, Phys. Lett. B 606 (2005) 12–24. [arXiv:hep-ex/0407048](#).

- [244] J. H. Kühn, G. Rodrigo, The Radiative return at small angles: Virtual corrections, *Eur. Phys. J. C* 25 (2002) 215–222. [arXiv:hep-ph/0204283](#).
- [245] S. J. Brodsky, T. Kinoshita, H. Terazawa, Dominant colliding beam cross-sections at high-energies, *Phys. Rev. Lett.* 25 (1970) 972–975.
- [246] S. J. Brodsky, T. Kinoshita, H. Terazawa, Two Photon Mechanism of Particle Production by High-Energy Colliding Beams, *Phys. Rev. D* 4 (1971) 1532–1557.
- [247] C.-N. Yang, Selection Rules for the Dematerialization of a Particle Into Two Photons, *Phys. Rev.* 77 (1950) 242–245.
- [248] M. Hoferichter, B. Kubis, S. Leupold, F. Niecknig, S. P. Schneider, Dispersive analysis of the pion transition form factor, *Eur. Phys. J. C* 74 (2014) 3180. [arXiv:1410.4691](#).
- [249] M. Hoferichter, B.-L. Hoid, B. Kubis, S. Leupold, S. P. Schneider, Pion-pole contribution to hadronic light-by-light scattering in the anomalous magnetic moment of the muon, *Phys. Rev. Lett.* 121 (2018) 112002. [arXiv:1805.01471](#).
- [250] M. Hoferichter, B.-L. Hoid, B. Kubis, S. Leupold, S. P. Schneider, Dispersion relation for hadronic light-by-light scattering: pion pole, *JHEP* 10 (2018) 141. [arXiv:1808.04823](#).
- [251] M. Benayoun, S. Eidelman, K. Maltman, H. B. O’Connell, B. Shwartz, A. G. Williams, New results in ρ^0 meson physics, *Eur. Phys. J. C* 2 (1998) 269–286. [arXiv:hep-ph/9707509](#).
- [252] V. V. Anashin, et al., Measurement of the τ lepton mass at the KEDR detector, *JETP Lett.* 85 (2007) 347–352.
- [253] T. Luo [BESIII], Precision Measurement of the Mass of the τ Lepton at BESIII, *Nucl. Part. Phys. Proc.* 260 (2015) 23–26.
- [254] Y.-S. Tsai, Decay Correlations of Heavy Leptons in $e^+e^- \rightarrow \ell^+\ell^-$, *Phys. Rev. D* 4 (1971) 2821, [Erratum: *Phys. Rev. D* 13 (1976) 771].
- [255] N. Cabibbo, Unitary Symmetry and Leptonic Decays, *Phys. Rev. Lett.* 10 (1963) 531–533.
- [256] M. Davier, A. Hoecker, Z. Zhang, The Physics of Hadronic Tau Decays, *Rev. Mod. Phys.* 78 (2006) 1043–1109. [arXiv:hep-ph/0507078](#).
- [257] A. Pich, Precision Tau Physics, *Prog. Part. Nucl. Phys.* 75 (2014) 41–85. [arXiv:1310.7922](#).
- [258] M. Artuso, B. Meadows, A. A. Petrov, Charm Meson Decays, *Ann. Rev. Nucl. Part. Sci.* 58 (2008) 249–291. [arXiv:0802.2934](#).
- [259] M. Ablikim, et al. [BESIII], Measurement of $e^+e^- \rightarrow D\bar{D}$ cross sections at the $\psi(3770)$ resonance, *Chin. Phys. C* 42 (2018) 083001. [arXiv:1803.06293](#).
- [260] D. Cronin-Hennessy, et al. [CLEO], Measurement of Charm Production Cross Sections in e^+e^- Annihilation at Energies between 3.97 and 4.26 GeV, *Phys. Rev. D* 80 (2009) 072001. [arXiv:0801.3418](#).
- [261] R. M. Baltrusaitis, et al. [MARK-III], Direct Measurements of Charmed D -Meson Hadronic Branching Fractions, *Phys. Rev. Lett.* 56 (1986) 2140.

- [262] J. Adler, et al. [MARK-III], A Reanalysis of Charmed D Meson Branching Fractions, Phys. Rev. Lett. 60 (1988) 89.
- [263] H. Albrecht, et al. [ARGUS], Search for Hadronic $b \rightarrow u$ Decays, Phys. Lett. B 241 (1990) 278–282.
- [264] E. A. Kuraev, V. S. Fadin, On Radiative Corrections to e^+e^- Single Photon Annihilation at High-Energy, Sov. J. Nucl. Phys. 41 (1985) 466–472, [Yad. Fiz.41 (1985) 733].
- [265] G. Montagna, O. Nicosini, F. Piccinini, The QED radiator at order α^3 , Phys. Lett. B 406 (1997) 243–248. [arXiv:hep-ph/9611463](#).
- [266] S. Actis, et al. [Working Group on Radiative Corrections and Monte Carlo Generators for Low Energies], Quest for precision in hadronic cross sections at low energy: Monte Carlo tools vs. experimental data, Eur. Phys. J. C 66 (2010) 585–686. [arXiv:0912.0749](#).
- [267] V. L. Ivanov, et al., Study of the process $e^+e^- \rightarrow K^+K^-\eta$ with the CMD-3 detector at the VEPP-2000 collider, Phys. Lett. B 798 (2019) 134946. [arXiv:1906.08006](#).
- [268] T. Aoyama, M. Hayakawa, T. Kinoshita, M. Nio, Tenth-Order QED Contribution to the Electron $g-2$ and an Improved Value of the Fine Structure Constant, Phys. Rev. Lett. 109 (2012) 111807. [arXiv:1205.5368](#).
- [269] T. Aoyama, T. Kinoshita, M. Nio, Revised and Improved Value of the QED Tenth-Order Electron Anomalous Magnetic Moment, Phys. Rev. D 97 (2018) 036001. [arXiv:1712.06060](#).
- [270] R. H. Parker, C. Yu, W. Zhong, B. Estey, H. Müller, Measurement of the fine-structure constant as a test of the Standard Model, Science 360 (2018) 191. [arXiv:1812.04130](#).
- [271] L. Morel, Z. Yao, P. Cladé, S. Guellati-Khélifa, Determination of the fine-structure constant with an accuracy of 81 parts per trillion, Nature 588 (2020) 61–65.
- [272] F. Jegerlehner, Hadronic contributions to the photon vacuum polarization and their role in precision physics, J. Phys. G 29 (2003) 101–110. [arXiv:hep-ph/0104304](#).
- [273] M. Ablikim, et al. [BESIII], Measurement of the phase between strong and electromagnetic amplitudes of J/ψ decays, Phys. Lett. B 791 (2019) 375–384. [arXiv:1808.02166](#).
- [274] F. Jegerlehner, Precision measurements of σ_{hadronic} for $\alpha_{\text{eff}}(E)$ at ILC energies and $(g-2)_\mu$, Nucl. Phys. Proc. Suppl. 162 (2006) 22–32. [arXiv:hep-ph/0608329](#).
- [275] F. Jegerlehner, Electroweak effective couplings for future precision experiments, Nuovo Cim. C 034S1 (2011) 31–40. [arXiv:1107.4683](#).
- [276] A. Anastasi, et al. [KLOE-2], Measurement of the running of the fine structure constant below 1 GeV with the KLOE Detector, Phys. Lett. B 767 (2017) 485–492. [arXiv:1609.06631](#).
- [277] G. J. Gounaris, J. J. Sakurai, Finite width corrections to the vector meson dominance prediction for $\rho \rightarrow e^+e^-$, Phys. Rev. Lett. 21 (1968) 244–247.
- [278] A. Heister, et al. [ALEPH], Inclusive production of the ω and η mesons in Z decays, and the muonic branching ratio of the ω , Phys. Lett. B 528 (2002) 19–33. [arXiv:hep-ex/0201012](#).
- [279] A. Sommerfeld, Atombau und Spektrallinien, F. Vieweg & Sohn, 1921.
- [280] G. Gamow, Zur Quantentheorie des Atomkernes, Z. Phys. 51 (1928) 204–212.

- [281] A. D. Sakharov, Interaction of an Electron and Positron in Pair Production, *Sov. Phys. Usp.* 34 (1991) 375–377.
- [282] G. R. Farrar, D. R. Jackson, The Pion Form-Factor, *Phys. Rev. Lett.* 43 (1979) 246.
- [283] G. P. Lepage, S. J. Brodsky, Exclusive Processes in Quantum Chromodynamics: Evolution Equations for Hadronic Wave Functions and the Form-Factors of Mesons, *Phys. Lett. B* 87 (1979) 359–365.
- [284] V. L. Chernyak, A. R. Zhitnitsky, Asymptotic Behavior of Exclusive Processes in QCD, *Phys. Rept.* 112 (1984) 173.
- [285] R. R. Akhmetshin, et al. [CMD-2], Reanalysis of hadronic cross-section measurements at CMD-2, *Phys. Lett. B* 578 (2004) 285–289. [arXiv:hep-ex/0308008](#).
- [286] R. R. Akhmetshin, et al. [CMD-2], Measurement of $e^+e^- \rightarrow \phi \rightarrow K^+K^-$ cross section with the CMD-2 detector at VEPP-2M Collider, *Phys. Lett. B* 669 (2008) 217–222. [arXiv:0804.0178](#).
- [287] M. N. Achasov, et al., Study of the process $e^+e^- \rightarrow \pi^+\pi^-$ in the energy region $400 < s^{1/2} < 1000$ MeV, *J. Exp. Theor. Phys.* 101 (2005) 1053–1070. [arXiv:hep-ex/0506076](#).
- [288] F. Ambrosino, et al. [KLOE], Measurement of $\sigma(e^+e^- \rightarrow \pi^+\pi^-\gamma(\gamma))$ and the dipion contribution to the muon anomaly with the KLOE detector, *Phys. Lett. B* 670 (2009) 285–291. [arXiv:0809.3950](#).
- [289] F. Ambrosino, et al. [KLOE], Measurement of $\sigma(e^+e^- \rightarrow \pi^+\pi^-)$ from threshold to 0.85 GeV^2 using Initial State Radiation with the KLOE detector, *Phys. Lett. B* 700 (2011) 102–110. [arXiv:1006.5313](#).
- [290] D. Babusci, et al. [KLOE], Precision measurement of $\sigma(e^+e^- \rightarrow \pi^+\pi^-\gamma)/\sigma(e^+e^- \rightarrow \mu^+\mu^-\gamma)$ and determination of the $\pi^+\pi^-$ contribution to the muon anomaly with the KLOE detector, *Phys. Lett. B* 720 (2013) 336–343. [arXiv:1212.4524](#).
- [291] B. Aubert, et al. [BaBar], Precise measurement of the $e^+e^- \rightarrow \pi^+\pi^-(\gamma)$ cross section with the Initial State Radiation method at BaBar, *Phys. Rev. Lett.* 103 (2009) 231801. [arXiv:0908.3589](#).
- [292] J. P. Lees, et al. [BaBar], Precise Measurement of the $e^+e^- \rightarrow \pi^+\pi^-(\gamma)$ Cross Section with the Initial-State Radiation Method at BaBar, *Phys. Rev. D* 86 (2012) 032013. [arXiv:1205.2228](#).
- [293] M. Ablikim, et al. [BESIII], Measurement of the $e^+e^- \rightarrow \pi^+\pi^-$ cross section between 600 and 900 MeV using initial state radiation, *Phys. Lett. B* 753 (2016) 629–638. [arXiv:1507.08188](#).
- [294] S. R. Amendolia, et al., Measurement of the Pion Form-factor in the Timelike Region for q^2 Values Between $0.1 \text{ GeV}/c^2$ and $0.18 \text{ GeV}/c^2$, *Phys. Lett. B* 138 (1984) 454–458.
- [295] M. Davier, A. Hoecker, B. Malaescu, Z. Zhang, Reevaluation of the hadronic vacuum polarisation contributions to the Standard Model predictions of the muon $g - 2$ and $\alpha(m_Z^2)$ using newest hadronic cross-section data, *Eur. Phys. J. C* 77 (2017) 827. [arXiv:1706.09436](#).
- [296] A. Keshavarzi, D. Nomura, T. Teubner, Muon $g - 2$ and $\alpha(M_Z^2)$: a new data-based analysis, *Phys. Rev. D* 97 (2018) 114025. [arXiv:1802.02995](#).
- [297] M. Davier, A. Hoecker, B. Malaescu, Z. Zhang, A new evaluation of the hadronic vacuum polarisation contributions to the muon anomalous magnetic moment and to $\alpha(m_Z^2)$, *Eur. Phys. J. C* 80 (2020) 241, [Erratum: *Eur. Phys. J. C* 80 (2020) 410]. [arXiv:1908.00921](#).

- [298] A. Keshavarzi, D. Nomura, T. Teubner, $g - 2$ of charged leptons, $\alpha(M_Z^2)$, and the hyperfine splitting of muonium, Phys. Rev. D 101 (2020) 014029. [arXiv:1911.00367](#).
- [299] H. Leutwyler, Electromagnetic form factor of the pion, in: Continuous Advances in QCD 2002 / Arkadyfest (honoring the 60th birthday of Prof. Arkady Vainshtein), 2002, pp. 23–40. [arXiv:hep-ph/0212324](#).
- [300] G. Colangelo, Hadronic contributions to a_μ below one GeV, Nucl. Phys. B Proc. Suppl. 131 (2004) 185–191. [arXiv:hep-ph/0312017](#).
- [301] C. Bruch, A. Khodjamirian, J. H. Kühn, Modeling the pion and kaon form factors in the timelike region, Eur. Phys. J. C 39 (2005) 41–54. [arXiv:hep-ph/0409080](#).
- [302] J. H. Kühn, A. Santamaria, Tau decays to pions, Z. Phys. C 48 (1990) 445–452.
- [303] C. Hanhart, S. Holz, B. Kubis, A. Kupść, A. Wirzba, C.-W. Xiao, The branching ratio $\omega \rightarrow \pi^+\pi^-$ revisited, Eur. Phys. J. C 77 (2017) 98, [Erratum: Eur. Phys. J. C 78 (2018) 450]. [arXiv:1611.09359](#).
- [304] L. M. Barkov, et al., Electromagnetic Pion Form-Factor in the Timelike Region, Nucl. Phys. B 256 (1985) 365–384.
- [305] C. Hanhart, A New Parameterization for the Pion Vector Form Factor, Phys. Lett. B 715 (2012) 170–177. [arXiv:1203.6839](#).
- [306] V. Cirigliano, G. Ecker, H. Neufeld, Isospin violation and the magnetic moment of the muon, Phys. Lett. B 513 (2001) 361–370. [arXiv:hep-ph/0104267](#).
- [307] V. Cirigliano, G. Ecker, H. Neufeld, Radiative tau decay and the magnetic moment of the muon, JHEP 08 (2002) 002. [arXiv:hep-ph/0207310](#).
- [308] R. Alemany, M. Davier, A. Hoecker, Improved determination of the hadronic contribution to the muon ($g - 2$) and to $\alpha(M_Z^2)$ using new data from hadronic τ decays, Eur. Phys. J. C 2 (1998) 123–135. [arXiv:hep-ph/9703220](#).
- [309] M. Davier, A. Hoecker, G. López Castro, B. Malaescu, X.-H. Mo, G. Toledo Sánchez, P. Wang, C.-Z. Yuan, Z. Zhang, The Discrepancy Between tau and e^+e^- Spectral Functions Revisited and the Consequences for the Muon Magnetic Anomaly, Eur. Phys. J. C 66 (2010) 127–136. [arXiv:0906.5443](#).
- [310] F. Jegerlehner, R. Szafron, $\rho^0 - \gamma$ mixing in the neutral channel pion form factor F_π^e and its role in comparing e^+e^- with τ spectral functions, Eur. Phys. J. C 71 (2011) 1632. [arXiv:1101.2872](#).
- [311] S. Anderson, et al. [CLEO], Hadronic structure in the decay $\tau^- \rightarrow \pi^-\pi^0\nu_\tau$, Phys. Rev. D 61 (2000) 112002. [arXiv:hep-ex/9910046](#).
- [312] S. Schael, et al. [ALEPH], Branching ratios and spectral functions of τ decays: Final ALEPH measurements and physics implications, Phys. Rept. 421 (2005) 191–284. [arXiv:hep-ex/0506072](#).
- [313] M. Fujikawa, et al. [Belle], High-Statistics Study of the $\tau^- \rightarrow \pi^-\pi^0\nu_\tau$ Decay, Phys. Rev. D 78 (2008) 072006. [arXiv:0805.3773](#).
- [314] E. B. Dally, et al., Direct measurement of the negative kaon form factor, Phys. Rev. Lett. 45 (1980) 232–235.

- [315] S. R. Amendolia, et al., A Measurement of the Kaon Charge Radius, Phys. Lett. B 178 (1986) 435–440.
- [316] E. A. Kozyrev, et al. [CMD-3], Study of the process $e^+e^- \rightarrow K_S^0 K_L^0$ in the center-of-mass energy range 1004–1060 MeV with the CMD-3 detector at the VEPP-2000 e^+e^- collider, Phys. Lett. B 760 (2016) 314–319. [arXiv:1604.02981](#).
- [317] E. A. Kozyrev, et al., Study of the process $e^+e^- \rightarrow K^+K^-$ in the center-of-mass energy range 1010–1060 MeV with the CMD-3 detector, Phys. Lett. B 779 (2018) 64–71. [arXiv:1710.02989](#).
- [318] J. P. Lees, et al. [BaBar], Precision measurement of the $e^+e^- \rightarrow K^+K^-(\gamma)$ cross section with the initial-state radiation method at BaBar, Phys. Rev. D 88 (2013) 032013. [arXiv:1306.3600](#).
- [319] A. Bramon, R. Escribano, J. L. Lucio M., G. Pancheri, The Ratio $\phi \rightarrow K^+K^-/K^0\bar{K}^0$, Phys. Lett. B 486 (2000) 406–413. [arXiv:hep-ph/0003273](#).
- [320] F. V. Flores-Baéz, G. López Castro, Structure-dependent radiative corrections to $\phi \rightarrow K^+K^-/K_L K_S$ decays, Phys. Rev. D 78 (2008) 077301. [arXiv:0810.4349](#).
- [321] M. Benayoun, P. David, L. DelBuono, F. Jegerlehner, Upgraded Breaking Of The HLS Model: A Full Solution to the $\tau^-e^+e^-$ and ϕ Decay Issues And Its Consequences On $g-2$ VMD Estimates, Eur. Phys. J. C 72 (2012) 1848. [arXiv:1106.1315](#).
- [322] M. N. Achasov, et al., Measurement of the $e^+e^- \rightarrow K^+K^-$ cross section in the energy range $\sqrt{s} = 1.05 - 2.0$ GeV, Phys. Rev. D 94 (2016) 112006. [arXiv:1608.08757](#).
- [323] J. P. Lees, et al. [BaBar], Cross sections for the reactions $e^+e^- \rightarrow K_S^0 K_L^0$, $K_S^0 K_L^0 \pi^+ \pi^-$, $K_S^0 K_S^0 \pi^+ \pi^-$, and $K_S^0 K_S^0 K^+ K^-$ from events with initial-state radiation, Phys. Rev. D 89 (2014) 092002. [arXiv:1403.7593](#).
- [324] M. N. Achasov, et al., Measurement of the $e^+e^- \rightarrow K^+K^-$ process cross-section in the energy range $\sqrt{s} = 1.04 - 1.38$ GeV with the SND detector in the experiment at VEPP-2M e^+e^- collider, Phys. Rev. D 76 (2007) 072012. [arXiv:0707.2279](#).
- [325] R. R. Akhmetshin, et al., Study of the process $e^+e^- \rightarrow K_L^0 K_S^0$ in the CM energy range 1.05 GeV to 1.38 GeV with CMD-2, Phys. Lett. B 551 (2003) 27–34. [arXiv:hep-ex/0211004](#).
- [326] M. N. Achasov, et al., Experimental study of the reaction $e^+e^- \rightarrow K_S K_L$ in the energy range $\sqrt{s} = 1.04$ GeV to 1.38 GeV, J. Exp. Theor. Phys. 103 (2006) 720–727, [Zh. Eksp. Teor. Fiz. 130 (2006) 831]. [arXiv:hep-ex/0606057](#).
- [327] K. I. Beloborodov, V. P. Druzhinin, S. I. Serednyakov, Isoscalar and Isovector Kaon Form Factors from e^+e^- and τ Data, J. Exp. Theor. Phys. 129 (2019) 386–390.
- [328] M. Ablikim, et al. [BESIII], Measurement of $e^+e^- \rightarrow K^+K^-$ cross section at $\sqrt{s} = 2.00-3.08$ GeV, Phys. Rev. D 99 (2019) 032001. [arXiv:1811.08742](#).
- [329] J. P. Lees, et al. [BaBar], Measurement of the spectral function for the $\tau^- \rightarrow K^- K_S \nu_\tau$ decay, Phys. Rev. D 98 (2018) 032010. [arXiv:1806.10280](#).
- [330] J. P. Lees, et al. [BaBar], Resonances in e^+e^- annihilation near 2.2 GeV, Phys. Rev. D 101 (2020) 012011. [arXiv:1912.04512](#).
- [331] J. P. Lees, et al. [BaBar], Study of the $e^+e^- \rightarrow K^+K^-$ reaction in the energy range from 2.6 to 8.0 GeV, Phys. Rev. D 92 (2015) 072008. [arXiv:1507.04638](#).

- [332] S. González-Solís, P. Roig, A dispersive analysis of the pion vector form factor and $\tau^- \rightarrow K^- K_S \nu_\tau$ decay, *Eur. Phys. J. C* 79 (2019) 436. [arXiv:1902.02273](#).
- [333] L. G. Landsberg, Electromagnetic Decays of Light Mesons, *Phys. Rept.* 128 (1985) 301–376.
- [334] S. Pacetti, A Practical guide to unravel time-like transition form-factors, *Eur. Phys. J. A* 38 (2008) 331–343. [arXiv:0807.1399](#).
- [335] C. Hanhart, A. Kupść, U.-G. Meißner, F. Stollenwerk, A. Wirzba, Dispersive analysis for $\eta \rightarrow \gamma\gamma^*$, *Eur. Phys. J. C* 73 (2013) 2668, [Erratum: *Eur. Phys. J. C* 75 (2015) 242]. [arXiv:1307.5654](#).
- [336] G. Colangelo, M. Hoferichter, B. Kubis, M. Procura, P. Stoffer, Towards a data-driven analysis of hadronic light-by-light scattering, *Phys. Lett. B* 738 (2014) 6–12. [arXiv:1408.2517](#).
- [337] C. Terschläsen, S. Leupold, Electromagnetic transition form factors of light vector mesons, *Phys. Lett. B* 691 (2010) 191–201. [arXiv:1003.1030](#).
- [338] C. Terschläsen, S. Leupold, M. F. M. Lutz, Electromagnetic Transitions in an Effective Chiral Lagrangian with the η' and Light Vector Mesons, *Eur. Phys. J. A* 48 (2012) 190. [arXiv:1204.4125](#).
- [339] Y.-H. Chen, Z.-H. Guo, H.-Q. Zheng, Radiative transition processes of light vector resonances in a chiral framework, *Phys. Rev. D* 90 (2014) 034013. [arXiv:1311.3366](#).
- [340] Y.-H. Chen, Z.-H. Guo, B.-S. Zou, Unified study of $J/\psi \rightarrow PV$, $P\gamma^{(*)}$ and light hadron radiative processes, *Phys. Rev. D* 91 (2015) 014010. [arXiv:1411.1159](#).
- [341] M. N. Achasov, et al., The Process $e^+e^- \rightarrow \omega\pi^0 \rightarrow \pi^0\pi^0\gamma$ up to 1.4 GeV, *Phys. Lett. B* 486 (2000) 29–34. [arXiv:hep-ex/0005032](#).
- [342] M. N. Achasov, et al., Updated measurement of the $e^+e^- \rightarrow \omega\pi^0 \rightarrow \pi^0\pi^0\gamma$ cross section with the SND detector, *Phys. Rev. D* 94 (2016) 112001. [arXiv:1610.00235](#).
- [343] R. R. Akhmetshin, et al. [CMD-2], Study of the process $e^+e^- \rightarrow \omega\pi^0 \rightarrow \pi^0\pi^0\gamma$ in c.m. energy range 920 MeV–1380 MeV at CMD-2, *Phys. Lett. B* 562 (2003) 173–181. [arXiv:hep-ex/0304009](#).
- [344] J. P. Lees, et al. [BaBar], Measurement of the $e^+e^- \rightarrow \pi^+\pi^-\pi^0\pi^0$ cross section using initial-state radiation at BaBar, *Phys. Rev. D* 96 (2017) 092009. [arXiv:1709.01171](#).
- [345] R. Araldi, et al. [NA60], Precision study of the $\eta \rightarrow \mu^+\mu^-\gamma$ and $\omega \rightarrow \mu^+\mu^-\pi^0$ electromagnetic transition form-factors and of the $\rho \rightarrow \mu^+\mu^-$ line shape in NA60, *Phys. Lett. B* 757 (2016) 437–444. [arXiv:1608.07898](#).
- [346] P. Adlarson, et al., Measurement of the $\omega \rightarrow \pi^0 e^+ e^-$ and $\eta \rightarrow e^+ e^- \gamma$ Dalitz decays with the A2 setup at MAMI, *Phys. Rev. C* 95 (2017) 035208. [arXiv:1609.04503](#).
- [347] M. N. Achasov, et al., Measurement of the cross section for the $e^+e^- \rightarrow \omega\pi^0 \rightarrow \pi^0\pi^0\gamma$ process in the energy range of 1.1 GeV – 1.9 GeV, *JETP Lett.* 94 (2012) 734–737.
- [348] M. N. Achasov, et al., Study of $e^+e^- \rightarrow \omega\pi^0 \rightarrow \pi^0\pi^0\gamma$ in the energy range 1.05 – 2.00 GeV with SND, *Phys. Rev. D* 88 (2013) 054013. [arXiv:1303.5198](#).
- [349] S. I. Dolinsky, et al., The Reaction $e^+e^- \rightarrow \omega\pi^0$ in the Center-of-mass Energy Range From 1.0 GeV to 1.4 GeV, *Phys. Lett. B* 174 (1986) 453–457.

- [350] M. Ablikim, et al. [BESIII], Observation of a resonant structure in $e^+e^- \rightarrow \omega\eta$ and another in $e^+e^- \rightarrow \omega\pi^0$ at center-of-mass energies between 2.00 and 3.08 GeV, Phys. Lett. B 813 (2021) 136059. [arXiv:2009.08099](#).
- [351] G. Köpp, Dispersion calculation of the transition form factor $f_{\pi\omega\gamma}(t)$ with cut contributions, Phys. Rev. D 10 (1974) 932–940.
- [352] S. P. Schneider, B. Kubis, F. Niecknig, The $\omega \rightarrow \pi^0\gamma^*$ and $\phi \rightarrow \pi^0\gamma^*$ transition form factors in dispersion theory, Phys. Rev. D 86 (2012) 054013. [arXiv:1206.3098](#).
- [353] I. V. Danilkin, C. Fernández-Ramírez, P. Guo, V. Mathieu, D. Schott, M. Shi, A. P. Szczepaniak, Dispersive analysis of $\omega/\phi \rightarrow 3\pi, \pi^0\gamma$, Phys. Rev. D 91 (2015) 094029. [arXiv:1409.7708](#).
- [354] M. Albaladejo, I. Danilkin, S. Gonzalez-Solís, D. Winney, C. Fernández-Ramírez, A. N. H. Blin, V. Mathieu, M. Mikhasenko, A. Pilloni, A. Szczepaniak [JPAC], $\omega \rightarrow 3\pi$ and $\omega\pi^0$ transition form factor revisited, Eur. Phys. J. C 80 (2020) 1107. [arXiv:2006.01058](#).
- [355] B. Ananthanarayan, I. Caprini, B. Kubis, Constraints on the $\omega\pi$ form factor from analyticity and unitarity, Eur. Phys. J. C 74 (2014) 3209. [arXiv:1410.6276](#).
- [356] I. Caprini, Testing the consistency of the $\omega\pi$ transition form factor with unitarity and analyticity, Phys. Rev. D 92 (2015) 014014. [arXiv:1505.05282](#).
- [357] F. Ambrosino, et al. [KLOE], Study of the process $e^+e^- \rightarrow \omega\pi^0$ in the ϕ -meson mass region with the KLOE detector, Phys. Lett. B 669 (2008) 223–228. [arXiv:0807.4909](#).
- [358] V. M. Aulchenko, et al., The process $e^+e^- \rightarrow \omega\pi^0$ near the ϕ resonance, J. Exp. Theor. Phys. 90 (2000) 927–938, [Zh. Eksp. Teor. Fiz.117 (2000) 1067].
- [359] M. N. Achasov, et al., Measurement of the $e^+e^- \rightarrow \omega\eta$ cross section below $\sqrt{s} = 2$ GeV, Phys. Rev. D 94 (2016) 092002. [arXiv:1607.00371](#).
- [360] B. Aubert, et al. [BaBar], The $e^+e^- \rightarrow 3(\pi^+\pi^-), 2(\pi^+\pi^-\pi^0)$ and $K^+K^-2(\pi^+\pi^-)$ cross sections at center-of-mass energies from production threshold to 4.5-GeV measured with initial-state radiation, Phys. Rev. D 73 (2006) 052003. [arXiv:hep-ex/0602006](#).
- [361] B. Aubert, et al. [BaBar], Measurements of $e^+e^- \rightarrow K^+K^-\eta, K^+K^-\pi^0$ and $K_S^0K^\pm\pi^\mp$ cross-sections using initial state radiation events, Phys. Rev. D 77 (2008) 092002. [arXiv:0710.4451](#).
- [362] R. R. Akhmetshin, et al. [CMD-3], Study of the process $e^+e^- \rightarrow \pi^+\pi^-\pi^0\eta$ in the c.m. energy range 1394–2005 MeV with the CMD-3 detector, Phys. Lett. B 773 (2017) 150–158. [arXiv:1706.06267](#).
- [363] D. Babusci, et al. [KLOE-2], Study of the Dalitz decay $\phi \rightarrow \eta e^+e^-$ with the KLOE detector, Phys. Lett. B 742 (2015) 1–6. [arXiv:1409.4582](#).
- [364] M. Ablikim, et al. [BESIII], Observation of a structure in $e^+e^- \rightarrow \phi\eta'$ at \sqrt{s} from 2.05 to 3.08 GeV, Phys. Rev. D 102 (2020) 012008. [arXiv:2003.13064](#).
- [365] J. P. Lees, et al. [BaBar], Cross sections for the reactions $e^+e^- \rightarrow K_S^0K_L^0\pi^0, K_S^0K_L^0\eta$, and $K_S^0K_L^0\pi^0\pi^0$ from events with initial-state radiation, Phys. Rev. D 95 (2017) 052001. [arXiv:1701.08297](#).
- [366] M. N. Achasov, et al., Measurement of the $e^+e^- \rightarrow \eta K^+K^-$ Cross Section by Means of the SND Detector, Phys. Atom. Nucl. 81 (2018) 205–213, [Yad. Fiz.81 (2018) 195].

- [367] J. P. Lees, et al. [BaBar], Cross Sections for the Reactions $e^+e^- \rightarrow K^+K^-\pi^+\pi^-$, $K^+K^-\pi^0\pi^0$, and $K^+K^-K^+K^-$ Measured Using Initial-State Radiation Events, Phys. Rev. D 86 (2012) 012008. [arXiv:1103.3001](#).
- [368] C. P. Shen, et al. [Belle], Observation of the $\phi(1680)$ and the $Y(2175)$ in $e^+e^- \rightarrow \phi\pi^+\pi^-$, Phys. Rev. D 80 (2009) 031101. [arXiv:0808.0006](#).
- [369] M. Ablikim, et al. [BES], Observation of $Y(2175)$ in $J/\psi \rightarrow \eta\phi f_0(980)$, Phys. Rev. Lett. 100 (2008) 102003. [arXiv:0712.1143](#).
- [370] M. Ablikim, et al. [BESIII], Study of $J/\psi \rightarrow \eta\phi\pi^+\pi^-$ at BESIII, Phys. Rev. D 91 (2015) 052017. [arXiv:1412.5258](#).
- [371] A. Anastasi, et al. [KLOE-2], Measurement of the $\phi \rightarrow \pi^0 e^+ e^-$ transition form factor with the KLOE detector, Phys. Lett. B 757 (2016) 362–367. [arXiv:1601.06565](#).
- [372] S. Pacetti, Study of the $\phi\pi^0$ transition form factor, Nucl. Phys. A 919 (2013) 15–31. [arXiv:0904.3684](#).
- [373] A. Aloisio, et al. [KLOE], Study of the decay $\phi \rightarrow \pi^+\pi^-\pi^0$ with the KLOE detector, Phys. Lett. B 561 (2003) 55–60, [Erratum: Phys. Lett. B 609 (2005) 449]. [arXiv:hep-ex/0303016](#).
- [374] M. Ablikim, et al. [BESIII], Observation of $J/\psi \rightarrow \gamma\eta\pi^0$, Phys. Rev. D 94 (2016) 072005. [arXiv:1608.07393](#).
- [375] R. R. Akhmetshin, et al. [CMD-2], First observation of the $\phi \rightarrow \pi^+\pi^-\gamma$ decay, Phys. Lett. B 462 (1999) 371. [arXiv:hep-ex/9907005](#).
- [376] F. Ambrosino, et al. [KLOE], Study of the $a_0(980)$ meson via the radiative decay $\phi \rightarrow \eta\pi^0\gamma$ with the KLOE detector, Phys. Lett. B 681 (2009) 5–13. [arXiv:0904.2539](#).
- [377] M. Ablikim, et al. [BES], Partial wave analyses of $J/\psi \rightarrow \gamma\pi^+\pi^-$ and $\gamma\pi^0\pi^0$, Phys. Lett. B 642 (2006) 441–448. [arXiv:hep-ex/0603048](#).
- [378] M. Ablikim, et al. [BESIII], Partial wave analysis of $J/\psi \rightarrow \gamma\eta\eta$, Phys. Rev. D 87 (2013) 092009, [Erratum: Phys. Rev. D 87 (2013) 119901]. [arXiv:1301.0053](#).
- [379] M. Ablikim, et al. [BESIII], Amplitude analysis of the $K_S K_S$ system produced in radiative J/ψ decays, Phys. Rev. D 98 (2018) 072003. [arXiv:1808.06946](#).
- [380] V. M. Aulchenko, et al. [SND], First observation of $\phi(1020) \rightarrow \pi^0\pi^0\gamma$ decay, Phys. Lett. B 440 (1998) 442–448. [arXiv:hep-ex/9807016](#).
- [381] M. N. Achasov, et al., Evidence of the $\phi \rightarrow \eta\pi^0\gamma$ decay, Phys. Lett. B 438 (1998) 441–445. [arXiv:hep-ex/9809010](#).
- [382] M. N. Achasov, et al., The $\phi(1020) \rightarrow \pi^0\pi^0\gamma$ decay, Phys. Lett. B 485 (2000) 349–356. [arXiv:hep-ex/0005017](#).
- [383] R. R. Akhmetshin, et al. [CMD-2], Study of the ϕ decays into $\pi^0\pi^0\gamma$ and $\eta\pi^0\gamma$ final states, Phys. Lett. B 462 (1999) 380. [arXiv:hep-ex/9907006](#).
- [384] G. Isidori, L. Maiani, M. Nicolaci, S. Pacetti, The $e^+e^- \rightarrow P_1 P_2 \gamma$ processes close to the ϕ peak: Toward a model-independent analysis, JHEP 05 (2006) 049. [arXiv:hep-ph/0603241](#).

- [385] N. N. Achasov, V. N. Ivanchenko, On a Search for Four Quark States in Radiative Decays of ϕ Meson, Nucl. Phys. B 315 (1989) 465–476.
- [386] A. Bramon, A. Grau, G. Pancheri, Chiral perturbation theory and radiative $V_0 \rightarrow$ two neutral pseudoscalar gamma decays, Phys. Lett. B 289 (1992) 97–102.
- [387] N. N. Achasov, V. V. Gubin, Search for the scalar a_0 and f_0 mesons in the reactions $e^+e^- \rightarrow \gamma\pi^0\pi^0(\eta)$, Phys. Rev. D 56 (1997) 4084–4097. [arXiv:hep-ph/9703367](#).
- [388] N. N. Achasov, A. V. Kiselev, Properties of the light scalar mesons face the experimental data on the $\phi \rightarrow \pi^0\pi^0\gamma$ decay and the $\pi\pi$ scattering, Phys. Rev. D 73 (2006) 054029, [Erratum: Phys. Rev. D 74 (2006) 059902]. [arXiv:hep-ph/0512047](#).
- [389] F. Ambrosino, et al. [KLOE], Study of the decay $\phi \rightarrow f_0(980)\gamma \rightarrow \pi^+\pi^-\gamma$ with the KLOE detector, Phys. Lett. B 634 (2006) 148–154. [arXiv:hep-ex/0511031](#).
- [390] N. N. Achasov, V. V. Gubin, Interference in the reaction $e^+e^- \rightarrow \gamma\pi^+\pi^-$ and the final state interaction, Phys. Rev. D 57 (1998) 1987–1990. [arXiv:hep-ph/9706363](#).
- [391] A. Aloisio, et al. [KLOE], Study of the decay $\phi \rightarrow \eta\pi^0\gamma$ with the KLOE detector, Phys. Lett. B 536 (2002) 209–216. [arXiv:hep-ex/0204012](#).
- [392] D. Besson, et al. [CLEO], Inclusive Radiative J/ψ Decays, Phys. Rev. D 78 (2008) 032012. [arXiv:0806.0315](#).
- [393] J. Z. Bai, et al. [BES], Partial wave analyses of $J/\psi \rightarrow \gamma K^+K^-$ and $\gamma K_S^0 K_S^0$, Phys. Rev. D 68 (2003) 052003. [arXiv:hep-ex/0307058](#).
- [394] S. Dobbs, A. Tomaradze, T. Xiao, K. K. Seth, Comprehensive Study of the Radiative Decays of J/ψ and $\psi(2S)$ to Pseudoscalar Meson Pairs, and Search for Glueballs, Phys. Rev. D 91 (2015) 052006. [arXiv:1502.01686](#).
- [395] B. Kubis, J. Plenter, Anomalous decay and scattering processes of the η meson, Eur. Phys. J. C 75 (2015) 283. [arXiv:1504.02588](#).
- [396] J. Wess, B. Zumino, Consequences of anomalous Ward identities, Phys. Lett. B 37 (1971) 95–97.
- [397] E. Witten, Global Aspects of Current Algebra, Nucl. Phys. B223 (1983) 422–432.
- [398] M. Gell-Mann, D. Sharp, W. G. Wagner, Decay rates of neutral mesons, Phys. Rev. Lett. 8 (1962) 261.
- [399] W. Bartel, et al. [JADE], A Measurement of the Reaction $e^+e^- \rightarrow e^+e^-\eta'$ and the Radiative Width $\Gamma(\eta' \rightarrow \gamma\gamma)$ at PETRA, Phys. Lett. B 113 (1982) 190–194.
- [400] H. J. Behrend, et al. [CELLO], Determination of the Radiative Widths of the η' and A_2 From Two Photon Exchange Production, Phys. Lett. B 114 (1982) 378, [Erratum: Phys. Lett. B 125 (1983) 518].
- [401] C. Berger, et al. [PLUTO], Measurement of Exclusive η' Production in $\gamma\gamma$ Reactions, Phys. Lett. B 142 (1984) 125–129.
- [402] M. Althoff, et al. [TASSO], Measurement of the Radiative Width of the η' (958) in Two Photon Interactions, Phys. Lett. B 147 (1984) 487–492.

- [403] H. Aihara, et al. [TPC/Two Gamma], A study of η' formation in photon-photon collisions, Phys. Rev. D 35 (1987) 2650.
- [404] H. Albrecht, et al. [ARGUS], Measurement of $\eta' \rightarrow \pi^+\pi^-\gamma$ in $\gamma\gamma$ Collisions, Phys. Lett. B 199 (1987) 457–461.
- [405] S. I. Bityukov, et al., Study of the radiative decay $\eta' \rightarrow \pi^+\pi^-\gamma$, Z. Phys. C 50 (1991) 451–454.
- [406] M. Benayoun, M. Feindt, M. Girone, A. Kirk, P. Leruste, J. L. Narjoux, K. Safarik, Experimental evidences for the box anomaly in η/η' decays and the electric charge of quarks, Z. Phys. C 58 (1993) 31–54.
- [407] A. Abele, et al. [Crystal Barrel], Measurement of the decay distribution of $\eta' \rightarrow \pi^+\pi^-\gamma$ and evidence for the box anomaly, Phys. Lett. B 402 (1997) 195–206.
- [408] M. Acciarri, et al. [L3], Measurement of $\eta'(958)$ formation in two photon collisions at LEP-1, Phys. Lett. B 418 (1998) 399–410.
- [409] M. Ablikim, et al. [BESIII], Precision Study of $\eta' \rightarrow \gamma\pi^+\pi^-$ Decay Dynamics, Phys. Rev. Lett. 120 (2018) 242003. [arXiv:1712.01525](#).
- [410] F. Stollenwerk, C. Hanhart, A. Kupść, U.-G. Meißner, A. Wirzba, Model-independent approach to $\eta \rightarrow \pi^+\pi^-\gamma$ and $\eta' \rightarrow \pi^+\pi^-\gamma$, Phys. Lett. B 707 (2012) 184–190. [arXiv:1108.2419](#).
- [411] D. Babusci, et al. [KLOE], Measurement of $\Gamma(\eta \rightarrow \pi^+\pi^-\gamma)/\Gamma(\eta \rightarrow \pi^+\pi^-\pi^0)$ with the KLOE Detector, Phys. Lett. B 718 (2013) 910–914. [arXiv:1209.4611](#).
- [412] P. Adlarson, et al. [WASA-at-COSY], Exclusive Measurement of the $\eta \rightarrow \pi^+\pi^-\gamma$ Decay, Phys. Lett. B 707 (2012) 243–249. [arXiv:1107.5277](#).
- [413] M. Antonelli, et al., Flavor Physics in the Quark Sector, Phys. Rept. 494 (2010) 197–414. [arXiv:0907.5386](#).
- [414] M. Ablikim, et al. [BESIII], Study of the decay $D^0 \rightarrow \bar{K}^0\pi^-e^+\nu_e$, Phys. Rev. D 99 (2019) 011103. [arXiv:1811.11349](#).
- [415] M. Ablikim, et al. [BESIII], Observation of $D^+ \rightarrow f_0(500)e^+\nu_e$ and Improved Measurements of $D \rightarrow \rho e^+\nu_e$, Phys. Rev. Lett. 122 (2019) 062001. [arXiv:1809.06496](#).
- [416] M. Wirbel, B. Stech, M. Bauer, Exclusive Semileptonic Decays of Heavy Mesons, Z. Phys. C 29 (1985) 637.
- [417] C. L. Y. Lee, M. Lu, M. B. Wise, B_{l4} and D_{l4} decay, Phys. Rev. D 46 (1992) 5040–5048.
- [418] J. D. Richman, P. R. Burchat, Leptonic and semileptonic decays of charm and bottom hadrons, Rev. Mod. Phys. 67 (1995) 893–976. [arXiv:hep-ph/9508250](#).
- [419] C. G. Boyd, B. Grinstein, R. F. Lebed, Precision corrections to dispersive bounds on form-factors, Phys. Rev. C 56 (1997) 6895–6911. [arXiv:hep-ph/9705252](#).
- [420] B. Ananthanarayan, I. Caprini, I. Sentitemsu Imsong, Implications of unitarity and analyticity for the $D\pi$ form factors, Eur. Phys. J. A 47 (2011) 147. [arXiv:1108.0284](#).
- [421] B. Grinstein, R. F. Lebed, Above-Threshold Poles in Model-Independent Form Factor Parametrizations, Phys. Rev. D 92 (2015) 116001. [arXiv:1509.04847](#).

- [422] I. Caprini, B. Grinstein, R. F. Lebed, Model-independent constraints on hadronic form factors with above-threshold poles, Phys. Rev. D 96 (2017) 036015. [arXiv:1705.02368](#).
- [423] V. Lubicz, L. Riggio, G. Salerno, S. Simula, C. Tarantino [ETM], Scalar and vector form factors of $D \rightarrow \pi(K)\ell\nu$ decays with $N_f = 2 + 1 + 1$ twisted fermions, Phys. Rev. D 96 (2017) 054514, [Erratum: Phys. Rev. D 99 (2019) 099902, Erratum: Phys. Rev. D 100 (2019) 079901]. [arXiv:1706.03017](#).
- [424] J. M. Link, et al. [FOCUS], A Non-parametric approach to the $D^+ \rightarrow \bar{K}^{*0}\mu^+\nu$ form-factors, Phys. Lett. B 633 (2006) 183–189. [arXiv:hep-ex/0509027](#).
- [425] M. R. Shepherd, et al. [CLEO], Model independent measurement of form-factors in the decay $D^+ \rightarrow K^-\pi^+e^+\nu_e$, Phys. Rev. D 74 (2006) 052001. [arXiv:hep-ex/0606010](#).
- [426] S. Fajfer, J. F. Kamenik, Note on helicity amplitudes in $D \rightarrow V$ semileptonic decays, Phys. Rev. D 73 (2006) 057503. [arXiv:hep-ph/0601028](#).
- [427] J. M. Link, et al. [FOCUS], Evidence for New Interference Phenomena in the Decay $D^+ \rightarrow K^-\pi^+\mu^+\nu$, Phys. Lett. B 535 (2002) 43–51. [arXiv:hep-ex/0203031](#).
- [428] J. R. Peláez, A. Rodas, Pion-kaon scattering amplitude constrained with forward dispersion relations up to 1.6 GeV, Phys. Rev. D 93 (2016) 074025. [arXiv:1602.08404](#).
- [429] R. A. Briere, et al. [CLEO], Analysis of $D^+ \rightarrow K^-\pi^+e^+\nu_e$ and $D^+ \rightarrow K^-\pi^+\mu^+\nu_\mu$ Semileptonic Decays, Phys. Rev. D 81 (2010) 112001. [arXiv:1004.1954](#).
- [430] P. del Amo Sanchez, et al. [BaBar], Analysis of the $D^+ \rightarrow K^-\pi^+e^+\nu_e$ decay channel, Phys. Rev. D 83 (2011) 072001. [arXiv:1012.1810](#).
- [431] M. Ablikim, et al. [BESIII], Study of $D^+ \rightarrow K^-\pi^+e^+\nu_e$, Phys. Rev. D 94 (2016) 032001. [arXiv:1512.08627](#).
- [432] S. Dobbs, et al. [CLEO], First Measurement of the Form Factors in the Decays $D^0 \rightarrow \rho^-e^+\nu_e$ and $D^+ \rightarrow \rho^0e^+\nu_e$, Phys. Rev. Lett. 110 (2013) 131802. [arXiv:1112.2884](#).
- [433] M. Ablikim, et al. [BESIII], Observation of the Semileptonic Decay $D^0 \rightarrow a_0(980)^-e^+\nu_e$ and Evidence for $D^+ \rightarrow a_0(980)^0e^+\nu_e$, Phys. Rev. Lett. 121 (2018) 081802. [arXiv:1803.02166](#).
- [434] J. P. Lees, et al. [BaBar], Study of the reactions $e^+e^- \rightarrow \pi^+\pi^-\pi^0\pi^0\pi^0\gamma$ and $\pi^+\pi^-\pi^0\pi^0\eta\gamma$ at center-of-mass energies from threshold to 4.35 GeV using initial-state radiation, Phys. Rev. D 98 (2018) 112015. [arXiv:1810.11962](#).
- [435] M. Ablikim, et al. [BESIII], Observation and study of the decay $J/\psi \rightarrow \phi\eta\eta'$, Phys. Rev. D 99 (2019) 112008. [arXiv:1901.00085](#).
- [436] L. S. Brown, R. N. Cahn, Chiral Symmetry and $\psi' \rightarrow \psi\pi\pi$ Decay, Phys. Rev. Lett. 35 (1975) 1.
- [437] R. N. Cahn, Angular Distributions in the Decay $\psi' \rightarrow \psi\pi\pi$, Phys. Rev. D 12 (1975) 3559.
- [438] J. Z. Bai, et al. [BES], $\psi(2S) \rightarrow \pi^+\pi^-J/\psi$ decay distributions, Phys. Rev. D 62 (2000) 032002. [arXiv:hep-ex/9909038](#).
- [439] M. Ablikim, et al. [BES], Production of σ in $\psi(2S) \rightarrow \pi^+\pi^-J/\psi$, Phys. Lett. B 645 (2007) 19–25. [arXiv:hep-ex/0610023](#).

- [440] M. Ishida, The Present status on sigma and kappa meson properties, Prog. Theor. Phys. Suppl. 149 (2003) 190–202. [arXiv:hep-ph/0212383](#).
- [441] F.-K. Guo, P.-N. Shen, H.-C. Chiang, R.-G. Ping, Heavy quarkonium $\pi^+\pi^-$ transitions and a possible $b\bar{b}q\bar{q}$ state, Nucl. Phys. A 761 (2005) 269–282. [arXiv:hep-ph/0410204](#).
- [442] J. A. Oller, E. Oset, Chiral symmetry amplitudes in the S -wave isoscalar and isovector channels and the σ , $f_0(980)$, $a_0(980)$ scalar mesons, Nucl. Phys. A 620 (1997) 438–456, [Erratum: Nucl. Phys. A 652 (1999) 407–409]. [arXiv:hep-ph/9702314](#).
- [443] M. Ablikim, et al. [BES], The σ pole in $J/\psi \rightarrow \omega\pi^+\pi^-$, Phys. Lett. B 598 (2004) 149–158. [arXiv:hep-ex/0406038](#).
- [444] M. Ablikim, et al. [BES], Resonances in $J/\psi \rightarrow \phi\pi^+\pi^-$ and ϕK^+K^- , Phys. Lett. B 607 (2005) 243–253. [arXiv:hep-ex/0411001](#).
- [445] M. Ablikim, et al. [BES], Study of $J/\psi \rightarrow \omega K^+K^-$, Phys. Lett. B 603 (2004) 138–145. [arXiv:hep-ex/0409007](#).
- [446] B.-S. Zou, D. V. Bugg, Covariant tensor formalism for partial wave analyses of ψ decay to mesons, Eur. Phys. J. A 16 (2003) 537–547. [arXiv:hep-ph/0211457](#).
- [447] D. Morgan, M. R. Pennington, The Decay $J/\psi \rightarrow \phi(MM)$ demands the $f_0(S^*)$ be narrow, Phys. Rev. D 48 (1993) 5422–5424.
- [448] R. H. Dalitz, S. F. Tuan, The phenomenological description of π - K -nucleon reaction processes, Annals Phys. 10 (1960) 307–351.
- [449] U.-G. Meißner, J. A. Oller, $J/\psi \rightarrow \phi\pi\pi(K\bar{K})$ decays, chiral dynamics and OZI violation, Nucl. Phys. A 679 (2001) 671–697. [arXiv:hep-ph/0005253](#).
- [450] T. A. Lähde, U.-G. Meißner, Improved Analysis of J/ψ Decays into a Vector Meson and Two Pseudoscalars, Phys. Rev. D 74 (2006) 034021. [arXiv:hep-ph/0606133](#).
- [451] L. Roca, J. E. Palomar, E. Oset, H. C. Chiang, Unitary chiral dynamics in $J/\psi \rightarrow VPP$ decays and the role of scalar mesons, Nucl. Phys. A 744 (2004) 127–155. [arXiv:hep-ph/0405228](#).
- [452] B. Liu, M. Büscher, F.-K. Guo, C. Hanhart, U.-G. Meißner, Final state interactions in the decays $J/\psi \rightarrow VPP$, Eur. Phys. J. C 63 (2009) 93–99. [arXiv:0901.1185](#).
- [453] N. N. Achasov, S. A. Devyanin, G. N. Shestakov, $S^* - \delta^0$ Mixing as the Threshold Phenomenon, Phys. Lett. B 88 (1979) 367–371.
- [454] B. Kerbikov, F. Tabakin, Mixing of the f_0 and a_0 scalar mesons in threshold photoproduction, Phys. Rev. C 62 (2000) 064601. [arXiv:nucl-th/0006017](#).
- [455] F. E. Close, A. Kirk, Isospin breaking exposed in $f_0(980)$ – $a_0(980)$ mixing, Phys. Lett. B 489 (2000) 24–28. [arXiv:hep-ph/0008066](#).
- [456] N. N. Achasov, A. V. Kiselev, Once more on mixing of the $a_0(980)$ and $f_0(980)$ mesons, Phys. Lett. B 534 (2002) 83–86. [arXiv:hep-ph/0203042](#).
- [457] N. N. Achasov, G. N. Shestakov, To search for $a_0^0(980)$ – $f_0(980)$ mixing in polarization phenomena, Phys. Rev. Lett. 92 (2004) 182001. [arXiv:hep-ph/0312214](#).

- [458] J.-J. Wu, Q. Zhao, B.-S. Zou, Possibility of measuring $a_0(980) - f_0(980)$ mixing from $J/\psi \rightarrow \phi a_0(980)$, Phys. Rev. D 75 (2007) 114012. [arXiv:0704.3652](#).
- [459] C. Hanhart, B. Kubis, J. R. Peláez, Investigation of $a_0 - f_0$ mixing, Phys. Rev. D 76 (2007) 074028. [arXiv:0707.0262](#).
- [460] J.-J. Wu, B.-S. Zou, Study $a_0^0(980) - f_0(980)$ mixing from $a_0^0(980) \rightarrow f_0(980)$ transition, Phys. Rev. D 78 (2008) 074017. [arXiv:0808.2683](#).
- [461] M. Ablikim, et al. [BESIII], Observation of $a_0^0(980)$ - $f_0(980)$ Mixing, Phys. Rev. Lett. 121 (2018) 022001. [arXiv:1802.00583](#).
- [462] M. Ablikim, et al. [BESIII], Observation of a Charged Charmoniumlike Structure in $e^+e^- \rightarrow \pi^+\pi^- J/\psi$ at $\sqrt{s} = 4.26$ GeV, Phys. Rev. Lett. 110 (2013) 252001. [arXiv:1303.5949](#).
- [463] Z. Q. Liu, et al. [Belle], Study of $e^+e^- \rightarrow \pi^+\pi^- J/\psi$ and Observation of a Charged Charmoniumlike State at Belle, Phys. Rev. Lett. 110 (2013) 252002, [Erratum: Phys. Rev. Lett. 111 (2013) 019901]. [arXiv:1304.0121](#).
- [464] T. Xiao, S. Dobbs, A. Tomaradze, K. K. Seth, Observation of the Charged Hadron $Z_c^\pm(3900)$ and Evidence for the Neutral $Z_c^0(3900)$ in $e^+e^- \rightarrow \pi\pi J/\psi$ at $\sqrt{s} = 4170$ MeV, Phys. Lett. B 727 (2013) 366–370. [arXiv:1304.3036](#).
- [465] M. Ablikim, et al. [BESIII], Observation of $Z_c(3900)^0$ in $e^+e^- \rightarrow \pi^0\pi^0 J/\psi$, Phys. Rev. Lett. 115 (2015) 112003. [arXiv:1506.06018](#).
- [466] D.-Y. Chen, X. Liu, T. Matsuki, Two Charged Strangeonium-Like Structures Observable in the $Y(2175) \rightarrow \phi(1020)\pi^+\pi^-$ Process, Eur. Phys. J. C 72 (2012) 2008. [arXiv:1112.3773](#).
- [467] M. Ablikim, et al. [BESIII], Search for a strangeonium-like structure Z_s decaying into $\phi\pi$ and a measurement of the cross section $e^+e^- \rightarrow \phi\pi\pi$, Phys. Rev. D 99 (2019) 011101. [arXiv:1801.10384](#).
- [468] M. Hoferichter, B.-L. Hoid, B. Kubis, Three-pion contribution to hadronic vacuum polarization, JHEP 08 (2019) 137. [arXiv:1907.01556](#).
- [469] M. N. Achasov, et al., Measurements of the parameters of the $\phi(1020)$ resonance through studies of the processes $e^+e^- \rightarrow K^+K^-$, $K_S K_L$, and $\pi^+\pi^-\pi^0$, Phys. Rev. D 63 (2001) 072002. [arXiv:hep-ex/0009036](#).
- [470] M. N. Achasov, et al., Study of the process $e^+e^- \rightarrow \pi^+\pi^-\pi^0$ in the energy region \sqrt{s} from 0.98 GeV to 1.38 GeV, Phys. Rev. D 66 (2002) 032001. [arXiv:hep-ex/0201040](#).
- [471] M. N. Achasov, et al., Study of the process $e^+e^- \rightarrow \pi^+\pi^-\pi^0$ in the energy region \sqrt{s} below 0.98 GeV, Phys. Rev. D 68 (2003) 052006. [arXiv:hep-ex/0305049](#).
- [472] V. M. Aulchenko, et al., Study of the $e^+e^- \rightarrow \pi^+\pi^-\pi^0$ process in the energy range 1.05–2.00 GeV, J. Exp. Theor. Phys. 121 (2015) 27–34, [Zh. Eksp. Teor. Fiz. 148 (2015) 34].
- [473] R. R. Akhmetshin, et al., Measurement of ϕ meson parameters with CMD-2 detector at VEPP-2M collider, Phys. Lett. B 364 (1995) 199–206.
- [474] R. R. Akhmetshin, et al., Study of dynamics of $\phi \rightarrow \pi^+\pi^-\pi^0$ decay with CMD-2 detector, Phys. Lett. B 434 (1998) 426–436.

- [475] R. R. Akhmetshin, et al., Study of $\phi \rightarrow \pi^+\pi^-\pi^0$ with CMD-2 detector, Phys. Lett. B 642 (2006) 203–209.
- [476] A. Cordier, et al., Cross-section of the Reaction $e^+e^- \rightarrow \pi^+\pi^-\pi^0$ for Center-of-mass Energies From 750 MeV to 1100 MeV, Nucl. Phys. B 172 (1980) 13–24.
- [477] A. Antonelli, et al. [DM2], Measurement of the $e^+e^- \rightarrow \pi^+\pi^-\pi^0$ and $e^+e^- \rightarrow \omega\pi^+\pi^-$ reactions in the energy interval 1350 MeV – 2400 MeV, Z. Phys. C 56 (1992) 15–20.
- [478] B. Aubert, et al. [BaBar], Study of $e^+e^- \rightarrow \pi^+\pi^-\pi^0$ process using initial state radiation with BaBar, Phys. Rev. D 70 (2004) 072004. [arXiv:hep-ex/0408078](#).
- [479] M. Ablikim, et al., Measurement of the $e^+e^- \rightarrow \pi^+\pi^-\pi^0$ cross section from 0.7 GeV to 3.0 GeV via initial-state radiation (2019). [arXiv:1912.11208](#).
- [480] B.-L. Hoid, M. Hoferichter, B. Kubis, Hadronic vacuum polarization and vector-meson resonance parameters from $e^+e^- \rightarrow \pi^0\gamma$, Eur. Phys. J. C 80 (2020) 988. [arXiv:2007.12696](#).
- [481] R. R. Akhmetshin, et al. [CMD-2], Study of the process $e^+e^- \rightarrow \pi^+\pi^-\pi^+\pi^-\pi^0$ with CMD-2 detector, Phys. Lett. B 489 (2000) 125–130. [arXiv:hep-ex/0009013](#).
- [482] M. N. Achasov, et al., Measurement of the $e^+e^- \rightarrow \eta\pi^+\pi^-$ cross section in the $\sqrt{s} = 1.04$ GeV–1.38 GeV energy range with a spherical neutral detector at the VEPP-2M collider, JETP Lett. 92 (2010) 80–84.
- [483] V. M. Aulchenko, et al. [SND], Measurement of the $e^+e^- \rightarrow \eta\pi^+\pi^-$ cross section in the center-of-mass energy range 1.22 – 2.00 GeV with the SND detector at the VEPP-2000 collider, Phys. Rev. D 91 (2015) 052013. [arXiv:1412.1971](#).
- [484] M. N. Achasov, et al., Measurement of the $e^+e^- \rightarrow \eta\pi^+\pi^-$ cross section with the SND detector at the VEPP-2000 collider, Phys. Rev. D 97 (2018) 012008. [arXiv:1711.08862](#).
- [485] S. S. Gribov, et al., Measurement of the $e^+e^- \rightarrow \eta\pi^+\pi^-$ cross section with the CMD-3 detector at the VEPP-2000 collider, JHEP 01 (2020) 112. [arXiv:1907.08002](#).
- [486] B. Aubert, et al. [BaBar], The $e^+e^- \rightarrow 2(\pi^+\pi^-)\pi^0$, $2(\pi^+\pi^-)\eta$, $K^+K^-\pi^+\pi^-\pi^0$ and $K^+K^-\pi^+\pi^-\eta$ Cross Sections Measured with Initial-State Radiation, Phys. Rev. D 76 (2007) 092005, [Erratum: Phys. Rev. D 77 (2008) 119902]. [arXiv:0708.2461](#).
- [487] J. P. Lees, et al. [BaBar], Study of the process $e^+e^- \rightarrow \pi^+\pi^-\eta$ using initial state radiation, Phys. Rev. D 97 (2018) 052007. [arXiv:1801.02960](#).
- [488] N. N. Achasov, V. A. Karnakov, On the research of the $e^+e^- \rightarrow \eta\pi^+\pi^-$ reaction, JETP Lett. 39 (1984) 342.
- [489] S. Holz, J. Plenter, C.-W. Xiao, T. Dato, C. Hanhart, B. Kubis, U.-G. Meißner, A. Wirzba, Towards an improved understanding of $\eta \rightarrow \gamma^*\gamma^*$ (9 2015). [arXiv:1509.02194](#).
- [490] L.-Y. Dai, J. Portoles, O. Shekhovtsova, Three pseudoscalar meson production in e^+e^- annihilation, Phys. Rev. D 88 (2013) 056001. [arXiv:1305.5751](#).
- [491] W. Qin, L.-Y. Dai, J. Portoles, Two and three pseudoscalar production in e^+e^- annihilation and their contributions to $(g - 2)_\mu$, JHEP 03 (2021) 092. [arXiv:2011.09618](#).
- [492] F. J. Gilman, Tau Decays Involving the η Meson, Phys. Rev. D 35 (1987) 3541.

- [493] S. I. Eidelman, V. N. Ivanchenko, e^+e^- annihilation into hadrons and exclusive τ decays, Phys. Lett. B 257 (1991) 437–440.
- [494] D. Gomez Dumm, P. Roig, Resonance Chiral Lagrangian analysis of $\tau^- \rightarrow \eta^{(\prime)}\pi^-\pi^0\nu_\tau$ decays, Phys. Rev. D 86 (2012) 076009. [arXiv:1208.1212](#).
- [495] J. Buon, D. Bisello, J. C. Bizot, A. Cordier, B. Delcourt, F. Mane, J. Layssac, Interpretation of DM1 Results on e^+e^- Annihilation Into Exclusive Channels Between 1.4 GeV and 1.9 GeV With a $\rho'\omega'\phi'$ Model, Phys. Lett. B 118 (1982) 221.
- [496] D. Bisello, et al., Observation of an isoscalar vector meson at $\simeq 1650 \text{ MeV}/c^2$ in the $e^+e^- \rightarrow K\bar{K}\pi$ reaction, Z. Phys. C 52 (1991) 227–230.
- [497] M. N. Achasov, et al., Measurement of the $e^+e^- \rightarrow K_S K_L \pi^0$ cross section in the energy range $\sqrt{s} = 1.3 - 2.0 \text{ GeV}$, Phys. Rev. D 97 (2018) 032011. [arXiv:1711.07143](#).
- [498] M. Ablikim, et al. [BESIII], Study of J/ψ and $\psi(3686)$ decays to $\pi^+\pi^-\eta'$, Phys. Rev. D 96 (2017) 112012. [arXiv:1709.00018](#).
- [499] S. Leupold, M. F. M. Lutz, Hadronic three-body decays of light vector mesons, Eur. Phys. J. A39 (2009) 205–212. [arXiv:0807.4686](#).
- [500] C. Zemach, Three pion decays of unstable particles, Phys. Rev. 133 (1964) B1201.
- [501] M. Hoferichter, B. Kubis, D. Sakkas, Extracting the chiral anomaly from $\gamma\pi \rightarrow \pi\pi$, Phys. Rev. D 86 (2012) 116009. [arXiv:1210.6793](#).
- [502] M. Hoferichter, B. Kubis, M. Zanke, Radiative resonance couplings in $\gamma\pi \rightarrow \pi\pi$, Phys. Rev. D 96 (2017) 114016. [arXiv:1710.00824](#).
- [503] M. Dax, T. Isken, B. Kubis, Quark-mass dependence in $\omega \rightarrow 3\pi$ decays, Eur. Phys. J. C 78 (2018) 859. [arXiv:1808.08957](#).
- [504] P. Adlarson, et al. [WASA-at-COSY], Measurement of the $\omega \rightarrow \pi^+\pi^-\pi^0$ Dalitz plot distribution, Phys. Lett. B 770 (2017) 418–425. [arXiv:1610.02187](#).
- [505] M. Ablikim, et al. [BESIII], Dalitz Plot Analysis of the Decay $\omega \rightarrow \pi^+\pi^-\pi^0$, Phys. Rev. D 98 (2018) 112007. [arXiv:1811.03817](#).
- [506] M. Ablikim, et al. [BESIII], Precision measurement of the branching fractions of $J/\psi \rightarrow \pi^+\pi^-\pi^0$ and $\psi' \rightarrow \pi^+\pi^-\pi^0$, Phys. Lett. B 710 (2012) 594–599. [arXiv:1202.2048](#).
- [507] J. P. Lees, et al. [BaBar], Dalitz plot analyses of $J/\psi \rightarrow \pi^+\pi^-\pi^0$, $J/\psi \rightarrow K^+K^-\pi^0$, and $J/\psi \rightarrow K_S^0 K^\pm \pi^\mp$ produced via e^+e^- annihilation with initial-state radiation, Phys. Rev. D 95 (2017) 072007. [arXiv:1702.01551](#).
- [508] A. P. Szczepaniak, M. R. Pennington, Application of the Veneziano Model in Charmonium Dalitz Plot Analysis, Phys. Lett. B 737 (2014) 283–288. [arXiv:1403.5782](#).
- [509] M. Ablikim, et al. [BES], Partial wave analysis of $\psi' \rightarrow \pi^+\pi^-\pi^0$ at BESII, Phys. Lett. B 619 (2005) 247–254.
- [510] M. Ablikim, et al. [BES], Observation of a broad 1^{--} resonant structure around $1.5 \text{ GeV}/c^2$ in the K^+K^- mass spectrum in $J/\psi \rightarrow K^+K^-\pi^0$, Phys. Rev. Lett. 97 (2006) 142002. [arXiv:hep-ex/0606047](#).

- [511] M. Ablikim, et al. [BESIII], Partial-wave analysis of $J/\psi \rightarrow K^+K^-\pi^0$, Phys. Rev. D 100 (2019) 032004. [arXiv:1904.10630](#).
- [512] S. J. Brodsky, D. G. Coyne, T. A. DeGrand, R. R. Horgan, The Decay of the Upsilon Into Photons and Gluons, Phys. Lett. B 73 (1978) 203–206.
- [513] M. Ablikim, et al. [BES], Observation of a resonance $X(1835)$ in $J/\psi \rightarrow \gamma\pi^+\pi^-\eta'$, Phys. Rev. Lett. 95 (2005) 262001. [arXiv:hep-ex/0508025](#).
- [514] M. Ablikim, et al. [BESIII], Spin-Parity Analysis of $p\bar{p}$ Mass Threshold Structure in J/ψ and ψ' Radiative Decays, Phys. Rev. Lett. 108 (2012) 112003. [arXiv:1112.0942](#).
- [515] G.-J. Ding, M.-L. Yan, Proton-antiproton annihilation in baryonium, Phys. Rev. C 72 (2005) 015208. [arXiv:hep-ph/0502127](#).
- [516] S.-L. Zhu, C.-S. Gao, $X(1835)$: A Possible baryonium?, Commun. Theor. Phys. 46 (2006) 291. [arXiv:hep-ph/0507050](#).
- [517] T. Huang, S.-L. Zhu, $X(1835)$: A Natural candidate of η' 's second radial excitation, Phys. Rev. D 73 (2006) 014023. [arXiv:hep-ph/0511153](#).
- [518] B. A. Li, A Possible 0^{-+} glueball candidate $X(1835)$, Phys. Rev. D 74 (2006) 034019. [arXiv:hep-ph/0510093](#).
- [519] G.-J. Ding, M.-L. Yan, Productions of $X(1835)$ as baryonium with sizable gluon content, Eur. Phys. J. A 28 (2006) 351–360. [arXiv:hep-ph/0511186](#).
- [520] M. Ablikim, et al. [BESIII], Confirmation of the $X(1835)$ and observation of the resonances $X(2120)$ and $X(2370)$ in $J/\psi \rightarrow \gamma\pi^+\pi^-\eta'$, Phys. Rev. Lett. 106 (2011) 072002. [arXiv:1012.3510](#).
- [521] M. Ablikim, et al. [BESIII], Observation of an anomalous line shape of the $\eta'\pi^+\pi^-$ mass spectrum near the $p\bar{p}$ mass threshold in $J/\psi \rightarrow \gamma\eta'\pi^+\pi^-$, Phys. Rev. Lett. 117 (2016) 042002. [arXiv:1603.09653](#).
- [522] M. Ablikim, et al. [BESIII], Observation and Spin-Parity Determination of the $X(1835)$ in $J/\psi \rightarrow K_S^0K_S^0\eta$, Phys. Rev. Lett. 115 (2015) 091803. [arXiv:1506.04807](#).
- [523] M. Ablikim, et al. [BESIII], Measurement of the branching fraction of $J/\psi \rightarrow \omega\eta'\pi^+\pi^-$ and search for $J/\psi \rightarrow \omega X(1835)$, $X(1835) \rightarrow \eta'\pi^+\pi^-$ decay, Phys. Rev. D 99 (2019) 071101. [arXiv:1902.04862](#).
- [524] M. Ablikim, et al. [BESIII], Study of $\eta(1475)$ and $X(1835)$ in radiative J/ψ decays to $\gamma\phi$, Phys. Rev. D 97 (2018) 051101. [arXiv:1801.02127](#).
- [525] M. Ablikim, et al. [BESIII], Observation of the $X(2370)$ and Search for the $X(2120)$ in $J/\psi \rightarrow \gamma K\bar{K}\eta'$, Eur. Phys. J. C 80 (2020) 746. [arXiv:1912.11253](#).
- [526] M. Ablikim, et al. [BESIII], First observation of $\eta(1405)$ decays into $f_0(980)\pi^0$, Phys. Rev. Lett. 108 (2012) 182001. [arXiv:1201.2737](#).
- [527] M. Ablikim, et al. [BESIII], Study of $a_0^0(980) - f_0(980)$ mixing, Phys. Rev. D 83 (2011) 032003. [arXiv:1012.5131](#).
- [528] R. R. Akhmetshin, et al. [CMD-3], Search for the process $e^+e^- \rightarrow \eta'(958)$ with the CMD-3 detector, Phys. Lett. B 740 (2015) 273–277. [arXiv:1409.1664](#).

- [529] M. N. Achasov, et al., Search for the $\eta' \rightarrow e^+e^-$ decay with the SND detector, Phys. Rev. D 91 (2015) 092010. [arXiv:1504.01245](#).
- [530] M. N. Achasov, et al. [SND], Search for direct production of the $f_1(1285)$ resonance in e^+e^- collisions, Phys. Lett. B 800 (2020) 135074. [arXiv:1906.03838](#).
- [531] R. E. Mitchell, et al. [CLEO], J/ψ and $\psi(2S)$ Radiative Decays to η_c , Phys. Rev. Lett. 102 (2009) 011801, [Erratum: Phys. Rev. Lett. 106, 159903 (2011)]. [arXiv:0805.0252](#).
- [532] M. Ablikim, et al. [BESIII], Measurements of the mass and width of the η_c using $\psi' \rightarrow \gamma\eta_c$, Phys. Rev. Lett. 108 (2012) 222002. [arXiv:1111.0398](#).
- [533] V. V. Anashin, et al., Measurement of $J/\psi \rightarrow \gamma\eta_c$ decay rate and η_c parameters at KEDR, Phys. Lett. B 738 (2014) 391–396. [arXiv:1406.7644](#).
- [534] D. G. Sutherland, Current algebra and the decay $\eta \rightarrow 3\pi$, Phys. Lett. 23 (1966) 384–385.
- [535] J. S. Bell, D. G. Sutherland, Current algebra and $\eta \rightarrow 3\pi$, Nucl. Phys. B 4 (1968) 315–325.
- [536] R. Baur, J. Kambor, D. Wyler, Electromagnetic corrections to the decays $\eta \rightarrow 3\pi$, Nucl. Phys. B 460 (1996) 127–142. [arXiv:hep-ph/9510396](#).
- [537] C. Ditsche, B. Kubis, U.-G. Meißner, Electromagnetic corrections in $\eta \rightarrow 3\pi$ decays, Eur. Phys. J. C 60 (2009) 83–105. [arXiv:0812.0344](#).
- [538] H. Osborn, D. J. Wallace, $\eta - x$ mixing, $\eta \rightarrow 3\pi$ and chiral lagrangians, Nucl. Phys. B 20 (1970) 23–44.
- [539] W. A. Bardeen, L. S. Brown, B. W. Lee, H. T. Nieh, η Decay and Current Algebra, Phys. Rev. Lett. 18 (1967) 1170.
- [540] J. Gasser, H. Leutwyler, $\eta \rightarrow 3\pi$ to One Loop, Nucl. Phys. B 250 (1985) 539–560.
- [541] H. Leutwyler, The Ratios of the light quark masses, Phys. Lett. B 378 (1996) 313–318. [arXiv:hep-ph/9602366](#).
- [542] C. Roiesnel, T. N. Truong, Resolution of the $\eta \rightarrow 3\pi$ Problem, Nucl. Phys. B 187 (1981) 293–300.
- [543] J. Bijnens, K. Ghorbani, $\eta \rightarrow 3\pi$ at Two Loops In Chiral Perturbation Theory, JHEP 11 (2007) 030. [arXiv:0709.0230](#).
- [544] J. Kambor, C. Wiesendanger, D. Wyler, Final state interactions and Khuri-Treiman equations in $\eta \rightarrow 3\pi$ decays, Nucl. Phys. B 465 (1996) 215–266. [arXiv:hep-ph/9509374](#).
- [545] A. V. Anisovich, H. Leutwyler, Dispersive analysis of the decay $\eta \rightarrow 3\pi$, Phys. Lett. B 375 (1996) 335–342. [arXiv:hep-ph/9601237](#).
- [546] K. Kampf, M. Knecht, J. Novotný, M. Zdráhal, Analytical dispersive construction of $\eta \rightarrow 3\pi$ amplitude: first order in isospin breaking, Phys. Rev. D 84 (2011) 114015. [arXiv:1103.0982](#).
- [547] P. Guo, I. V. Danilkin, D. Schott, C. Fernández-Ramírez, V. Mathieu, A. P. Szczepaniak, Three-body final state interaction in $\eta \rightarrow 3\pi$, Phys. Rev. D 92 (2015) 054016. [arXiv:1505.01715](#).
- [548] P. Guo, I. V. Danilkin, C. Fernández-Ramírez, V. Mathieu, A. P. Szczepaniak, Three-body final state interaction in $\eta \rightarrow 3\pi$ updated, Phys. Lett. B 771 (2017) 497–502. [arXiv:1608.01447](#).

- [549] G. Colangelo, S. Lanz, H. Leutwyler, E. Passemar, $\eta \rightarrow 3\pi$: Study of the Dalitz plot and extraction of the quark mass ratio Q , Phys. Rev. Lett. 118 (2017) 022001. [arXiv:1610.03494](#).
- [550] G. Colangelo, S. Lanz, H. Leutwyler, E. Passemar, Dispersive analysis of $\eta \rightarrow 3\pi$, Eur. Phys. J. C 78 (2018) 947. [arXiv:1807.11937](#).
- [551] K. Kampf, M. Knecht, J. Novotný, M. Zdráhal, Dispersive construction of two-loop $P \rightarrow \pi\pi\pi$ ($P = K, \eta$) amplitudes, Phys. Rev. D 101 (2020) 074043. [arXiv:1911.11762](#).
- [552] S. Gardner, J. Shi, Patterns of CP violation from mirror symmetry breaking in the $\eta \rightarrow \pi^+\pi^-\pi^0$ Dalitz plot, Phys. Rev. D 101 (2020) 115038. [arXiv:1903.11617](#).
- [553] S. P. Schneider, B. Kubis, C. Ditsche, Rescattering effects in $\eta \rightarrow 3\pi$ decays, JHEP 02 (2011) 028. [arXiv:1010.3946](#).
- [554] A. Anastasi, et al. [KLOE-2], Precision measurement of the $\eta \rightarrow \pi^+\pi^-\pi^0$ Dalitz plot distribution with the KLOE detector, JHEP 05 (2016) 019. [arXiv:1601.06985](#).
- [555] M. Ablikim, et al. [BESIII], Measurement of the matrix elements for the decays $\eta' \rightarrow \eta\pi^+\pi^-$ and $\eta' \rightarrow \eta\pi^0\pi^0$, Phys. Rev. D 97 (2018) 012003. [arXiv:1709.04627](#).
- [556] P. Adlarson, et al., Measurement of the decay $\eta' \rightarrow \pi^0\pi^0\eta$ at MAMI, Phys. Rev. D 98 (2018) 012001. [arXiv:1709.04230](#).
- [557] V. Dorofeev, et al., Study of $\eta' \rightarrow \eta\pi^+\pi^-$ Dalitz plot, Phys. Lett. B 651 (2007) 22–26. [arXiv:hep-ph/0607044](#).
- [558] B. Borasoy, R. Nisßler, Hadronic η and η' decays, Eur. Phys. J. A 26 (2005) 383–398. [arXiv:hep-ph/0510384](#).
- [559] B. Kubis, S. P. Schneider, The Cusp effect in $\eta' \rightarrow \eta\pi\pi$ decays, Eur. Phys. J. C 62 (2009) 511–523. [arXiv:0904.1320](#).
- [560] T. Isken, B. Kubis, S. P. Schneider, P. Stoffer, Dispersion relations for $\eta' \rightarrow \eta\pi\pi$, Eur. Phys. J. C 77 (2017) 489. [arXiv:1705.04339](#).
- [561] R. Escribano, P. Masjuan, J. J. Sanz-Cillero, Chiral dynamics predictions for $\eta' \rightarrow \eta\pi\pi$, JHEP 05 (2011) 094. [arXiv:1011.5884](#).
- [562] S. González-Solís, E. Passemar, $\eta' \rightarrow \eta\pi\pi$ decays in unitarized resonance chiral theory, Eur. Phys. J. C 78 (2018) 758. [arXiv:1807.04313](#).
- [563] G. Colangelo, J. Gasser, B. Kubis, A. Rusetsky, Cusps in $K \rightarrow 3\pi$ decays, Phys. Lett. B 638 (2006) 187–194. [arXiv:hep-ph/0604084](#).
- [564] J. Gasser, B. Kubis, A. Rusetsky, Cusps in $K \rightarrow 3\pi$ decays: a theoretical framework, Nucl. Phys. B 850 (2011) 96–147. [arXiv:1103.4273](#).
- [565] N. Cabibbo, Determination of the $a_0 - a_2$ pion scattering length from $K^+ \rightarrow \pi^+\pi^0\pi^0$ decay, Phys. Rev. Lett. 93 (2004) 121801. [arXiv:hep-ph/0405001](#).
- [566] N. Cabibbo, G. Isidori, Pion–pion scattering and the $K \rightarrow 3\pi$ decay amplitudes, JHEP 03 (2005) 021. [arXiv:hep-ph/0502130](#).

- [567] D. J. Gross, S. B. Treiman, F. Wilczek, Light Quark Masses and Isospin Violation, *Phys. Rev. D* 19 (1979) 2188.
- [568] B. Borasoy, U.-G. Meißner, R. Nisßler, On the extraction of the quark mass ratio $(m_d - m_u)/m_s$ from $\Gamma(\eta' \rightarrow \pi^0 \pi^+ \pi^-)/\Gamma(\eta' \rightarrow \eta \pi^+ \pi^-)$, *Phys. Lett. B* 643 (2006) 41–45. [arXiv:hep-ph/0609010](#).
- [569] M. Ablikim, et al. [BESIII], Amplitude Analysis of the Decays $\eta' \rightarrow \pi^+ \pi^- \pi^0$ and $\eta' \rightarrow \pi^0 \pi^0 \pi^0$, *Phys. Rev. Lett.* 118 (2017) 012001. [arXiv:1606.03847](#).
- [570] T. Isken, Dispersion relations for mesonic three-body decays, *PoS CD2018* (2019) 068.
- [571] M. Ablikim, et al. [BESIII], Measurement of the Matrix Elements for the Decays $\eta \rightarrow \pi^+ \pi^- \pi^0$ and $\eta/\eta' \rightarrow \pi^0 \pi^0 \pi^0$, *Phys. Rev. D* 92 (2015) 012014. [arXiv:1506.05360](#).
- [572] J. P. Lees, et al. [BaBar], Dalitz plot analysis of $\eta_c \rightarrow K^+ K^- \eta$ and $\eta_c \rightarrow K^+ K^- \pi^0$ in two-photon interactions, *Phys. Rev. D* 89 (2014) 112004. [arXiv:1403.7051](#).
- [573] J. P. Lees, et al. [BaBar], Measurement of the $I = 1/2$ $K\pi$ S -wave amplitude from Dalitz plot analyses of $\eta_c \rightarrow K \bar{K} \pi$ in two-photon interactions, *Phys. Rev. D* 93 (2016) 012005. [arXiv:1511.02310](#).
- [574] E. M. Aitala, et al. [E791], Model independent measurement of S -wave $K^- \pi^+$ systems using $D^+ \rightarrow K \pi \pi$ decays from Fermilab E791, *Phys. Rev. D* 73 (2006) 032004, [Erratum: *Phys. Rev. D* 74 (2006) 059901]. [arXiv:hep-ex/0507099](#).
- [575] M. Ablikim, et al. [BESIII], Measurement of χ_{cJ} decaying into $\eta' K^+ K^-$, *Phys. Rev. D* 89 (2014) 074030. [arXiv:1402.2023](#).
- [576] M. Ablikim, et al. [BESIII], Amplitude analysis of the $\chi_{c1} \rightarrow \eta \pi^+ \pi^-$ decays, *Phys. Rev. D* 95 (2017) 032002. [arXiv:1610.02479](#).
- [577] M. J. Lee, et al. [Belle], Measurement of the branching fractions and the invariant mass distributions for $\tau^- \rightarrow h^- h^+ h^- \nu_\tau$ decays, *Phys. Rev. D* 81 (2010) 113007. [arXiv:1001.0083](#).
- [578] I. M. Nugent [BaBar], Invariant mass spectra of $\tau^- \rightarrow h^- h^- h^+ \nu_\tau$ decays, *Nucl. Phys. B Proc. Suppl.* 253-255 (2014) 38–41. [arXiv:1301.7105](#).
- [579] I. M. Nugent, T. Przedziński, P. Roig, O. Shekhovtsova, Z. Wąs, Resonance chiral Lagrangian currents and experimental data for $\tau^- \rightarrow \pi^- \pi^- \pi^+ \nu_\tau$, *Phys. Rev. D* 88 (2013) 093012. [arXiv:1310.1053](#).
- [580] J. J. Sanz-Cillero, O. Shekhovtsova, Refining the scalar and tensor contributions in $\tau \rightarrow \pi \pi \pi \nu_\tau$ decays, *JHEP* 12 (2017) 080. [arXiv:1707.01137](#).
- [581] I. Lorenz, E. Passemar, a_1 properties in hadronic τ decays, *PoS ICHEP2016* (2016) 539. [arXiv:1702.05432](#).
- [582] M. Mikhasenko, A. Pilloni, M. Albaladejo, C. Fernández-Ramírez, A. Jackura, V. Mathieu, J. Nys, A. Rodas, B. Ketzner, A. P. Szczepaniak [JPAC], Pole position of the $a_1(1260)$ from τ -decay, *Phys. Rev. D* 98 (2018) 096021. [arXiv:1810.00016](#).
- [583] J. M. Link, et al. [FOCUS], Dalitz plot analysis of the $D^+ \rightarrow K^- \pi^+ \pi^+$ decay in the FOCUS experiment, *Phys. Lett. B* 653 (2007) 1–11. [arXiv:0705.2248](#).

- [584] J. M. Link, et al. [FOCUS], The $K^-\pi^+$ S-wave from the $D^+ \rightarrow K^-\pi^+\pi^+$ decay, Phys. Lett. B 681 (2009) 14–21. [arXiv:0905.4846](#).
- [585] G. Bonvicini, et al. [CLEO], Dalitz plot analysis of the $D^+ \rightarrow K^-\pi^+\pi^+$ decay, Phys. Rev. D 78 (2008) 052001. [arXiv:0802.4214](#).
- [586] J. A. Oller, Final state interactions in hadronic D decays, Phys. Rev. D 71 (2005) 054030. [arXiv:hep-ph/0411105](#).
- [587] D. R. Boito, R. Escribano, $K\pi$ form factors and final state interactions in $D^+ \rightarrow K^-\pi^+\pi^+$ decays, Phys. Rev. D 80 (2009) 054007. [arXiv:0907.0189](#).
- [588] D. Boito, J.-P. Dedonder, B. El-Bennich, R. Escribano, R. Kamiński, L. Leśniak, B. Loiseau, Parametrizations of three-body hadronic B - and D -decay amplitudes in terms of analytic and unitary meson-meson form factors, Phys. Rev. D 96 (2017) 113003. [arXiv:1709.09739](#).
- [589] P. C. Magalhães, M. R. Robilotta, K. S. F. F. Guimarães, T. Frederico, W. de Paula, I. Bediaga, A. C. dos Reis, C. M. Maekawa, G. R. S. Zarnauskas, Towards three-body unitarity in $D^+ \rightarrow K^-\pi^+\pi^+$, Phys. Rev. D 84 (2011) 094001. [arXiv:1105.5120](#).
- [590] S. X. Nakamura, Coupled-channel analysis of $D^+ \rightarrow K^-\pi^+\pi^+$ decay, Phys. Rev. D 93 (2016) 014005. [arXiv:1504.02557](#).
- [591] F. Niecknig, B. Kubis, Dispersion-theoretical analysis of the $D^+ \rightarrow K^-\pi^+\pi^+$ Dalitz plot, JHEP 10 (2015) 142. [arXiv:1509.03188](#).
- [592] M. Ablikim, et al. [BESIII], Amplitude Analysis of the $D^+ \rightarrow K_S^0\pi^+\pi^0$ Dalitz Plot, Phys. Rev. D 89 (2014) 052001. [arXiv:1401.3083](#).
- [593] F. Niecknig, B. Kubis, Consistent Dalitz plot analysis of Cabibbo-favored $D^+ \rightarrow \bar{K}\pi\pi^+$ decays, Phys. Lett. B 780 (2018) 471–478. [arXiv:1708.00446](#).
- [594] L. Köpke, N. Wermes, J/ψ Decays, Phys. Rept. 174 (1989) 67.
- [595] C. Adolph, et al. [COMPASS], Resonance Production and $\pi\pi$ S -wave in $\pi^- + p \rightarrow \pi^-\pi^-\pi^+ + p_{\text{recoil}}$ at 190 GeV/c, Phys. Rev. D 95 (2017) 032004. [arXiv:1509.00992](#).
- [596] B. Ketzer, B. Grube, D. Ryabchikov, Light-Meson Spectroscopy with COMPASS, Prog. Part. Nucl. Phys. 113 (2019) 103755. [arXiv:1909.06366](#).
- [597] D. M. Asner, et al., Physics at BES-III, Int. J. Mod. Phys. A 24 (2009) S1–794. [arXiv:0809.1869](#).
- [598] M. Ablikim, et al. [BESIII], Future Physics Programme of BESIII, Chin. Phys. C 44 (2020) 040001. [arXiv:1912.05983](#).
- [599] A. Denig, Recent results from the Mainz Microtron MAMI and an outlook for the future, AIP Conf. Proc. 1735 (1) (2016) 020006.
- [600] B. A. Mecking, et al. [CLAS], The CEBAF Large Acceptance Spectrometer (CLAS), Nucl. Instrum. Meth. A 503 (2003) 513–553.
- [601] D. Lawrence [GlueX], The GlueX detector, AIP Conf. Proc. 1182 (1) (2009) 811–815.
- [602] M. Amaryan, et al., Strange Hadron Spectroscopy with Secondary K_L Beam in Hall D (8 2020). [arXiv:2008.08215](#).

- [603] A. A. Alves, Jr., et al. [LHCb], The LHCb Detector at the LHC, JINST 3 (2008) S08005.
- [604] T. Sato, T. Takahashi, K. Yoshimura (Eds.), Particle and nuclear physics at J-PARC, Vol. 781, 2009.
- [605] A. E. Bondar, et al. [Charm-Tau Factory], Project of a Super Charm-Tau factory at the Budker Institute of Nuclear Physics in Novosibirsk, Yad. Fiz. 76 (2013) 1132–1145.
- [606] H. P. Peng, Y. H. Zheng, X. R. Zhou, Super Tau-Charm Facility of China, Physics 49 (2020) 513–524.
- [607] J. H. Kühn, E. Mirkes, Structure functions in τ decays, Z. Phys. C 56 (1992) 661–672, [Erratum: Z. Phys. C 67 (1995) 364].
- [608] Y. S. Tsai, Production of polarized τ pairs and tests of CP violation using polarized e^\pm colliders near threshold, Phys. Rev. D 51 (1995) 3172–3181. [arXiv:hep-ph/9410265](https://arxiv.org/abs/hep-ph/9410265).